THE UNIVERSITY OF QUEENSLAND

AUSTRALIA

Beach Recovery and Studies in Accretive Sediment Transport

Tomoko Shimamoto

B.E. (UQ)

A thesis submitted for the degree of Doctor of Philosophy at

The University of Queensland in 2016

School of Civil Engineering

Abstract

Erosion has been a focal point in sediment transport research while sediment accretion has been neglected until recent times. This thesis addresses some components of accretive sediment transport through modelling and new experimental measurements.

The existing Grab and Dump model (Nielsen, 1988), a simple sediment transport model over rippled beds, is generalised to reflect a wider range of flow conditions, including acceleration skewed flows, boundary layer streaming, sheet flows, and cases with superimposed current. The revised model is compared to another semi-empirical sediment transport model and is found to have similar predictive abilities for small scale laboratory data. The results show that there are limitations to the model and more work is required to accommodate flows with no acceleration skewness and under the sheet flow regime.

The local approximation method for non-linear irregular waves (Nielsen, 1989) is updated for converting surface elevation data into velocity, as many sediment transport models require velocity time series as input while surface elevation data are more readily measured and available. Data from three experiments are used to investigate this method, which was previously used to convert pressure measurements to surface elevation. The results are compared to the spectral transfer method, and found to perform similarly in most locations apart from near the breakpoint, where it performs better due to an additional multiplier which accounts for the increasingly negative time-mean velocities closer to shore.

New beach profile experiments were undertaken with an emphasis on the beach profile at equilibrium under random waves. The beach profiles were subjected to waves of various heights, with each case run until the profile appeared to be at equilibrium, for both accretive and erosive conditions. It was observed that the profile under accretive conditions behaves in a cyclic manner, where the outer bar is destroyed and recreated from the inner bar moving offshore, a process which also has a much longer time scale compared to the profile evolution under erosive conditions.

The experimental profile measurements are used to evaluate an equilibrium type total sediment transport model utilising the relationship between the dimensionless fall velocity parameter and cross-shore bulk sediment transport proposed by Baldock et al. (2011). The model is applied to both laboratory and field measurements, and compared to an existing equilibrium shoreline model. The model is found to perform well under laboratory conditions where the profiles reach equilibrium but faces limitations with field measurements, which is an area for future work.

Declaration by author

This thesis is composed of my original work, and contains no material previously published or written by another person except where due reference has been made in the text. I have clearly stated the contribution by others to jointly-authored works that I have included in my thesis.

I have clearly stated the contribution of others to my thesis as a whole, including statistical assistance, survey design, data analysis, significant technical procedures, professional editorial advice, and any other original research work used or reported in my thesis. The content of my thesis is the result of work I have carried out since the commencement of my research higher degree candidature and does not include a substantial part of work that has been submitted to qualify for the award of any other degree or diploma in any university or other tertiary institution. I have clearly stated which parts of my thesis, if any, have been submitted to qualify for another award.

I acknowledge that an electronic copy of my thesis must be lodged with the University Library and, subject to the General Award Rules of The University of Queensland, immediately made available for research and study in accordance with the *Copyright Act 1968*.

I acknowledge that copyright of all material contained in my thesis resides with the copyright holder(s) of that material.

Publications during candidature

Atkinson, A, Shimamoto, T, Wu, S, Birren, F & Baldock, TE 2015, 'Beach profile evolution under cyclic wave climates', in *Coasts & Ports Conference 2015*, Auckland, New Zealand

Nielsen, P & Shimamoto, T 2015, 'Bar response to tides under regular waves', *Coastal Engineering*, vol. 106, pp. 1-3.

Shimamoto, T, Nielsen, P & Baldock, TE 2013, 'Updated "grab and dump" model for sediment transport under acceleration skewed waves', in *Coastal Dynamics*, Arcachon, France, pp. 1495-504.

Publications included in this thesis

Shimamoto, T, Nielsen, P & Baldock, TE 2013, 'Updated "grab and dump" model for sediment transport under acceleration skewed waves', in *Coastal Dynamics*, Arcachon, France, pp. 1495-504. - incorporated as part of Chapter 3.

Contributor	Statement of contribution
Shimamoto, T. (Candidate)	Analysed data (100%) Wrote the paper (80%)
Nielsen, P.	Edited paper (10%)
Baldock, T. E.	Edited paper (10%)

Contributions by others to the thesis

No contribution by others.

Statement of parts of the thesis submitted to qualify for the award of another degree

None.

Acknowledgements

I would like to thank firstly my principal supervisor Professor Tom Baldock for his support and guidance. Thank you to Professor Peter Nielsen for his support, encouragement, and sparking my interest in coastal engineering as an undergraduate. Also thank you to Dr David Callaghan for his support, especially regarding numerical modelling and coding. Thank you to the members of the coastal research group from the past and present; I count myself very lucky to have worked in such a friendly, supportive environment.

Thank you to Dr Iván Cáceres, Dr David Hurther, and Dr Dominic van der A for their helpful advice and hospitality when I had the opportunity to visit their research groups. Also thank you to Dr Jose Alsina for his hospitality at UPC and experimental data and Professor Andrew Short for use of the Narrabeen beach profiles.

Thank you to Mr Jason van der Gevel and Mr Stewart Matthews for their help in the hydraulics laboratory during my experiments. Also thank you to Ms Sheng Wu and Mr Alex Atkinson for their assistance in the experimental measurements, and Dr Van Thuan Nguyen for his expertise with the data acquisition software.

Thank you to my extended family for your support. I would especially like to thank my very patient and supportive husband John and our toddler son, for keeping things in perspective.

Finally, thanks to the Australian government and UQ graduate school for funding my scholarships.

Keywords

sediment transport, acceleration skewness, bed shear stress, equilibrium beach profile, beach accretion, beach morphodynamics

Australian and New Zealand Standard Research Classifications (ANZSRC)

ANZSRC code: 090599, Civil Engineering not elsewhere classified, 100%

Fields of Research (FoR) Classification

FoR code: 0905, Civil Engineering, 100%.

Table of Contents

List of Tables

List of Figures

List of Symbols

Symbol	Dimension	Definition
A	[L]	Orbital amplitude
A_b	[-]	Entrainment coefficient (backwards)
A_f	[-]	Entrainment coefficient (forwards)
a	[L]	Equilibrium slope coefficient from Yates et al. (2009)
b	[L^2]	y-intercept value from Yates et al. (2009)
c	[LT^{-1}]	Wave celerity
c_f	[-]	Drag coefficient
C	[-]	Model constant
$C^{\pm}$	[$L^{-2}T^{-1}$]	Change rate coefficient
C_{0s}	[-]	Reference sediment concentration
d	[L]	Sediment grain diameter
d_{50}	[L]	Median sediment grain diameter
D	[L]	Still water depth
D_*	[-]	Non-dimensional sediment grain size
e_d	[-]	Porosity from Jacobsen and Fredsøe (2014)
E	[L^2]	Wave energy, as defined by Yates et al. (2009)
E_{eq}	[L^2]	Equilibrium wave energy, as defined by Yates et al. (2009)
f_{max}	[T^{-1}]	Cut-off frequency for local approximation method
f_G	[T^{-1}]	Group frequency
f_p	[T^{-1}]	Peak frequency
f_w	[-]	Wave friction factor
f_1	[T^{-1}]	Primary frequency
f_2	[T^{-1}]	Secondary frequency
$f_{2.5}$	[-]	Grain roughness friction factor
F_D	[MLT^{-2}]	Drag force
F_P	[MLT^{-2}]	Pressure force
g	[LT^{-2}]	Acceleration due to gravity
h	[L]	Water depth
h_b	[L]	Water depth at the mean position of the breakpoint
H	[L]	Wave height
H_b	[L]	Breaker height
H_o	[L]	Deep water wave height
H_{rms}	[L]	Root-mean-square wave height
H_{rmso}	[L]	Offshore root-mean-square wave height
H_{sig}	[L]	Significant wave height
k	[L^{-1}]	Wave number
L	[L]	Wave length
L_o	[L]	Deep water wave length
m	[-]	Solid fraction or model constant
M	[-]	M^{th} neighbour in Local Approximation method
n	[-]	Power value for various equations or scale parameter
n_H	[-]	Wave height scale
n_L	[-]	Length scale
p_m	various	Parameter value in model
p_p	various	Parameter value in prototype
P	[-]	Phase lag parameter
q_b	[L^2T^{-1}]	Bedload sediment flux

Symbol	Dimension	Definition
q_{net}	[L^2T^{-1}]	Net sediment flux
q_r	[L^2T^{-1}]	Sediment flux from ripple migration
q_s	[L^2T^{-1}]	Sediment flux
q_{ss}	[L^2T^{-1}]	Sediment flux from suspended sediment
Q	[L^3T^{-1}]	Cross-shore bulk sediment transport
Q_e	[L^3]	Cross-shore bulk sediment transport at equilibrium
r	[L]	Hydraulic roughness
s	[-]	Relative density of sediment
S	[L]	Shoreline position
S_{eq}	[L]	Equilibrium shoreline position
T	[T]	Wave period
T_M	[T]	Morphological time scale
u	[LT^{-1}]	Horizontal velocity
$u_\infty(t)$	[LT^{-1}]	Free-stream velocity
u_E	[LT^{-1}]	Eulerian time-averaged velocity
u_m	[LT^{-1}]	Peak bed orbital velocity
u_{max}	[LT^{-1}]	Maximum velocity
u_{rms}	[LT^{-1}]	Root-mean-square velocity
V	[LT^{-1}]	Current speed
w	[LT^{-1}]	Vertical velocity
w_s	[LT^{-1}]	Sediment settling velocity
x	[L]	Horizontal coordinate
x_0	[L]	Horizontal coordinate at h $(h / \tan\beta)$
z	[L]	Vertical coordinate
α_r	[-]	Scaling factor for phase lag from Van der A et al. (2013)
α_s	[-]	Multiplier for streaming velocity
α_v	[-]	Multiplier for current
β	[-]	Beach slope
δ	[T]	Sampling interval for local approximation method
δ_s	[L]	Sheet flow layer thickness
δ_u	[-]	Dimensionless steady flow
ϵ_b	[-]	Bed load efficiency
ϵ_s	[-]	Suspended load efficiency
λ	[L]	Ripple length
η	[L]	Ripple height or surface elevation
$\theta_{2.5}$	[-]	Grain roughness Shields parameter
θ'	[-]	Skin friction Shields parameter
θ_c	[-]	Critical Shields parameter
θ_r	[-]	Effective Shields parameter over ripples
ρ	[ML^{-3}]	Fluid density
ρ_s	[ML^{-3}]	Sediment density
ρ_w	[ML^{-3}]	Water density
$\tau(o,t)$	[$ML^{-2}T^{-2}$]	Bed shear stress
τ'	[$ML^{-2}T^{-2}$]	Skin friction
Φ_B	[-]	Non-dimensional bedload transport rate
φ	[-]	Internal angle of friction of the sediment
φ_τ	[-]	Phase shift between bed shear stress and free stream velocity

Symbol	Dimension	Definition
χ_1	[-]	Dimensionless first odd moment of velocity
χ_2	[-]	Dimensionless second odd moment of velocity
Ω	[-]	Gourlay number
Ω_{eq}	[-]	Equilibrium Gourlay number
ω	[T^{-1}]	Radian frequency, $2\pi/T$
ω_n	[T^{-1}]	Local angular frequency
ω_{max}	[T^{-1}]	Cut off frequency for local approximation method
$\bar{}$		Time-average
$\sim$		Periodic component
Δ		Incremental change

List of Abbreviations

Abbreviation	Definition
AOFT	Aberdeen Oscillatory Flow Tunnel
ADV	Acoustic Doppler Velocimeter
AWG	Acoustic Wave Gauge
BAS	Factor for the wave asymmetry component of sediment transport
BSL	Factor for the downslope gravity component of sediment transport
BUN	Factor for the mean flow component of sediment transport
CIEM	Canal d'Investigació i Experimentació Marítima
COULWAVE	Cornell University Long and Intermediate Wave Modeling Package
DH	Decreasing wave height
GD	Grab-and-Dump model
GWK	Grosser Wellen Kanal
IH	Increasing wave height
LBT	Longshore bar-trough
LTT	Low tide terrace/ridge and runnel
LWT	Large Wave Tank
MSL	Mean sea level
MWS	Mean water surface
RBB	Rhythmic bar and beach
SANTOSS	Sand transport in oscillatory flows in the sheet-flow regime
SASME	Surf and swash zone mechanics
SUSCO	Swash zone response under grouping wave conditions
SWL	Still water line
TBR	Transverse bar and rip
UPC	Universitat Politècnica de Catalunya
UQ	University of Queensland
WG	Wave gauge (resistance wave gauge)

1 Introduction

The interaction of coastal hydrodynamics and sediment movement has been a long studied topic; from experiments such as the prototype scale beach profiles of Saville (1957) to the detailed measurements of sediment concentrations over migrating ripples by Hurther and Thorne (2011), numerous experiments in both the laboratory and field have contributed to the advancement of understanding of coastal processes. Despite these efforts and improvements in the last few decades, including more accurate measurement techniques and increased computational ability, the problem is far from solved.

The sediment transport which occurs on a real beach is a combination of longshore and cross-shore transport; the former is predominantly caused by a longshore current, while the latter is driven by waves and undertow (Dean & Dalrymple, 2002). These two types of transport are often modelled separately, as the models must first be able to predict the sediment transport under simplified conditions (i.e. each in isolation). This thesis will focus on the cross-shore transport component. The cross-shore sediment transport modes are shown in Figure 1-1.

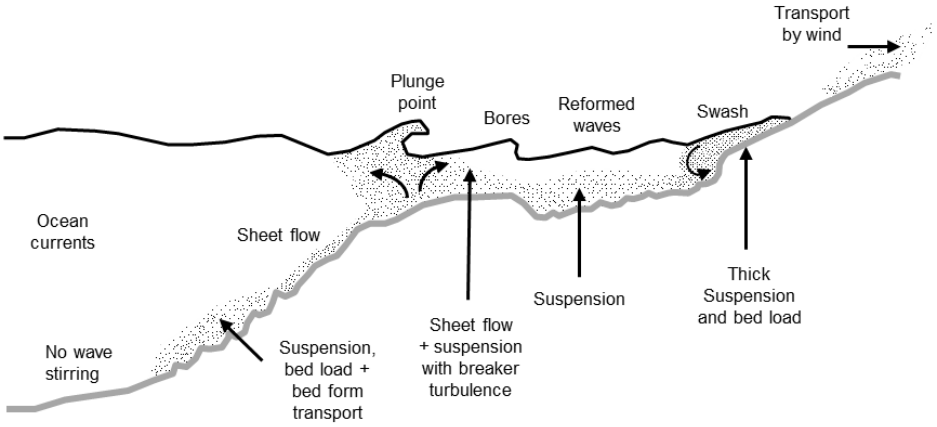

Figure 1-1. Sediment transport modes on a two-dimensional beach, adapted from Nielsen (2009).

The sediment transport modes vary across the profile, depending on the wave conditions and the bed type; transport via suspension or bedload over flat beds compared to rippled beds has different physical characteristics and therefore different sediment transport formulae are required for each condition.

Modelling of cross-shore sediment transport, or shore-normal sediment transport, has been predominantly focused on the erosive process and therefore many process-based morphological models perform well under erosive conditions but struggle to predict onshore sediment transport.

There have been developments in modelling accretive beach profiles using process-based models (e.g. Dubarbier et al., 2015; Kobayashi & Jung, 2012) but many challenges for sediment transport models under accretive conditions still remain.

A flow chart showing the steps to a morphodynamic model is shown in Figure 1-2. Models require hydrodynamic input, often originating from fixed bed fluid mechanics to calculate the fluid velocity vector $\overrightarrow{u_f}$ (a), which is then applied to a sediment transport model (b). The change in sediment transport rate vector $\overrightarrow{q_s}$ and sediment bed elevation z_b is derived by conservation of sediment volume in a control volume (see 6.5.2.2 in Nielsen (2009)) (c), where the rate of change of z_b is approximately equal to the divergence of $\overrightarrow{q_s}$. The equilibrium beach state model (d) bypasses (a) and (b) and predicts beach morphology based on parameterisations, where the rate of change of the beach state is dependent on its disequilibrium. The morphological time scale T_M is unknown for most beaches, but is an essential part of the model. S represents a certain beach state, such as shoreline, and S_{eq} is the equilibrium beach state.

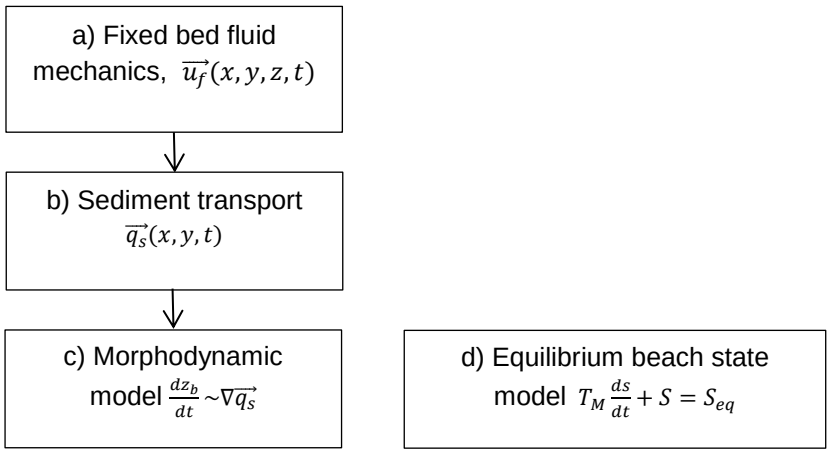

Figure 1-2. Flow chart of a process-based morphodynamic model versus an equilibrium type beach state model

These aforementioned coastal morphological models require input from sediment transport formulae; parameterised models are often preferred over process-based formulae for they are simpler and less computationally intensive (Van der A et al., 2013). Hence one of the main aims of this thesis was to update an existing practical sediment transport model, with an emphasis on factors affecting onshore sediment transport. This addresses Figure 1-2 (b). A net sediment transport model over ripples, the grab and dump model (Nielsen, 1988), is updated through changes to the model formulation to incorporate the effects of flow acceleration and a threshold for sediment transport.

A new method of converting surface elevation to velocity is also investigated. This is due to many practical sediment transport models requiring the near-bed velocity time series as input; often the velocity is not recorded at many locations, but surface elevation data are more easily measured and available. A new method is developed, based on the local approximation method (Nielsen, 1989) originally developed to convert subsurface pressure measurements to surface elevation. This addresses Figure 1-2 (a).

As mentioned previously, there is a wealth of data available that has been measured in both laboratory and field settings. While the whole purpose of coastal sediment dynamics research is to understand the coastal processes on a natural beach, field measurements are often difficult to obtain, and are significantly more complex when compared to those from a laboratory setting. Models predicting various beach states such as shoreline and bar characteristics also often require sufficiently long time series and particular frequencies of measurements; this is why a long period of measurements becomes beneficial and therefore established field sites such as Duck, North Carolina (e.g. Birkemeier, 1984; Larson & Kraus, 1992), Hasaki, Japan (e.g. Banno & Kuriyama, 2014; Kuriyama, 2012) or Narrabeen, Australia (e.g. Harley et al., 2011; Wright & Short, 1984) become very valuable.

The development of coastal monitoring systems such as Argus (Holman & Stanley, 2007), remote sensing technology such as LiDAR, and surveying vehicles such as the CRAB (Coastal Research Amphibious Buggy) (Birkemeier & Mason, 1984) have made field measurements considerably easier. However, measurements can be limited by accessibility, and can be hindered by uncontrolled factors such as unfavourable weather conditions. Therefore in order to investigate a simplified beach under erosive and accretive conditions, laboratory experiments were conducted in the University of Queensland (UQ) hydraulics laboratory. To focus on the cross-shore sediment transport, the beach is kept uniform in the longshore direction in the laboratory flume. The beach profile is able to be measured at high frequency intervals until the profile reaches equilibrium under one wave condition, hence small changes in the beach profile can be detected. Random waves with H_{rms} from 0.01m and 0.1m were run by the wave maker.

An equilibrium type total sediment transport model is developed from this laboratory data, based on the relationship between Gourlay number and cross-shore bulk transport proposed by Baldock et al. (2011). This addresses Figure 1-2 (d).The concept of the equilibrium beach profile or an equilibrium state is often used in coastal engineering, to assign a particular profile shape for particular wave and sediment conditions, for use in design and analysis (Larson et al., 1999). Although in nature, as the wave conditions are constantly changing, the equilibrium profile is a

dynamic concept; an equilibrium profile in nature is more a mean profile over an extended period (Dean & Dalrymple, 2002). There are various models which utilise the disequilibrium of various parameters (i.e. the difference of the present value to the equilibrium value) such as wave energy and Gourlay number to predict beach states (e.g. Splinter et al., 2014; Yates et al., 2009).

This thesis consists of seven chapters in total. The relevant literature on net sediment transport modelling and beach state modelling is reviewed in Section 2. The grab and dump model (Nielsen, 1988), a semi-unsteady, parametric sediment transport model over rippled beds, is developed further and generalised in Section 3. The resulting model is also applied to sheet flow conditions, superimposed currents, and compared to an existing semi-unsteady parametric model from Van der A et al. (2010b). Methods for conversion of surface elevation to velocity are investigated in Section 4. A new method, based on the local approximation method by Nielsen (1989) is developed and applied to three sets of experiments. Beach profile experiments under random waves in the University of Queensland hydraulics flume are outlined in Section 5. Equilibrium type total sediment transport modelling based on the collected experimental data, existing laboratory and field data are discussed in Section 6. Finally, conclusions and loose ends are discussed in Section 7.

2 Literature review

The relevant literature for net sediment transport prediction models and beach state models are reviewed. Three sediment transport models and the model components which contribute to onshore sediment transport are discussed in detail. Various predictors for beach state, such as wave energy, are also reviewed. Three variables which significantly affect the model capabilities and lastly suitable beach states for prediction including shoreline position and bar properties are discussed.

2.1 Net sediment transport prediction models

There are essentially two classes of sediment transport models in development; process-based models and parameterised models. Process-based models consist of detailed equations which represent the physical processes, while parameterised models involve simpler equations which are often semi-empirical. The latter is often preferred as input into morphodynamic models as they are less time-consuming and cover a larger range of flow and bed conditions (Van der A et al., 2013).

Parameterised models can be quasi-steady or semi-unsteady. Quasi-steady models calculate the instantaneous sediment transport rate from the instantaneous velocity or shear stress (e.g. Bailard, 1981) and assume that the sediment entrainment and settling must occur at a time scale much shorter than the wave period (Van der A et al., 2013). This assumption does not hold for cases where phase lag between sediment concentration and velocity is significant, such as sediment transport over rippled beds (e.g. Schepers, 1978; Van der Werf et al., 2007) or fine sediment sheet flow sediment transport (e.g. Van der A et al., 2010a). Semi-unsteady models on the other hand, can accommodate this phase lag.

The focus of this review will be two semi-unsteady models for predicting the net sediment transport, originally by Nielsen (1988) and Dibajnia and Watanabe (1992). The classical Meyer-Peter and Müller (1948) model will also be reviewed, as this steady bedload sediment transport model is the basis for numerous existing sediment transport models under waves.

2.1.1 Meyer-Peter & Müller model

Meyer-Peter and Müller (1948) proposed a steady bedload sediment transport model based on a non-dimensional shear stress, i.e. Shields number, and a critical shear stress at which sediment would commence movement. The Shields number θ represents the ratio of the disturbing and stabilising forces on a sediment grain; the bed shear stress and the lift being the disturbing force and gravity being the stabilising force. The bed shear stress consists of the form drag and the skin

friction components, with the latter component causing the majority of disruption to sediment particles (Nielsen, 1992). The skin friction Shields parameter is given by Eq.(2.1):

$$\theta' = \frac{\tau'}{\rho(s-1)gd_{50}} \tag{2.1}$$

where τ' is the skin friction, ρ is the fluid density, s is the relative density of sediment (typically 2.65), g is the acceleration from gravity, and d_{50} is the median grain diameter. However, as the skin friction stress is often difficult to quantify, often the grain roughness Shields parameter (Nielsen, 1992) is used in its place; it is shown in Eq. (2.2):

$$\theta_{2.5} = \frac{\frac{1}{2}f_{2.5}(A\omega)^2}{(s-1)gd_{50}} \tag{2.2}$$

where $f_{2.5}$ is the grain roughness friction factor, A is the orbital amplitude, ω is the radian frequency. The grain roughness friction factor is based on formulation from Swart (1974) and a roughness of $2.5d_{50}$:

$$f_{2.5} = \exp[5.213\left(\frac{2.5d_{50}}{A}\right)^{0.194} - 5.977] \tag{2.3}$$

The bedload sediment transport model in its non-dimensional state can be written as:

$$\Phi_B = \frac{q_B}{d\sqrt{(s-1)gd}} = C(\theta' - \theta_c)^n \tag{2.4}$$

where the constant C is 8, power n is 1.5 and the critical shear stress θ_c is 0.047 (Meyer-Peter & Müller, 1948). Nielsen (1992) found that C=12 is appropriate for cases with θ larger than 1. Where the skin friction Shields parameter is less than the critical Shields parameter, θ_c, the sediment flux will be zero.

The original Meyer-Peter and Müller (1948) formula has been adapted into quasi-steady bedload models under waves, with different C and n values. Smaller C values (C=5.7) are more suitable for cases with flows near the threshold of sediment motion, while larger C values (C=12) are more suitable for the sheet flow regime (Ribberink, 1998). Cases under oscillatory flow were found to have the best agreement with experimental data when C=11 and n=1.65 (Ribberink, 1998).

Various sediment transport models have used a modified form of the Meyer-Peter and Müller (1948) model as a base (e.g. Nielsen, 2006; Van der A et al., 2013) and this suggests that a power function of the Shields number is still relevant to more complicated sediment transport mechanisms reflected in modern experimental measurement campaigns. For example, some studies have

identified bedload as a sufficient proxy for ripple migration (e.g. Traykovski et al., 1999), comparing measured migration rates with bedload models, which suggests the Meyer-Peter and Müller (1948) type model may also be suitable for sediment transport over ripples.

2.1.2 Grab and dump model

The grab and dump (GD) model (Nielsen, 1988) was one of three simple models developed to predict shore normal sediment flux over horizontal rippled beds for two datasets from small-scale laboratory flume experiments (Schepers, 1978; Tilmans, 1979). The model uses a pick-up function based on parameters which represent parcels of sediment which become entrained ("grabbed") at times of free stream reversal (Nielsen, 1988). One parcel moves a distance *A* onshore and the other moves distance *A* offshore, where *A* is the orbital amplitude. The sediment flux is calculated using Eq. (2.5).

$$q_s = C_{0s} w_s (A_b - A_f) A \tag{2.5}$$

A_b and A_f are backwards (offshore) and forwards (onshore) entrainment coefficients respectively, w_s is the settling velocity, and C_{0s} is the reference concentration for a sine wave of velocity amplitude of the first harmonic, U_1 (Nielsen, 1988). The sediment transport is directed in the opposite direction to the velocity that entrained it. The entrainment coefficients as described by Nielsen (1988) are the velocity amplitude to the sixth power, as the reference concentration was found to be proportional to the cube of the Shields parameter (Nielsen, 1986b). U_{max} is the maximum velocity, U_{min} is the minimum, and these are scaled by U_1:

$$(A_f, A_b) = \left[0.5\left(\frac{U_{max}}{U_1}\right)^6, 0.5\left(\frac{U_{min}}{U_1}\right)^6\right] \tag{2.6}$$

The reference concentration is a function of the Shields parameter modified for flow over ripples, θ_r, (Nielsen, 1986b) shown in Eq.(2.7). The Shields parameter needs to be adjusted for the presence of ripples, as the flow is enhanced at the crest of the ripple; this is shown in Eq. (2.8). η/λ is the ratio of ripple height to ripple length.

$$C_{0s} = 0.005\,\theta_r^{\,3} \tag{2.7}$$

$$\theta_r = \frac{\theta_{2.5}}{(1 - \pi\eta/\lambda)^2} \tag{2.8}$$

The model was applied to the data from Schepers (1978), collected in a small scale wave flume, which measured the sediment flux $q_s(x)$ along a flume with wave conditions which vary due to the presence of free as well as bound 2nd wave harmonics. There were three different d_{50} values tested; 0.125mm, 0.25mm and 0.465mm. The velocity used in the wave flume was in the form of waves with two harmonics and a phase shift angle between the harmonics. Nielsen (1988) found that while

the model was able to predict both the magnitude and cross-shore variation of the sediment flux accurately for the finest sediment (d_{50}=0.125mm), it performed poorly for the coarsest sediment (d_{50}=0.465mm). This is shown in Figure 2-1 below.

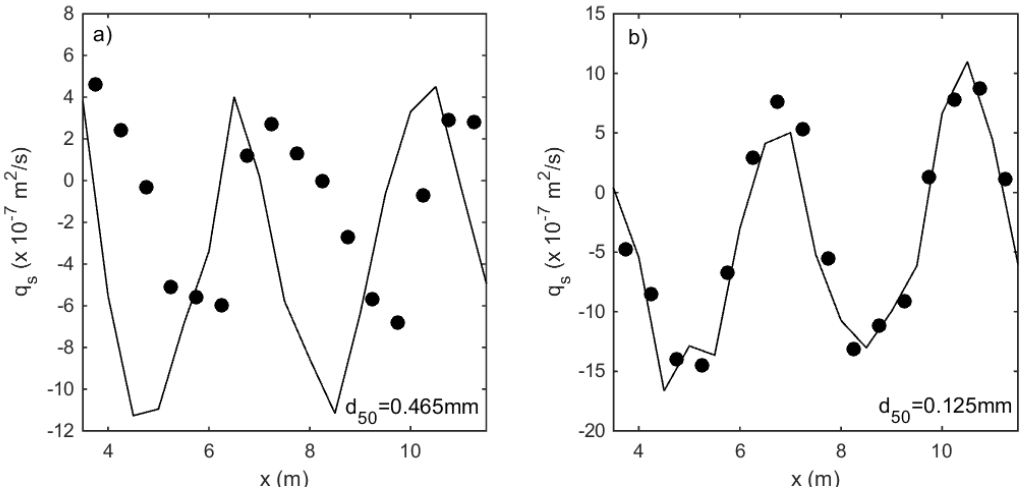

Figure 2-1. Predicted sediment flux from GD model for a) d_{50}=0.465mm and b) d_{50}=0.125mm from Nielsen (1988). Predicted sediment flux (black line), measured sediment flux (circles).

This model requires no calibration parameters and relies on the empirical relationship between C_{0s} and θ_r for the magnitude of sediment transport, but determines the sediment transport direction from the observation that suspended sediment transport in the ripple regime is directed in the opposite direction to the velocity that entrained it. With no calibration required and relatively simple structure, this model is ideal to develop further for application to a wider range of conditions. The poor performance of the model with respect to the coarse sediment suggests that the sediment transport mechanism for this case is fundamentally different to that of the fine sediment, which Schepers (1978) had noted in his original thesis.

The main empirical relationship that determines the magnitude of the sediment transport that occurs for this model is the reference concentration. The relationship described in Eq. (2.7) is based on data between 1965 and 1984, which may require some updating.

2.1.3 'Half- cycle' models

The concept of the 'half-cycle' model was first presented by Dibajnia and Watanabe (1992). This model calculates the net sediment transport rate as the difference between the sediment loads transported during the 'crest' and 'trough' half-cycles. Their model has been incrementally upgraded over the last 20 years, the most recent being Van der A et al. (2013). Dibajnia and Watanabe (1996) extended their half-cycle model for sheet flow (Dibajnia & Watanabe, 1992), to accommodate bedload and suspended sediment transport over ripples (Dibajnia et al., 1994). This model will be reviewed in this section.

Their model is based on a dimensionless parameter Γ, defined

$$\Gamma = \frac{u_c T_c \left(\Omega_c^3 + \Omega'^3_t\right) - u_t T_t \left(\Omega_t^3 + \Omega'^3_c\right)}{(u_c + u_t)T} \tag{2.9}$$

Where Ω_t and Ω_c refers to the sediment load, and subscripts represent which half-cycle the sediment was entrained by, i.e. either trough (*t*) or crest (*c*). The apostrophe refers to when the sediment is transported by a different half-cycle; for example, Ω'_t represents the sediment load which is entrained by the trough half-cycle but transported by the crest half-cycle. Where there is no apostrophe, the sediment is entrained and transported by the same half-cycle. The u_t and u_c terms represent the velocity amplitudes for each half-cycle, and the *T* is wave period.

The non-dimensional net transport rate is then calculated by:

$$\Phi = \frac{q_{net}}{w_s d_{50}}\ 0.0015\ \text{sign}(\Gamma) \cdot |\Gamma|^{0.5} \tag{2.10}$$

where q_{net} is the net sediment flux. The direction of the transport (negative or positive) is incorporated into the model through $sign(\Gamma)$. The components of dimensionless parameter Γ are calculated by Eq. (2.11) to (2.13).

$$u_c^2 = \frac{2}{T_c}\int_0^{T_c} u^2 dt\ , \qquad u_t^2 = \frac{2}{T_t}\int_{T_c}^{T} u^2 dt \tag{2.11}$$

$$\omega_j = \frac{T_{fall}}{T_j} = \frac{u_j^2}{2(s-1)g w_s T_j} \tag{2.12}$$

$$\begin{cases} if\ \omega_j \le \omega_{cr} \begin{cases} \Omega_j = \omega_j T_j \sqrt{\dfrac{(s-1)g}{d_{50}}} \\ \Omega'_j = 0 \end{cases} \\ if\ \omega_j > \omega_{cr} \begin{cases} \Omega_j = \omega_{cr} T_j \sqrt{\dfrac{(s-1)g}{d_{50}}} \\ \Omega'_j = (\omega_j - \omega_{cr}) T_j \sqrt{\dfrac{(s-1)g}{d_{50}}} \end{cases} \end{cases} \tag{2.13}$$

Where *j* is either *t* or *c*, the trough or crest half-cycle respectively.

ω_j represents the ratio of the time period in which the sediment particle is expected to settle to the bed to the half-cycle period. The model suggests that if this ratio is larger than ω_{cr}, hence if the sediment is in suspension longer than the half-cycle period, it will be transported by the next half-cycle. This concept is similar to the use of the Gourlay number, which is the ratio of the wave height to the distance the sediment will fall within one wave period; this is discussed further in

Section 2.3.1.2). The value of ω_{cr} for sheet flow is 1, however for rippled beds, the critical values were found to be ω_{cr}=0.03 for d_{50}=0.2mm and ω_{cr}=0.05 for d_{50}=0.87mm sediment (Dibajnia & Watanabe, 1996).

The cnoidal waves, which Dibajnia and Watanabe (1996)'s model is based on, have velocity skewness, but not acceleration skewness. Therefore the model is not able to account for saw-tooth waves, where acceleration skewness has a significant impact. Velocity skewness is defined by Eq. (2.14) and acceleration skewness is calculated by Eq.(2.15); the overbar represents time-averaging over the timescale of seconds.

$$\text{velocity skewness} = \overline{u^3} / \left(\overline{u^2}\right)^{3/2} \tag{2.14}$$

$$\text{acceleration skewness} = \overline{\left(\frac{du}{dt}\right)^3} / \left(\overline{\left(\frac{du}{dt}\right)^2}\right)^{3/2} \tag{2.15}$$

Various amendments have been made to Dibajnia and Watanabe (1996)'s model to accommodate acceleration skewness (eg. Van der A et al., 2010b; Watanabe & Sato, 2004) and larger mobility numbers (Van der Werf et al., 2006). The predominant features for all of the updated models are to incorporate bed shear stress in lieu of velocity and a larger emphasis on phase lag. Phase lags account for the sediment which become entrained in one cycle and transported in the following cycle; this is dependent on the sediment settling time and the wave period (Van der A et al., 2010b). Additionally, Van der Werf et al. (2006) employed the vortex suspension parameter, which is a ratio of the ripple height to median sediment grain size, as an indicator of sediment transport mechanism. The amended models considerably improve sediment transport predictions compared to the original, albeit becoming more complicated in their formulation. Van der A et al. (2013) with the most recent update of the 'half-cycle' model utilised a large database of over 200 experimental cases, covering a range of flow conditions and sediment transport regimes to develop the model. This model will be discussed in detail.

This model used a revised form of Eq. (2.10), with updated notations, shown in Eq. (2.16):

$$\Phi = \frac{q_s}{\sqrt{(s-1)g d_{50}^3}} = \frac{\sqrt{|\theta_c|}T_c\left(\Omega_{cc} + \frac{T_c}{2T_{cu}}\Omega_{tc}\right)\frac{\theta_c}{|\theta_c|} + \sqrt{|\theta_t|}T_t\left(\Omega_{tt} + \frac{T_t}{2T_{tu}}\Omega_{ct}\right)\frac{\theta_t}{|\theta_t|}}{T} \tag{2.16}$$

Where q_s is the volumetric net transport rate per unit width, s is the relative density of sediment, θ is the Shields parameter, subscripts 't' and 'c' are for trough and crest half-cycles. T_t and T_c are the periods for the trough and crest half-cycle respectively. Similarly, T_{cu} and T_{tu} refer to the period of accelerating flow for the crest and trough half-cycles. The first subscript on the Ω_{ij} terms refers to

the half-cycle when sediment is entrained and the second subscript refers to the half-cycle when the sediment is transported. For example, Ω_{tc} refers to the sediment load which is entrained during the trough period and transported during the crest period. The sediment load is a function of the Shields parameter, shown in Eq. (2.17).

$$\Omega_i = \begin{cases} 0 \quad if\ |\theta_i| \leq \theta_{cr} \\ m(|\theta_i| - \theta_{cr})^n\ if\ |\theta_i| > \theta_{cr} \end{cases} \tag{2.17}$$

Where the subscript 'i' refers to either the trough or the crest half-cycle. The coefficients *m* and *n* are two of the three main calibration parameters in the model.

This updated model has the improvement of differentiating between oscillatory tunnel flow and progressive surface waves. The effects of progressive surface waves are represented through several adjustments to the model; through boundary layer streaming and associated bed shear stress (Nielsen, 2006), adjustments to the settling velocity from vertical orbital velocities, and adjustment of the phase-lag parameter time scale (Kranenburg et al., 2013) to account for the enhanced horizontal sediment flux in the direction of wave propagation stemming from horizontal wave non-uniformity (Van der A et al., 2013).

The model has the advantage of having a large dataset to which the model was calibrated. The SANTOSS (*SANd Transport in OScillatory flows in the Sheet-flow regime*) dataset covers a wide range of conditions, including velocity-skewed, acceleration skewed flows, rippled beds, sheet flow, and graded sands. The full list can be seen in Van der A et al. (2013).

The phase lag parameter which describes the lag between velocity and sediment concentration features prominently in this model; the sediment load Ω_i value is based on whether this value is less than or exceeds the value of 1. The phase lag parameter is calculated as below:

$$P_i = \begin{cases} \alpha\left(\frac{1 \pm \xi\hat{u}_i}{c_w}\right)\frac{\eta}{2(T_i - T_{iu})w_{si}} & if\ \eta > 0\ (ripple\ regime) \\ \alpha\left(\frac{1 \pm \xi\hat{u}_i}{c_w}\right)\frac{\delta_{si}}{2(T_i - T_{iu})w_{si}} & if\ \eta = 0\ (sheet\ flow\ regime) \end{cases} \tag{2.18}$$

The subscript 'i' refers to either *'t'* or '*c*' for trough or crest, α is a calibration coefficient, η is the ripple height, δ_{si} is the sheet flow thickness, w_{si} is the settling velocity, T_i and T_{iu} are the wave period and the accelerating portion of the wave period. The model also makes allowance for the influence of the vertical orbital velocities on settling velocity under progressive surface waves. The term $\left(\frac{1\pm\xi\hat{u}_i}{c_w}\right)$ accounts for the horizontal sediment advection caused by progressive waves, where

c_w is the wave speed and ξ is a calibration factor. The term is $\left(\frac{1+\xi\hat{u}_i}{c_w}\right)$ for the trough half-cycle and $\left(\frac{1-\xi\hat{u}_i}{c_w}\right)$ for the crest half-cycle.

The phase lag parameter is a ratio between a representative stirring height and the settling distance for one half-cycle (Van der A et al., 2013). This contrasts with a formulation of phase lag from pure gradient diffusion, which is proportional to $\frac{\omega\varepsilon_s}{w_s^2}$, which can be thought as $\frac{(\frac{\varepsilon_s}{w_s})/w_s}{T}$; this is essentially a ratio of the typical time the sediment takes to settle to the wave period (Nielsen, 1992), with the ε_s representing diffusivity. In reality, sediment suspension would be a combination of the orderly convection and disorderly diffusion process, but Clark and Nielsen (1996) have found the simpler convection representation is adequate when laboratory data were analysed for sediment suspension.

The half-cycle model, and its most recent revision by Van der A et al. (2013) is able to predict the net sediment transport rate for a range of conditions due to its calibration to a large dataset, but this requires 3 calibration parameters. An additional calibration parameter is also required to account for the impact of progressive waves on the phase lag parameter. This model, while it covers many flow conditions, and predicts the net sediment transport rate within a factor of 2 for 78% of cases tested, is much more complex compared to the GD model.

2.2 Onshore sediment transport components

With increasing information about what drives onshore shore-normal sediment transport, model components are correspondingly updated. Analyses of experimental and field data have suggested flow acceleration is a key parameter for sediment transport (e.g. Hanes & Huntley, 1986; King, 1991). Nielsen (1992) has highlighted that sediment transport models which predict the sheet flow or bedload sediment transport from free-stream velocity (e.g. Bailard, 1981; Ribberink & Al-Salem, 1990) are unable to account for sediment transport under waves with acceleration (sawtooth) skewness, and bed shear stress is a better model driver to reflect this wave condition. Boundary layer streaming has also been identified as a reason as to why measured onshore sediment transport rates in a wave flume are much larger than that from an oscillatory flow tunnel (Ribberink et al., 2000). These three components which affect onshore sediment transport- acceleration skewness, shear stress, and boundary layer streaming will be discussed in this section.

2.2.1 Acceleration skewness

Waves tend to become saw-tooth shaped when coming onshore into shallow water and shoaling, and hence increase in acceleration skewness. Acceleration skewness has been identified as a key parameter in sediment transport, for both suspended load and bedload.

Various experiments have been undertaken to determine the influence of acceleration skewness on sediment transport rate. King (1991) investigated bedload sediment transport under acceleration skewed waves on a flat bed in an oscillatory tunnel. Sawtooth waves with a steep front and mirror images with a steep rear were tested. King (1991) found that the net transport for sediment of d_{50}=1.1mm was approximately 1.7 times higher for the steeper fronted (high acceleration) flow compared to the gradual fronted flow. Watanabe and Sato (2004) conducted sheet flow experiments with sediment with d_{50} of 0.2 and 0.74mm in an oscillatory flow tunnel. They ran experimental cases of acceleration skewed waves with no velocity skewness, so that the impact of acceleration skewness on the sediment transport could be isolated. Watanabe and Sato (2004) showed that the net transport rate is in the direction of the highest acceleration and is positively correlated with acceleration skewness. Van der A et al. (2010a) also undertook experiments in the Aberdeen Oscillatory Flow Tunnel (AOFT) to investigate the effect of acceleration skewness on sheet flow sediment transport. Three sediment sizes were considered, with d_{50} of 0.15mm, 0.27mm, and 0.46mm, under various degrees of acceleration skewness. This study found that the net transport rate was always positive and increased with increasing acceleration skewness. It should be noted that skewness referred here is $\frac{\dot{u}_{max}}{\dot{u}_{max}-\dot{u}_{min}}$, not Fisher skewness, Eq.(2.14). $\dot{u}_{max}$ and $\dot{u}_{min}$ are the maximum and minimum free stream acceleration respectively. The sediment transport under acceleration skewness for fine sand was exceedingly positive, due to the positive velocity peaking early in the positive half-cycle and the negative velocity peaking late in the negative half-cycle; therefore the time to flow reversal is quite long and the sediment has a longer time to settle, so there is less sediment in suspension to be transported by the negative half-cycle (Van der A et al., 2010a).

Various models have incorporated acceleration skewness terms to reflect the observations made from experiments which have isolated acceleration skewness effects (e.g. Silva et al., 2011; Van der A et al., 2010a; Watanabe & Sato, 2004). As mentioned in Section 2.1.3, Van der A et al. (2010b) extended the "half-cycle" concept of transport modelling (Dibajnia & Watanabe, 1992) by incorporating acceleration skewness effects. Hoefel and Elgar (2003) also incorporated acceleration skewness in an energetics model of bar migration at Duck, North Carolina (Gallagher et al., 1998) and noted an improved ability to predict onshore bar migration. Austin et al. (2009) highlighted the significance of acceleration skewness in onshore sediment transport in the field compared to velocity skewness. Acceleration skewness is a significant component of sediment transport processes and should be included in the development of sediment transport models.

2.2.2 Shear stress

Sediment transport models based on velocity exist such as Bailard (1981), who formulated a quasi-steady sediment transport based on the energetics model for both suspended load and bedload by Bagnold (1963), where the sediment load is described in terms of the energy that is required to transport it. While these models have performed well under some circumstances (e.g. Bailard, 1981; Ribberink & Al-Salem, 1990), they are unable to model the sediment transport resulting from sawtooth asymmetry (Nielsen, 1992). As discussed in Section 2.2.1, acceleration skewness has been found to be an essential component in sediment transport modelling (e.g. King, 1991; Watanabe & Sato, 2004); sediment transport rate as a function of bed shear stress in lieu of velocity is able to account for the difference in sediment transport behaviour with varying acceleration skewness. Nielsen (1992) demonstrated that the shear stress based transport rate is able to reflect the impact of the sawtooth asymmetry, having higher τ- values with the faster $\frac{du}{dt}$ of a sawtooth wave (see Figure 2-2). Accordingly, models which have been functions of the velocity have been updated to be functions of shear stress instead; this is discussed in Section 2.1.3.

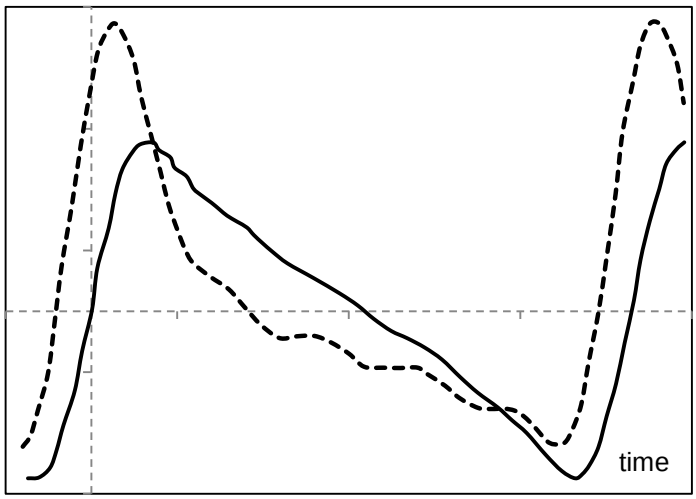

Figure 2-2. Bed shear stress (dashed) and free stream velocity (solid) from Nielsen (1992).

Shear stress has been a key parameter in sediment transport models such as Meyer-Peter and Müller (1948), through the Shields parameter which is essentially a non-dimensional shear stress. As discussed in Section 2.1.1, the grain roughness Shields number $\theta_{2.5}$ is often used in place of the skin friction Shields number θ'; this shear stress would not account for the flow acceleration skewness. Nielsen (1992) suggested a bed shear stress formula based on the free stream velocity u_∞ and acceleration $\frac{du_\infty}{dt}$,

$$\tau(o,t) = \frac{1}{2}\rho f_{2.5} A(cos\varphi_\tau\, \omega\, u_\infty(t) + sin\varphi_\tau \frac{du_\infty}{dt}) \quad (2.19)$$

with φ_τ representing the phase shift between velocity and shear stress. Nielsen and Callaghan (2003) and Nielsen (2006) utilised this shear stress equation as input into a Meyer-Peter and Müller (1948) type model and fitted a $\varphi_\tau$value of 40 degrees and 51 degrees respectively using data from Ribberink et al. (2000) and Watanabe and Sato (2004). There is no set guideline for determining φ_τ, therefore currently it acts similarly to a calibration coefficient. As more datasets are compared to this shear stress equation, the prediction of φ_τ could be improved.

An added complication of using shear stress as a model driver is that literature refers to the "bed shear stress" in mobile beds but its definition is unclear due to its highly variable nature (Nielsen & Guard, 2010). While bed shear stress is obvious in immobile beds, in mobile beds, it varies significantly with changes in elevation; a clear definition is perhaps required in future iterations of sediment transport models requiring shear stress as input.

2.2.3 Boundary layer streaming

Boundary layer streaming has been considered to be a characteristic which is found in real waves, and it has been found to be directed onshore (Longuet-Higgins, 1957). It has been considered to be important in flat beds, but has been found to be heavily dependent on the bed roughness and the velocity skewness (Davies & Villaret, 1999). Bijker et al. (1974) observed a marked decrease in near-bed drift over rippled beds compared to smooth or flat sandy bed. Davies and Villaret (1999) also observed and modelled Eulerian drift from weakly asymmetric waves on rough and rippled beds and found that the drift was reversing at the edge of the boundary layer. This suggests that while boundary layer streaming for rippled beds may impact the velocity, the impact would be weaker compared to that of a flat bed.

Sediment transport models incorporate boundary layer streaming through bed shear stress (e.g. Henderson et al., 2004; Nielsen & Callaghan, 2003; Van der A et al., 2013). Nielsen (2006) incorporated boundary layer streaming into a Meyer-Peter and Müller (1948) style model by adding the streaming related bed shear stress into their calculations, shown in Eq. (2.20).

$$-\rho(\widetilde{\tilde{u}\tilde{w}})_\infty = \rho \frac{1}{4\sqrt{2}} k A^3 \omega^2 f_w \quad (2.20)$$

$\tilde{u}$ is the horizontal oscillatory velocity, $\tilde{w}$ is the vertical oscillatory velocity, k is the wave number, A is the orbital amplitude, ω is the radian frequency, and f_w is the wave friction factor. The subscript ∞ refers to being above the bottom boundary layer.

As the model from Nielsen and Callaghan (2003) also incorporated acceleration effects, the relative importance of the boundary layer streaming could not be isolated. Additionally, as the data from Ribberink et al. (2000) which the model was tested on did not detail boundary layer streaming, it was not possible to directly compare the streaming related bed shear stress.

Schretlen et al. (2010) observed clear onshore streaming in the wave boundary layer from their experiments in the prototype scale wave flume at GWK. Additionally, Aagaard et al. (2012) presented field measurements from Pearl Beach, NSW which showed onshore Eulerian mean current approximately in the 10cm immediately above the bed, which is attributed to boundary layer streaming. The importance of boundary layer streaming hence should be considered in sediment transport modelling, especially for onshore directed flux.

2.3 Beach state modelling

Rather than focus on the individual processes which govern sediment transport, there are models which analyse the key parameters which are thought to reflect the general behaviour of the beach. There are various models which strive to predict certain characteristics of a beach profile, such as shoreline position or bar crest elevation. They can be considered 'beach states', driven by a multitude of variables such as wave characteristics and antecedent conditions. A number of parametric models for beach states will be reviewed in the following sections, through suitable model driver choices, variables which influence the beach state, and finally various 'beach state' alternatives.

2.3.1 Suitable predictors for beach state

Suitable parameters to determine the beach state have been investigated by numerous researchers to classify beaches more easily and to subsequently establish if a beach will accrete or erode under particular conditions. The models often combine a parameter which describes the wave characteristics and a parameter to reflect the sediment characteristics (Larson et al., 1990). Beach state prediction models are driven by a variety of parameters; they are reviewed in the following sections.

2.3.1.1 Wave steepness

Wave steepness is related to wave asymmetry and subsequently influences onshore and offshore sediment transport (Kraus et al., 1991). Analysis of beach profiles by Johnson (1949) established the link between deep water wave steepness H_o/L_o and whether the equilibrium beach profile would be a "ordinary" or "storm" profile, with the former possessing no offshore bar and the latter exhibiting an offshore bar and additional intermediate bar. After exhaustive analyses of various non-dimensional parameters relative to erosive and accretive profiles, Kraus et al. (1991) found that

a function of the wave steepness and 3rd power of the non-dimensional fall velocity, $\frac{H}{w_s T}$ can differentiate whether a beach is erosive or accretive. These relationships however, are basically a criterion to determine sediment transport direction (Larson et al., 1990).

The wave steepness also can be used as a model driver; Davidson et al. (2010) changed the driver of their Gold Coast shoreline prediction model to offshore wave steepness from non-dimensional fall velocity but found that the model skill decreased considerably.

2.3.1.2 Gourlay number

Gourlay (1968) first identified the non-dimensional fall velocity as a parameter which can differentiate between types of equilibrium beach profiles; it is shown in Eq. (2.21), and will be referred to as the Gourlay number. H is the wave height, T is the wave period, and w_s is the sediment settling velocity.

$$\Omega = \frac{H}{w_s T} \tag{2.21}$$

The parameter represents the ratio of the wave height to the distance the sediment particle will fall in one wave period. If the Gourlay number is smaller than 1, the sediment movement is expected to be largely bedload, and if larger than 1, it is expected to be predominantly suspended load (Gourlay, 1968).

Wright and Short (1984) associate morphodynamic states with the Gourlay number, using breaker height H_b as the numerator. Beaches are classified as dissipative to reflective with four intermediate states in between. Dissipative beaches are typically flat, with high wave energy and therefore erosive, while reflective beaches are steep with low wave energy and accretive. From data collected from 11 Australian beaches, they found threshold values between accretive and intermediate profiles to be $\Omega \sim 1$ and the threshold between intermediate and dissipative beaches to be $\Omega \sim 6$ (Wright & Short, 1984).

Wright et al. (1985) proposed that a disequilibrium value of Ω (i.e. how much it diverges from equilibrium Gourlay number, Ω_{eq}) would correlate to the rate of change of beach state. The Ω_{eq} is defined as where the beach state derivative with respect to time is zero. The rate of change of beach state over time was presented as a function of the disequilibrium $\Omega - \Omega_{eq}$ and an expression for wave energy in the form of Ω or Ω^2. Figure 2-3 shows the relationship between Ω and beach state. As Ω becomes larger, the beach erodes and changes beach state faster, while smaller Ω leads to accretion and slower change in beach state. The stable region is where the beach changes are very small and do not have a set direction. The abbreviated beach states referred to in the figure stand for

low tide terrace/ridge and runnel (LTT), transverse bar and rip (TBR), rhythmic bar and beach (RBB), and longshore bar-trough (LBT); their features are detailed in Wright et al. (1985).

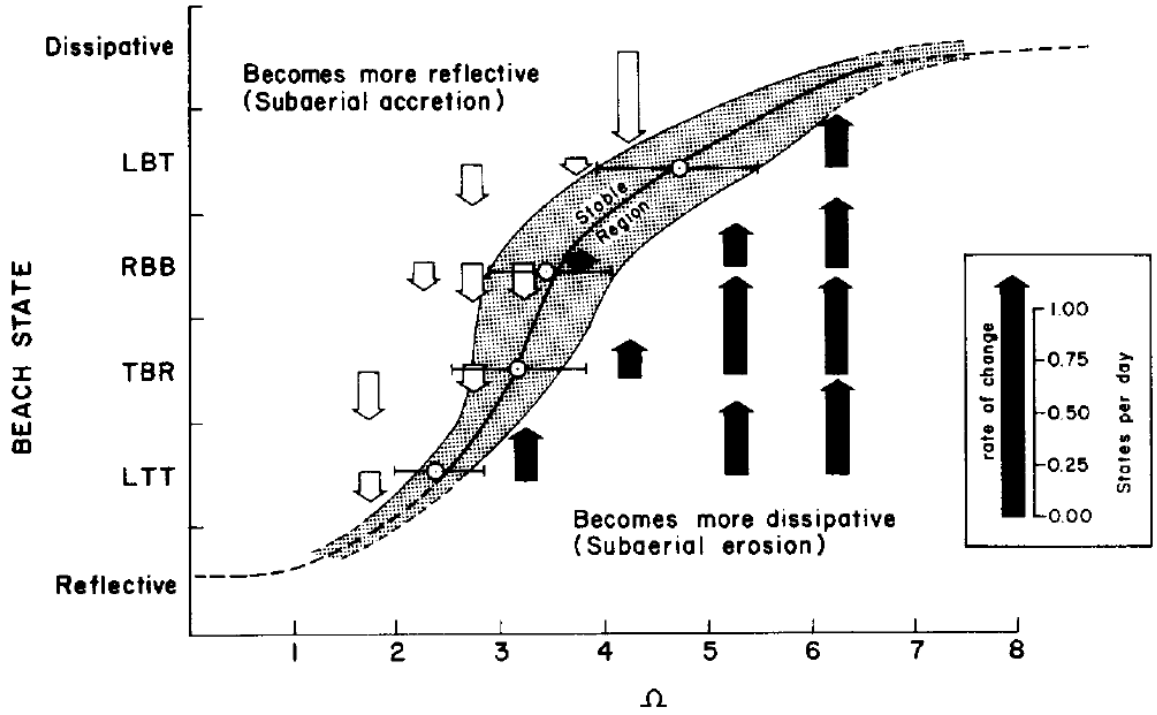

Figure 2-3. Gourlay number vs beach state (Wright et al., 1985)

Although the dataset available did not validate this hypothesis, using the disequilibrium of Ω features in many recent equilibrium shoreline models (e.g. Davidson et al., 2013; Splinter et al., 2014; Yates et al., 2009) and have been successful in the prediction of shoreline change.

Hattori and Kawamata (1980) additionally incorporated beach slope into the Gourlay number, $\frac{H}{w_s T}\tan\beta$, where $\tan\beta$ is the surf zone slope measured between the breaker location and shoreline. Their model is defined by Eq. (2.22), where H_o is the deep water wave height and L_o is the deep water wave length.

$$\frac{\left(\frac{H_o}{L_o}\right)\tan\beta}{w_s/gT} = C \tag{2.22}$$

This equation can be simplified into Eq. (2.23).

$$\frac{H_o \tan\beta}{w_s T} = C \tag{2.23}$$

C is a constant, and values smaller than C result in accretion and values larger than C result in erosion. They found a distinct change in beach profile for C=0.5 from small-scale laboratory

experiments. However, as Kraus et al. (1991) pointed out, slope is difficult to define, and is related to the sediment size (hence fall velocity) so the inclusion of the slope may not be necessary.

Davidson and Turner (2009) developed a model for predicting the Gold Coast shoreline on a seasonal to inter-annual timescale using the Gourlay number as a driver. The shoreline, defined here as the intersection of the mean water surface (MWS) and the sand surface; where the MWS is the water surface which reflects wave setup and setdown. It was found to respond to changes in Ω with time lags of 1 to 3 months, as does the rate of change of the shoreline position (Davidson & Turner, 2009). Davidson et al. (2010) simplified Davidson and Turner (2009)'s profile model from 2-D to 1-D. This model was used to predict future shoreline positions. The governing equation is

$$\frac{dx(t)}{dt} = b + c(\Omega_{eq} - \Omega(t))\Omega^{k}(t) \tag{2.24}$$

Where $\frac{dx(t)}{dt}$ is the rate of the cross-shore movement of the shoreline, b is the linear trend of the shoreline position, c and k are calibration parameters, and $\Omega_{eq} - \Omega(t)$ is the disequilibrium component. This model showed excellent model skill when predicting shoreline change over a period of 2.5 years.

Davidson et al. (2013) further developed the model named *ShoreFor* to rectify the previous model's inability to predict the change in shoreline for Narrabeen Beach NSW, with the following governing equation, shown in Eq. (2.25).

$$\frac{dx}{dt} = b + c^{\pm}P^{0.5}(\Omega_{eq}(t) - \Omega(t)) \tag{2.25}$$

The major changes include the time-varying equilibrium Gourlay number $\Omega_{eq}(t)$, and the inclusion of deep water wave power P as a model driver, and the separation of the free parameter c under erosive and accretive conditions. b is the linear trend of the shoreline position. The time-varying equilibrium, defined as the weighted mean antecedent Gourlay number, was adopted to reflect the effect of significant hysteresis in the Narrabeen data (Davidson et al., 2013). The key parameter in the time-varying equilibrium is the 'memory decay' parameter (Wright et al., 1985), which fits a time period to when the Gourlay number reaches various percentages of the instantaneous Gourlay number; this parameter reflects the speed of the shoreline response (Davidson et al., 2013). The calibration of this parameter showed Narrabeen beach had a significantly quicker shoreline response compared to the Gold Coast, and subsequently significantly improved the model performance for Narrabeen.

Splinter et al. (2014) applied a similar model to Davidson et al. (2013) to twelve shoreline datasets from seven different sites, with the aim to further generalise the *ShoreFor* model. They found that the calibration coefficients which represented the antecedent conditions and the sediment transport rate were significantly dependent on the Gourlay number for all sites (Splinter et al., 2014).

2.3.1.3 Wave energy

Wave energy has been used in various shoreline prediction models, whether using various powers of wave energy E (e.g. Yates et al., 2009) or other functions of wave energy, such as $(\log(E))^2$ (Banno & Kuriyama, 2014). Ludka et al. (2015) found that utilising wave energy instead of various functions of H and T resulted in least normalised mean square errors in their model. In Yates et al. (2009), it was found that a 0.5, 1 or 2 power of E in their model was equally successful in predicting the shoreline. Yates et al. (2009) developed a shoreline prediction model using a linear relationship between the shoreline position and wave energy; it is driven by the disequilibrium in wave energy. The governing equations of the model are shown in Eq.(2.26) to (2.29).

$$\frac{dS}{dt} = C^{\pm}E^{1/2}\Delta E \tag{2.26}$$

$$\Delta E(S) = E - E_{eq}(S) \tag{2.27}$$

$$E_{eq}(S) = aS + b \tag{2.28}$$

$$S_{eq}(E) = \frac{E - b}{a} \tag{2.29}$$

Where S is the shoreline position, a is the slope and b the y-intercept from the line E_{eq} (refer to Figure 2-4). $C^{\pm}$ is the change rate coefficient, with C^{-} for erosion and $C^{+}$for accretion, which are also calibration coefficients. Note that E in this paper is defined as $E = \frac{{H_{sig}}^2}{16}$, which does not take into account ρg.

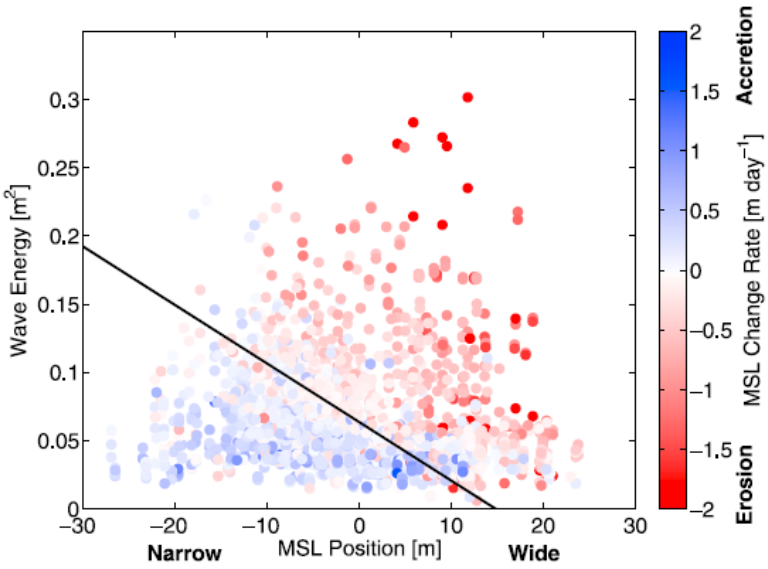

Figure 2-4. Shoreline position vs wave energy, with dots indicating shoreline change rate averaged between survey dates from Yates et al. (2009). The solid line is the best fit E_{eq} line from which coefficients *a* and *b* are calculated.

With any initial shoreline position S_0, the profile arrives at the same S_{eq} for a given E. S_{eq} is determined solely by the slope and the *y*-intercept from Figure 2-4, which is found from an analysis of a wide range of shoreline positions and corresponding wave energy. The model is able to predict the shoreline position for three Southern Californian beaches with 4 tuned calibration parameters.

The simplified empirical relationship between shoreline position and wave energy is not without criticism; Jara et al. (2015) consider the weighting factor of $E^{½}$ in Eq. (2.26) redundant, and are critical of its arbitrary nature. The claim is supported by findings from models by Yates et al. (2009) and Miller and Dean (2004) where various powers of *E* and *H* were trialled as the weighting factor; the models were found to function equally well in all cases. Jara et al. (2015) developed a function with varying slope relating the wave energy with the equilibrium shoreline position, called the Equilibrium Energy Function (EEF); it therefore rids the model of the need for an arbitrary weighting factor. Their EEF is an alternative to the relationship from Figure 2-4 from Yates et al. (2009) and represented by a relationship between several beach characteristics, including berm height and sediment volume in the active beach profile, as well as the wave energy and shoreline position. The relationship is shown in Figure 2-5.

Their equation for the rate of change of shoreline position is shown in Eq. (2.30):

$$\frac{dS(t)}{dt} = C^{\pm}(E - E_{\infty}(S)) \tag{2.30}$$

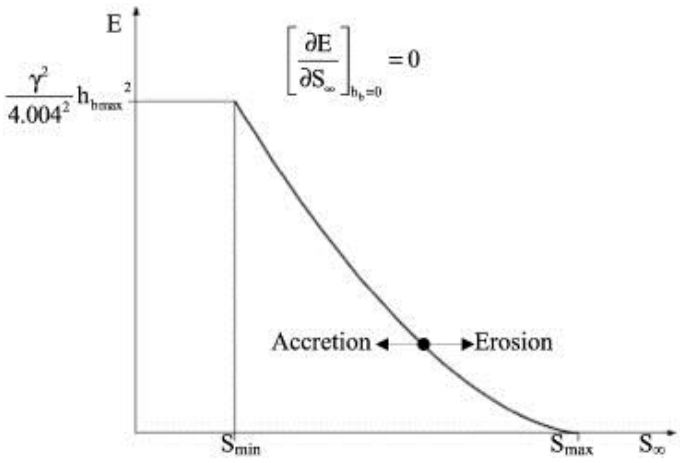

Figure 2-5. EEF scheme showing relationship between shoreline (*S*) and wave energy (*E*) from Jara et al. (2015)

This equation is very similar to the equation from Yates et al. (2009), but without the term $E^{½}$, which the authors insisted was not required for the model. However the lack of the $E^{½}$ term suggests that the shoreline still moves when there is zero energy.

Despite the method from Yates et al. (2009) of obtaining a linear relationship between *E* and shoreline position being over-simplified, a more complex asymptotic relationship between *E* and shoreline position would require another model parameter. While the asymptotic relationship would rid the model of an unrealistic upper limit to shoreline position when *E*=0, the data from Nova Icaria beach presented in Jara et al. (2015) do not clearly show an asymptotic relationship as *E* tends to 0. For a bulk-response model, the decision to employ some simplified methods is perhaps justified.

Their parabolic nature of the EEF as opposed to the linear relationship between shoreline and energy adopted by Yates (2009) is more realistic, yet a plot of their predicted and measured shoreline data do not suggest a significant improvement. Their model reflects the general behaviour of the shoreline, hence performing well for the medium to long term time scales, as shown in their Figure 8, shown in Figure 2-6.

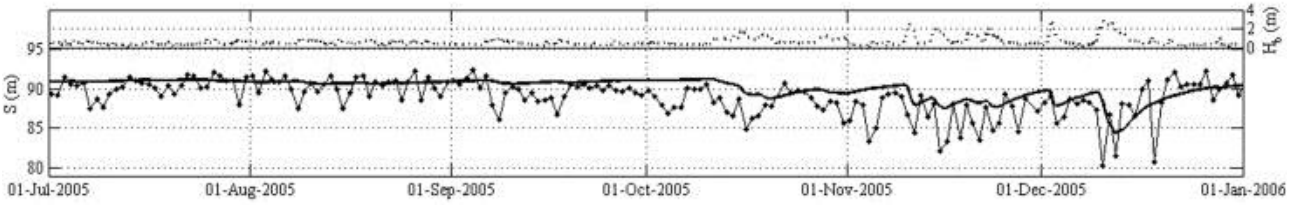

Figure 2-6. Extract from Jara et al. (2015)'s Figure 8, points show measurements and solid line shows the model results.

The key relationship between wave energy and beach state is one which requires the balance between model simplicity and sufficient parameters which reflect the overall behaviour of the beach profile, which would also be affected by the time period in which the model is expected to perform.

2.3.2 Other significant variables

There are several other beach characteristics which contribute to the beach state, which are not necessarily the key drivers for the models, but should be considered during model formulation and calibration. These include sediment size, the time period over which wave data are averaged, and antecedent conditions of the beach. These will be discussed briefly in the following section.

2.3.2.1 Sediment size

Sediment grain size is a key variable in beach state modelling, as the use of sediment fall velocity in many models can attest (e.g. Davidson et al., 2010; Wright et al., 1985) . The size of the sediment can change the sediment transport rates significantly; Yates et al. (2011) suggested that a beach with coarser sediment may have a stabilising effect and hence cause less change in shoreline position compared to a beach with a finer sediment. Yates et al. (2011) also found that their shoreline prediction model coefficients were transportable for a different beach with similar median sediment size (d_{50}=0.3mm), despite different wave conditions; this suggests that sediment size significantly influences the beach state, independent of wave conditions.

2.3.2.2 Wave averaging periods

With any dataset, the way in which it is processed can influence the model results significantly. Yates et al. (2009) had stressed the significance of using hourly wave data in their shoreline prediction model and warned against excessive averaging of wave input data, for it would miss individual storms and hence negatively affect model performance. Davidson et al. (2011) investigated the effect of wave averaging on shoreline model performance and concluded that for their Gold Coast shoreline prediction model, wave averaging over a maximum of 2 days did not inversely affect model performance, but quickly degraded when a longer time period was used to average wave data. When the measurements of beach states and the forces which drive them are measured at varying frequencies, it tends to cause issues with correlation (e.g. Larson & Kraus, 1992; Quartel et al., 2008). Therefore sensitivity analyses (e.g. Davidson et al., 2011) are useful in understanding both the critical timescales of the wave averaging periods and the resulting beach states.

2.3.2.3 Antecedent conditions

Antecedent conditions in shoreline models have been incorporated in the form of previous shoreline position (Yates et al., 2009) or a weighted average of the antecedent Gourlay number (Davidson et al., 2013; Splinter et al., 2014; Wright et al., 1985). Wright et al. (1985) developed a weighted mean Gourlay parameter, $\bar{\bar{\Omega}}$, which reflects antecedent conditions of 30 days before the measurement date; they found this is a better parameter for predicting beach state compared to Ω. Splinter et al. (2014) fit a function of weighted Gourlay number to the response factor ϕ, which essentially reflects the required period for the antecedent conditions. The weighted Gourlay number is the mean Gourlay number multiplied by the ratio of the temporal mean of the standard deviation at yearly and monthly intervals; larger values of this ratio suggests more seasonal behaviour and smaller values suggest the beach is more prone to effects of individual storms (Splinter et al., 2014). The inclusion of antecedent conditions becomes essential when beaches have significant hysteresis, as Davidson et al. (2013) found with Narrabeen beach data.

2.3.3 Suitable 'beach states'

The selection of a beach state to model is a difficult decision; it would be influenced by various factors including the ease of measurement of the beach state, the time scale over which the model seeks to predict the beach state, and the morphological time scale of the beach state. Some common 'beach states' will be discussed in this section.

2.3.3.1 Shoreline position

The shoreline position can be defined in a variety of ways; (see Boak and Turner (2005) for a review) for example, Yates et al. (2009) defined the shoreline as the cross-shore location of the mean sea level (MSL) contour, while Yates et al. (2011) used the Mean High Water (MHW) contour, as the MSL contour was submerged and hence difficult to access. Phillips et al. (2015) modelled beach width, the distance from the MHW contour to a fixed reference point in the backshore, therefore essentially the same as the shoreline position.

Many of the models which predict the shoreline are in fact predicting rate of change of shoreline position and often related this to how far the shoreline is to the equilibrium shoreline position, or the disequilibrium of the shoreline position (e.g. Miller & Dean, 2004; Splinter et al., 2014; Yates et al., 2009). Davidson et al. (2010)'s shoreline prediction model, outlined in Section 2.3.1.2, predicted erosion quite well but the suddenly accreting shoreline is largely unable to be represented by this model. This situation occurs when a bar moves onshore hence causing a sudden movement of the shoreline, otherwise referred to as bar welding. However, with a stronger emphasis on antecedent conditions, the prediction is significantly improved (Davidson et al., 2013; Splinter et al., 2014).

Many of these models are based on coastal monitoring systems like Argus (Holman & Stanley, 2007), an optical remote sensing system from which the shoreline can be identified from images. Determining the shoreline position has been made significantly easier with this technology and data are able to be collected more frequently compared to measurements such as beach profile. While this is suitable for certain coastlines where the shoreline can represent the sediment transport occurring over the profile, but for some coastlines, (e.g. where bar welding routinely occurs) it may not be a suitable approach.

2.3.3.2 Bar properties

Plant et al. (1999) developed a data-driven model predicting the cross-shore locations of the bar crest. The model formulation is similar to that of Wright et al. (1985), where the rate of change of the bar crest position is a function of how far the bar crest is from its equilibrium position. The rate of change of the bar crest position is also driven by the wave height, and performs well in predicting bar crest location for 7 years of data at Duck, North Carolina. Using a similar model, the bars in three other locations on the Gold Coast, Australia, Egmond, the Netherlands, and Hasaki, Japan were found to be well predicted when the local wave height was used as the model driver (Pape et al., 2010).

Larson and Kraus (1992) analysed longshore bars measured biweekly over an 8 year period at Duck, North Carolina. Both the inner bar and outer bar features were calculated, including depth to bar crest, the centre of mass, and the bar volume. These parameters were then correlated with the wave characteristics, which included mean significant wave height, mean peak spectral period and mean wave steepness. There was no correlation between the bar characteristics and the wave properties; this is thought to stem from the rapid pace of the bar response not being represented by the averaged wave characteristics as well as being influenced by other parameters such as the profile disequilibrium (Larson & Kraus, 1992). This further highlights the significance of considering timescales of the morphological characteristics when developing beach state models.

2.3.3.3 Cross-shore bulk sediment transport

Cross-shore bulk sediment transport is used as a measure of sediment transport across the active portion of the beach profile which is calculated by integrating the net sediment transport along the beach profile (Baldock et al., 2011; Jacobsen & Fredsøe, 2014).

The local sediment transport rate between two profiles can be calculated by:

$$q(x_i) = q(x_{i-1}) + \int_{x_{i-1}}^{x_i} m \frac{\Delta z}{\Delta t} dx \tag{2.31}$$

Where $q(x_i)$ is the integrated sediment transport (m^2/s) at position i, m is the solid fraction (usually 0.6), Δz is the change in bed elevation, and Δt is the difference in measurement periods. The cross-shore bulk transport is calculated by integrating over the x-limits.

$$Q = \int_{x_{min}}^{x_{max}} q\,(x)dx \tag{2.32}$$

Jacobsen and Fredsøe (2014) found with their morphological breaker bar model that the cross-shore bulk transport approached an equilibrium value with constant forcing, suggesting it was moving towards an equilibrium value. The cross-shore bulk transport represents the direction of net sediment transport and hence is a single parameter which can represent the general beach profile. It is however vital that the measured profile is measured sufficiently far offshore to capture the entire active profile; this is often where data from the field is lacking, as the measured profile is not wide enough.

2.4 Summary

Sediment transport prediction models of the parametric, semi-unsteady variety were reviewed, due to their reflection of an essential component of sediment transport, the phase lag between the sediment concentration and velocity. The two models reviewed, the grab and dump and the half-cycle models are able to capture the physical processes in relatively simple equations, although the empirical relationships which govern the models may require updating as more experimental data becomes available. The grab and dump model is especially a simple model which shows potential for further development. The classic Meyer-Peter and Müller (1948) model was also briefly reviewed; the traditional model has so far been widely applied to bed load models under waves and also to sediment transport from ripple migration.

Three components of sediment transport which are significant to onshore sediment transport were discussed, these being acceleration skewness, shear stress and boundary layer streaming. Increased acceleration skewness led to increased sediment transport (Van der A et al., 2010a) and was shown to be better represented by shear stress rather than velocity (Nielsen, 1992). Boundary layer streaming has been identified in real waves in the laboratory and the field, and is consistently directed onshore; its contribution to bed shear stress has been incorporated in some sediment transport models (Nielsen & Callaghan, 2003). Further development of net sediment transport prediction models should consider incorporating these components.

Beach state modelling was also reviewed, firstly by the common drivers of models. Wave steepness, Gourlay number and wave energy all have varied success at predicting the beach state depending on the type of the beach. Wave steepness is generally used to determine the direction of the sediment

transport, while Gourlay number and wave energy is often used to drive equilibrium type models. The multiplier in disequilibrium based models (e.g. the $E^{1/2}$ term in Eq. (2.26)) has been criticised as being arbitrary and unnecessary (Jara et al., 2015).

Significant variables in beach state modelling including sediment size, wave averaging periods and antecedent conditions also contribute to the performance of beach state prediction models. Sediment size impacts beach morphological behaviour and this is reflected through the settling velocity in the Gourlay number and adjustments to model parameters based on sediment size (Yates et al., 2011). The wave averaging period for the model inputs was found to influence the beach state model predictive capability; if individual storms were not reflected, the model performance was inversely affected. The significance of the antecedent conditions was also found to be related to the type of beach (Splinter et al., 2014); averaging time scales can range from the individual storm timescale to the long-term, seasonal timescale for different beach types.

Lastly, beach states which have been modelled by existing models; the shoreline position, various bar properties, and cross-shore bulk sediment transport, were reviewed. The shoreline position was found to be an easily measured beach state, although some features such as bar welding which causes significant movement of the shoreline, is difficult to reflect in morphological models. Bar properties such as the crest location can be predicted by wave characteristics; however the wave properties must reflect the time scale of the bar movement in order for models to succeed. Finally, cross-shore bulk sediment transport was shown to be an alternative beach state which can reflect the behaviour of the active beach profile.

3 Further development of the grab and dump model

Through the review of the available sediment transport models in Section 2.1 it was shown that the 'half-cycle' concept from Dibajnia and Watanabe (1992) has been improved upon with contributions from Kranenburg et al. (2013) and Dohmen-Janssen (1999), among others. Another semi-unsteady model is the grab and dump (GD) model from Nielsen (1988), which utilises the semi-empirical relationship between the sediment reference concentration and the Shields parameter, θ, which was reviewed in Section 2.1.2. This section will focus on the further development of this model.

3.1 Analysis of sediment transport data

The discrepancy in model performance between the coarse and fine sediment sizes discussed in Section 2.1.2 suggested that there may be differences in sediment transport behaviour between the two grain sizes. Along with Schepers (1978) noting that the sediment transport behaviour between the finer sediment and coarse sediment was markedly different, Bijker et al. (1976) found that coarser sediment was influenced by the asymmetry in the orbital velocity. Hence measured sediment flux data were analysed by comparing their relationship with velocity skewness and acceleration skewness. The skewness used in this instance refers to the Fisher skewness, shown in Eq. (2.14) and Eq.(2.15). The data points are coloured with respect to the magnitude of sediment flux q_s in Figure 3-1. While q_s for the finer sediment (test 6) shows a negative correlation to velocity skewness, q_s from the coarser sediment case (test 30) shows a positive correlation with acceleration skewness. This explains the better q_s prediction for the fine sediment, as the GD model (Nielsen, 1988) is based on velocity only. The positive correlation of the sediment flux with acceleration skewness for the coarse sediment suggests using an acceleration term, $\frac{du}{dt}$ may be more suitable than velocity for relatively coarse sediments. This is due to the ratio of the pressure force to the drag force on the sediment grain being greater for larger sediment diameter, as in the inverse of the Keulegan-Carpenter number , shown in Eq.(3.1):

$$\frac{F_p}{F_D} \approx \frac{Vol}{A} \sim \frac{d^3}{d^2} \tag{3.1}$$

where F_p is the pressure force and F_D represents the drag force. This requires a revision of the original model.

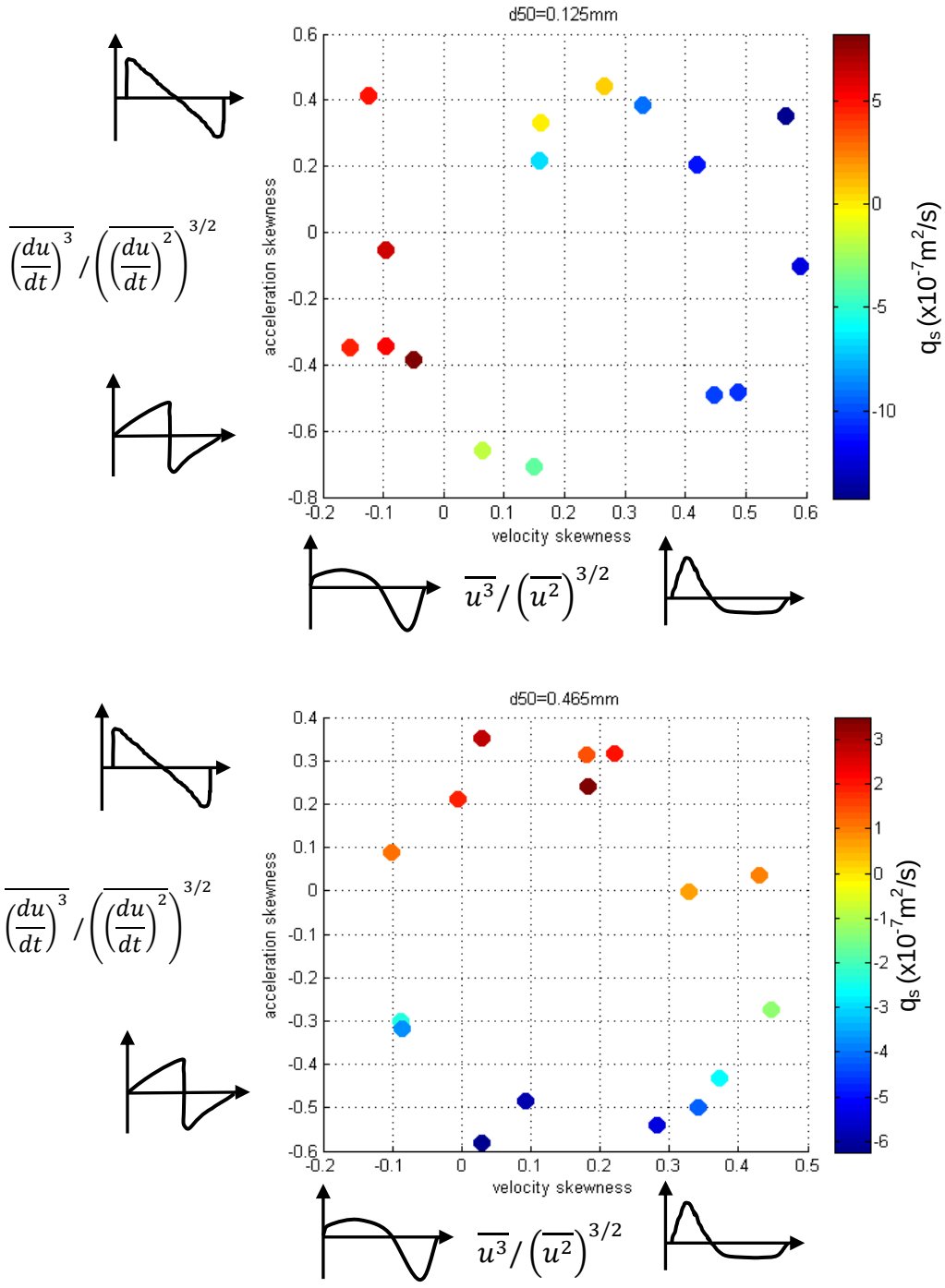

Figure 3-1. Velocity skewness and acceleration skewness for test 6 (top) and test 30 (bottom) with d_{50}=0.125mm and d_{50}=0.465mm respectively; q_s ranges from most positive (dark red) to most negative (dark blue). Data from Schepers (1978). Graphs show velocity shape according to levels of skewness.

The incorporation of $\frac{du}{dt}$ in wave sediment transport models is not a novel concept. The positive correlation of the acceleration skewness with sediment flux has also been observed by Drake and Calantoni (2001) and has led to a range of $\frac{du}{dt}$-based sediment transport models (e.g. Calantoni & Puleo, 2006; Nielsen, 2006). The significance of the $\frac{du}{dt}$ term has been related to the horizontal

pressure gradient caused by the passage of a wave, which leads to momentum transfer to the near-bed layer (Calantoni & Puleo, 2006). Whether or not $\frac{du}{dt}$ is a suitable proxy for the horizontal pressure gradient, or contributes directly to the shear stress (Nielsen, 2006), it is clear that $\frac{du}{dt}$ has a significant impact on the sediment transport rate.

There have been more updates to include acceleration skewness in existing sediment transport models in the last decade such as Watanabe and Sato (2004) extending the 'half-cycle' model that was developed by Dibajnia and Watanabe (1992) to accommodate acceleration skewness. More recently Van der A et al. (2010b; 2013) extended the model further and have succeeded in calibrating the model to a range of experiments in the SANTOSS dataset. This has led to the present update of the GD model in keeping with other updated models, and investigation of their comparative performance.

3.2 Model revision

In order to incorporate $\frac{du}{dt}$ effects into q_s for the coarse sediment, the model formulation was revised. The advantages of this are discussed in Section 2.2.1. Instead of q_s being a function of the velocity, it was written as a function of the shear stress; its benefits are discussed in Section 2.2.2.

Calculating the sediment flux based on shear stress was done through approximating the shear stress with an equation from Nielsen (1992), which is a function of both the free stream velocity u_∞ and acceleration, du_∞/dt, shown in Eq. (2.19) and repeated here:

$$\tau(o,t) = \frac{1}{2}\rho f_{2.5} A(cos\varphi_\tau\ \omega\ u_\infty(t) + sin\varphi_\tau \frac{du_\infty}{dt})$$

The $f_{2.5}$ refers to the wave friction factor with roughness equal to $2.5d_{50}$ and φ_τ is the phase shift, which is $\frac{\pi}{4}$ for laminar flows (Nielsen, 1992). For the coarser sediment cases, a phase shift of $\frac{\pi}{2}$ was used, which occurs when the shear stress term is dominated by the acceleration. Nielsen (1992) used $u_\infty(t) = Ae^{i\omega t}$ as the free stream velocity term and not a Stokes wave which is commonly used in laboratory experiments. However this is a reasonable simplification for preliminary model formulation purposes.

The entrainment coefficients in the revised model were calculated with maximum and minimum shear stresses, scaled by the average shear stress τ_{av} to the 3rd power, similarly to Eq. (2.6).

$$(A_f, A_b) = \left[0.5\left(\frac{\tau_{max}}{\tau_{av}}\right)^3, 0.5\left(\frac{\tau_{min}}{\tau_{av}}\right)^3\right] \quad (3.2)$$

The q_s calculation was changed to Eq. (3.3) to reflect the positive correlation of the q_s to $\frac{du}{dt}$, by adding the entrainment coefficients to maintain their respective directions.

$$q_s = C_{0s} w_s (A_b + A_f) A \tag{3.3}$$

3.2.1 Applying threshold of sediment motion

Similarly to traditional bedload formulas such as Meyer-Peter and Müller (1948), a critical Shields parameter at which sediment commences movement was specified in the revised GD model to reflect the lack of sediment mobility under low values of shear stress. The critical Shields number, Eq. (3.4), was calculated using the non-dimensional sediment grain size (D_*), Eq.(3.5), from Soulsby (1997) . v is the kinematic viscosity of water, and s is the relative density of sediment, typically 2.65.

$$\theta_c = \frac{0.3}{1 + 1.2D_*} + 0.055[1 - e^{-0.02D_*}] \tag{3.4}$$

$$D_* = \left[\frac{g(s-1)}{v^2}\right]^{1/3} d_{50} \tag{3.5}$$

When the Shields parameter is below the critical value, there was no sediment flux calculated. The proportion of the time that the threshold value was exceeded was calculated and applied as a multiplier to the entrainment coefficients in Eq. (3.2). The threshold multipliers C_f and C_b were applied to A_f and A_b respectively. A graphical representation of this process is shown in Figure 3-2. The multiplier is the ratio of the area which exceeds the critical shear stress (dotted area) to the total integrated shear stress (area under τ curve) in each direction.

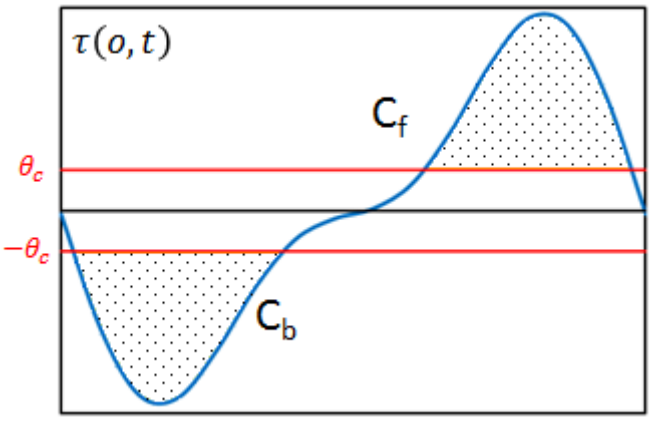

Figure 3-2. The threshold multipliers to the entrainment coefficients, C_f and C_b

The results from this modification to the model will be discussed in Section 3.2.3.

3.2.2 Mixture of sediment sizes

Depending on the sediment size distribution, sediment flux from both suspended sediment and ripple migration can occur. Calantoni and Puleo (2006) have suggested that one formula is insufficient to capture coastal sediment transport. Therefore some studies have calculated the sediment flux from each sediment transport mechanism separately (e.g. Traykovski et al., 1999; Van der Werf et al., 2008). They are then combined to calculate the net sediment flux. In the case of the GD model, the proportion of the suspended sediment flux, q_{ss}, can be calculated using the velocity-based original model (Nielsen, 1988), while the sediment flux due to ripple migration, q_r, can be calculated using the revised, shear stress-based model. The revised model is suitable for bedload sediment transport (i.e. not suspended), and ripple migration has been found to be forced by bedload sediment transport (Traykovski et al., 1999). Determining the percentage of the sediment which gets transported by suspension or ripple migration poses some challenges. Van der Werf et al. (2008) suggested the use of shear velocity to differentiate between the different sediment transport mechanisms.

In order to calculate the percentage of the sediment that can be suspended, the maximum sediment size that is able to be entrained was calculated by the criterion for maximum settling velocity based on maximum skin friction (Fredsøe & Deigaard, 1992), $u_{*2.5}$.

$$u_{*2.5} = \sqrt{1/2\, f_{2.5}} A\omega \tag{3.6}$$

The maximum settling velocity can be estimated from:

$$w_{s,max} = 0.8 u_{*2.5} \tag{3.7}$$

The critical grain diameter d_{crit} can be calculated from formulas from Hallermeier (1981), as well as Migniot's (cited in Hallermeier, 1981) simple equation:

$$w_{s,max} = 125 d_{crit} \quad \text{(cgs units)} \tag{3.8}$$

As there is a range of skin friction factors and semi-excursion lengths for each test case in Schepers (1978), there is a range of d_{crit} values. For test 30, d_{crit} was found to be between 0.14mm and 0.37mm for both methods. According to the sediment size distribution curve from Schepers (1978), all of the sediment is larger than this d_{crit}, which suggests minimal contribution from q_{ss} to the total sediment flux.

q_r was also compared with the measured sediment flux from test 18 with a smaller sediment size, with d_{50} = 0.25mm. d_{crit} was calculated to be between 0.13 mm and 0.36mm. This represents quite a spread with the two different methods, with Hallermeier's (1981) equations suggesting a majority of q_{ss} (90 to 100%) and Migniot's (cited in Hallermeier, 1981) method suggesting a majority of q_r

(95 to 100%). q_{ss} and q_r were weighted by the respective percentages and compared in Figure 3-3. The measured sediment flux shows a better fit with Migniot's method, which suggests there is a higher percentage of q_r for this test case.

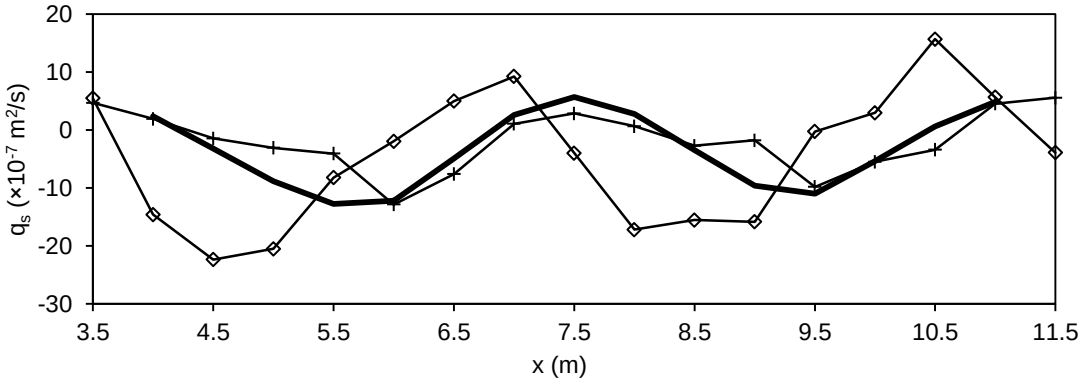

Figure 3-3. Measured data (thick black line) and predicted sediment flux using suspended sediment percentages from Hallermeier (squares) and Migniot (crosses).

The percentage of suspended sediment was also calculated for the experiments of Hurther and Thorne (2011), as it was directly measured in their experiments. From their observations, q_{ss} is approximately 40% and q_r is approximately 60%. Using Migniot's Eq. (3.8), 36% is predicted to be q_{ss}, while Hallermeier's equations suggest 100% is q_{ss}. Migniot's Eq. (3.8) although simple, appears to achieve more sensible results.

The settling velocity used in calculating q_{ss} from the GD model will most likely have to be modified to reflect the median suspended sediment size, rather than the total median sediment size. This would decrease the settling velocity and hence the total sediment flux. The contribution from the suspended sediment flux will however have only a minor impact on the overall sediment flux in test 18 in Schepers (1978) due to the very small percentage of q_{ss}. The significance of altering the settling velocity will have to be estimated by applying the model to a case which has more equal split of sediment transport mechanisms, such as in Hurther and Thorne (2011).

There is no consensus regarding what criteria determines sediment suspension. It is recommended that datasets such as Anderson (1942) and Nielsen (1983) which show sediment grain distribution inside and above the bed should be studied in detail in order to develop an alternative method.

3.2.3 Boundary layer streaming

Boundary layer streaming induces a net velocity in the shoreward direction (Longuet-Higgins, 1957). This suggests that the distance over which the parcel of sediment moves shoreward should have a contribution from the streaming velocity. The streaming velocity used was the Eulerian time-averaged velocity u_E, shown below, where c is the wave celerity.

$$u_E = \frac{3(A\omega)^2}{4c} \tag{3.9}$$

The influence of including a streaming term in the GD model was therefore also tested. The streaming velocity multiplied by half the wave period was added to distance *A* for the shoreward motion, and subtracted from distance *A* for the offshore motion.

$$q = C_{0s} w_s \left(A_b (A + \frac{\alpha_s u_E T}{2}) - A_f (A - \frac{\alpha_s u_E T}{2}) \right) \tag{3.10}$$

The streaming velocity was also multiplied by a multiplication factor α_s in order to modify the contribution from the streaming velocity to the calculated sediment flux to best fit the measured sediment flux.

The modification in sediment flux calculations suggest that boundary layer streaming does not affect the cross-shore variation of the sediment flux, but has the effect of vertically shifting the calculated sediment flux; this is shown in Figure 3-4.

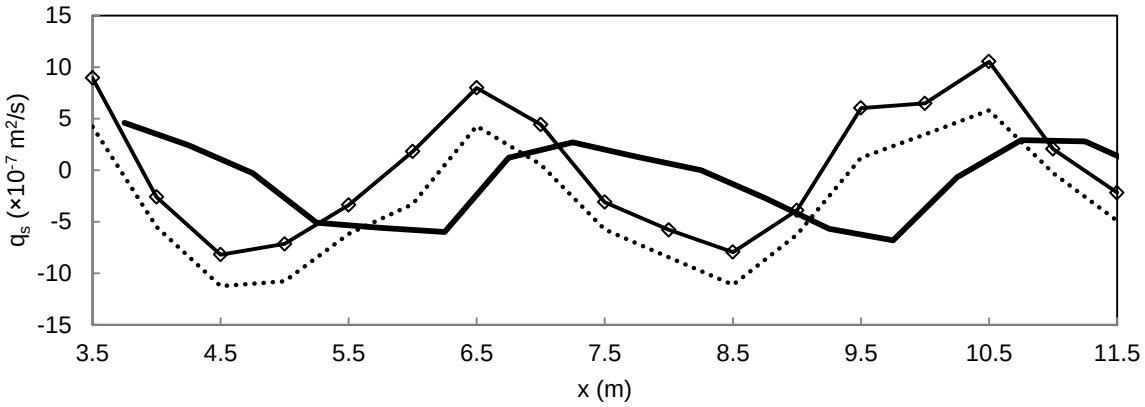

Figure 3-4. Measured data (thick black line) for d_{50}=0.465mm, test 30 (Schepers, 1978), original grab and dump model (dotted), Eq. (3.10) with α_s=0.1 (diamonds).

This result suggests that the discrepancy between the measured and predicted sediment flux by the GD model found by Nielsen (1988) was unlikely to be due to the lack of streaming velocity in the model. Additionally, Davies and Villaret (1999) found that vortex ripples make boundary layer streaming weaker, and Bijker et al. (1974) observed that bottom drift velocities for rippled beds are considerably reduced compared to flat beds.

3.3 Model performance

3.3.1 Application to Schepers' (1978) data set

The results of the revised GD model when applied to the data from test 30 from Schepers (1978) are shown in Figure 3-5. The original GD model, as shown previously in Figure 2-1a, cannot predict the sediment flux for this case. The revised GD model shows very good agreement with the measured data, apart from the most negative sediment flux values. This was resolved by incorporating a critical shear stress term (discussed in 3.2.1) which governs when the sediment transport formula is applicable. Interestingly, the traditional bedload formula from Meyer-Peter and Müller (1948) also predicts the sediment flux well when the shear stress term incorporating $\frac{du}{dt}$ (Eq. (2.19)) is used. This is thought to be due to the high proportion of q_r that is contributing to the total sediment flux, which was also established in Section 3.2.2.

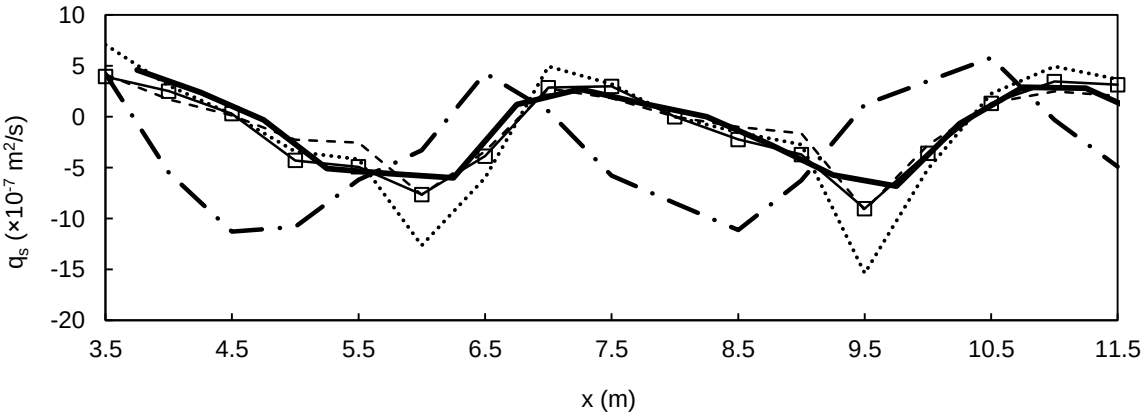

Figure 3-5. Measured data (thick black line) for d_{50}=0.465mm, test 30 (Schepers, 1978), original grab and dump model (dash-dotted), revised grab and dump model (dotted), with critical shear stress (dashed) and traditional Meyer-Peter & Müller model using Eq.(2.19) (squares).

3.3.2 Comparison to existing model by Van der A et al. (2010b)

The revised GD model was compared to another semi-unsteady model by Van der A et al. (2010b) (SANTOSS model). Their model is a 'half-cycle' type model, which accounts for acceleration skewness similarly to Watanabe and Sato (2004). They calibrated their new model against the large SANTOSS dataset. The sediment flux measurements from test 30 in Schepers (1978) are used to compare the performance of the SANTOSS model to the revised GD model. There are three calibration parameters; α_r, m and n, which are the multiplier for the phase lag parameter, the multiplier for the Shields parameter, and the power of the Shields parameter respectively. As their calibration parameters (α_r=9.3, m=9.48, n=1.2) were specific to the SANTOSS data set, they were changed for use with data from Schepers (1978). The new calibration parameters used were α_r=8,

m=6.8 and *n*=1. These parameters were fitted using the method outlined in Van der A et al. (2010b). The predicted sediment flux against the measured sediment flux is shown in Figure 3-6.

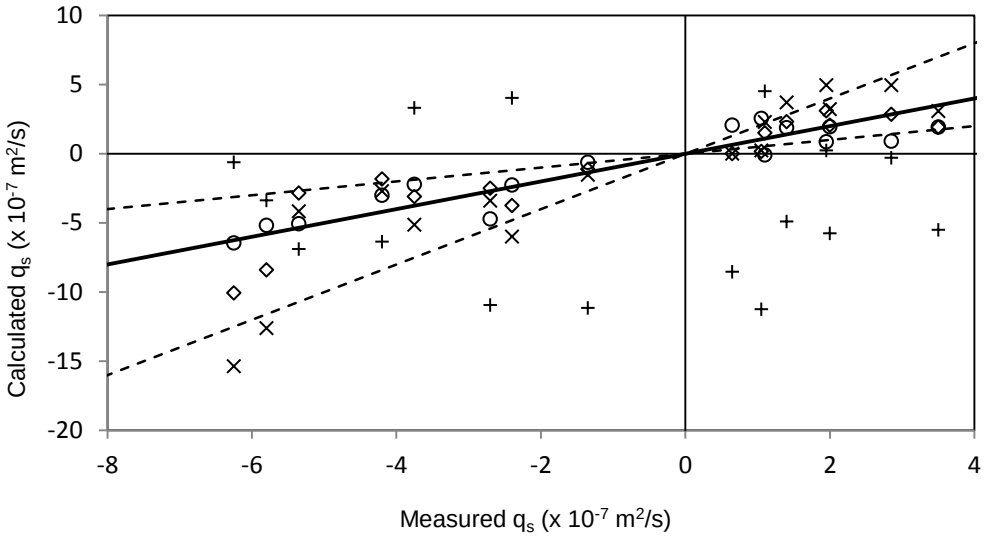

Figure 3-6. Model performance for original GD model (+), revised GD model (x), revised GD model with critical shear stress (◊), and van der A et al.'s (2010b) model (○) for test 30 from Schepers (1978). The solid line indicates 1:1 line, and the dotted lines show the lines for a factor 2 difference.

The predicted q_s from the revised GD model showed a significant improvement from the predictions from Nielsen (1988) for the coarser sediment. For test 30, while the original model predicted the direction of q_s poorly, the revised model with critical shear stress was able to accurately predict the direction for 15 out of 16 measured points and for all but two points, the predicted q_s magnitude was within a difference of factor of two (see Figure 3-6). The SANTOSS model on the other hand, had 12 out of 16 points within a factor of 2, and also 15 out of 16 points predicted in the right direction. The model performance for these two models is similar. The one point predicted in the wrong direction for the GD had a relatively small measured sediment flux (6.5×10^{-8} m^2/s) and the predicted sediment flux was very close to zero (-5×10^{-10} m^2/s). Therefore the margin of error was insignificant despite the error in sediment transport direction. The root mean square errors for the SANTOSS model and the GD model with critical shear stress are 1.18×10^{-7} and 1.61×10^{-7} m^2/s respectively. Considering the significantly simpler nature of the revised GD model, the comparable performance to the SANTOSS model is surprising.

The significance of the changes made to the calibration parameters from the default values are yet to be understood, especially for α_r, an arbitrary scaling factor for *P*, the phase lag parameter. The model results for the default calibration parameters and the re-calibrated parameters are shown in

Figure 3-7. The default parameters under predict the sediment flux; this is perhaps a reflection of the dataset the parameters were calibrated to, which were all full-scale laboratory experiments. The parameters *m* and *n* are a factor and a power for the Shields number respectively, and have previously been used in models based on Meyer-Peter and Müller (1948). The variation of *m* and *n* in bedload sediment transport has been investigated (e.g. Ribberink, 1998). Fernandez Luque and Van Beek (1976) found that *m*=5.7 and *n*=1.5 fit their experiments, which had lower Shields numbers ($\theta < 0.1$). This would help explain the much lower *m* for Schepers' (1978) data.

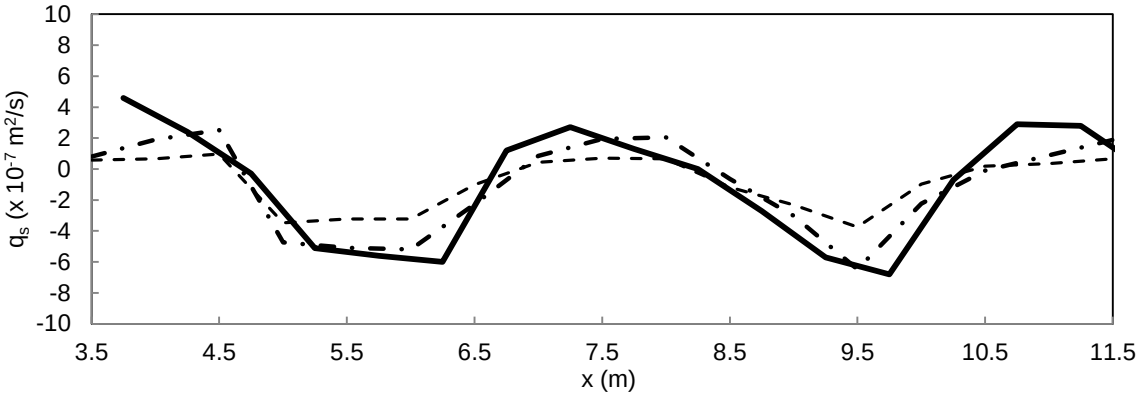

Figure 3-7. Measured data (thick black line) for d_{50}=0.465mm, test 30 (Schepers, 1978), Van der A et al. (2010b) model with original calibration parameters (dashed), model with re-calibrated parameters (dash-dot)

3.4 Application to existing sheet flow data

Although the GD model was updated using data from a rippled bed, as the dominant sediment transport mechanism for the coarse sediment was bedload, the model was further applied to sheet flow datasets. As there is much data collected in the sheet flow regime in large-scale experimental facilities such as CIEM in UPC Barcelona, AOFT (Aberdeen Oscillatory Flow Tunnel) and GWK (Grosser Wellen Kanal) in Hannover, adapting the model to sheet flow experiments was a natural progression of model development. As previously discussed, Van der A et al. (2010a) observed acceleration skewed waves under sheet flow sediment transport in an oscillatory flow tunnel. The majority of the experimental cases were acceleration skewed with little or no velocity skewness. Three sediment sizes were tested; fine (d_{50}=0.15mm), medium (d_{50}=0.27mm), and coarse (d_{50}=0.46mm).

Van der A et al. (2010a) had noted that q_s appears to be proportional to $\beta = \frac{\dot{u}_{max}}{\dot{u}_{max}-\dot{u}_{min}}$ (the acceleration skewness as they have defined it), with dependencies on d_{50} and *T*, with higher q_s

values observed in the fine sediment cases. $\dot{u}_{max}$ and $\dot{u}_{min}$ are the maximum and minimum free stream acceleration respectively.

In order to apply the GD model to sheet flow data, minor changes were made; mainly the shear stress driver lacks the ripple dimensions in Eq. (2.8), therefore making C_{0s} simply a function of $\theta_{2.5}$. The phase shift angle φ_τ in Eq. (2.19) will act as a calibration parameter in this case, which can subsequently be analysed for correlation to other parameters. As φ_τ values found in flat rough beds are typically 15-30 degrees, (Hurther & Thorne, 2011), φ_τ =20° was applied to the entire dataset as an initial test. The results are shown in Figure 3-8. While the coarse and medium sediment q_s is generally over predicted, the fine sediment q_s tends to be under predicted. The scatter of results could be attributed to the variation in T and β.

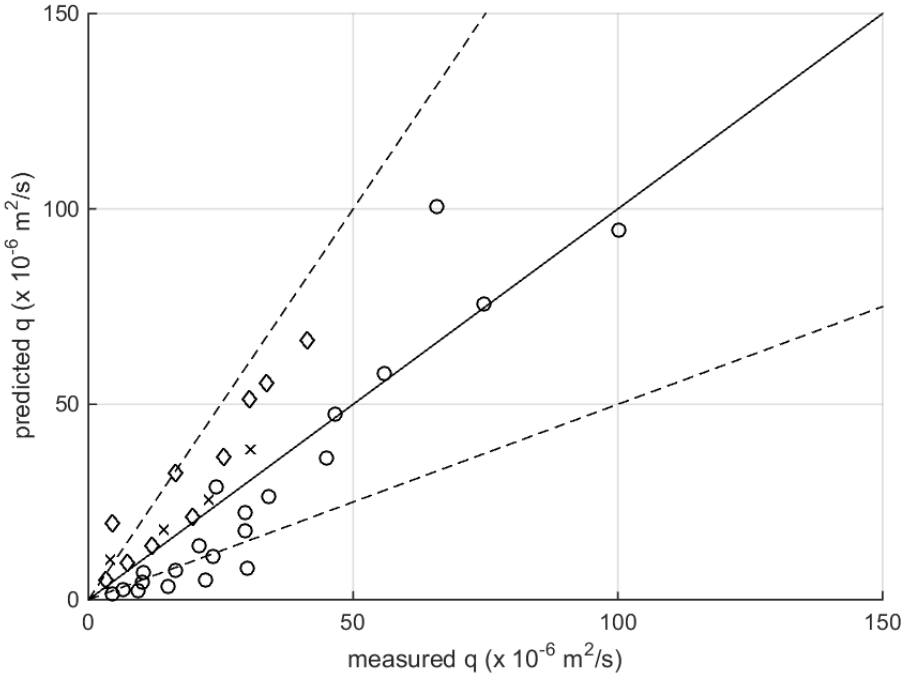

Figure 3-8. Measured and predicted q_s, fine sediment (circles), medium sediment (diamonds), and coarse sediment (crosses) for φ_τ =20°. The solid line indicates 1:1 line, and the dotted lines show the lines for a factor 2 ratio. Data from Van der A et al. (2010a)

In order for the GD model to have some predictive capability, being able to determine the optimal φ_τ becomes essential. Therefore optimal values of φ_τ were fitted for each case to achieve the best fit with the measurements. A table of optimal φ_τ values is shown in Table 3-1. For the coarse and medium sediment, the optimal φ_τ is lower than 20°, and range from 12 to 19°. For the fine sediment, the T=5s cases have much larger φ_τ of over 30°, and the T=9s φ values range from 21 to 28°. T=6 and 7s cases have φ_τ of between 19 and 23°.

Table 3-1. Optimal φ values for Van der A et al. (2010a) data

Experiment ID	T (s)	$\overline{\langle q_s \rangle}$ (10^{-6} m^2/s)	Optimal φ_τ
S556015c	6	4.15	14.6
S606015c	6	14.21	18.5
S656015c	6	22.82	19.3
S706015c	6	30.57	18.6
S556015m	6	4.43	12.1
S606015m	6	16.52	15.9
S656015m	6	30.39	16.9
S706015m	6	41.24	17.2
S557012m	7	3.28	17.2
S607012m	7	7.44	18.4
S657012m	7	11.96	19.1
S707012m	7	19.59	19.5
S757012m	7	25.56	17.9
S807012m	7	33.72	16.9
S555010f	5	4.5	29.2
S605010f	5	9.28	32.9
S655010f	5	14.94	33.6
S705010f	5	22.09	33.2
S755010f	5	29.98	32.6
S556015f	6	24.23	18.8
S606015f	6	46.61	19.9
S656015f	6	74.73	19.9
S706015f	6	100.22	20.4
S557012f	7	10.47	22.9
S607012f	7	20.89	23.0
S657012f	7	29.58	21.9
S707012f	7	44.97	21.4
S757012f	7	55.79	19.8
S807012f	7	65.73	17.1
S559010f	9	6.53	27.8
S609010f	9	10.2	26.4
S659010f	9	16.47	26.3
S709010f	9	23.56	25.8
S759010f	9	29.56	23.6
S809010f	9	33.97	21.7

While for some cases, the φ_τ =20° initial guess appears to be close or at the optimal value, some of the fine sediment cases under predict sediment flux. This could be due to the revised GD model not explicitly accounting for phase lag between sediment concentration and velocity, which features prominently in other semi-empirical models (Van der A et al., 2013). The phase lag parameter for the sheet-flow regime is defined in Eq. (2.18) and simplified here:

$$P = \frac{\delta_s}{T w_s} \tag{3.11}$$

δ_s is the sheet flow layer thickness which is defined by Dohmen-Janssen (1999) as:

$$\frac{\delta_s}{d_{50}} = \begin{cases} 25|\theta_i| & for\ d_{50} \leq 0.15mm \\ 13|\theta_i| & for\ d_{50} \geq 0.20mm \end{cases} \tag{3.12}$$

where the subscript *i* refers to either the crest or trough. Note that the constant 25 was changed from the original 35 by Van der A et al. (2010b). Phase lags and the measured sediment flux for each of the cases are plotted in Figure 3-9. It appears from calculation of the phase-lag parameter that among the fine sediment cases, the data points with *T*=6s has the biggest phase lag effects, followed by 7s, 5s, and 9s. As discussed previously in Section 2.1.3, the phase lag parameter contrasts with definitions of phase lag from Nielsen (1992), however as this data are part of the SANTOSS dataset , the phase lag parameter defined by the SANTOSS model is used.

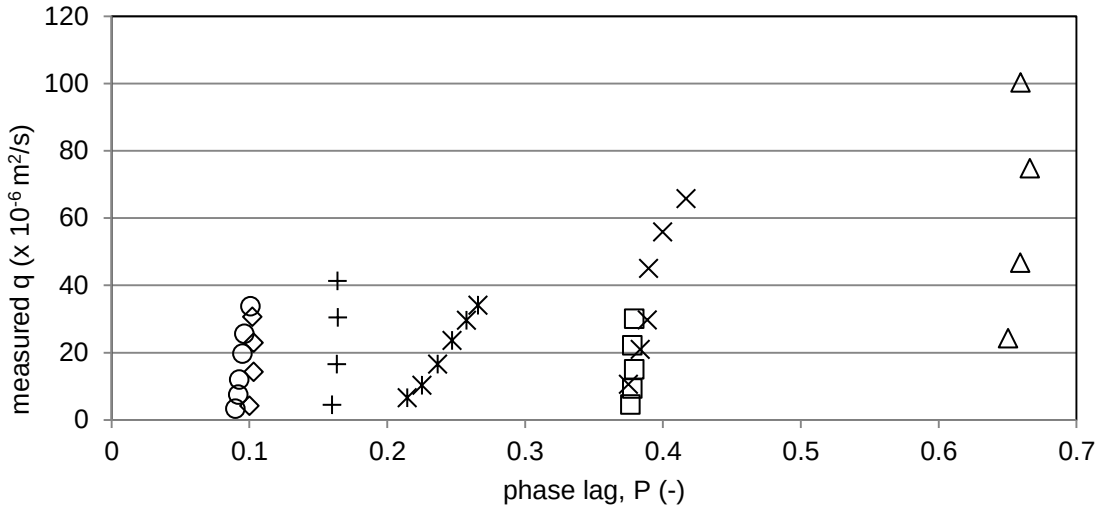

Figure 3-9. Phase lag parameter vs measured qs. Coarse *T*=6s (◊), medium *T*=6s (+), medium *T*=7s (o), fine *T*=5s (□), fine *T*=6s (Δ), fine *T*=7s (x), fine *T*=9s (*).

The optimal φ_τ values were plotted against various parameters, such as phase lag parameter and Reynolds number to see if the scatter in φ_τ can be accounted for by these parameters. Figure 3-10 shows the phase lag parameter plotted against φ_τ. There is no clear relationship between these parameters, which suggests that perhaps the omission of a phase lag parameter between velocity and sediment concentration in the updated GD model is not a significant shortcoming.

Two parameters that show some correlation with the optimal φ_τ values are the Reynolds number and roughess, *r*. Nielsen (1992) showed that the roughness for oscillatory sheet flow in flat beds is

$$r = 170\sqrt{\theta_{2.5} - 0.05}d \tag{3.13}$$

The Reynolds number and roughness relative to φ_τ is shown in Figure 3-11 and Figure 3-12 respectively.

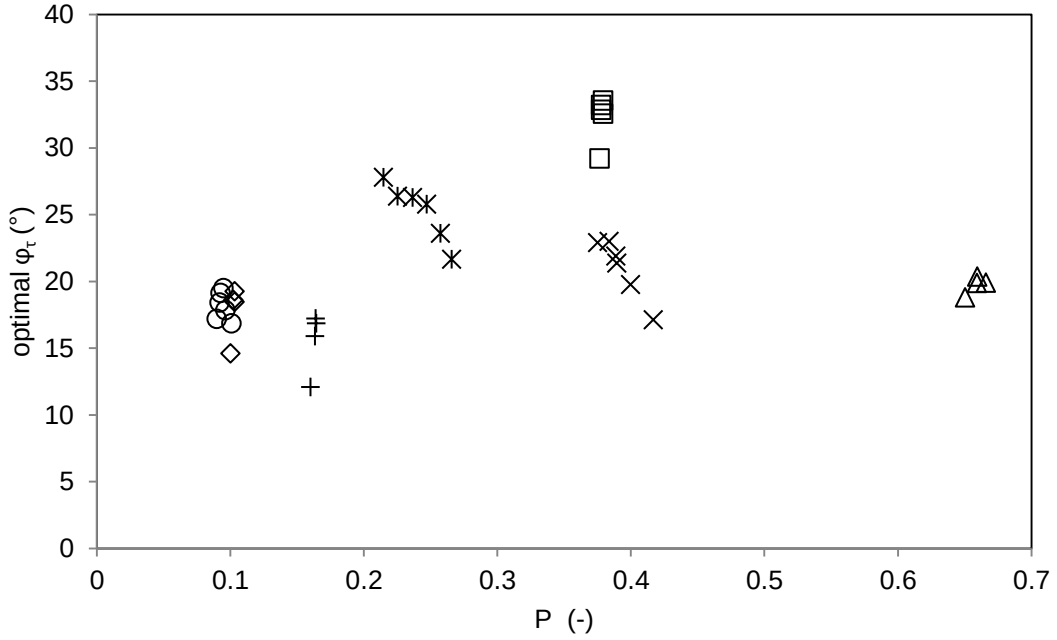

Figure 3-10. Phase lag parameter vs optimal φ_τ. Coarse T=6s (◊), medium T=6s (+), medium T=7s (o), fine T=5s (□), fine T=6s (Δ), fine T=7s (x), fine T=9s (*).

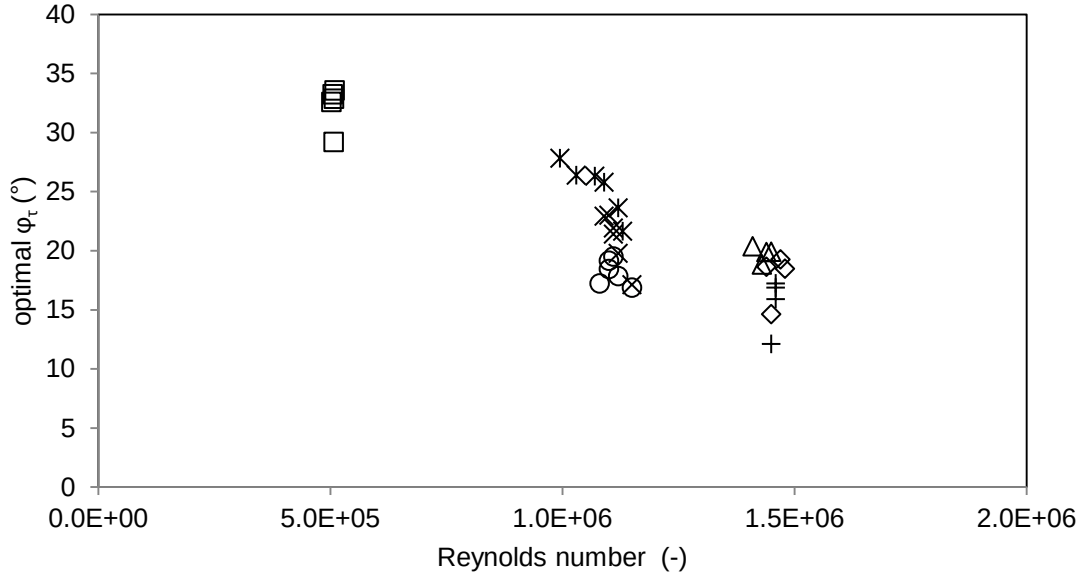

Figure 3-11. Reynolds number vs optimal φ_τ. Coarse T=6s (◊), medium T=6s (+), medium T=7s (o), fine T=5s (□), fine T=6s (Δ), fine T=7s (x), fine T=9s (*).

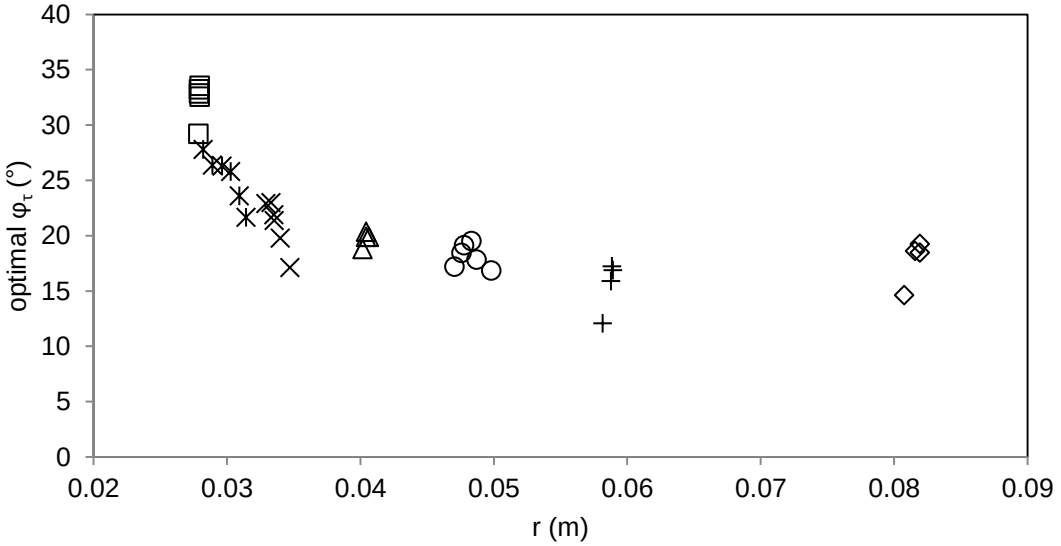

Figure 3-12. Roughness vs optimal φ_τ. Coarse *T*=6s (◊), medium *T*=6s (+), medium *T*=7s (o), fine *T*=5s (□), fine *T*=6s (Δ), fine *T*=7s (x), fine *T*=9s (*).

The optimal φ_τ therefore correlates with some function of velocity and d_{50}. The fine sediment with the shortest *T* has the lowest roughness and highest φ_τ.

3.5 Impact of superimposed current on sediment transport

3.5.1 Schepers' (1978) data with superimposed current

In the experiments run by Schepers (1978), there were cases with varying degrees of superimposed uniform flow. The relevant cases from the fine sediment tests were analysed. The original GD model (Nielsen, 1988) was used for this fine sediment size, as previous analysis showed these cases were predominantly suspended sediment rather than the ripple migration sediment transport observed for the coarser sediment.

Schepers (1978) had showed that sediment flux that occurs with varying superimposed currents (see Figure 3-13) for the fine sediment is not linear (solid line). While the average sediment flux increases for the 5cm/s and 7.5cm/s current in the direction of wave propagation, it decreases for the 2.5m/s current. Similar behaviour of sediment flux with respect to increasing superimposed current was also observed in Vellinga (1975) and Inman and Bowen (1962).

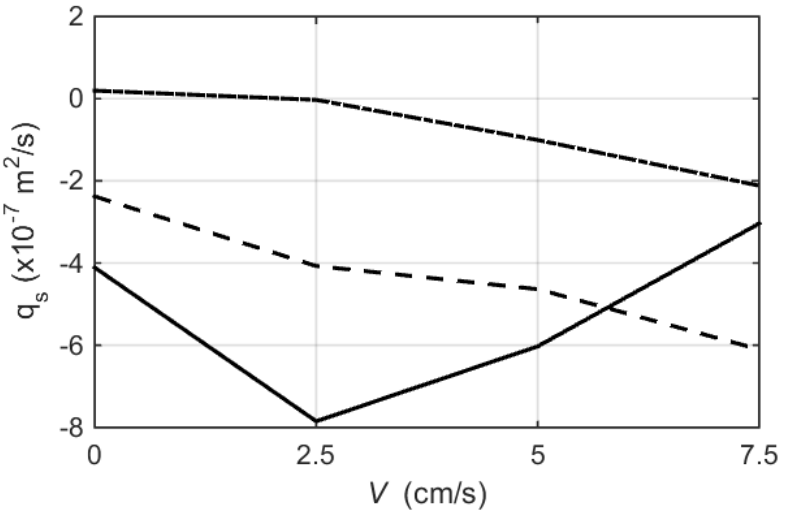

Figure 3-13. Plot of superimposed current vs sediment flux from Schepers (1978)

In order to account for the superimposed current in the GD model, the distance travelled by the sediment is changed. The sediment transport going onshore is accentuated, so the current velocity multiplied by half the wave period $\left(\frac{VT}{2}\right)$ is added, and then the same value is subtracted from the offshore moving sediment distance. α_v is a scaling factor, to adjust the contribution of the current on the sediment flux. The sediment flux equation Eq.(2.5) becomes:

$$q = C_{0s} w_s \left(A_b (A + \alpha_v \frac{VT}{2}) - A_f (A - \alpha_v \frac{VT}{2}) \right) \tag{3.14}$$

When this formula was applied to the data with α_v=1, it overestimated the sediment flux. The factor α_v was adjusted to match the measured sediment flux, and ranged between 0.2 and 0.6 for the four cases tested. The results from the GD are plotted in Figure 3-14 to Figure 3-17. The case details are shown in Table 3-2.

Table 3-2. Test conditions analysed with GD with current

Case	Current (cm/s)	d_{50} (mm)	α_v
1	0	0.125	-
6	2.5	0.125	0.2
7	5	0.125	0.6
12	7.5	0.125	0.6

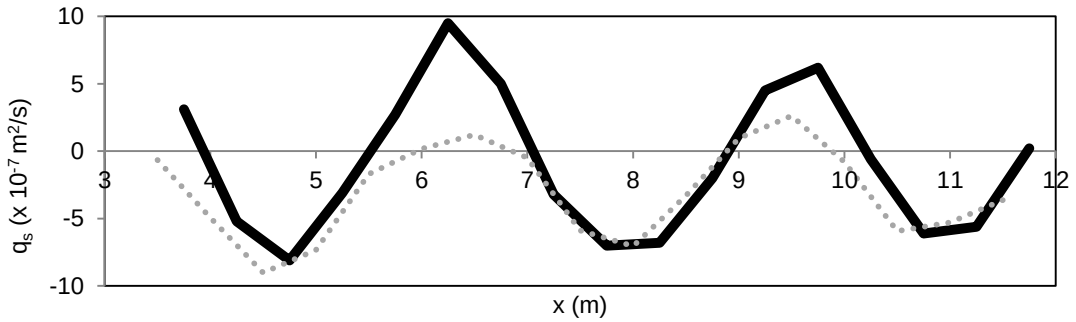

Figure 3-14. Test 1, V=0cm/s , Measured q_s (solid), original GD (..)

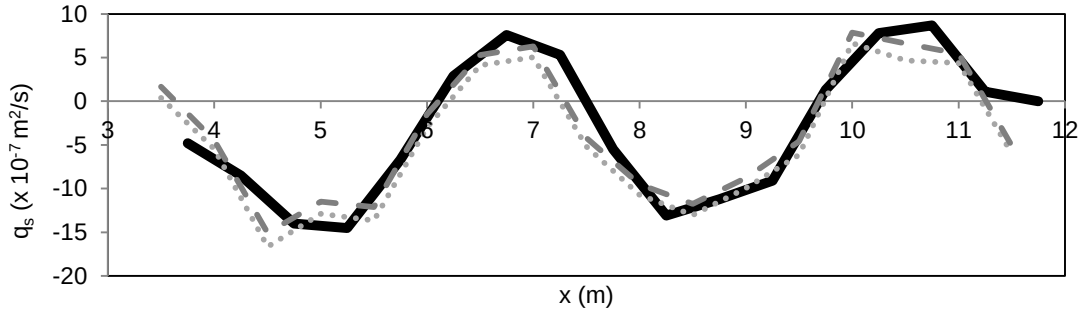

Figure 3-15. Test 6, V=2.5cm/s , Measured q_s (solid), original GD (..), GD with current (--)

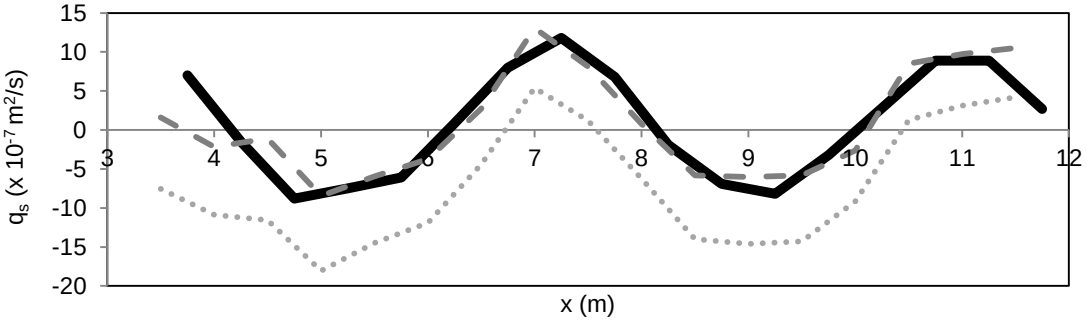

Figure 3-16. Test 7, V=5cm/s, Measured q_s (solid), original GD (..), GD with current (--)

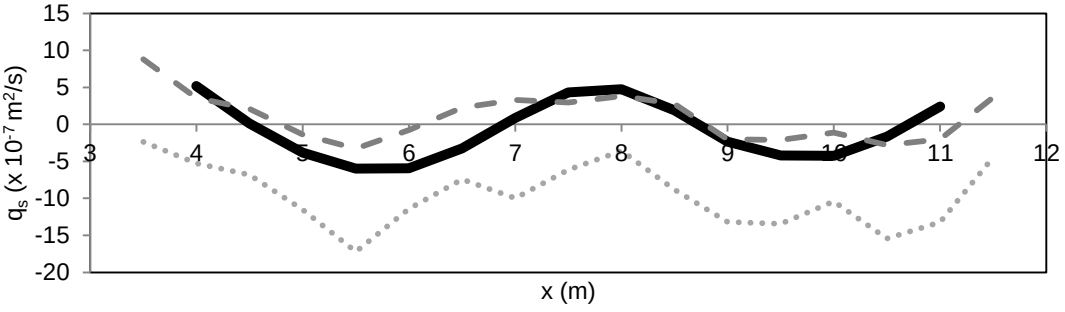

Figure 3-17. Test 12, V=7.5cm/s, Measured q_s (solid), original GD (..), GD with current (--)

This smaller α_v value could be due to the impact of the current decreasing towards the bed compared to the wave due to its thicker boundary layer and hence decrease the effect on the distance travelled by the sediment. Rather than separating the current from the wave sediment transport, the original GD model (Nielsen, 1988) is able to predict the measured sediment flux effectively.

For *V*=0cm/s (Figure 3-14), the contribution of the current is zero, so the GD model is unchanged from the original model, Eq.(2.5). Although the negative sediment flux points are predicted well by the model, the positive sediment flux is greatly underestimated. This remains an issue which requires further development. Similar effects were identified in test 6 from Tilmans (1979) which was also presented in Nielsen (1988) and compared with the GD (original) model.

For *V*=2.5cm/s (Figure 3-15), Eq.(3.14) with α_v=0.2 improves the prediction of the positive sediment flux but underestimates the negative sediment flux, as the original GD model predicted the negative flux well and the current contribution has an effect of shifting the flux in the direction of the current. For *V*=5cm/s and *V*=7.5cm/s (Figure 3-16 and Figure 3-17), α_v=0.6 was used. In both cases, the original GD model shows that the predicted sediment flux is too negative and the inclusion of the current in the model improves the sediment flux prediction.

The sediment flux for the cases with d_{50}=0.465mm and d_{50}=0.25mm appeared to have very little impact from the superimposed current; the revised GD model (Eq. (3.3)) performed quite well in all of the 4 different current flows without the current term. This is due to the current effect being applicable only to suspended sediment. Due to the medium and coarse sediment having ripple migration as the major sediment transport mechanism rather than sediment suspension, the current lacks impact on the sediment flux.

The results from analysing data from Schepers (1978) suggest that the difference between positive and negative sediment flux under the ripple regime is unaffected by a superimposed current; the points are merely shifted in the positive direction. All the currents tested were in the same direction as the wave (i.e., positive); an opposing current may influence the wave differently, as Kemp and Simons (1983) found with their experimental cases.

Van Rijn et al. (1993) had found that the superimposed current had little impact on the reference concentration, which supports the exclusion of the current velocity when calculating the entrainment coefficients in the GD model. It appears that the approach of incorporating the current via the sediment travel distance is sound, but the equation requires a calibration factor, α_v.

3.5.2 Analysis of the Silva et al. (2011) data

As part of the *Transport induced by Skewed waves and currents* (TRANSKEW) project, the impact of sediment transport from various wave conditions were tested, mainly acceleration skewness, acceleration skewness with a current, and acceleration skewness combined with velocity skewness. The tests were undertaken in the Large Oscillating Water Tunnel (LOWT) at Deltares. These experiments tested currents in the negative direction, -0.22m/s and -0.44m/s. All the experiments were in the sheet flow regime, so the updated GD model (Eq.(3.3)) was applied.

Under the assumption that the effect of the superimposed current could be represented by the increase/decrease in sediment transport distance, the fitted phase difference (φ_τ) should be similar under similar flow conditions. The amount by which the current would influence the sediment travel distance could then be determined by applying an efficiency factor on the current. A summary of the test cases is shown in Table 3-3.

Table 3-3. Test conditions and fitted φ and α_v values for data from Silva et al. (2011)

test	u_{rms}(m/s)	V (m/s)	φ	α_v
A1	0.90	0	15	-
A3	0.88	0	16	-
B1	0.89	-0.22	15	0.06
B2	0.88	-0.44	15	0.12
B3	0.86	-0.22	16	0.03
B4	0.86	-0.44	16	0.07

Firstly, the cases with acceleration skewness were tested. $u_{rms}$was approximately 0.9m/s. Sediment flux for Cases A1 and A3 were predicted well with φ_τ values of 15 and 16 degrees, respectively. Cases B1 and B3 roughly correspond to A1 and A3, but with a superimposed current of -0.22m/s. These cases were run with the same φ_τ values but also with the contribution from the current. As the updated GD model is being used, Eq. (3.14) becomes

$$q = C_{0s} w_s \left(A_b \left(A - \alpha_v \frac{VT}{2} \right) + A_f \left(A + \alpha_v \frac{VT}{2} \right) \right) \tag{3.15}$$

The factor (α_v) required was approximately 0.06 and 0.03 for B1 and B3 respectively. The cases B2 and B4 correspond to A1 and A3, but superimposed with a larger -0.44m/s current. Again the φ_τ values were maintained, but α_v required was 0.12 and 0.07 respectively. This suggests that the larger the current, a larger value of α_v is required, which was also the case in the data from Schepers (1978), but with the current in the opposite direction.

3.5.3 Analysis of the Watanabe & Sato (2004) data

Watanabe and Sato (2004) undertook experiments which incorporated negative current into their tunnel experiments so to recreate an undertow. The experiments were mostly concerned with sheet flow for a d_{50}=0.2mm sediment under varying degrees of acceleration skewness and various maximum velocity values. There were two currents tested, -0.1m/s and -0.2m/s.

Nielsen (2006) incorporated the current directly into the free-stream velocity, i.e. $u = u_\infty + V$ to be used in his model. This appeared to be suitable for a preliminary application. The optimal φ_τ value was fitted for each test and subsequently analysed.

When measured sediment transport rates are compared for different currents and acceleration skewness, more negative currents and smaller acceleration skewness tend to result in more negative (offshore) sediment flux. This results in smaller $\frac{du}{dt}$ and more negative currents requiring higher φ_τ values. Higher u_{max} values result in higher sediment flux, requiring lower φ_τ values.

For the purposes of investigating the effects of a superimposed current, the cases with similar experimental conditions but with varying superimposed current values were compared. There are three cases where 0, -0.1m/s and -0.2m/s currents were run under the same wave conditions. These tests are shown in Table 3-4. Unfortunately, there is only one case where Eq. (3.15) is able to predict q_s effectively. For the case with u_{max}=1.07m/s, the case with no current requires φ_τ=42°. The cases with -0.1m/s and -0.2m/s current can use the same φ_τ value with α_v of 0.48 and 0.12 respectively. This has the opposite trend to the previous cases, as a bigger current has a smaller α_v value. For the other cases where all current magnitudes were tested with the same wave conditions (which have higher u_{max} values of 1.25 and 1.43 m/s) the sediment flux was not able to be predicted using the φ_τ from the V=0m/s case plus the current contribution. The φ_τ required was much larger in both cases, which suggests that the impact of the current on the sediment transport is unlikely to be a simple relationship as suggested by Eq.(3.14) or Eq. (3.15).

Table 3-4. Test conditions and fitted φ and α_v values for Watanabe and Sato (2004) data

test	u_{max} (m/s)	V (m/s)	φ	α_v
8	1.07	0	42	-
47	1.07	-0.1	42	0.48
38	1.07	-0.2	42	0.12
3	1.25	0	34	-
44	1.25	-0.1	39	0.15
35	1.25	-0.2	39	0.07
6	1.42	0	32	-
50	1.43	-0.1	40	0.7
41	1.43	-0.2	40	0.08

3.6 Cases with velocity skewness

As highlighted in the previous section, the original GD model gives zero q_s for data without velocity skewness, and the updated GD model cannot be applied to cases without acceleration skewness. This is due to the updated GD model for Schepers' data using φ_τ=90°, completely ignoring the effect of the velocity skewness and hence the velocity component of Eq. (2.19). This leads to the question: how should the model work when there is no acceleration skewness? Various modifications can be made to the updated model- namely integrating the velocity and separating the positive and negative velocities, and using these values as a scaling factor instead of the maximum velocity or shear stress values. However this sort of model becomes very similar to the traditional Meyer-Peter and Müller (1948) formula. This remains a topic for further investigation.

3.7 Conclusions

The GD model originally proposed by Nielsen (1988) was updated, mainly to accommodate flows with acceleration skewness for a relatively coarse sediment grain size. Updates made to the model include modifying the model to be a function of shear stress rather than velocity and applying a threshold of sediment motion. The resulting model performed well compared to an established semi-empirical sediment transport model when predicting small-scale laboratory results over a rippled bed. The updated model has been found to be equally applicable to sheet flow, with the optimal phase shift angle φ_τ fitted for each case in Van der A et al. (2010a) found to scale roughly with Reynolds number and hydraulic roughness. Additionally, sheet flow experiments with superimposed currents were investigated and a potential modification to the model was explored. Various challenges remain for the model, which include how to best represent the split between suspended sediment and bed load, how to accommodate cases without acceleration skewness, and resolving the issues encountered with the Watanabe and Sato (2004) data and superimposed currents.

4 Methods for conversion from surface elevation to velocity

The reality of many practical sediment transport models such as the GD model discussed in Section 3 are that they require a near-bed velocity time series, $u(z,t)$, (e.g. Nielsen, 2006) or $u(t)$ shape (e.g. Dibajnia & Watanabe, 1996; Van der A et al., 2013) as input. Measurement campaigns in laboratories or in the field often include velocity measurements alongside sediment transport measurements, but this has not always been the case, as velocity is more difficult to measure compared to other parameters such as water surface elevation. Thus, where there are inadequate velocity measurements, it is useful to have a method which can convert an easily measured record, such as surface elevation, $\eta(t)$ or bottom pressure, $p(0,t)$, to $u(z,t)$. This chapter aims to address this gap in information, to employ readily available data to convert to key parameters required for sediment transport calculations. Various types of waves are analysed from three experiments and discussed in the following sections.

4.1 Experiment overviews

4.1.1 SAMSE experiment overview

Experimental data from the SASME Project (*Surf and swash zone mechanics*) from Plymouth University (1997-2000) was used to analyse the surface elevation and velocity measurements along a sloping bed. The experiments were conducted in a wave flume 18m long and 0.9m wide with a water depth of 0.8m and a beach with a slope of 1:10. A detailed description of the experiment is outlined in Baldock and Huntley (2002). The flume configuration is shown in Figure 4-1.

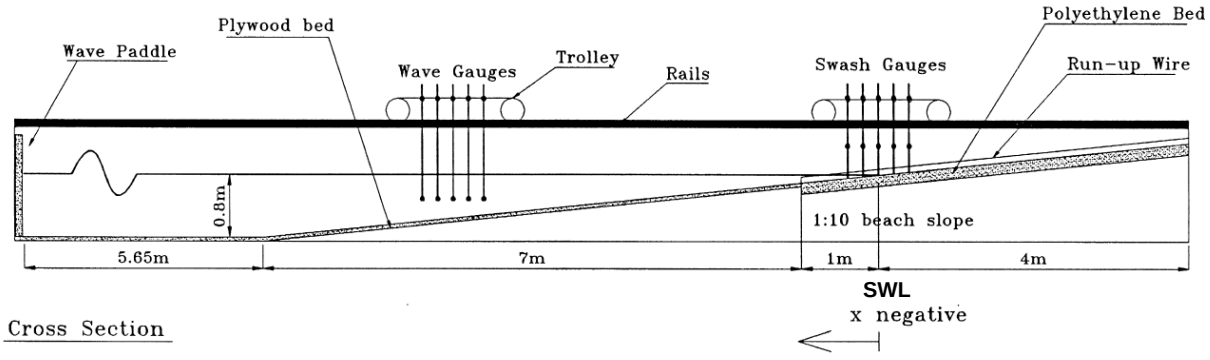

Figure 4-1. Cross-section of wave flume, figure from Baldock et al. (2000).

There were a range of test conditions including regular, short waves, bichromatic waves, and random waves. There were 14 cross-shore measurement locations in total, ranging from 4m to 0.4m offshore from the still water line (SWL); the *K*-values (measurement points) and corresponding *x*-locations and the water depths and *z/h* values for the velocity measurements are listed in Table 4-1.

The *x* locations are measured from the SWL, with the negative direction representing locations further seaward.

Table 4-1. *K*-values and their *x*-locations, *h* values, and *z/h* values for velocity measurements

K	**1**	**2**	**3**	**4**	**5**	**6**	**7**	**8**	**9**	**10**	**11**	**12**	**13**	**14**
***x* (m)**	-4	-3.6	-3.2	-2.8	-2.4	-2	-1.8	-1.6	-1.4	-1.2	-1	-0.8	-0.6	-0.4
***h* (m)**	0.4	0.36	0.32	0.28	0.24	0.2	0.18	0.16	0.14	0.12	0.1	0.08	0.06	0.04
***z/h* (-)**	0.52	0.46	0.39	0.31	0.19	0.03	0.03	0.04	0.04	0.05	0.06	0.08	0.1	0.15

4.1.2 SUSCO experiment overview

Data from the SUSCO (*Swash zone response under grouping wave conditions*) experiments undertaken in the CIEM (Canal d'Investigació i Experimentació Marítima) lab at UPC (Universitat Politècnica de Catalunya) were analysed for wave shapes. There were monochromatic, bichromatic, combinations of monochromatic and bichromatic, and random waves tested under both erosive and accretive conditions. The monochromatic wave for the accretive condition will be primarily used for further analysis. There have been extensive profile measurements at CIEM (e.g. Baldock et al., 2011; Cáceres & Sanchez-Arcilla, 2015) alongside surface water elevations and selected velocity measurements, which enables detailed testing of the q_s models based on $u(z,t)$ data. The wave flume is 3m wide and 5m high and 100m long. The wave flume layout is shown in Figure 4-2, with instrumentation locations shown in the upper panel. Note that the instrumentation locations shown are the distance from the paddle, but subsequent locations will be measured from the zero reference point, which is 7.4m from the paddle. As there are only two locations where there are both surface elevation and velocity measurements in close proximity, these points will be analysed in detail.

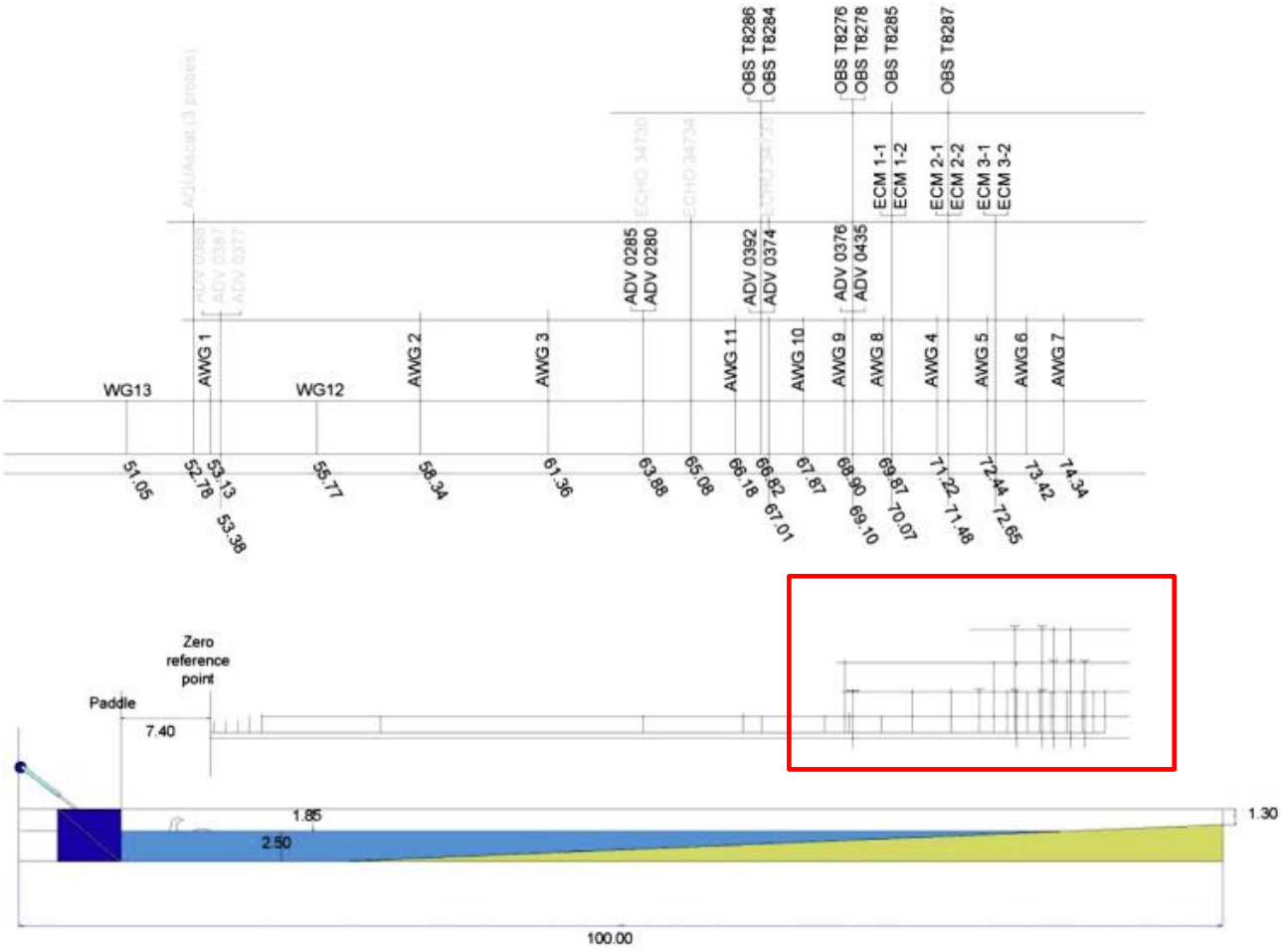

Figure 4-2. Wave flume layout of CIEM (lower panel) and detailed SUSCO instrumentation layout in the active beach profile (indicated by square), (upper panel). Measurement units are in metres. Figure from Baldock et al. (2011)

4.1.3 Experiments from Flick (1978)

Flick (1978) investigated shoaling waves in a 30m long flume with a glass beach and measured surface elevation and velocity concurrently under various types of breakers. There are measurements at various locations including at pre-breaking, at breaking and under bores. Unfortunately, the data only provides phase-averaged surface elevation and bottom velocity rather than a time series. Therefore only one time period is available for analysis. The spilling waves from this dataset will be analysed in detail; the wave type, wave height and water depth are outlined in Table 4-2 and will be referred to by their symbols in this chapter.

Table 4-2. Spilling waves investigated in Flick (1978), with T=1.14s and H_o=11.6cm

Name	type	H (cm)	h (cm)
S1	pre-breaking	10.7	18.1
S2	break point	11.9	15.3
S3	bore	8.5	13.7
S4	bore	6.4	12.3

Due to the velocity measurement method utilised for this experiment, the wave records with a large amount of high frequency components could not be analysed with the traditional spectral method (Flick et al., 1981).

4.2 Analysis

Various types of analyses are undertaken for the experimental data presented in the previous section. These analyses will be outlined briefly in the following sections.

4.2.1 Numerical modelling using COULWAVE

COULWAVE (*Cornell University Long and Intermediate Wave Modeling Package*) (Lynett & Liu, 2008) is a free surface wave modelling package developed by Cornell University. The governing equations for this model are the fully nonlinear, extended Boussinesq equations. The monochromatic waves from the SASME and SUSCO data were input into the model and the output surface elevations and velocities were compared with the measurements. The finite volume option of the model was used as recommended by the developers. There will be slight differences in *z* elevation between the measured and predicted velocity as the output velocity from COULWAVE is shown at approximately mid-depth and the measured velocities are at specific *z* elevations.

4.2.2 Spectral transfer method

The velocity calculated by using a spectral transfer function was compared to the measured velocity at several points in the flume for both the SUSCO and SASME experiments. As there were only two to three locations of ADV (Acoustic Doppler Velocimeter) measurements of $u(z,t)$ that coincide with the AWG (acoustic wave gauge) measurements of $\eta(t)$for the SUSCO experiments, comparison of the spectral transfer method is limited to these locations.

To convert $\eta(t)$ to $u(z,t)$, the transfer function using sine wave theory can be expressed

$$u = \eta\omega \frac{coshk(z+h)}{\sinh(kh)} \tag{4.1}$$

where the wave number *k* is a function of ω and the depth *h* as per the sine wave dispersion relation

$$kh\ tanhkh = \frac{\omega^2}{g} h \tag{4.2}$$

For nearshore non-linear waves, this transfer function will over-estimate u under the strongly curved crest and vice versa under the flat trough. As shown by Nielsen (1986a, 1989) this problem

can be overcome by using local frequencies determined from η, which can be approximated using the local approximation method, which will be discussed in the next section.

4.2.3 Local approximation method

Nielsen (1989) used the local approximation method to convert $p(0,t)$ measurements to $\eta(t)$for irregular, non-linear waves. The same principle can be used for converting $\eta(t)$ to $u(z,t)$. The method is based on the idea that if a time series can locally be fitted by a simple harmonic function, e.g. $\eta(t) = Acos(\omega t - \varphi)$, a local angular frequency can be determined from

$$\omega_n = \sqrt{-\frac{\eta''}{\eta}} \approx \sqrt{\frac{-\eta_{n-1} + 2\eta_n - \eta_{n+1}}{\eta_n \delta^2}} \tag{4.3}$$

and this can in turn be used to generate wave related transfer functions. η'' denotes the second derivative of $\eta(t)$ and δ is the sampling interval.

The frequency can also be derived from its *M*th neighbours as well as adjacent points in order to address noise issues (Nielsen, 1989), which can be calculated using Eq. (4.4).

$$\omega_n \approx \sqrt{\frac{-\eta_{n-M} + 2\eta_n - \eta_{n+M}}{\eta_n (M\delta)^2}} \tag{4.4}$$

The same transfer function from the spectral transfer method outlined in Eq. (4.1) and (4.2) can be used with the calculated frequency.

4.3 Results

4.3.1 SASME experiments

Monochromatic case 1005, with a peak frequency (f_p) of 0.9766 *Hz* and H_{rms}=0.05m, was used for preliminary analysis. Typical surface elevation and velocity at two points (at *x*=-3.6m and *x*=-0.8m) over one wave period are plotted in Figure 4-3 and Figure 4-4 respectively. The mean is not removed for both cases. At *x*=-3.6m, both the surface elevation and velocity are close to sinusoidal, but closer to the shoreline at *x*=-0.8m, the wave shapes become more skewed and asymmetrical, due to the waves being near-breaking. When the velocity at *x*=-0.8m is compared with the velocity at *x*=-3.6m, the wave shape suggests a clear negative mean velocity.

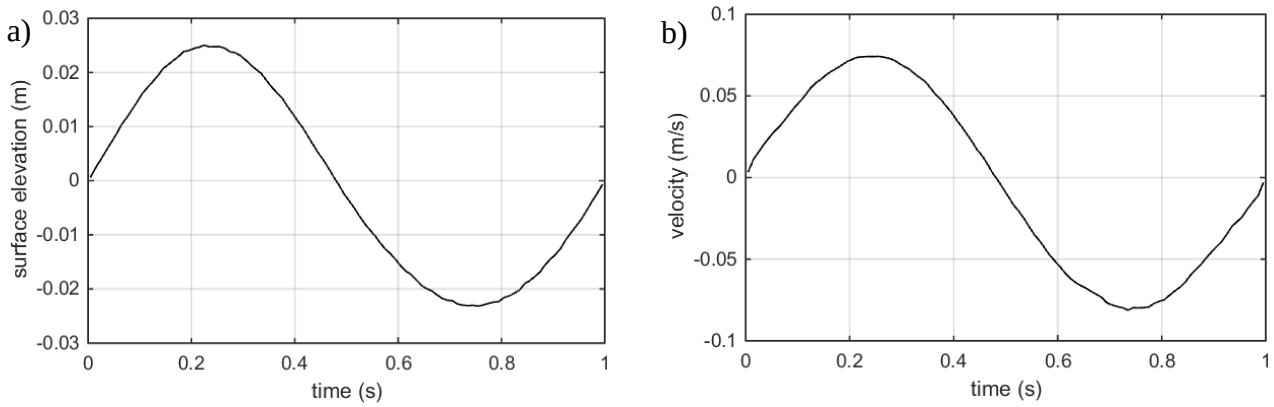

Figure 4-3. a) Surface elevation at *x*=-3.6m and b) velocity at *x*=-3.6m and *z*=0.17m.

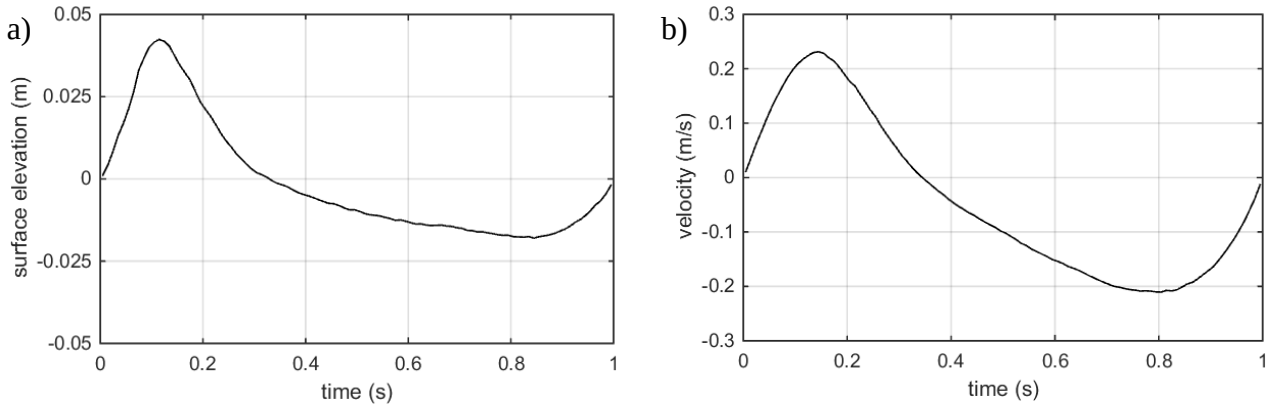

Figure 4-4. a) Surface elevation at *x*=-0.8m and b) velocity at *x*=-0.8m and *z*=0.006m.

The variation in wave height, mean surface elevation, mean velocity and skewness in Test 1005 is plotted in Figure 4-5. The wave height increases as the *x*-location nears the shoreline, until the last cross-shore measurement point, where it decreases dramatically due to breaking. The mean surface elevation and velocity are shown to become more negative approaching the break point. The velocity in particular has a more dramatic decrease at the most shoreward measurement point, highlighting the negative mean velocity near the break point, and the significant impact of undertow.

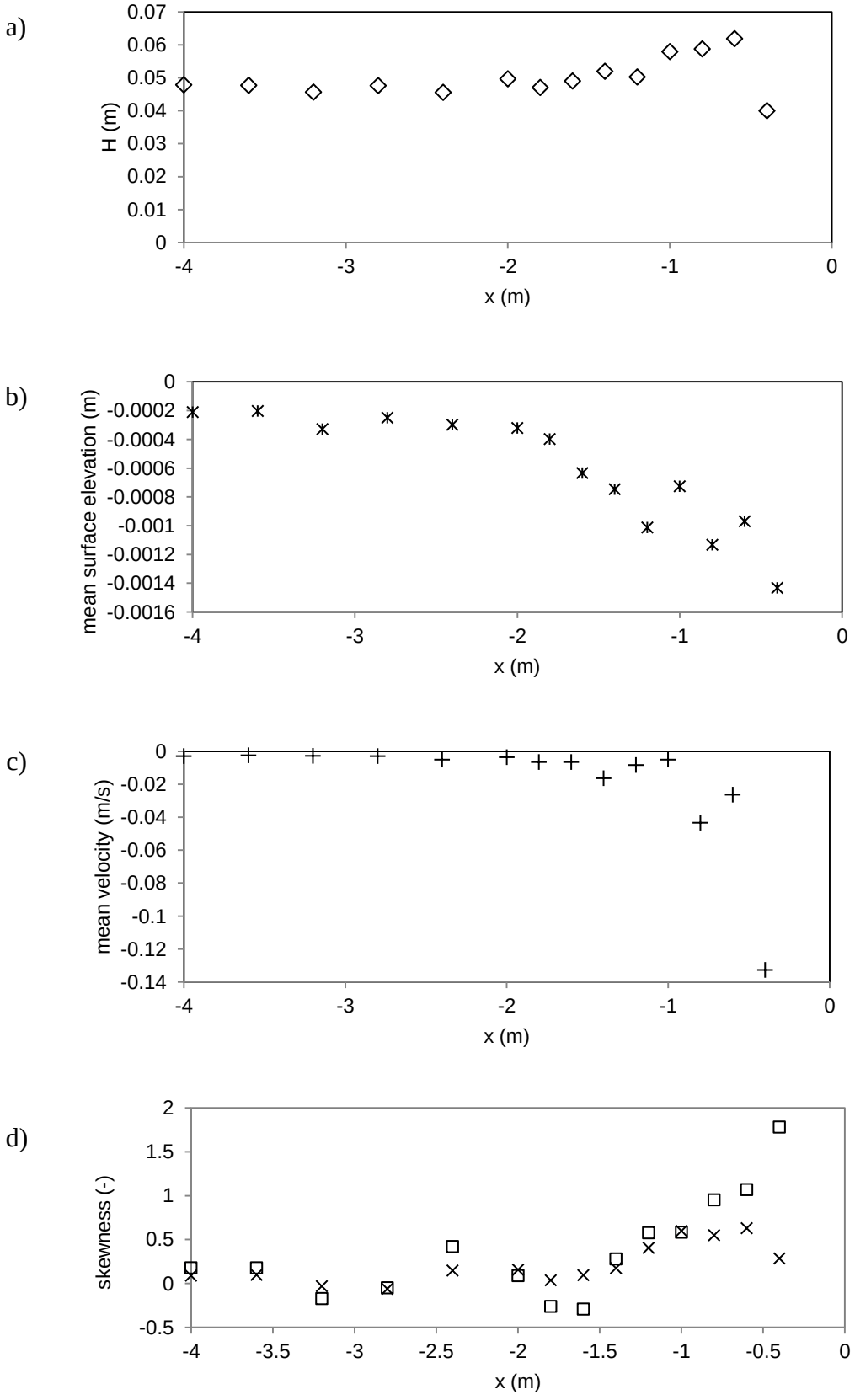

Figure 4-5. Cross-shore variation of a) Wave height (◊), b) mean surface elevation (*), c) mean velocity (+), and d) velocity skewness (x) and acceleration skewness (□) for Test 1005

The velocity skewness and acceleration skewness, Eq. (2.14) and Eq.(2.15) respectively, are shown again here:

$$\text{velocity skewness} = \overline{u^3} / \left(\overline{u^2}\right)^{3/2}$$

$$\text{acceleration skewness} = \overline{\left(\frac{du}{dt}\right)^3} / \left(\overline{\left(\frac{du}{dt}\right)^2}\right)^{3/2}$$

The plotted mean velocity $\bar{u}(x,z)$ are close to zero until approximately *x*=-1m. The *z/h* values for each point are listed in Table 4-1. The acceleration skewness increases further close to the shoreline while the velocity skewness decreases after an initial increase.

4.3.1.1 Numerical model prediction of velocity and surface elevation

The parameters used in the SASME experiments were input into the COULWAVE model and output surface elevation and velocities were compared to the measured values. The inputs *H*=0.05m, sine wave wavelength of 1.64m, and initial depth of 0.8m were used. The time series were compared for a period of approximately 16 seconds and R^2 values were calculated and presented in Table 4-3. The values further offshore surprisingly do not exhibit as high R^2 values as the others. Overall, 12 out of 14 *x*-locations show a good agreement between the modelled COULWAVE output and measured values. The data closest to the shoreline at *x*=-0.4m has a relatively low R^2 value. The model cannot predict the mid-depth velocity accurately when a wave is near breaking or broken. Measured and modelled surface elevation and velocity for two locations (*x*=-1.6m and *x*=-0.6m) are shown in Figure 4-6 for comparison. Overall the COULWAVE model predicts the surface elevation and velocity well until the last measurement position.

Table 4-3. R^2 values of compared COULWAVE and measured velocity at mid-depth

***x* (m)**	-4	-3.6	-3.2	-2.8	-2.4	-2	-1.8	-1.6	-1.4	-1.2	-1	-0.8	-0.6	-0.4
***R^2* (*u*)**	0.86	0.72	0.93	0.93	0.92	0.96	0.92	0.97	0.86	0.96	0.92	0.84	0.86	0.53

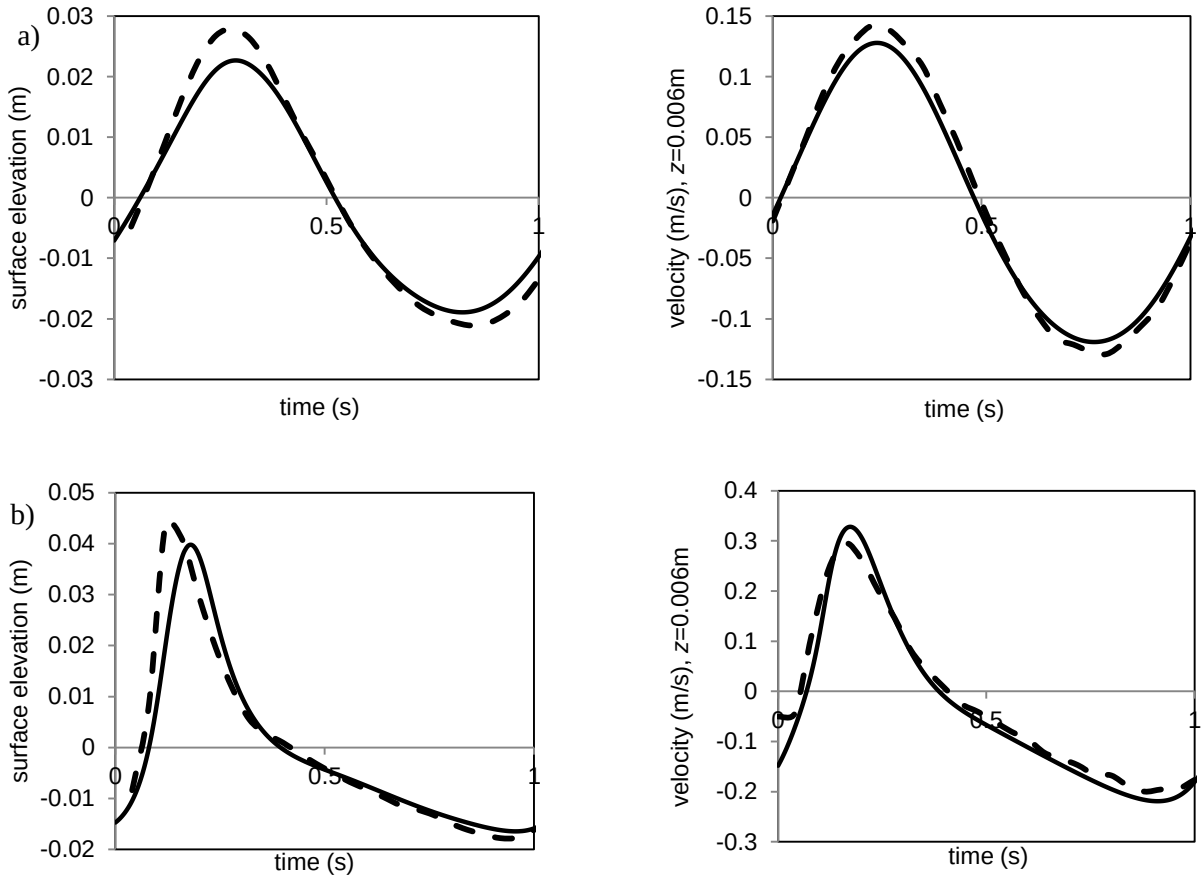

Figure 4-6. Measured (dashed) and modelled (solid) surface elevation and velocity at z=0.006m for a) x=-1.6m and b) x=-0.6m.

4.3.1.2 Spectral transfer method

As there are 14 locations available for analysis in these experiments, harmonic analysis was undertaken on the velocity (z/h values are listed in Table 4-1) and surface elevation by Fast-Fourier Transform (FFT) for the whole dataset. The transfer functions were calculated by dividing the FFT of the near-bed velocity by the FFT of the surface elevation. The resulting magnitudes of the first two harmonics for Case 1005 were plotted against the x-location and compared with transfer function magnitudes calculated from the spectral method and Stokes theory using Fenton (1985) in Figure 4-7.

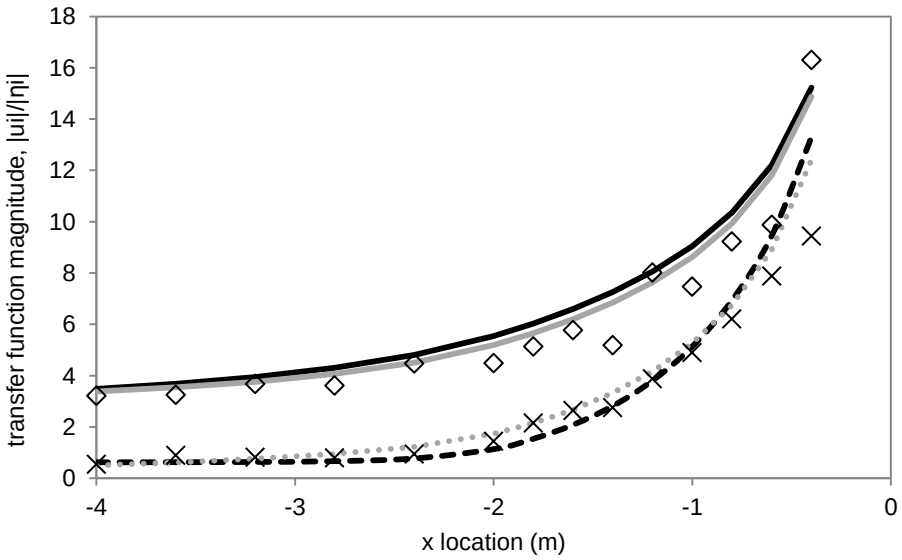

Figure 4-7. Test 1005 transfer function phase magnitude for 2 harmonics (1st harmonic- diamonds, 2nd harmonic- crosses). Black lines show transfer function magnitude predicted by spectral transfer method (1st harmonic- solid, 2nd harmonic- dashed), grey lines predicted by Stokes theory (1st harmonic- solid, 2nd harmonic- dotted)

The magnitudes of the second harmonic of the transfer function are relatively small until approximately *x*=-2m, when they start increasing gradually. Both of the harmonics gradually increase with increasing proximity to the shoreline. The transfer functions predicted by the spectral method show good agreement with the data for the first harmonic and the second harmonic up until the three points closest to the shoreline, suggesting that waves with significant higher harmonics are more difficult to predict with the spectral method, i.e. with waves approaching the breakpoint. This is in accordance with findings from Guza and Thornton (1980), who found that linear wave theory performs well except in the vicinity of the breakpoint. Stokes theory from Fenton (1985) predicts the transfer function better than the spectral method; the spectral method gives R^2=0.89 and Stokes theory gives R^2=0.93 for the first harmonic, while the spectral method gives R^2=0.82 and Stokes theory gives R^2=0.90 for the second harmonic.

While steady wave theories generally have $u(z,t)$ in phase with η, phase shifts were systematically found in the measurements of $\eta(x,t)$ and $u(x,z,t)$ over sloping bottoms. The phase lag of the transfer functions calculated from the data were also calculated and plotted in Figure 4-8. The surface elevation is consistently ahead of the velocity in phase. The phase lag tends to increase just prior to the break point and increases rapidly as the *x*-location approaches the shoreline for both harmonics. This also suggests that the lack of a phase term in the spectral and Stokes method is problematic when attempting to predict velocities further onshore.

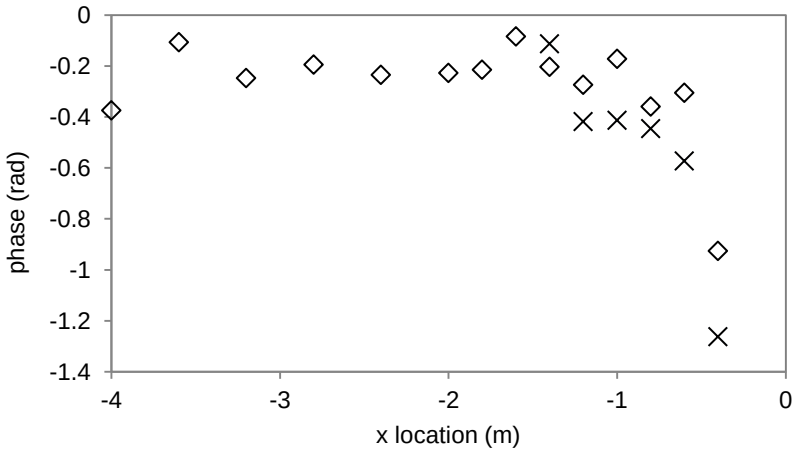

Figure 4-8. Test 1005 transfer function phase values for the first two harmonics (1st harmonic-diamonds, 2nd harmonic- crosses)

It was found that there is no obvious correlation with the magnitudes or the phase lag of the data that could be used in some predictive capacity. The inability to predict phase lag would have significant impacts for waves which are more acceleration skewed, near breaking (see Figure 4-9b). The waves situated further offshore would be able to be predicted by spectral method from fewer harmonics and no phase lag, as they are more predominantly velocity skewed.

Figure 4-9 shows the measured and predicted velocity by the spectral method for *x*=-1.6m and *x*=-0.4m. The location further offshore shows no phase lag and is able to be well predicted by the spectral transfer method. However, for *x*=-0.4m, the predicted velocity underestimates the negative velocity, overestimates the positive velocity and also starts to show a phase lead, being in phase with the surface elevation. This confirms the difficulties in predicting waves near breaking with the spectral transfer method.

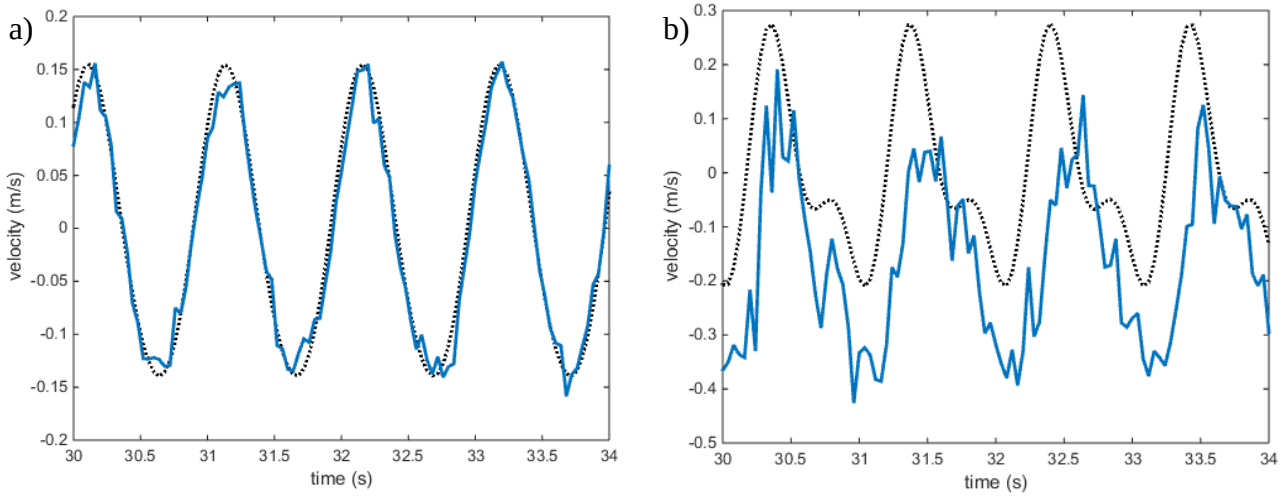

Figure 4-9. Measured (solid) vs predicted velocity (dashed) by spectral transfer method for a) *x*=-1.6m and b) *x*=-0.4m for *z*=0.006m.

4.3.1.3 Local approximation method

The SASME experiment data were used for the development of this local approximation method from surface elevation to velocity, firstly using monochromatic waves. The method was subsequently applied to random and bichromatic waves.

4.3.1.3.1 Monochromatic waves

The local approximation method was applied to the surface elevation measurements from experiment Case 1005.

With finite *H/h*, a correction is needed relative to sine wave theory which has infinitesimal *H/h* and hence zero flow between the MWL and the crest. While $\bar{u}$ becomes increasingly negative close to the shore, $\bar{q} \approx \overline{u(h+\eta)}$ must still be zero (See Figure 4-10). $u(z,t)$ can no longer be predicted by simply using Eq. (4.1), but requires this correction necessitated by finite *H/h*. An additional multiplier $\frac{h}{(\eta+h)}$ was introduced to account for this change in wave signal near breaking, shown in Eq.(4.5).

$$u = \eta\omega \frac{coshk(z+h)}{\sinh(kh)} \frac{h}{(\eta+h)} \tag{4.5}$$

For further offshore locations, where $\eta(t)$ is close to sinusoidal and $\frac{\eta}{h} \ll 1$, the multiplier $\frac{h}{(\eta+h)}$ is very close to 1 and has little effect. Further onshore, $\eta(t)/h$ is more substantial and hence the multiplier has a stronger influence on the velocity. This multiplier has the effect of balancing the velocities generated by the peaks and the troughs in order for $\bar{q} = 0$. Figure 4-10 shows the velocities under sine wave theory, where $\bar{q} \neq 0$ and with the multiplier applied.

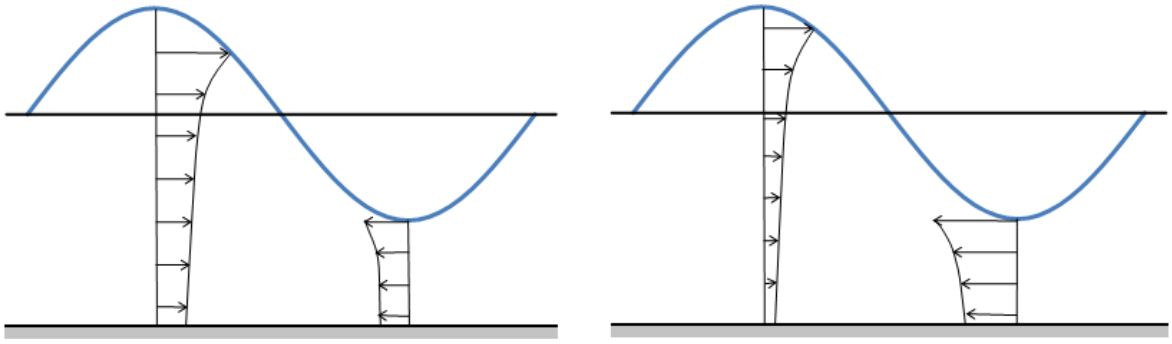

Figure 4-10. Horizontal velocities- Left under sine wave theory where $\bar{q} \neq 0$, Right with $\frac{h}{(\eta+h)}$ applied, leading to $\bar{q} \approx 0$.

It is clear that the addition of the multiplier $\frac{h}{(\eta+h)}$ improves the $u(z,t)$ prediction dramatically, as shown in Figure 4-11a (with no multiplier) with respect to Figure 4-11b (with multiplier). Although some phase difference between $\eta(t)$ and $u(z,t)$ is observed, Eq. (4.5) fares quite well in predicting $u(z,t)$.

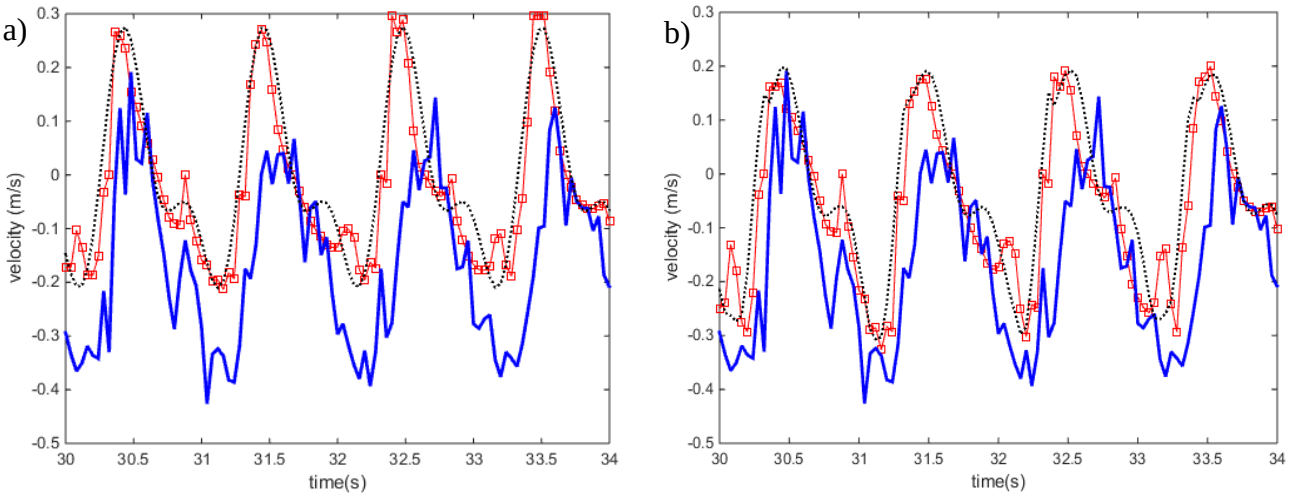

Figure 4-11. *x*=- 0.4m, *H/h*=1.25, for *M*=2, solid-measured velocity, a) □- Eq. (4.1), ⋯- spectral transfer method; b) □- Eq.(4.5), ⋯- spectral transfer method with multiplier.

The traditional spectral transfer method and local approximation method perform very similarly, with very high correlation between the predicted and measured $u(z,t)$ data for more offshore locations where $\frac{\eta}{h} \ll 1$ and there is little phase difference between $\eta(t)$ and $u(t)$.

At *x*-locations closer to the shoreline, it becomes more difficult for the spectral transfer method to predict $u(t)$ from $\eta(t)$ based on sine wave theory, shown in Figure 4-11a. This is due to the increasing $\frac{\eta}{h}$ with which the wave motion contains more forced harmonics, which do not obey the sine wave dispersion relation (Eq.(4.2)). Hence the multiplier $\frac{h}{(\eta+h)}$ to the spectral transfer method would also be beneficial at this location (see Figure 4-11b). Eq. (4.5) is applied instead of Eq. (4.1) in this case.

The local approximation method in its current state is unable to resolve the phase lag between $\eta(t)$ and $u(t)$ which is apparent in Figure 4-11b. While this is a minor issue for locations further offshore, the phase lag becomes more prominent as measurements are taken closer to the shoreline. Fortunately however there is no reason to believe that a simple phase shift of u should change $\overline{q_s}$.

Phase lags were also identified in data from Flick (1978), where one of the spilling breaker observations showed a 17 degrees phase lag for the bottom velocity at the breakpoint. Thornton et

al. (1976) found from field data that in breaking waves, the phase lag between $\eta(t)$ and $u(t)$ varied from between 5 and 20 degrees for the first harmonic. These values are very similar to the phase lags observed for all cross-shore locations in the SASME experiments, except for *x*=-0.4m, which had a significantly larger phase lag of approximately 50 degrees. Quantifying the phase lag between $\eta(t)$ and $u(t)$ remains presently unresolved, and should be considered in future developments.

4.3.1.3.2 Random waves

The local approximation method was also applied to random wave cases; the experimental data are presented in Baldock and Huntley (2002). Case 6033B with a f_p=0.6*Hz* and H_{rmso}=0.075m was used for this analysis. As the local approximation was initially developed for random wave cases, it performs very well in converting surface elevation measurements to velocity. However, once the waves approach the breakpoint, again, the measured velocity with a negative mean is not sufficiently predicted by local approximation.

The measured and predicted velocities are plotted in Figure 4-12; there is a significant portion where the measured velocity becomes increasingly negative between 52 and 61 seconds. The local approximation method, even with the multiplier which had the effect of shifting the velocity downwards, is not sufficient in the random wave case.

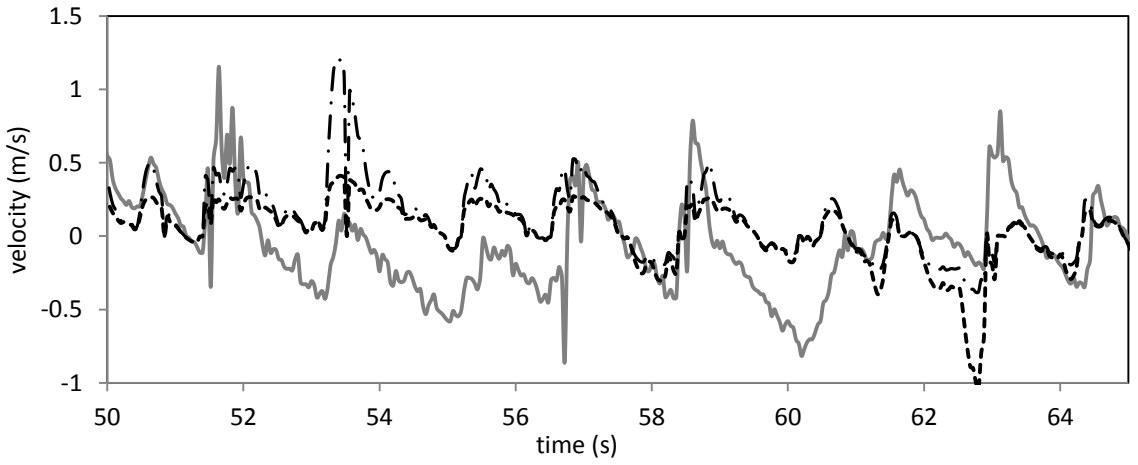

Figure 4-12. Case 6033B time series at *x*=-0.4m and *z*=0.006m of measured velocity (solid), predicted velocity with local approximation (dash-dotted), and predicted velocity with multiplier (dashed).

The traditional spectral method was also applied to this data set for comparison with the local approximation method. A similar method outlined in Nielsen (1986a) was used, using the surface elevation spectrum and a local wave number calculated from the local frequency from the dispersion relation and subsequently applying the transfer function. The results plotted in Figure

4-13 show that the local approximation method and spectral analysis method do not show a significant difference in velocity prediction capabilities.

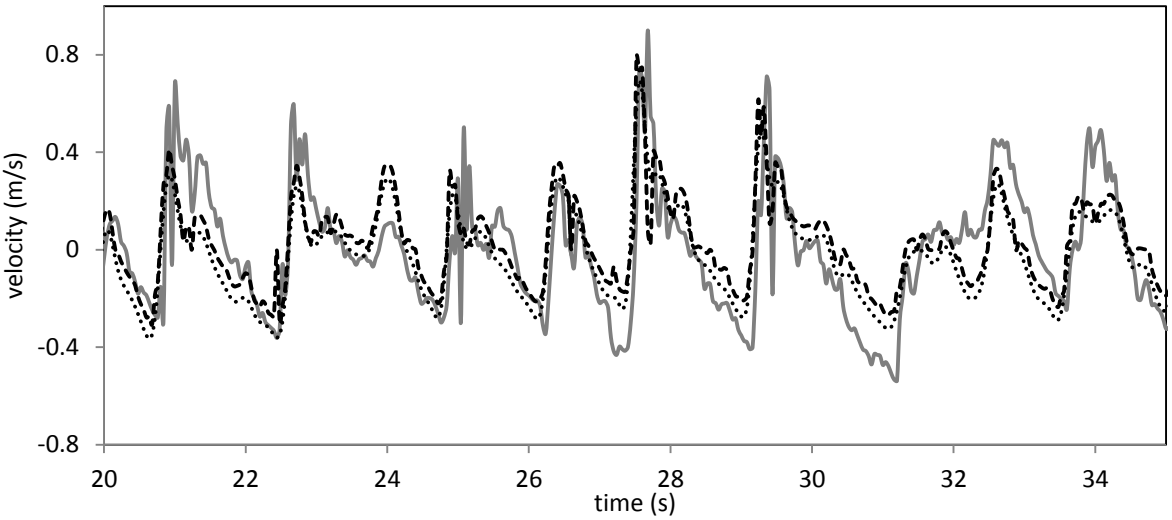

Figure 4-13. Case 6033B time series at x=-0.4m and z=0.006m of measured velocity (solid), velocity predicted with spectral method (dotted) and local approximation method (dashed)

R^2 values for the local approximation method with and without the multiplier and the spectral method for two x-locations are shown in Table 4-4. The local approximation method performs better than the spectral method at the most onshore measurement location. However, all three methods perform quite poorly for this x-location, compared to further offshore (e.g. x=-1.6m).

Table 4-4. Comparison of R^2 values for Case 6033B, h_b=0.053m

Method	Case	x (m)	R^2
Local approximation	6033B	-0.4	0.145
Local approximation with multiplier	6033B	-0.4	0.039
Spectral method	6033B	-0.4	0.06
Local approximation	6033B	-1.6	0.66
Local approximation with multiplier	6033B	-1.6	0.64
Spectral method	6033B	-1.6	0.66

The multiplier in Eq. (4.5) which was able to account for the strong negative mean at x=-0.4m for monochromatic cases gives no significant improvement for the random wave cases. Two other cases from the random wave experiments, with the same peak frequency but different H_{rmso}, were examined for the location x=-0.4m; results from Case 6033A are shown in Table 4-5 and Case 6033C are shown in Table 4-6.

Table 4-5. Comparison of R^2 values for Case 6033A, H_{rmso}=0.1m, h_b=0.07m (broken at x=-0.4m).

Method	Case	x (m)	R^2
Local approximation	6033A	-0.4	0.28
Local approximation with multiplier	6033A	-0.4	0.052
Spectral method	6033A	-0.4	0.15

Table 4-6. Comparison of R^2 values for Case 6033C, H_{rmso}=0.05m, h_b=0.035m (not broken at x=-0.4m)

Method	Case	x (m)	R^2
Local approximation	6033C	-0.4	0.09
Local approximation with multiplier	6033C	-0.4	0.22
Spectral method	6033C	-0.4	0.22

It is rather interesting for the spectral method that the R^2 value is worst when the wave has just broken. (It is worst for case 6033B). R^2 for the local approximation method is better for the broken waves than the unbroken; this is unexpected. The local approximation method with the additional multiplier does not seem to be an improvement on the original local approximation method, apart from case 6033C. Both the local approximation and the spectral method are unable to predict the velocity when very near breaking or when the waves have broken. Further offshore however, both methods successfully predict the velocity.

In order to determine whether the local approximation and spectral transfer methods are unable to predict low frequency long waves, analysis was repeated with filtered surface elevation data. From the wave energy spectra, a cut off frequency of 0.4*Hz* was chosen; the frequencies lower than this value were eliminated and the resulting surface elevation time series was used in subsequent analysis. The results from both the spectral transfer method and local approximation method (with multiplier) using the filtered surface elevation time series are plotted in Figure 4-14. This figure can be compared to Figure 4-12, where the same time period is plotted for the unfiltered data. The velocity predictions for both methods improve considerably when the low frequency waves are filtered out. It was found when the local approximation method result presented in Figure 4-12 was filtered, the prediction is better compared to when the surface elevation is filtered first and the local approximation method applied. This is due to the local approximation method emphasising recreating the shape of the signal rather than the specific spectra, as the spectral method does; this results in lower harmonics being present in the results from the local approximation method, even after the surface elevation input is filtered.

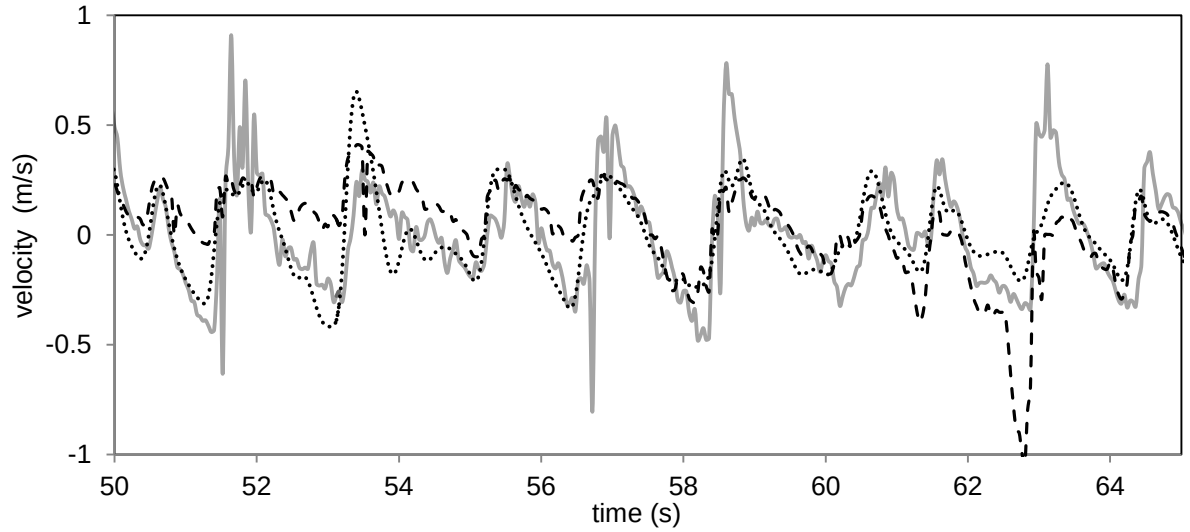

Figure 4-14. Case 6033B measured velocity, filtered, at *x*=-0.4m and *z*=0.006m (solid), velocity predicted with spectral method (dotted) and local approximation method with multiplier (dashed) with filtered surface elevation data

The predicted velocity using the local approximation method with multiplier was filtered with a cut off frequency of 0.4*Hz*. The results are plotted in Figure 4-15. When the predicted velocity is filtered, the prediction is improved significantly compared to when the surface elevation is filtered first and local approximation method applied.

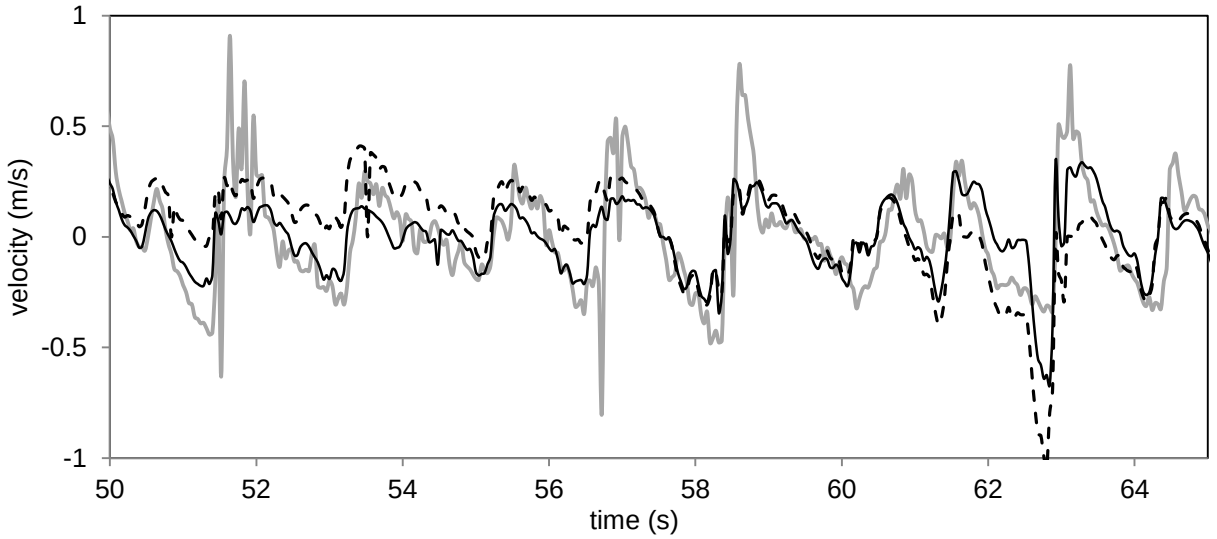

Figure 4-15. Case 6033B measured velocity, filtered, at *x*=-0.4m and *z*=0.006m (solid, thick), local approximation method with multiplier (dashed) predicted from filtered surface elevation data, local approximation method with multiplier, predicted velocity filtered (solid, thin)

The R^2 values for the methods using all harmonics, with filtered surface elevation, and filtered velocity result are shown in Table 4-7 for *x*=-0.4m.

Table 4-7. Comparison of R^2 values for Case 6033B for local approximation methods and spectral methods- with all harmonics, using cut off frequency for surface elevation input, and filtered predicted velocity

R^2	all harmonics	with 0.4Hz cut off input	Filtered velocity
Local approximation	0.145	0.11	0.42
Local approximation w multiplier	0.039	0.264	0.48
Spectral method	0.06	0.487	-

The local approximation method with multiplier has a similar R^2 value to the spectral method with filtered input when the predicted velocity (from all harmonics) is filtered. This suggests that the local approximation method is able to predict the higher harmonics when the original surface elevation time series is used as input; this implies that the local approximation method does not fare well with data consisting only of high frequency waves.

4.3.1.3.3 Bichromatic waves

The local approximation method was also applied to the bichromatic wave cases 1010A and 1060A. The primary (f_1), secondary (f_2), and group frequencies (f_G) (long wave component) for each case are shown in Table 4-8. As long waves become more dominant in shallow water, any model predictive capabilities need to incorporate the ability to predict the long wave component of a wave signal. A simple way of comparing the long wave component in a bichromatic signal would be to compare the single-sided amplitude spectrum of the measured velocity and the predicted velocity, normalised by the maximum amplitude value; this will be discussed in the following sections.

Table 4-8. Bichromatic wave experiment cases and frequencies, in *Hz*.

Case	f_1	f_2	f_G
1010A	1.025	0.928	0.098
1060A	1.269	0.683	0.586

Case 1010A

The local approximation method's predictive ability in the lower frequencies is inconsistent for this case. It should be noted that there are standing waves present. The f_G is approximately 0.1*Hz,* and as shown in Figure 4-16a, it is insignificant at the outermost point. Moving further onshore, the local approximation methods over predict the long wave component of the signal, see Figure 4-16b. As the measurements approach further onshore (Figure 4-16c-d), the long wave becomes more significant; the local approximation method still underestimates the magnitude, but with the

multiplier the method over predicts. The wave is broken by x=-1.1m, therefore locations further onshore are not considered for analysis. The primary and secondary frequencies are generally over predicted apart from at x=-1.4m. The spectral method also tends to over predict the primary and secondary frequencies and underestimates the group frequencies at locations close to the shoreline.

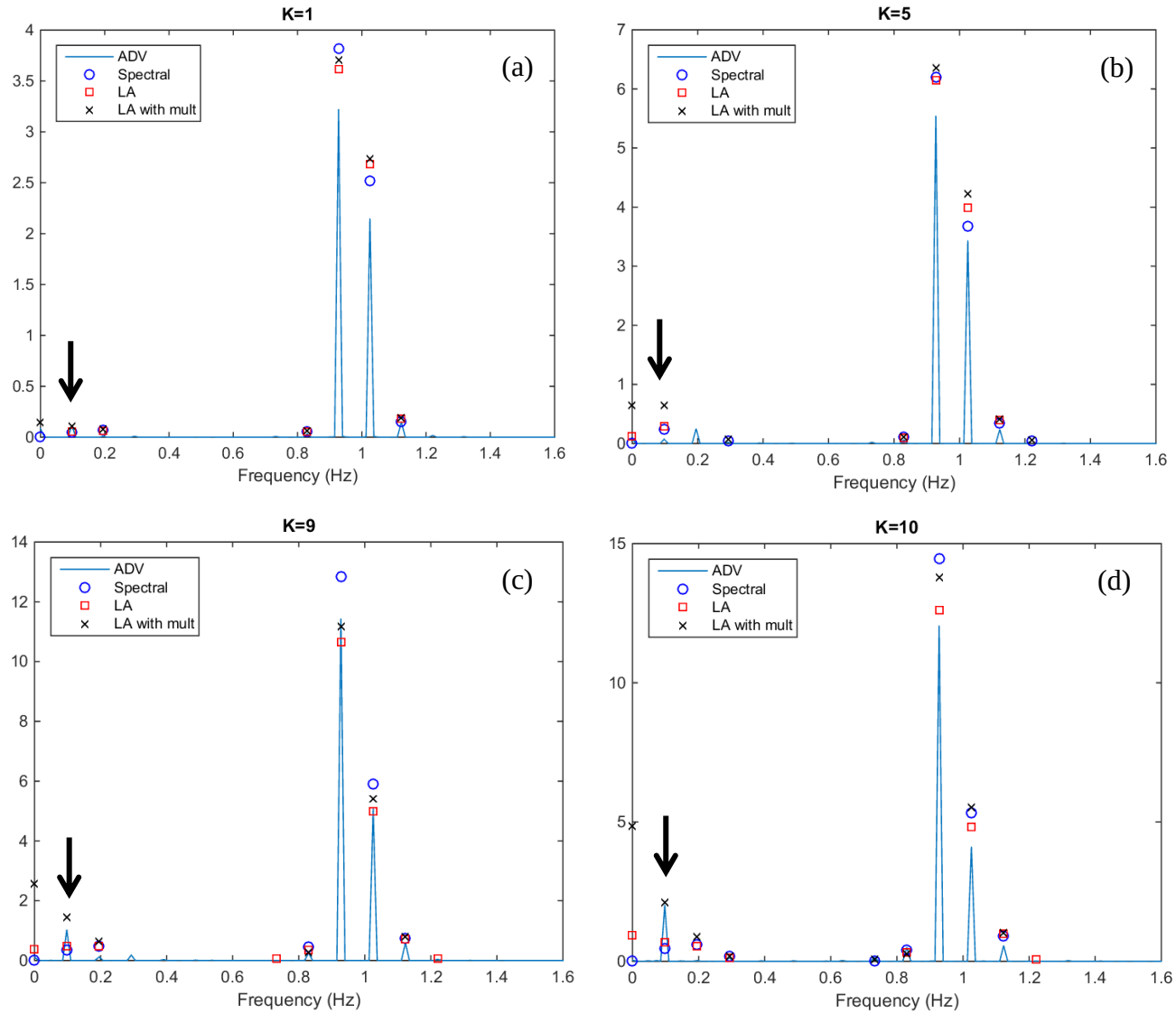

Figure 4-16. Case 1010A single-sided amplitude spectrum plots (a) x=-4m and z=0.206m, (b) x=-2.4m and z=0.046m, (c) x=-1.4m and z=0.006m, (d) x=-1.2m and z=0.006m, f_G points are indicated with arrows.

Case 1060A

This case follows a similar pattern to Case 1010A, as the local approximation method predicts the magnitude of the long wave better until approaching the shoreline, when the local approximation method with the multiplier becomes the better predictor of the long wave signal (Figure 4-17c-d). There are also standing waves present in this case, but less compared to case 1010A. Again, the long wave is not significant for the *x*-locations further offshore (Figure 4-17a-b) but becomes more prominent in shallower water depths (Figure 4-17c-d). By *x*=-0.8m, the wave has broken and therefore not able to be analysed. The primary frequency is consistently over predicted and secondary frequency is under predicted for this case. The spectral method tends to over predict both the primary and secondary frequencies, and behaves very similarly to the local approximation method without the multiplier for the group frequency.

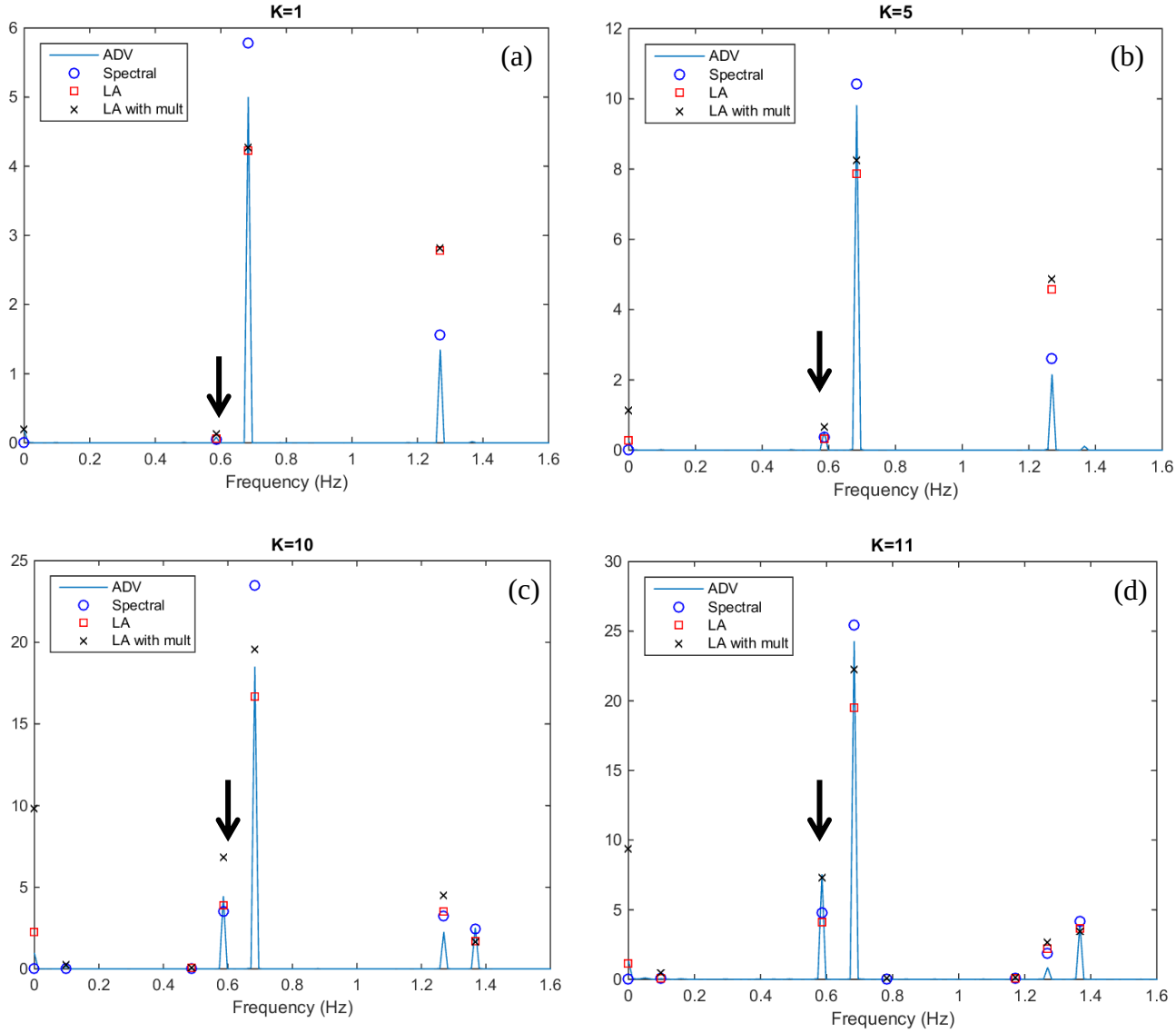

Figure 4-17. Case 1060A single-sided amplitude spectrum plots (a) *x*=-4m and *z*=0.206m, (b) *x*=-2.4m and *z*=0.046m, (c) *x*=-1.2m and *z*=0.006m, (d) *x*=-1m and *z*=0.006m, f_G points indicated with arrows.

The long wave analysis for these bichromatic wave cases indicate that the local approximation method is not consistently able to predict the long wave component of the bichromatic wave signal. There are times when the original local approximation method fares better, and others when the multiplier application improves the prediction. From the cases analysed, it appears that the multiplier should be applied when approaching the break point. However, applying this multiplier in an ad hoc manner defeats the purpose of being a predictive tool for velocities, therefore further work is required and more datasets should be analysed to determine at what point the multiplier should be applied. From the current analysis, the local approximation theory is not able to consistently predict the long waves in a wave signal.

Although the measured velocity clearly shows a negative mean for most cases, the multiplier from Eq. (4.5) which has the effect of shifting the predicted velocity towards lower values for monochromatic waves does not have the same effect on bichromatic waves; the multiplier tends to over predict the negative velocity. However, both 1010A and 1060A show that the local approximation with multiplier predicts the long wave the best for the measurement point just prior to breaking (see Figure 4-18). The same figure shows that spectral analysis behaves similarly for the local approximation method at this location. Overall, the local approximation method could not improve velocity predictions compared to the traditional spectral transfer method for bichromatic waves.

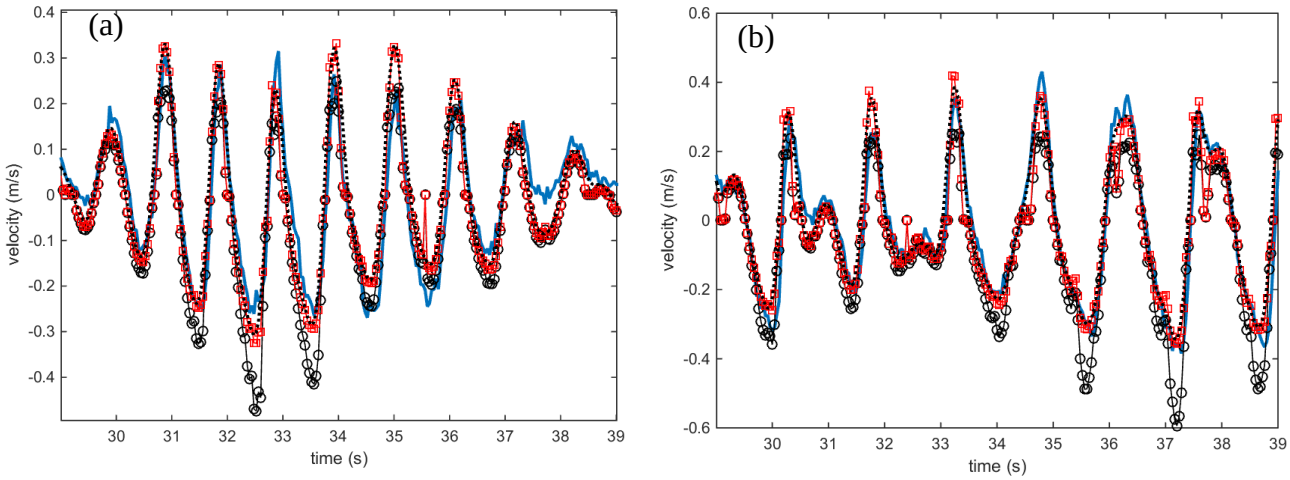

Figure 4-18. Measured velocity (solid), spectral method (dotted), local approximation (squares), local approximation with multiplier (circles) at x=-1.2 for Case 1010A (a) and x=-1m for z=0.006m for Case 1060A (b).

Similarly to the random wave analysis, the bichromatic wave data were reanalysed by filtering the long waves to determine whether the methods were able to predict the higher harmonics.

Case1010A was used for this analysis using a 0.9*Hz* cut off frequency, and the results are shown in Table 4-9.

Table 4-9. Comparison of R^2 values for Case 1010A for local approximation methods and spectral methods: with all harmonics, using cut off frequency for surface elevation input, and filtered predicted velocity.

R^2	all harmonics	with 0.9*Hz* cut off input	Filtered velocity
Local approximation	0.81	0.78	0.89
Local approximation w multiplier	0.70	0.57	0.88
Spectral method	0.82	0.91	-

Figure 4-19 shows the filtered measured velocity and the predicted velocities using the filtered surface elevation data. This figure can be compared to Figure 4-18a. The local approximation method does not improve its predictive ability when the low frequency harmonics are filtered, while the spectral method improves with filtering. When the predicted velocity from the local approximation methods using all the harmonics is filtered, it is clear that this method is able to predict the higher harmonics as well as the spectral method.

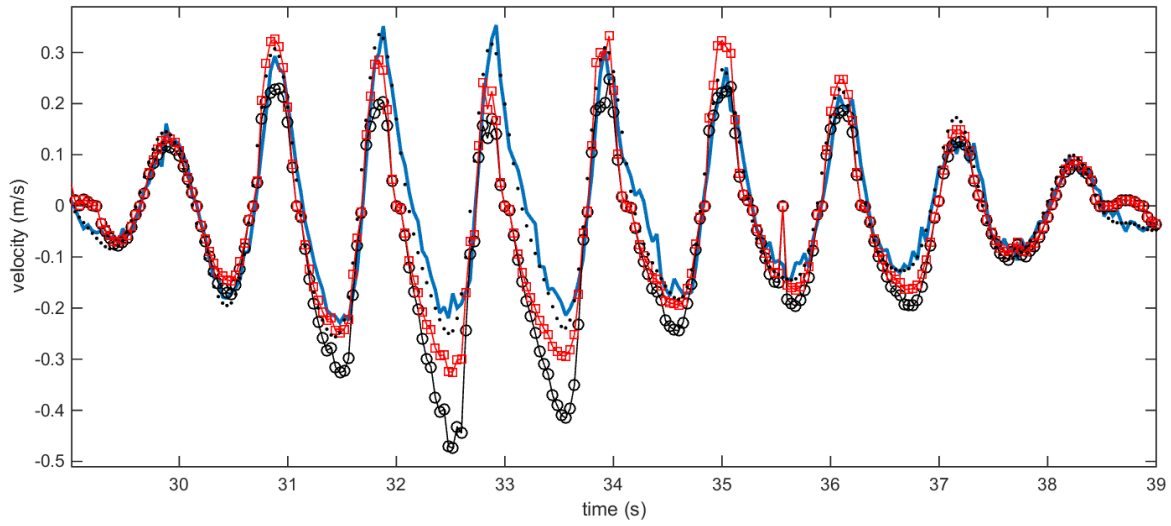

Figure 4-19. Measured filtered velocity (solid), predicted velocities using filtered surface elevation data for spectral method (dotted), local approximation (squares), and local approximation with multiplier (circles) at x=-1.2 and z=0.006m for Case 1010A

This result is very similar to the random wave case in the previous section. However, the multiplier in Eq. (4.5) does not improve the velocity prediction. Both the spectral method and the local approximation method was able to predict the bichromatic velocity quite well compared to the random waves, even at points close to the break point. When the low frequency harmonics are

filtered out from the surface elevation input, the spectral method result improves, while the local approximation method does not perform well when this filtering is applied. This leads to the conclusion that the local approximation method is best used on surface elevation data with a range of harmonics, but the method is still not an improvement on the traditional spectral method.

4.3.2 SUSCO experiments

The monochromatic, accretive wave case was used for preliminary analysis from the SUSCO experiments. Figure 4-20 shows surface elevation data from two wave gauges; there is obvious acceleration skewness present, especially in the gauge further onshore (AWG9), compared to the wave gauge outside of the surf zone (AWG0).

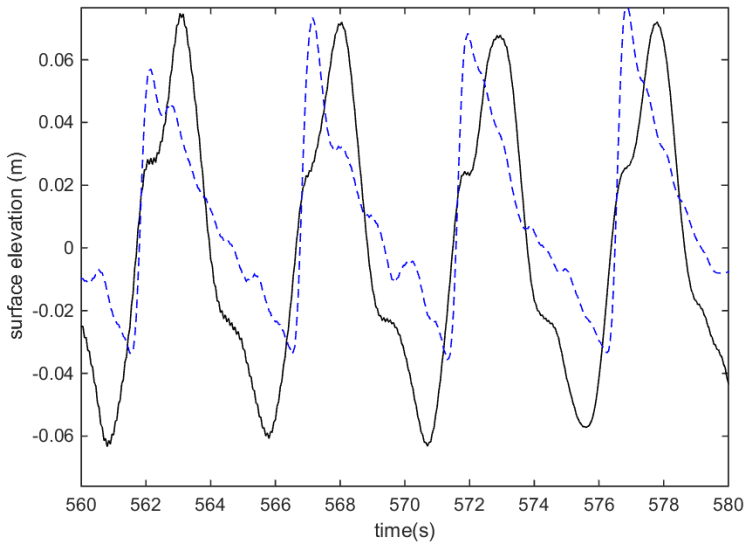

Figure 4-20. Wave gauge data from AWG0 (offshore, solid) and AWG 9 (onshore, dashed) for monochromatic accretive waves (case 65)

In comparing the velocity and wave gauge time series from ADV4 (x=76.51m) and AWG9 (x=76.38m) (the two closest locations available), it is apparent that these wave shapes are markedly different. Their $u(t)$ shapes over one wave period are plotted in Figure 4-21

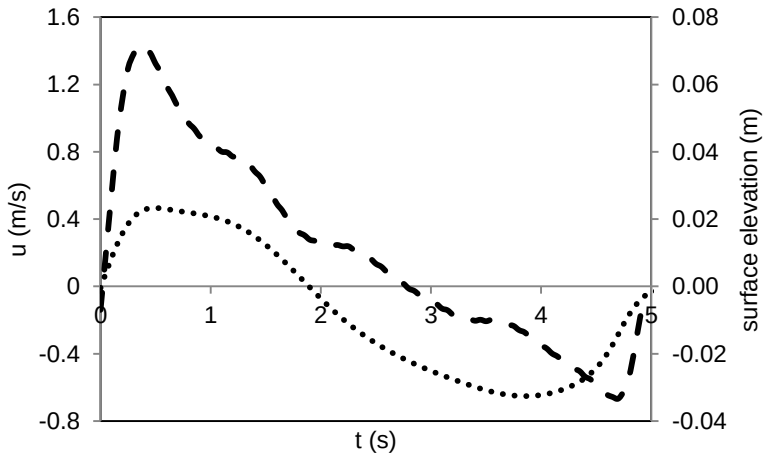

Figure 4-21. Velocity from ADV4 (dotted) at *z*=4cm and surface elevation from AWG9 relative to SWL (dashed) measurements under accretive monochromatic waves.

The time series of the velocity is much closer to a sinusoidal shape and lacks any significant velocity or acceleration skewness. The surface elevation measurements in contrast are much more skewed, exhibiting a typical sawtooth type wave shape. Any velocity time series based on the AWG9 measurement, using linear wave theory would produce a wave with significant negative mean.

When spectral analysis was undertaken for both the surface elevation and velocity time series, the results showed that the surface elevation has a more significant third harmonic than the velocity, see Figure 4-22. The single-sided amplitude spectrum is normalised by the maximum value in the spectrum for both cases. The higher harmonics decay more quickly for the velocity when compared to the surface elevation.

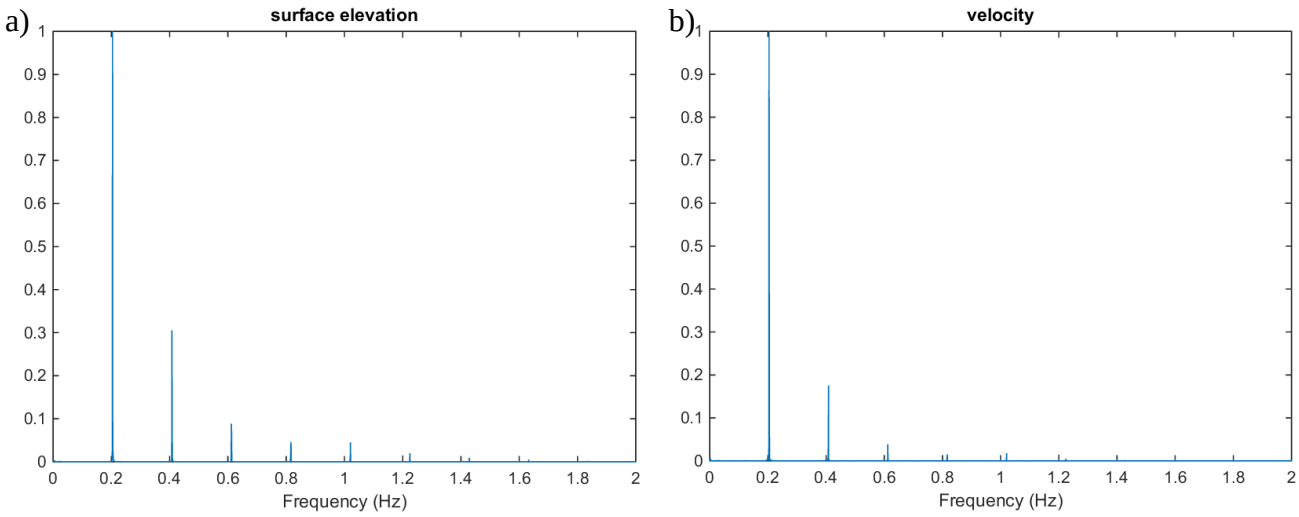

Figure 4-22. Single-sided amplitude spectrum of a) surface elevation from AWG9 and b) velocity from ADV4 (*z*=4cm) under monochromatic accretive conditions.

4.3.2.1 Numerical model prediction of velocity and surface elevation

In order to compare the measured surface elevation and velocity with those predicted by a numerical model, a COULWAVE model was run for the monochromatic accretive case 65, similarly to the SASME data. The modelled surface elevations and velocities were compared to measurements. Figure 4-23 shows the measured and modelled water surface elevation for AWG0. The COULWAVE input was a monochromatic wave as power spectral density analysis showed that the first harmonic was dominant. The wave height was specified as 0.15m, the water depth was 2.5m, and the sine wave wavelength was 25m. Despite the simplification of the input, the model predicts the magnitude of the surface elevation reasonably well, although it is evident that the measured surface elevation has many higher order harmonics present.

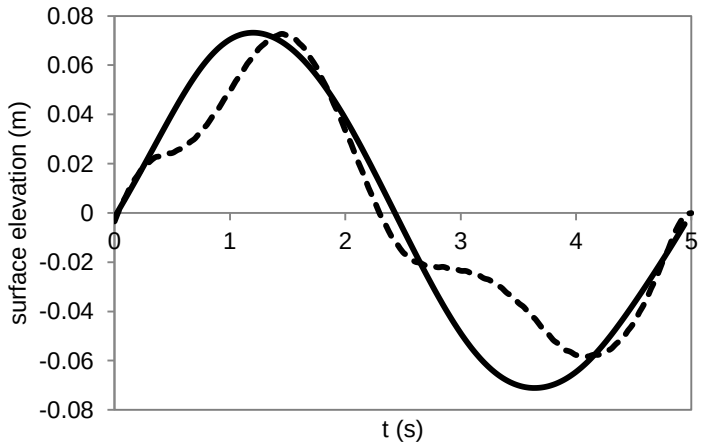

Figure 4-23. Comparison of measured surface elevation (dashed) and modelled surface elevation (solid) for AWG0 (x=51.67m) and COULWAVE (x=51.5m).

Comparing the cases further onshore, namely AWG10 and AWG9 in Figure 4-24, model predictive ability deteriorates in this zone. The measured surface elevation at AWG10 is both skewed and asymmetrical, while the model predicts a more typical sawtooth wave. The crest elevation is still predicted well, although the model predicts a more steep increase to the crest. AWG9 is also predicted poorly in comparison to the gauges further offshore. The magnitude of both the minimum and maximum surface elevation is overestimated.

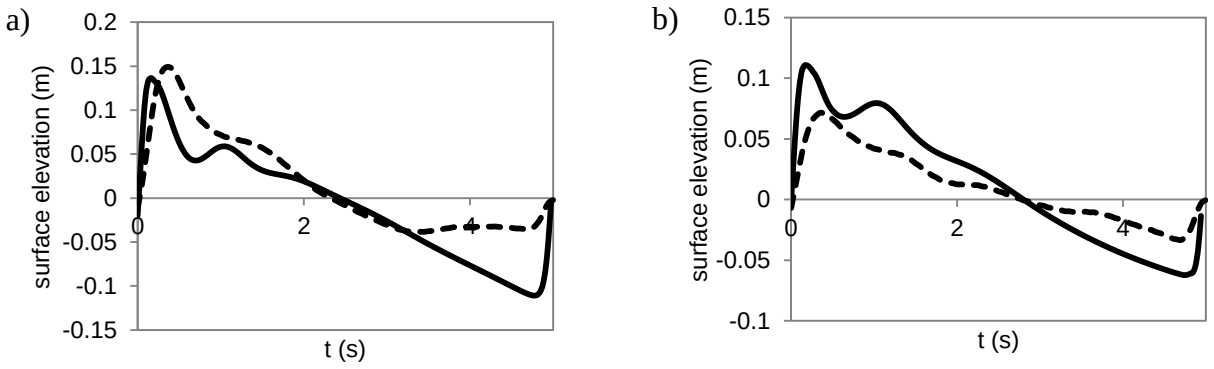

Figure 4-24. Comparison of measured surface elevation (dashed) and modelled surface elevation (solid) for: a) AWG10 (x=75.28m) and COULWAVE (x=75m) and b) AWG9 (x=76.38m) and COULWAVE (x=76.5m).

Figure 4-25 compares the measured and modelled velocity at two ADV locations. For ADV2, again both the minimum and maximum velocity is overestimated. For ADV1, the maximum is predicted better than the minimum velocity; the measurement shows a much flatter trough than the model. It is notable that the zero-crossings for all of the cases are predicted well, despite the general tendency of the model to overestimate the magnitude of both the surface elevation and velocity.

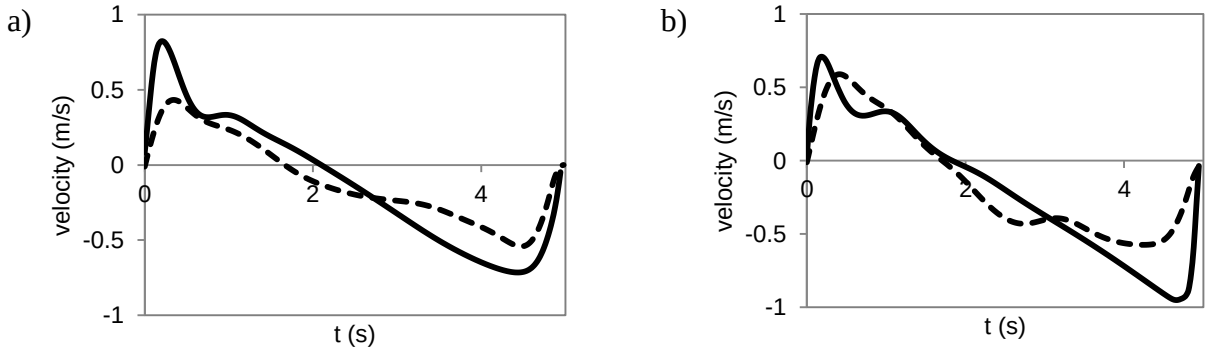

Figure 4-25. Comparison of measured velocity (dashed) and modelled velocity (solid) for: a) ADV2 (x=74.23m, z=10cm) and COULWAVE (x=74m), b) ADV1(x=76.51m, z=4cm) and COULWAVE (x=76.5m).

4.3.2.2 Spectral transfer method

As shown previously in Figure 4-21, the shapes of the velocity and water surface elevation were very different for the monochromatic accretive case. The spectral transfer method was applied to two locations from the experiment. Fifty waves were averaged for wave shapes from the ADV2 and ADV3 measurement at x=74.23m and the velocity calculated from AWG10 at x=75.28m are compared in Figure 4-26. The velocity predicted from the AWG measurement had a very peaked

positive *u* and plateaued negative *u*. The peaked maximum and plateaued minimum from the AWG calculations suggest there may have been some breaking occurring at this point.

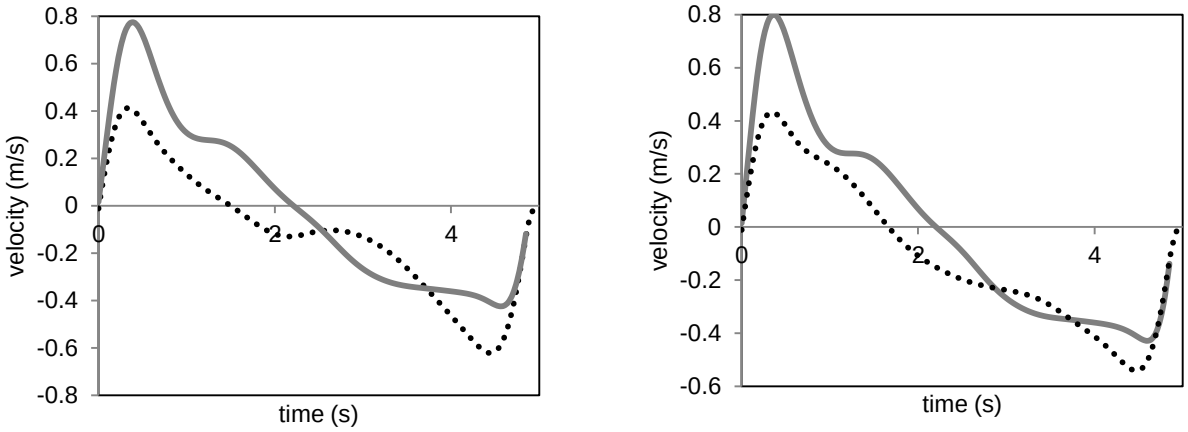

Figure 4-26. Measured velocity from a) ADV3 (dotted) compared to velocity calculated from wave gauge AWG10 (solid) at *z*=4cm, b) ADV2 (dotted) compared to velocity calculated from wave gauge AWG10 at *z*=10cm (solid),

Another wave gauge (AWG9 at *x*=76.38m) was compared with the ADV4 and ADV1 at *x*=76.51m and plotted in Figure 4-27. The wave shapes are quite different due to the wave breaking. The velocity calculated from the AWG exhibits a typical saw-tooth form while the velocity is much more rounded compared to the velocity measurement shown in Figure 4-26.

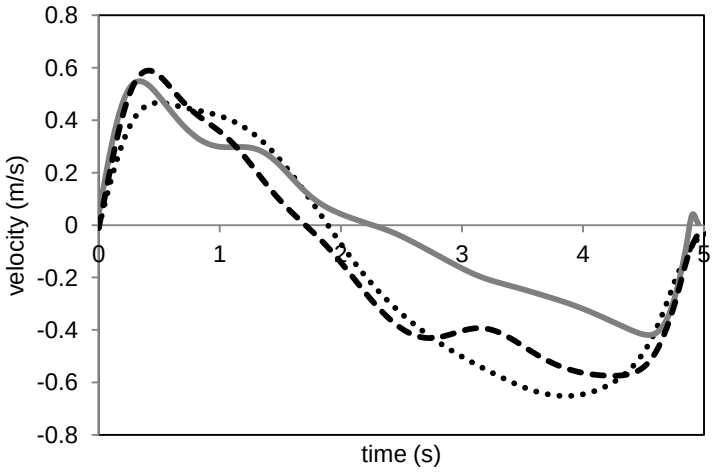

Figure 4-27. Measured velocity from ADV4 (dotted) and ADV1 (dashed) at *z*=4cm compared to velocity calculated from AWG9 (solid)

4.3.2.3 Local approximation method

The local approximation method was applied to the same locations as the spectral method. The first case compares the measured velocity from ADV1 and ADV4 (both *x*=76.51m) and AWG9 (*x*=76.38m), shown in Figure 4-28. An average velocity over 50 wave periods is plotted. The

measured velocity from both ADVs has a negative mean compared to the predicted velocity. The deceleration phase for the measured velocity is much steeper than that of the predicted velocity while the acceleration phase is predicted well, especially compared to ADV1. This leads to a good prediction for the crest but the trough is under predicted by a factor 2. The local approximation method with the multiplier does not improve predictions for this case.

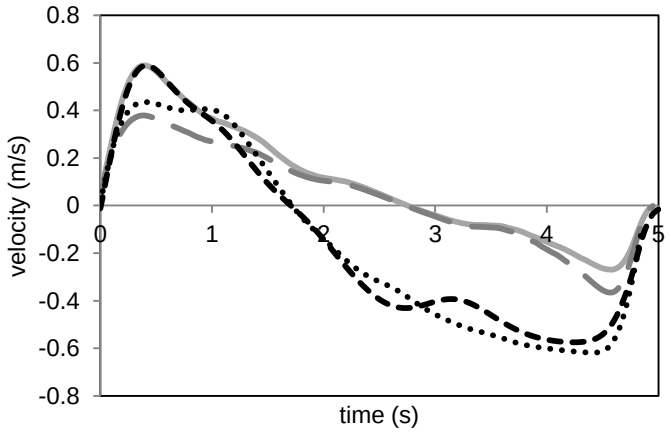

Figure 4-28. Measured velocity from ADV4 (dotted) and ADV 1 (dashed) at *z*=4cm, predicted velocity local approximation method (solid), with multiplier (long dashed) using AWG9.

The second case compares the measured velocity $u(74\text{m}, t)$ from ADV2 and ADV3 and $\eta(75\text{m}, t)$, plotted in Figure 4-29. ADV2 is measured at *z*=10cm while ADV3 is measured at *z*=4cm. There are phase lags present due to the slight difference in *x*-location when the time series of the predicted and measured velocities are plotted. Again, the deceleration phase is not predicted well by the local approximation method, while the acceleration phase is predicted well. The measured velocity shows a more typical sawtooth type wave shape while the predicted velocity exhibits a flatter trough, due to the input wave gauge data showing the same characteristics. The local approximation method with multiplier appears to improve predictions for these cases, as the local approximation method over predicts the peaks.

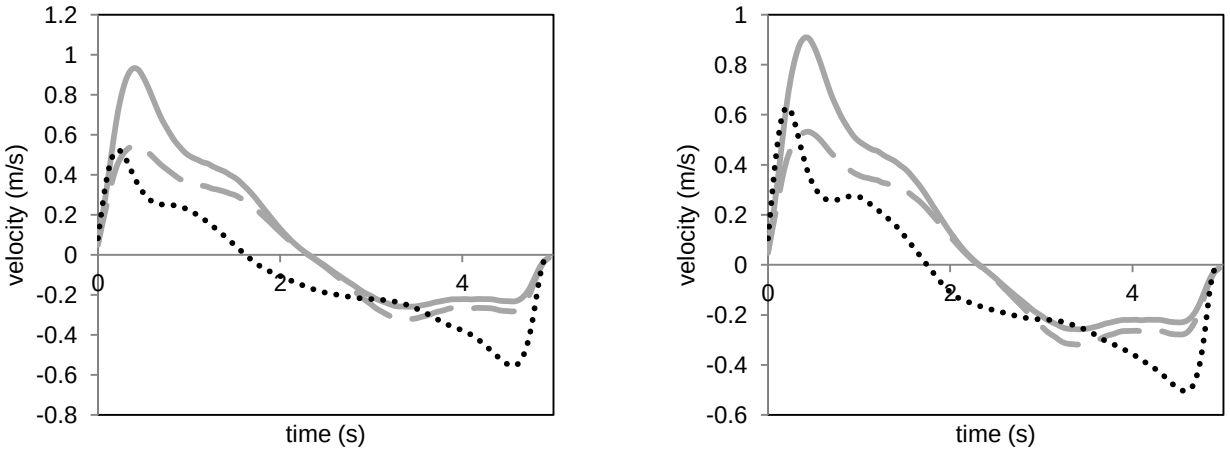

Figure 4-29. Measured velocity (dotted), predicted velocity using local approximation method (solid), with multiplier (long dashed) using data from a) ADV2 (z=10cm) and AWG10 b) ADV3 (z=4cm) and AWG10.

4.3.3 Flick (1978)'s experiments

As mentioned previously in Section 4.1.3, Flick (1978) collected data from spilling waves and plunging waves at various points prior to breaking, breaking and post-breaking. Figure 4-30 shows the mean velocity and surface elevation over one wave period for the spilling breakers, at pre-breaking and at the break point. The increasing non-linearity is evident at the break point.

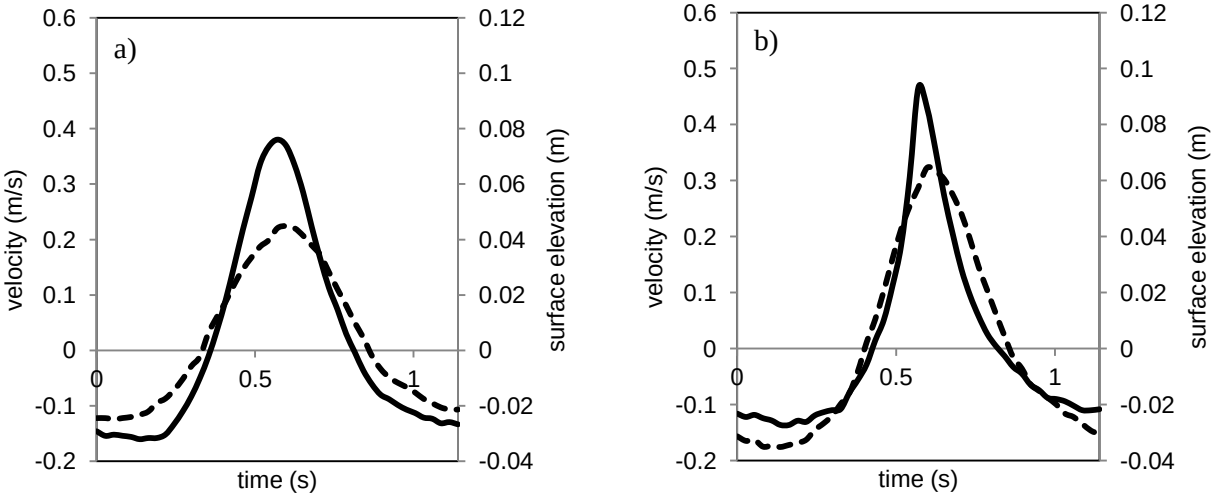

Figure 4-30. Measured surface elevation (solid) and velocity (dashed) for a) S1 (pre-breaking) and b) S2 (break point)

Preliminary application of the local approximation theory to spilling and plunging waves from Flick (1978) showed that the local approximation method works much better for spilling breakers than plunging breakers. This is thought to stem from the higher correlation between surface elevation and bottom velocity for spilling breakers (Flick et al., 1981). Plunging breakers have relatively

lower correlation prior to breaking and rapidly decrease in correlation after breaking. The application of the local approximation method will be discussed in detail for the spilling breakers.

Despite the mean values of surface elevation used for the prediction of velocity, some volatility of local angular frequency (ω_n) values are unavoidable (e.g. when the denominator in Eq. (4.4) is small). This issue can be rectified by setting an upper limit for ω_n (ω_{max}), and interpolating between acceptable values. Alternatively, the optimal *M* values can be calculated using the formula from Nielsen (1989), where *D* is the still-water depth, g is acceleration of gravity and δ is the sampling interval.

$$M \approx \frac{\left(\frac{D}{g}\right)^{0.5}}{\delta} \tag{4.6}$$

This gives an indication of optimal sampling interval multiplier, but as Nielsen (1989) points out, δ must be smaller than $\left(\frac{D}{g}\right)^{0.5}$ for this rule to be applied. The sampling interval hence plays a major role in this method, which suggests that the intrinsic time scale of the hydrodynamic processes involved needs to be considered when deciding measurement intervals, rather than limitations from instrumentation.

Nielsen (1989) also suggested a method to determine the cut off frequency, i.e. beyond which value is not considered realistic for calculations. This is done by plotting a histogram of weighted local frequencies ($f_n = \frac{\omega_n}{2\pi}$), in this case weighted by the surface elevation time series squared. Where there is a sharp drop-off, the frequencies beyond this point can be considered noise. This is plotted in Figure 4-31.

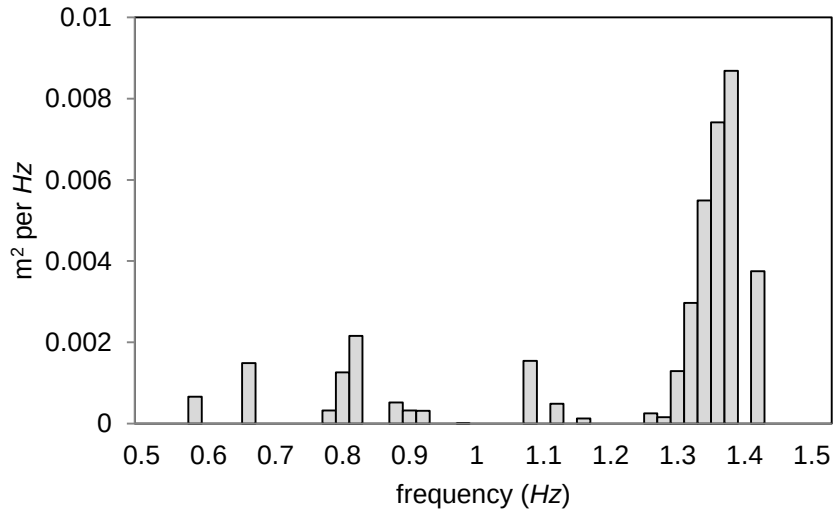

Figure 4-31. Example of histogram of weighted local frequencies for Case S2, using *M*=5

Of course the frequencies vary depending on ω_n, which varies with *M*. Therefore it is suggested to determine optimal *M* first, and then to adjust the ω values which are considered to be unacceptable for the dataset. Once the cut-off frequency f_{max} was determined from the histogram of local frequencies (Figure 4-31), the ω_{max} value was calculated. The parameters used in analysis are shown in Table 4-10. Calculations for *M* (Eq. (4.6)) indicated that the optimal *M* was between 4 and 5. Both these values were tested for the spilling breaker cases. S1 was omitted as it did not follow a similar pattern to that of S2 to S4.

Table 4-10. Local approximation method parameters tested for cases S2, S3 and S4.

Case	*M*	f_{max} (*Hz*)	ω_{max} (rad/s)	R^2
S2	4	2	12.5	0.807
S2	**5**	**1.6**	**10**	**0.875**
S3	4	2.2	13.8	0.867
S3	**5**	**3**	**18.8**	**0.879**
S4	4	2.5	15.7	0.936
S4	**5**	**2.6**	**16.3**	**0.943**

Nielsen (1989) suggested a rule of thumb, $\omega_{max} = 7\pi/T_p$, which equates to approximately ω_{max} of 19 rad/s; all the calculated ω_{max} values are smaller than this value. When the R^2 values obtained from this method were compared to trial and error adjustment of ω_{max} values to get the highest R^2, the result suggests that the ω_{max} values should be much less hence a smaller f_{max}. The discrepancy between cut-off frequencies is attributed to the very subjective nature of using the histogram of local frequencies.

The measured velocity for S2, and predicted velocity with *M*=5 with various values of ω_{max} are plotted in Figure 4-32. The local approximation method with multiplier (Eq. (4.5)) is used, as S2 is measured at the break point. The plot shows limiting ω_{max} to 10 rad/s does not change the predicted velocity significantly, but decreasing ω_{max} further has a larger impact and is able to improve the peak velocity prediction. Not limiting the ω_{max} does not result in a higher maximum velocity, as ω is positively correlated with *k*, but inversely correlated with $\frac{cosh k(z+h)}{\sinh(kh)}$ in Eq. (4.5).

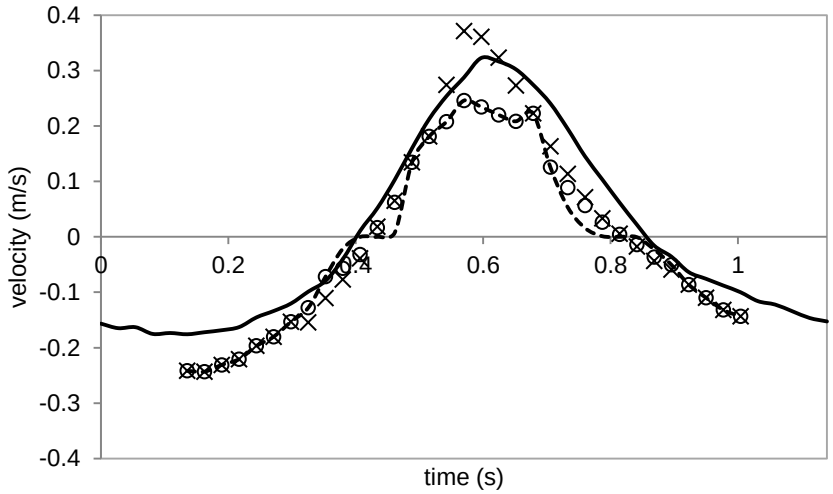

Figure 4-32. Case S2, Predicted velocity with *M*=5 and no ω_{max} limitation (dashed), $\omega_{max} = 7$ rad/s (crosses), $\omega_{max} = 10$ rad/s (circles), and measured velocity (solid).

Ultimately, the best fit between predicted and measured velocity becomes a balance of *M* and ω_{max} . R^2 values are similar for the plotted cases, but it is clear that a smaller ω_{max} predicts the velocity better. Since discounted ω_n values become infilled by interpolated values between two ω_n values which are less than the ω_{max}, the ω_n values become fairly homogenous, having the same effect as a constant ω_n value, which in effect makes the predicted velocity proportional to the surface elevation time series (see Figure 4-33 for comparison of ω_n values). This, as a result, makes the entire process rather futile, unless an alternative process of choosing the ω_{max} value is specified.

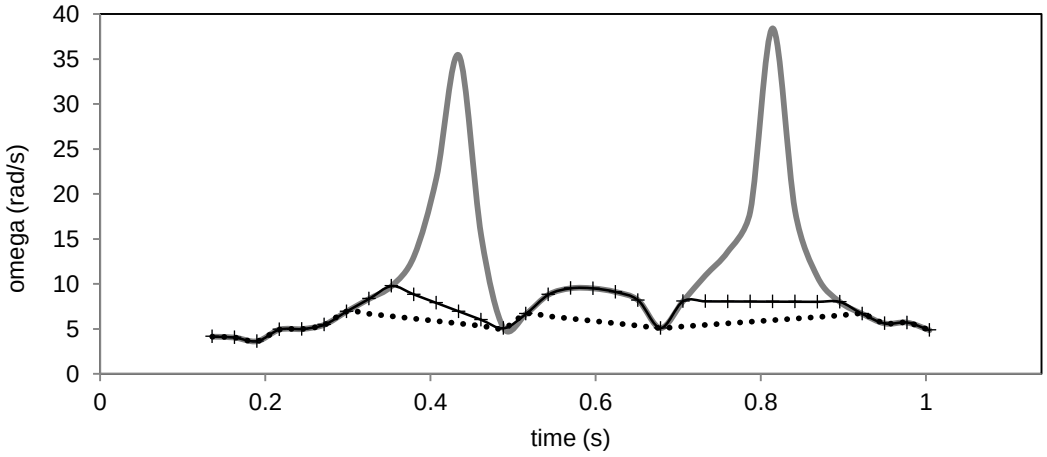

Figure 4-33. ω_n values over time (solid) and interpolated ω_n values with limiting $\omega_{max} = 7$ rad/s (dotted), $\omega_{max} = 10$ rad/s (crosses)

The local approximation method, which worked well for the monochromatic SASME data discussed in Section 4.3.1.3.1 has restrictions on the type of data that is able to be applied to in its

current state. However for this spilling wave data, despite not having time series data of the surface elevation, the local approximation method works reasonably well.

4.4 Conclusions

The local approximation method from Nielsen (1989) was adapted to estimate $u(z,t)$ from $\eta(t)$. Preliminary application to monochromatic short wave data shows that this method estimates $u(z,t)$ accurately, especially when $\frac{\eta}{h} \ll 1$. It was found that increasing nonlinearities further onshore and deviations from sine wave theory can be accounted for with an additional multiplier, $\frac{h}{(\eta+h)}$. This multiplier can be applied to both the spectral transfer and local approximation methods to improve $u(z,t)$ predictions significantly (shown in Figure 4-11b). The COULWAVE model is able to predict the monochromatic wave case quite well at all points except when the wave has broken.

Despite its successful application to the monochromatic waves in the SASME experiment data, the local approximation method did not improve upon the traditional spectral method for random and bichromatic waves. When the low frequency harmonics were filtered from the surface elevation input, the spectral method improved significantly but the local approximation method did not, due to the method not being focused on recreating the spectra of the signal, but the shape. The predicted velocity is improved when the predicted velocity from all harmonics using local approximation is filtered. The bichromatic wave could be predicted by all methods well even prior to the low frequency filtering, but the prediction is slightly improved by filtering.

The SUSCO data unfortunately only had two points which could be compared; one case showed improvement of velocity prediction with the local approximation method with additional multiplier, but the velocity was generally badly predicted by the spectral method, local approximation method as well as from the COULWAVE model.

The experimental data from Flick (1978) showed that the method was able to predict the velocity well when there were several limitations specified, such as limiting frequency ω_{max} and *M*. Ultimately, this identifies further challenges for the local approximation method, as determining these limits are still very subjective and hence require more stringent guidelines.

The local approximation method offers an alternative method to convert surface elevation to velocity, but in many cases is not an improvement on the spectral transfer method. The local approximation method enables the analysis of wave data in the time domain and focuses on recreating the shape of the wave rather than the spectra, which can be an advantage for irregular

waves. For some cases, the local approximation method still requires several amendments and limitations and in its current state, it is unable to be applied to cases which have a significant long wave contribution, especially for random waves.

It is noted that any phase difference between $\eta(t)$ and $u(z,t)$ is not accounted for in this present method, and neither by spectral transfer method using sine wave theory; this could be addressed in further research.

5 Beach profile experiments under random waves

Beach profile measurements in which each case is run until equilibrium with a variety of wave heights are very rare. Many experiments either do not have sufficiently regular measurement intervals, or the experiments are stopped before they reach equilibrium. Atkinson et al. (2015) recently investigated beach profiles under monochromatic waves in the University of Queensland (UQ) wave flume, with varying H for T=1s and 2s. This dataset shows the importance of antecedent conditions on the evolution of the beach. However, there are some shortcomings in running monochromatic waves, the main concern being that the waves are starkly different from real ocean waves, and the resulting beach profiles are often unlike those from field data. Few laboratory experiments have measured profiles under random waves over an extended time period. Some experiments have been run in large prototype scale flumes (e.g. Cáceres & Sanchez-Arcilla, 2015; Newe et al., 1999; Roelvink & Reniers, 1995; Uliczka & Dette, 1988) but these were either run for insufficient time periods, in which the profiles did not reach equilibrium, or have limited variations in test conditions. Swart (1974) conducted experiments with waves run in excess of 2800 hours for erosive profiles, but did not investigate any accretive waves. Therefore random wave experiments were undertaken in the UQ wave flume with varying H values. The profile measurements for one wave height were stopped when equilibrium was considered to be reached; this is discussed further in Section 5.3.4.

5.1 Method

Random wave experiments on a beach profile were carried out in the wave flume in the UQ hydraulics laboratory in Brisbane, Queensland, Australia from October to December, 2014. The UQ flume is approximately 20m long, 1m wide and 1m deep. The median sediment size d_{50} is 0.3mm. The beach covers approximately 9m of the flume. The initial beach slope used was 1 in 10. The experiments were run with an offshore water depth of 0.6m. The flume set up is shown in Figure 5-1.

a)

b)

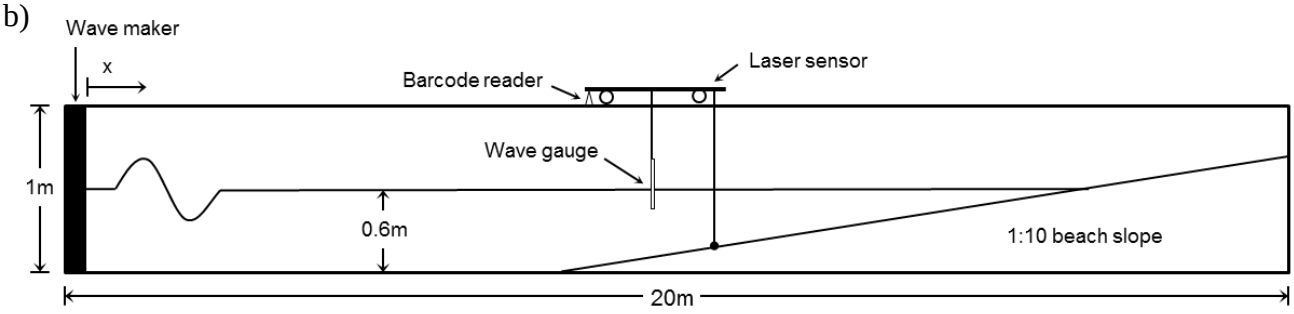

Figure 5-1. Wave flume set-up a) photograph of flume b) plan view diagram

5.1.1 Instrumentation and setup

The laboratory waves were generated using a DHI Wave Synthesizer, specifying irregular waves with a Pierson-Moskowitz spectrum. There were 8 lasers used for profile measurement. Laser distance sensors were used to measure the profile elevation (SICK DT50-P111 mid-range, red, class 2). These lasers have an analogue 4-20 mA output with a measurement range to 10 m with 1 mm resolution, 2.5 mm repeatability, high level of accuracy (± 10 mm over 10,000 mm in air), and an IP65 enclosure rating (Atkinson & Baldock, 2016). The *x*-coordinates were measured with a barcode reader (SICK OLM100), which uses a LED light source, barcode sensor and barcode tape which is fixed along the length of the flume. The barcode reader provides a good level of accuracy (0.1mm) and high repeatability (±1mm over 10km). The sensors and barcode reader are mounted on a trolley that is able to be pushed along the top of the wave flume, with the output being logged at 100*Hz* and 50*Hz* via analogue and digital signal respectively. The trolley was pulled along the flume manually. Atkinson and Baldock (2016) found that the repeatability was in the order of ±1mm, and there was approximately 4mm difference between measuring a dry and wet profile. The laser set-up is shown in Figure 5-2.

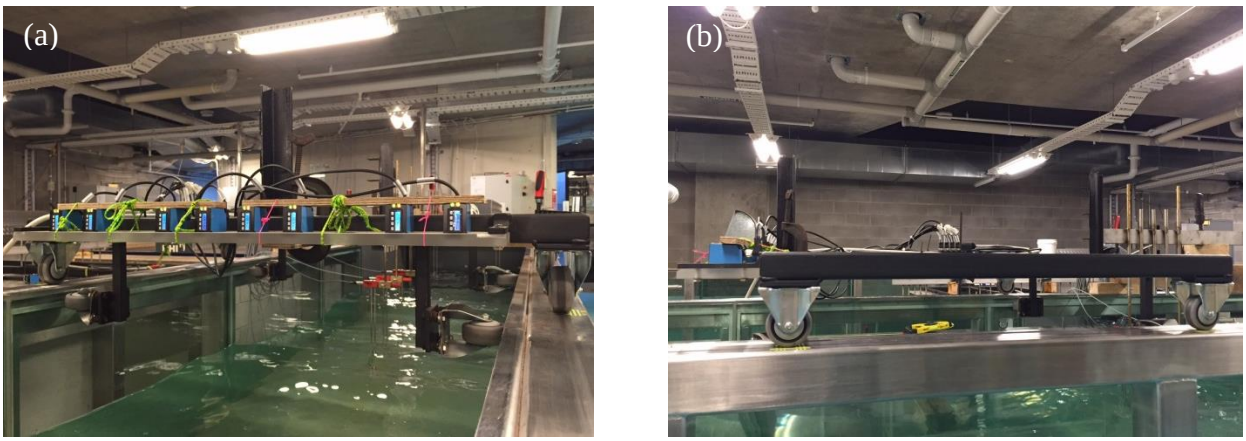

Figure 5-2. Laser measurement set up, a) front view, b) plan view

The channel was separated into three channels further onshore to prevent the beach from becoming non-uniform, see Figure 5-3. Laser 3 was not used in calculating the average profile due to its close proximity to the channel separators. Lasers 1 and 2 measure in the right channel, lasers 4, 5, and 6 measure in the central channel, and lasers 7 and 8 measure in the left channel.

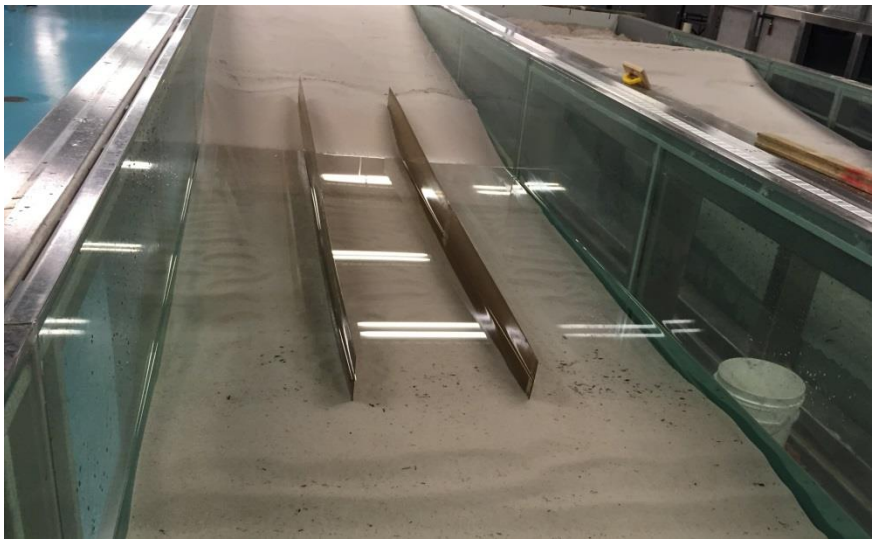

Figure 5-3. Channel separators

5.1.2 Use of multiple lasers

There were 8 lasers set up over the width of the wave flume, with laser 3 unused in analysis. Rather than having one central measurement, having multiple lasers helps resolve the preservation of overall sediment volume when calculating the sediment flux. The profile from each laser is shown in Figure 5-4; the slight changes in elevation are seen clearly, and ripples are also clearly captured by each laser. The profiles are laterally averaged and the resulting profile is used for analysis. The *x*-coordinate starts several metres offshore of the bottom of the beach, and increases towards the

shoreline. In Figure 5-5, the calculated cross-shore sediment flux is shown, using an estimated solid fraction of 0.6. Not all of the lasers have zero sediment flux at the offshore end (x=8m), therefore this suggests closure errors. Laser 7 for example, shows a negative closure error at the most offshore point, while for laser 4, there is a positive closure error. Figure 5-6 shows that when all the q curves are averaged, the q curve starts and ends at zero, so there is no transport beyond these points, and overall sediment volume is conserved.

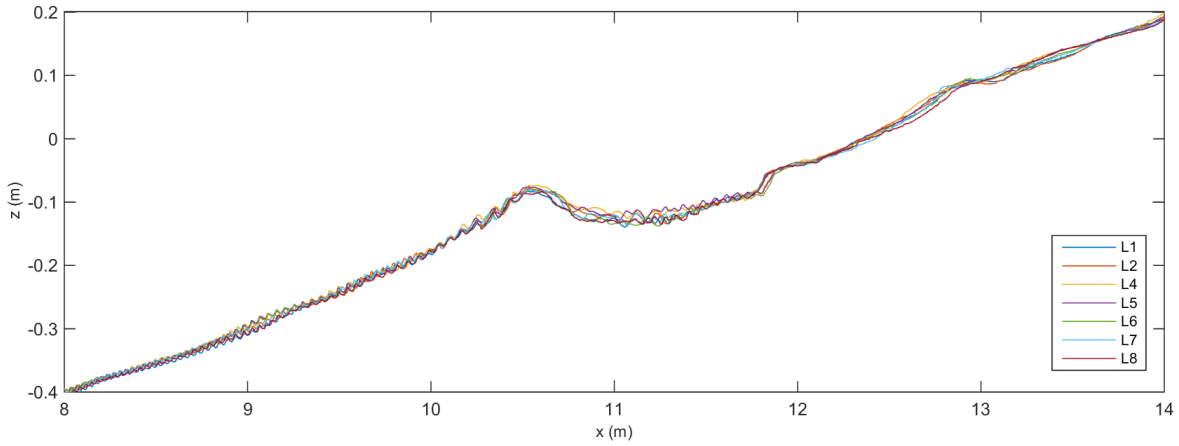

Figure 5-4. Beach profile after 40 hours of H_{rms}=0.08m waves measured by 7 lasers

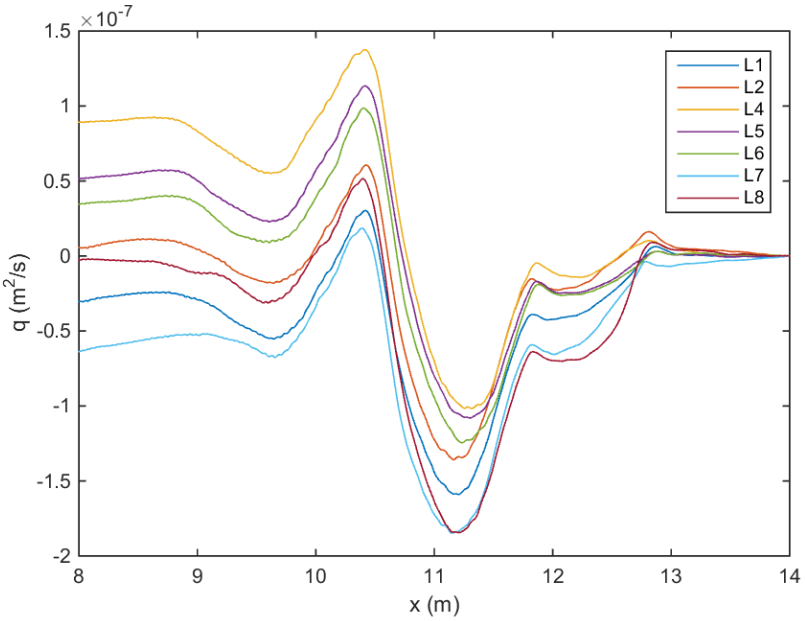

Figure 5-5. q curves for seven used lasers (H_{rms}=0.08m after 40 hours) relative to most eroded profile (14 hours of H_{rms}=0.1m waves)

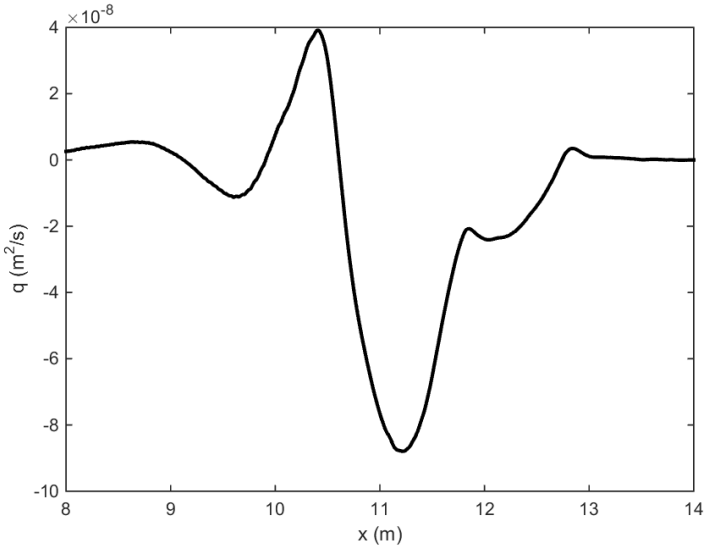

Figure 5-6. Averaged q curve using all seven lasers (H_{rms}=0.08m)

5.2 Experimental cases

The experiments were run with h=0.6m, T=1s and profiles were measured at 1 hour, 2 hours, and subsequent 2-hour increments until equilibrium was reached. A constant H_{rms} was used until equilibrium was reached, and then a new H_{rms} was used. The H_{rms} started from 0.01m and was increased incrementally to 0.1m, and then decreased down to 0.01m. While some cases only required 4 hours to reach equilibrium, others required more than 50 hours. The whole experiment was run for a total of 228 hours. The case names in chronological order are presented with the time to equilibrium in Table 5-1. The *IH*- prefix refers to the increasing H series, while the *DH*-prefix refers to the decreasing H series. The three numbers in the case name refer to the H_{rms} value (e.g. 001 is H_{rms}=0.01m).

Table 5-1. Experimental Test Cases

Case Name	Wave height, H_{rms} (m)	Duration to equilibrium (h)
IH001	0.01	4
IH002	0.02	4
IH004	0.04	6
IH006	0.06	8
IH008	0.08	14
IH010	0.10	14
DH008	0.08	42
DH006	0.06	58
DH004	0.04	34
DH002	0.02	24
DH001	0.01	20

5.3 Results

5.3.1 Calculation of sediment transport rates

The local sediment transport rate between two laterally averaged profiles was calculated using Eq. (2.31), shown again below:

$$q(x_i) = q(x_{i-1}) + \int_{x_{i-1}}^{x_i} m \frac{\Delta z}{\Delta t} dx$$

The cross-shore bulk transport is calculated by integrating over the x-limits, shown in Eq. (2.32).

$$Q = \int_{x_{min}}^{x_{max}} q\,(x) dx$$

Q can also be considered to be the derivative of the first moment (M1) of the sand surface.

$$M1 = \int_{x_{min}}^{x_{max}} zx\, dx \tag{5.1}$$

This is proven in Eq. (5.2), where $\frac{dq}{dx} = -\frac{dz}{dt}$.

$$Q = \int_{x_{min}}^{x_{max}} q\,(x) dx = [qx]_{x_{min}}^{x_{max}} - \int_{x_{min}}^{x_{max}} x\, dq = 0 + \int_{x_{min}}^{x_{max}} \frac{dz}{dt} x\, dx = \frac{dM1}{dt} \tag{5.2}$$

Q (m^3/s) values were evaluated at each equilibrium point, as well as at each measurement interval, relative to both the initial profile and the equilibrium profile of the previous case.

The cross-shore bulk transport can also be described as below, from Jacobsen and Fredsøe (2014):

$$Q(t_m) = -(1 - e_d) \int_0^{x_0} \left[\int_0^x \big(h(x, t_m) - h(x, 0)\big) dx' \right] dx \tag{5.3}$$

Where e_d is porosity, t_m is morphological time, x_0 is equal to $h\ /\ tan\beta$.

In the case of comparing equilibrium profiles, Δt in Eq. (2.31) is 1, as the time period required to equilibrium in each case is not the main focus, it is more the total sediment volume transported (i.e. if the profile is in equilibrium after 8 hours, it would remain the same after 10 hours and so the change in time period becomes irrelevant). The *Q* at equilibrium will be represented by Q_e (m^3).

5.3.2 *IH* series

The *IH* series of experiments were carried out with different wave height from H_{rms}=0.01m up to H_{rms} =0.1m. The final profiles for cases *IH004* to *IH010* are shown in Figure 5-7. The final profiles for *IH001* and *IH002* are similar to that of *IH004*, but on a smaller scale. A significant change in

profile occurs between *IH004* and *IH006*, with the latter forming an offshore bar, while the former only exhibited a berm and trough. With increasing wave height, the bar moves further offshore and ultimately the profile becomes double-barred with an additional inner bar. The trough becomes quite significant by the final *IH010* profile. The berm also slowly moves further onshore with increasing wave height, building at a higher *z* elevation. The wave maker reached its stroke and speed utilisation limit with the *IH010* case, so higher *H* values were not tested.

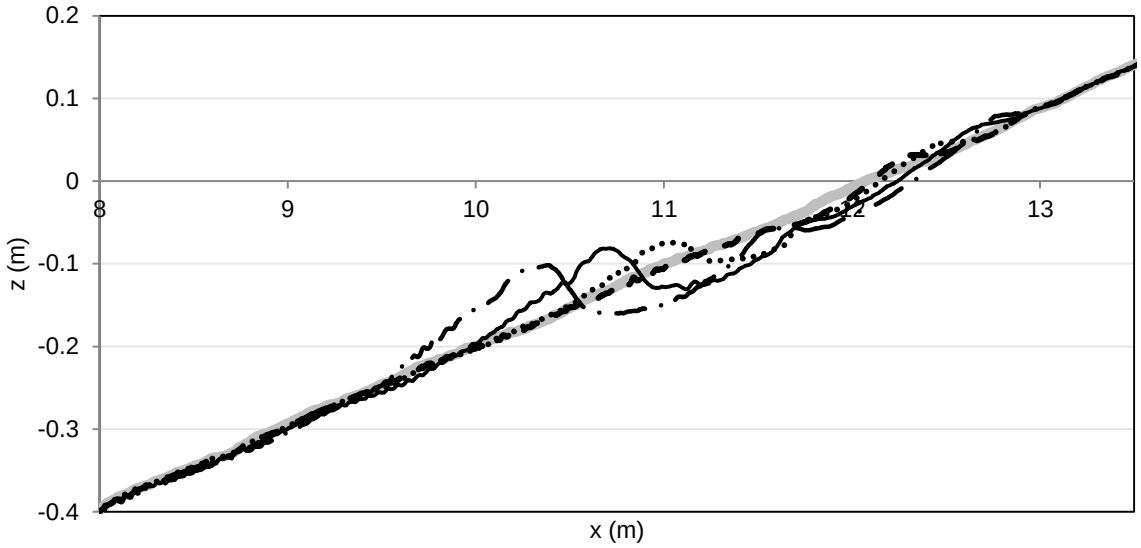

Figure 5-7. Final profiles from *IH004* (dashed), *IH006* (dotted), *IH008* (solid) and *IH010* (dash-dot). The thick line denotes the initial profile.

5.3.3 *DH* series

The *DH* series of experiments were undertaken starting from the final *IH010* profile with waves with H_{rms} of 0.08m to 0.01m. The final profiles for each case are plotted in Figure 5-8. The profile for *DH080* still has an outer bar present, but this is flattened by the final profile of *DH060*, where the sediment is moved onshore to build a larger inner bar and berm. After *DH060*, the flattened outer bar (at *x*=10m) ceases movement. With decreasing wave height, the inner bar moves onshore and additional berms are built at lower *z* and lower *x* values. The final profile for the *DH001* case shows that the profile does not recover to the initial plane beach. The outer bar is arrested, as the wave energy becomes too low to move the sediment any further onshore, after H_{rms} =0.06m.

Examples of arrested bars have also been found in field sites when the wave energy is decreased dramatically and it can no longer reach the threshold for morphological development (Aagaard, 1991; Hegge et al., 1996; Short & Aagaard, 1993).

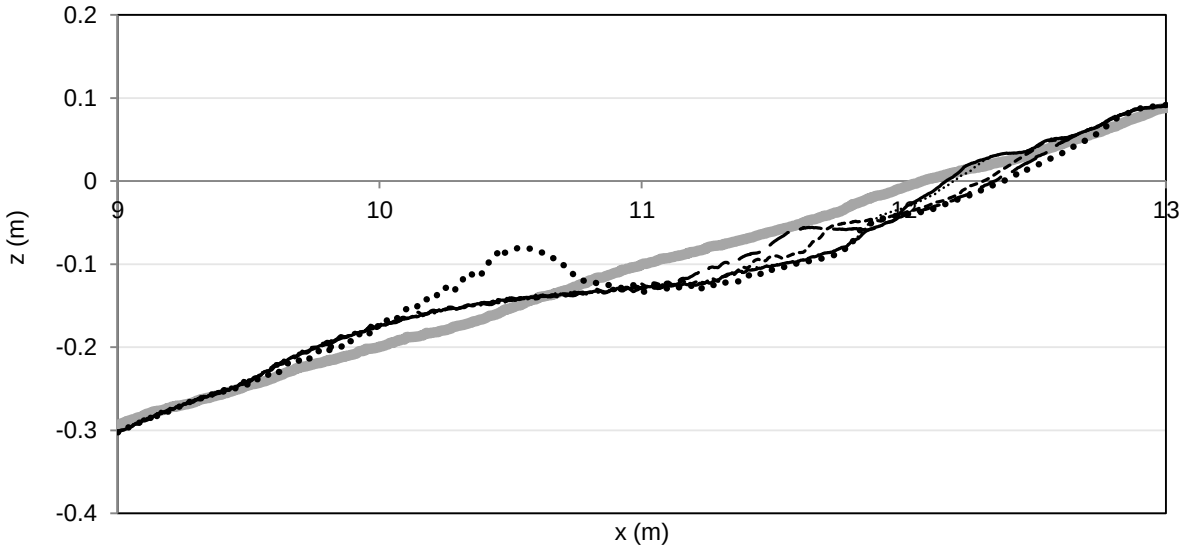

Figure 5-8. Final profiles from *DH008* (dotted), *DH006* (long dashed), *DH004* (short dashed), *DH002* (fine dotted), and *DH001* (solid). The thick line denotes the initial profile.

The pattern of net onshore migration is not as straightforward as the final profiles in Figure 5-8 would suggest, as shown by the progression from the final *IH010* profile to the final *DH008* profile in Figure 5-9.

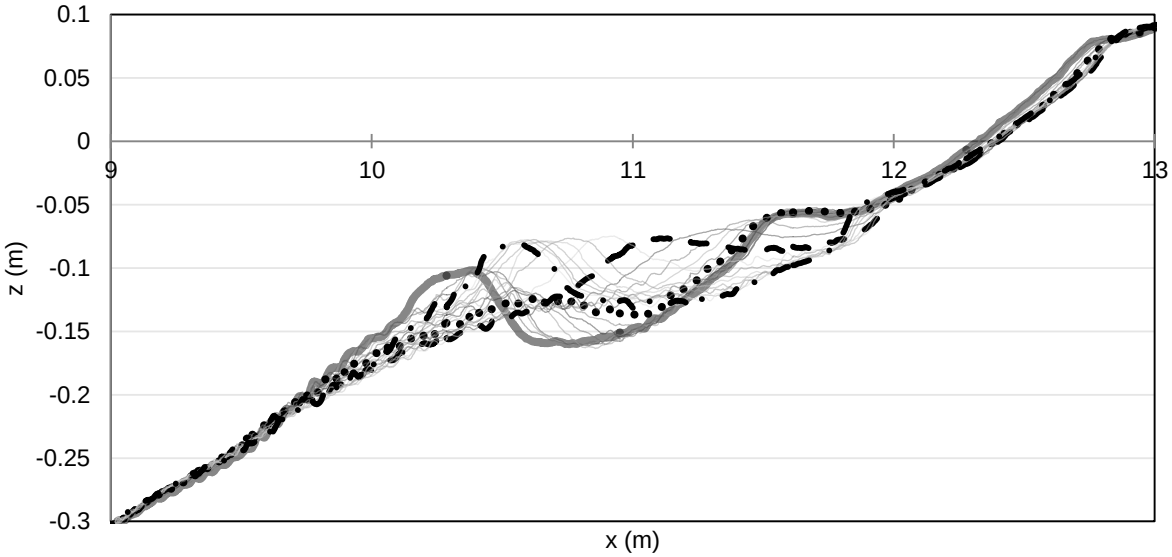

Figure 5-9. *IH010* final profile (solid) to final *DH008* profile *t*=42h (dash-dot), intermediate profiles *DH008 t*=16h (dot) and *t*=26h (dash). All other intermediate profiles are shown in thin grey lines.

During recovery, rather than the outer bar simply moving onshore, the outer bar becomes eroded and the inner bar grows to form a bar further offshore. Ultimately, the outer bar is flattened and a new outer bar is formed from the inner bar. The outer bar at *x*=10.3m from the final profile from *IH010* is flattened by *t*=16h in the *DH008* case but the inner bar around *x*=11.5m remains largely

stationary. By *t*=26h, the inner bar starts to move offshore, to approximately *x*=11m, before settling at *x*=10.5m at *t*=42h. The outer bar stayed relatively straight, despite the very long run time of the experiments, which is shown in Figure 5-10.

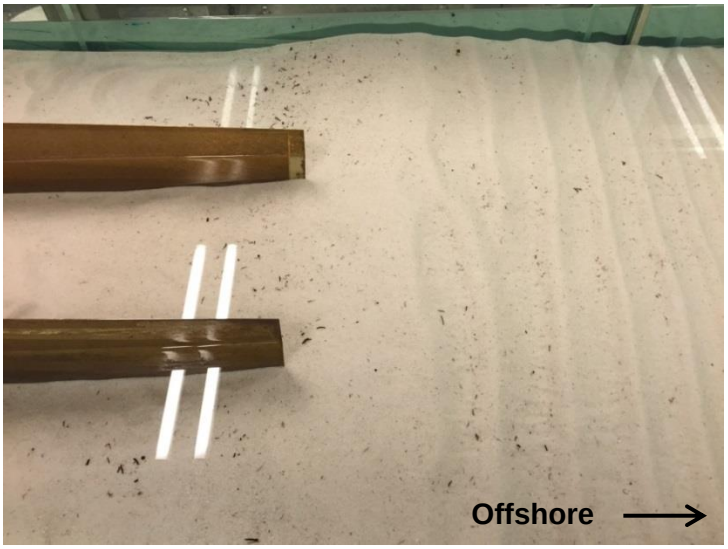

Figure 5-10. The bar formed during case *DH008* at *t*=36hours.

Similar behaviour of the outer bar being flattened and a new bar being created was also observed in accretion tests from Cáceres and Sanchez-Arcilla (2015), although their final outer bar does not originate from the inner bar as it does in *DH008*. However, there is evidence of the inner bar moving offshore to form the outer bar in field sites such as Duck, North Carolina (e.g. Birkemeier, 1984; Lippmann et al., 1993) and on the Dutch coastline (de Vroeg et al., 1988). *DH006* also shows a similar pattern of the outer bar being flattened, but the inner bar does not move as far offshore, becoming a more berm-type profile.

5.3.4 Concept of equilibrium

The equilibrium profile concept suggests that under constant forcing, a beach of a certain sediment size will reach a profile where it will cease to change (Larson et al., 1999). In a laboratory environment, the equilibrium profile, if it exists, can be achieved by running waves of constant forcing on a beach over a prolonged period. However in the field, this becomes more difficult as the wave characteristics and water levels are constantly changing; this leads to a slightly different definition of equilibrium beach profile, where the profiles over a long period are averaged (Dean & Dalrymple, 2002).

Figure 5-11 shows the change in the total bulk transport *Q* calculated relative to the final profile of *IH010* for the *DH008* case. The beach profile movement slows down after 30 hours of run time. Rather than a gradual progression, *Q* decreases or increases suddenly several times over 42 hours, due to the very dynamic nature of this profile. The sudden decrease in *Q* at *t*=16 hours is caused by

the inner bar commencing its movement offshore. *Q* becomes fairly constant between 30 and 42 hours of run time, hence it is considered to have reached equilibrium. Despite the offshore bar ultimately settling further onshore, the overall *Q* is negative, due to the berm eroding.

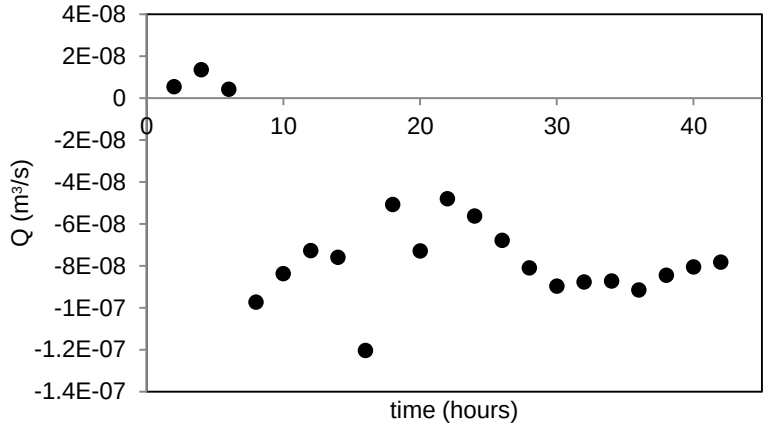

Figure 5-11. *Q* for *DH008* relative to final *IH010* profile

The laterally averaged profiles over 42 hours for case *DH008* are plotted in Figure 5-12. The dynamic bar system is shown clearly, with the initial outer bar being destroyed and the inner bar moving offshore. It also appears that the inner and outer bars are quite stable between *t*=36 hours and *t*=42 hours.

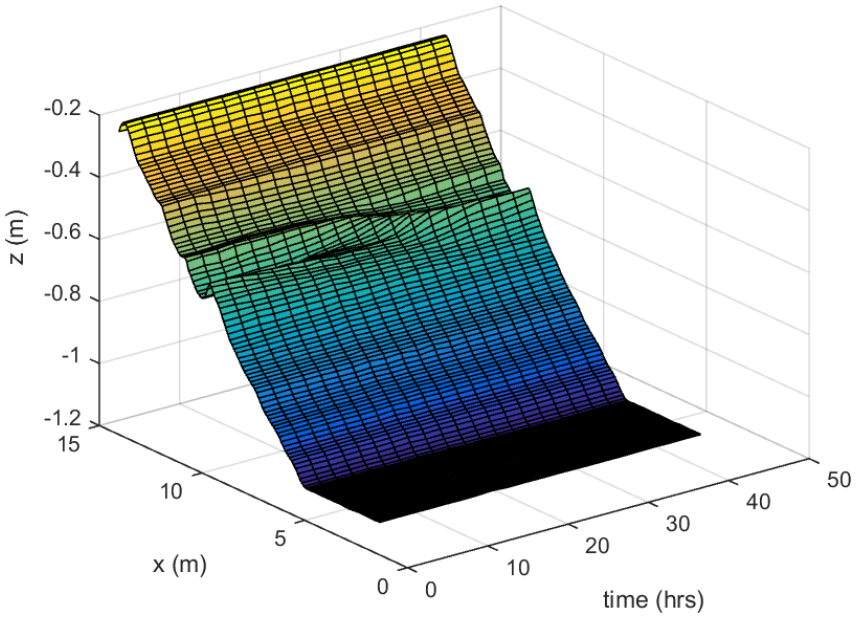

Figure 5-12. Laterally averaged profile for *DH008* over 42 hours

The cumulative mean for *DH008* is also plotted in Figure 5-13. The cumulative mean is calculated by averaging the profiles at each time step, i.e. at 8 hours, the cumulative mean is the average of the

profile measured at 2, 4, 6, and 8 hours. The cumulative mean also stabilises from t=36 hours. These plots suggest that the profile is reaching equilibrium.

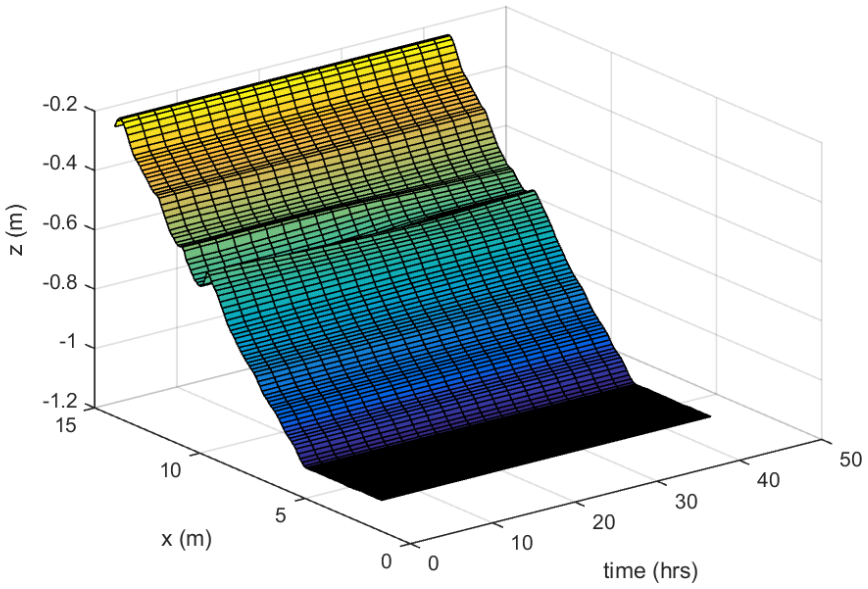

Figure 5-13. Cumulative mean profiles for *DH008*

5.4 Analysis

5.4.1 Variation of Q_e and shoreline position over time

Shoreline position is a parameter which is often used in profile modelling (Davidson et al., 2013; Splinter et al., 2014; Yates et al., 2009), hence it was extracted along with values of Q_e, the total bulk transport after equilibrium is reached. These were plotted over the total experiment run time to show the variation with wave height. Shoreline position here is defined as the cross-shore location where the still water surface crosses the beach profile. Q_e and shoreline position are shown in Figure 5-14 and Figure 5-15 respectively. Q_e is calculated with respect to the profile after 1 hour for H_{rms}=0.01m. Figure 5-14 shows that the profile never returns to the original Q_e value. This was expected, as the plane profile is an arbitrary starting point and far from what would be considered an equilibrium profile; any starting profile is equally arbitrary. The beach appears to be returning to a value of Q_e =-0.01 m^3.

As the x-axis is measured from the wave generator towards the shoreline, a larger shoreline position is equivalent to erosion and a smaller shoreline position is equal to accretion. The trend of the shoreline position is negatively correlated with the Q_e value. It is also noteworthy that the shoreline position is different for the same H, for example, 12.15m for *IH006* and 12.35m for *DH006*. This highlights the importance of antecedent conditions.

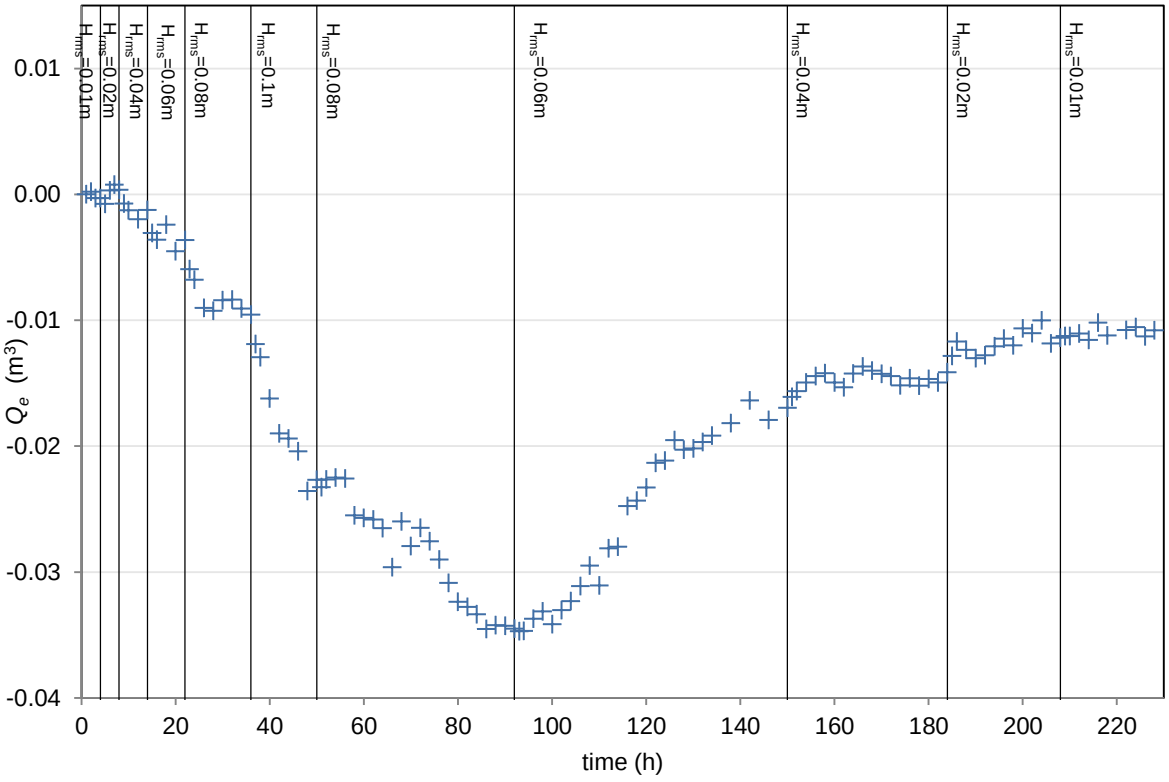

Figure 5-14. Variation in Q_e over total experiment run time

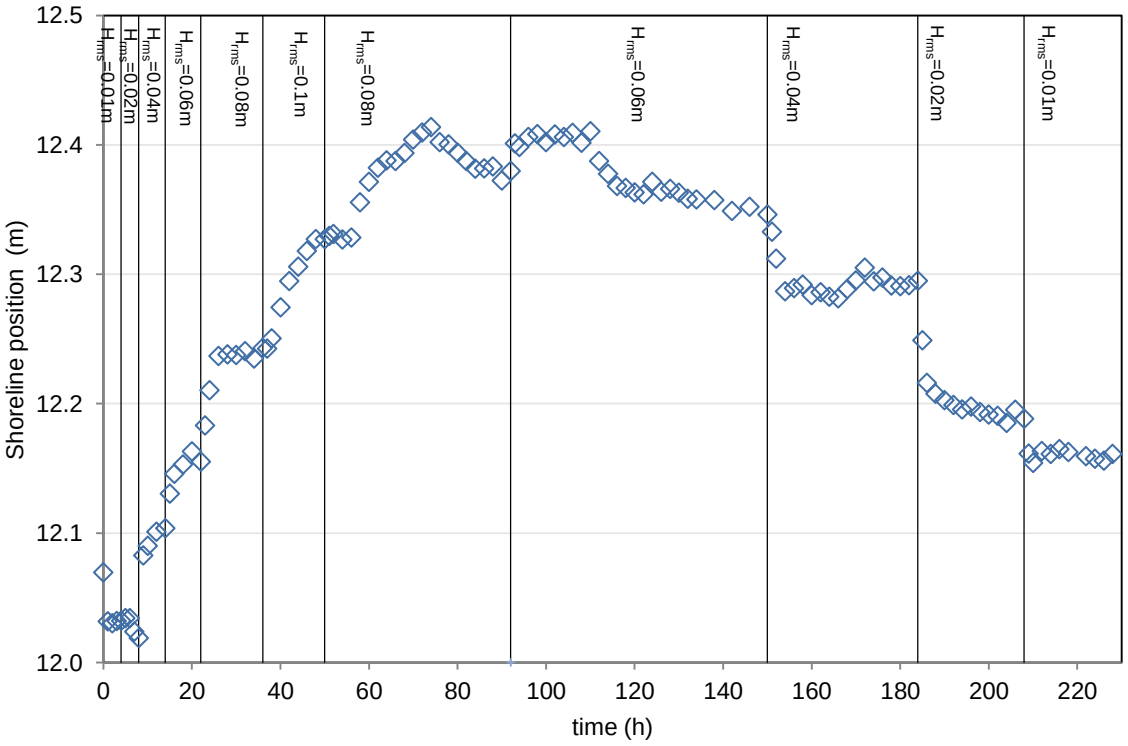

Figure 5-15. Evolution of shoreline position over time

5.4.2 Timescales of erosion and accretion

Through Figure 5-14 and Figure 5-15, it is clear that the *DH* cases generally take much longer to reach equilibrium compared to the *IH* cases. The *IH* cases take from 4 to 14 hours to reach equilibrium, while the *DH* cases can take more than 50 hours. This is due to the *IH* cases being predominantly erosional, and *DH* cases generally causing the profile to accrete, which tends to be a much slower process. Although ultimately erosive, the profile under *DH008* takes a long time (42 hours) to reach equilibrium due to the very dynamic nature of this case, as described in section 5.3.3. The following case *DH006*, which is an accretive case, takes even longer (58 hours) to reach equilibrium. This is much longer than the time it takes for *IH006* to reach equilibrium, even though the incident energy is the same. The subsequent cases *DH004* to *DH001* had shorter run times, as there was significantly less wave energy and the arrested outer bar decreased the amount of sediment available for movement for these cases.

5.4.3 Comparison of *IH*- and *DH*- equilibrium profiles

The equilibrium profiles for the *IH*- and *DH*- cases with the same wave height were compared. Figure 5-16 (a) and (b) show profiles resulting from H_{rms}=0.08m and H_{rms}=0.06m respectively. The H_{rms}=0.08m case shows the best agreement between the two profiles, with a slight difference in the bar and trough locations. The berm location in the *DH008* case is further onshore and smaller in comparison to the *IH008* case. It should be noted that the outer bar for case *DH008* is not the bar remaining from *IH008* and *IH010* but it is the new breaker bar that propagated offshore; it is further offshore than the original. The H_{rms}=0.06m case shows significantly more differences. Firstly, the outer bar in *DH006* is flattened, and does not return onshore. The inner bar location and shape is very different, and the berm is also built at different elevations.

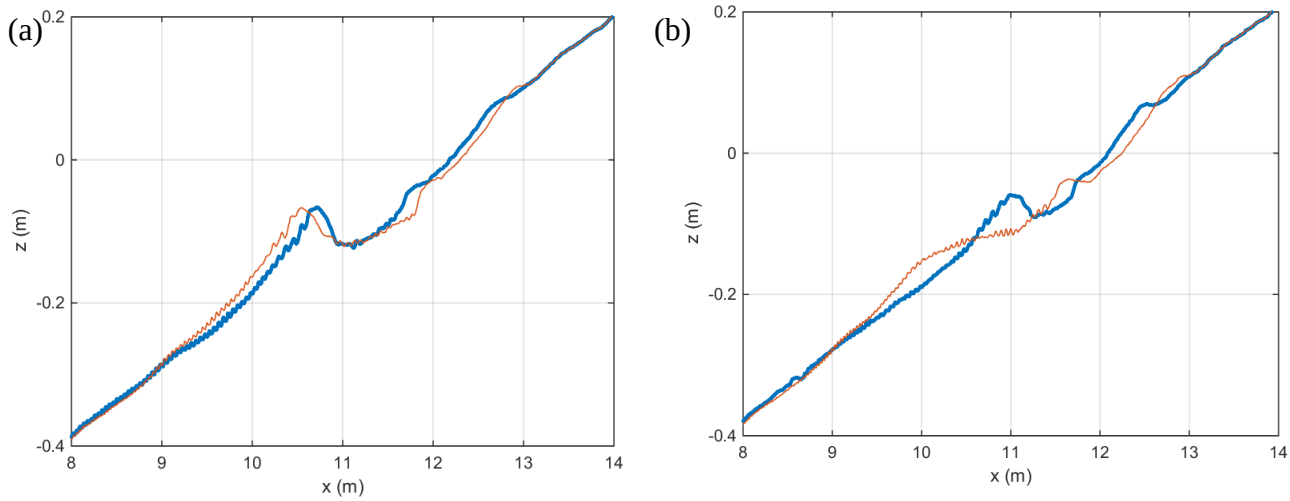

Figure 5-16. a) *IH008* (thick) and *DH008* (thin) final profiles b) *IH006* (thick) and *DH006* (thin) final profiles

The H_{rms}=0.04m profiles in Figure 5-17 show very different profiles, with the *DH004* case showing a flattened, arrested offshore bar where the outer bar was formerly positioned in *DH008*. The stark difference between these cases is not surprising, as the *IH004* case still has a predominantly plane profile, apart from the small berm and trough formed. The natural beach is unlikely to return to a plane beach profile, as this was merely a convenient starting profile and not an equilibrium profile.

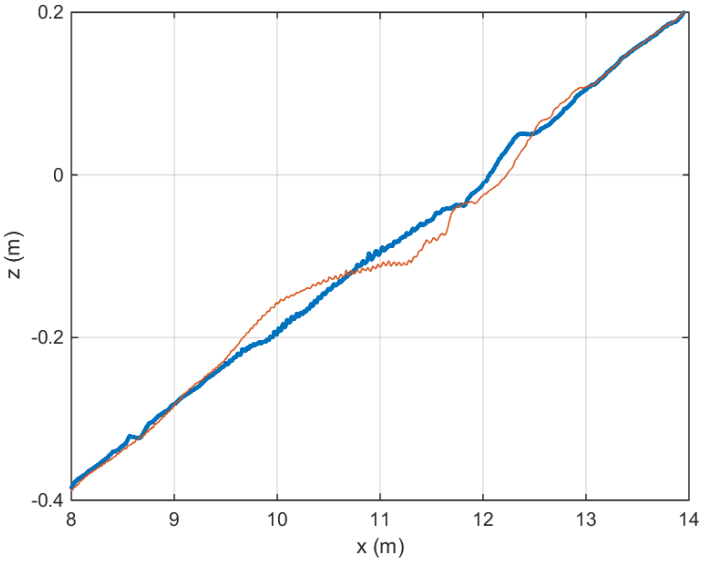

Figure 5-17. *IH004* (thick) and *DH004* (thin) final profiles

The comparison of the *IH* and *DH* profiles highlight that profiles which form under the same wave height could show significant differences depending on the antecedent conditions.

5.4.4 Comparison to monochromatic wave cases

Beach profiles under monochromatic waves were investigated under similar laboratory conditions by Atkinson et al. (2015) and compared with the current random wave experiments. Hughes and Fowler (1990) found that the best agreement between monochromatic and random waves is found when the H_{sig} is equivalent to the monochromatic H. They also found that the wave evolution for the random waves occurs more slowly, approximately double the time it takes for the monochromatic waves.

Jacobsen and Fredsøe (2014) suggested that, as regular and irregular waves create vastly different beach profiles, it is unlikely that a regular wave train is able to create a valid substitution for an irregular wave train, despite the wave energy being equivalent. This suggests that comparing results from the monochromatic wave cases to the random wave cases is not as simple as merely comparing the profiles under equivalent wave height. Comparing the profiles from monochromatic waves and random waves in this flume also has the added complication of having different starting

profiles, as the initial profile for each case was the final (equilibrium) profile from the previous wave height case. This effect was not considered to be significant, as each case was run to approximately equilibrium. Nonetheless, the H_{sig}=0.085m case for the random wave experiments and H=0.08m case from the monochromatic wave experiments were compared in Figure 5-18. These cases were compared as there was no case with H_{sig}=0.08m measured in the random wave case experiments.

Figure 5-18 (a) shows the beach profiles, and Figure 5-18 (b) show the change in volume ΔV calculated with respect to the initial plane profile. The obvious difference between the two cases is the presence of multiple offshore sand bars (between approximately x=8.5 and x=10.5 m) in the monochromatic case. The size of the major bar and trough are very different between the monochromatic and random cases. The random case has a positive (onshore) ΔV value from the berm and the monochromatic case has a larger offshore component due to the three bars which form further offshore.

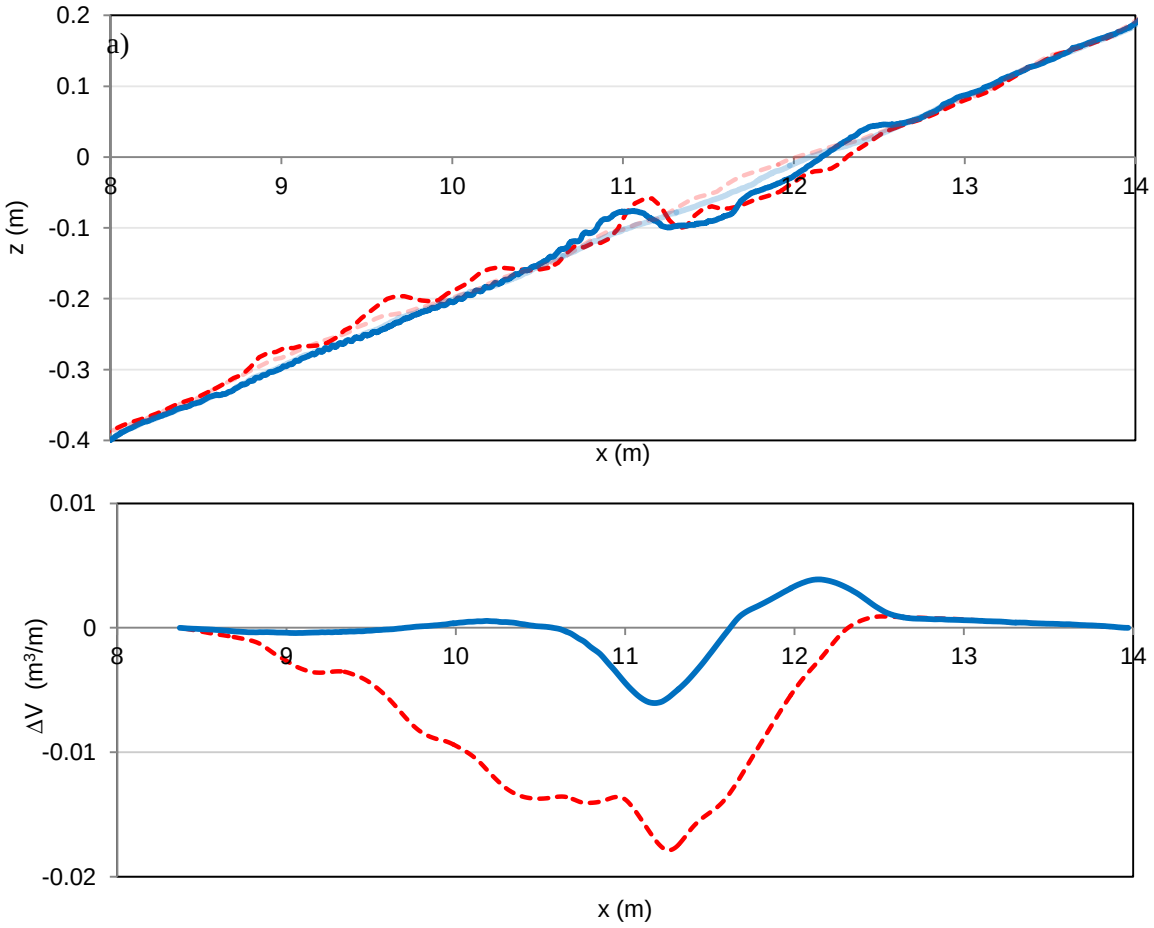

Figure 5-18. a) Beach profile for H_{sig}=0.085m case under random (solid) and H=0.08m for monochromatic (dashed) waves. Transparent lines show respective initial profiles. b) ΔV for random (solid) and monochromatic (dashed) case.

A plot of the Q_e values over the experimental time for the monochromatic wave experiment is plotted in Figure 5-19. There is a distinct difference in the behaviour of Q_e compared to the random wave experiment for this case. The Q_e value only starts recovering after H_{rms}=0.04m, but extremely slowly compared to the case for the random waves.

The difference of Q_e evolution between the monochromatic and random wave experiments can be mainly attributed to the multiple offshore bars identified in Figure 5-18. These bars are thought to stem from the presence of standing waves (O'Hare & Davies, 1993; Short, 1975). These sand bars remained in a similar position until the final profile for the H_{rms}=0.14m case, shown in Figure 5-20.

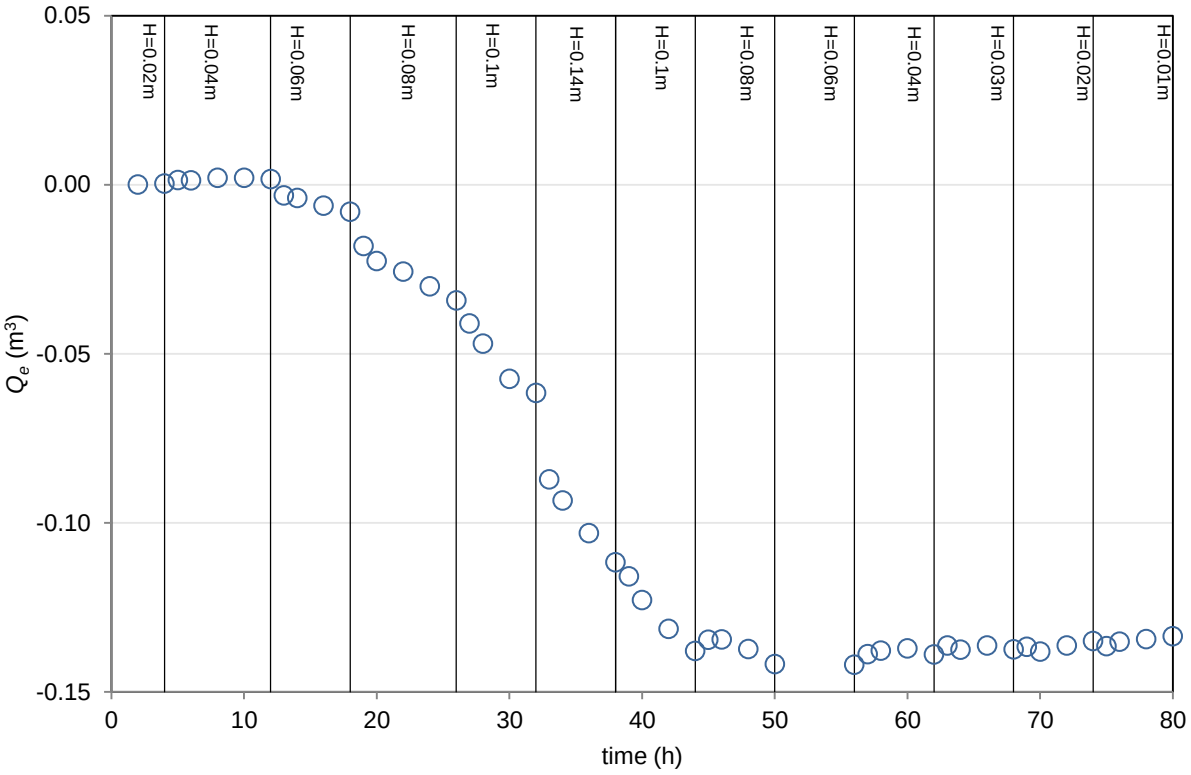

Figure 5-19. Q_e evolution over time, monochromatic wave case

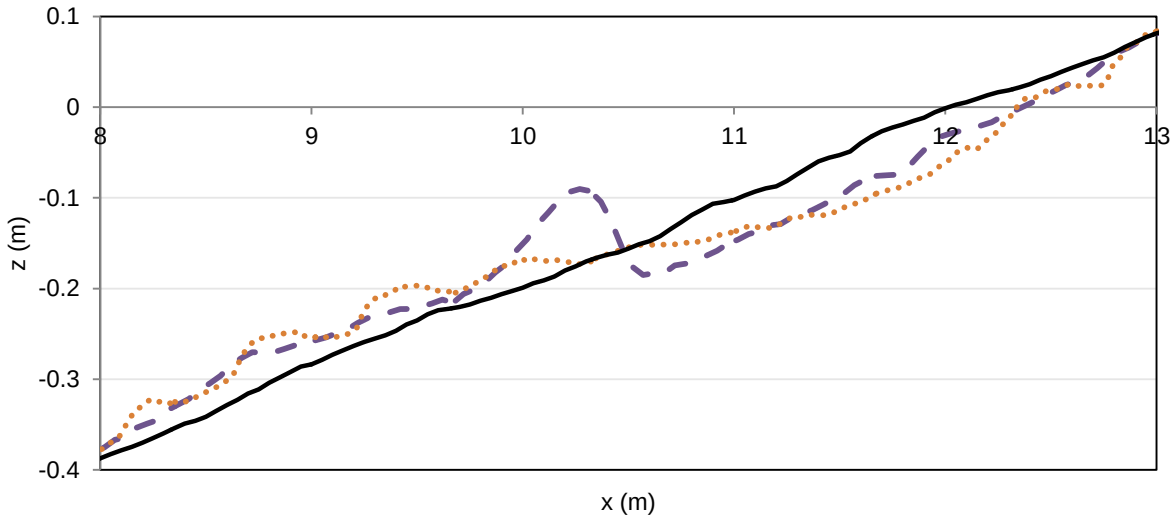

Figure 5-20. Final profile for monochromatic waves with H_{rms}=0.14m case (dashed), final profile for decreasing H_{rms}= 0.01m (dotted), initial profile (solid).

In the decreasing *H* series, for the final profile for H_{rms}=0.01m, the sand bars are still present. These bars were unable to move onshore once wave energy was decreased; this was also observed under random waves. However, the magnitude of the most negative Q_e is 3 times that of the random wave case. This is owed largely to these offshore sand bars.

Arrested bars are attributed to a drastic decrease in wave energy (Short & Aagaard, 1993); comparing the two profiles in Figure 5-20, the H_{rms}=0.01m profile shows remnants of the H_{rms}=0.14m bars. Although wave height was decreased gradually in 0.02m increments, the multiple bars which formed could evolve much further. This suggests that perhaps it is not merely a sharp drop in wave energy which is the cause of arrested bars, but a combination of the existing profile, the sequence of waves applied, and the lack of wave energy.

One similar feature of Figure 5-19 to the random wave case is that Q_e continues to decrease when the wave height is decreased from 0.14 to 0.1m, and the rate of change of Q_e only slows down when wave height is decreased further. Although there are some similarities between the random and monochromatic experiments, it is evident from these comparisons that the monochromatic waves produce extremely different profiles to random waves and may have profile features which are uncommon in real beaches.

5.5 Numerical modelling

5.5.1 Overview of COSMOS

The model COSMOS (Nairn, 1990; Nairn & Southgate, 1993; Southgate & Nairn, 1993) was used to model the same conditions used in the random wave experiments. This model combines the deterministic approach to wave energy dissipation from Battjes and Janssen (1978) and adopts the

energetics model from Bailard (1981) and Bagnold (1954; 1966) for sediment transport. The model has been tested with both small laboratory scale and prototype scale experiments with mixed results (Nairn & Southgate, 1993; Van Rijn et al., 2003). The cross-shore component of the total immersed weight transport rate is based on Stive (1986), which is described by the following:

$$\begin{aligned}(\rho_s - \rho_w) g q_s &= \langle i \rangle \\ &= \rho c_f u_m^3 \frac{\epsilon_b}{tan\varphi}\left(\chi_1 + \frac{3}{2}\delta_u - \frac{tan\beta}{tan\varphi}(u3)^*\right) \\ &+ \rho c_f u_m^4 \frac{\epsilon_s}{w}\left(\chi_2 + 4\delta_u(u3)^* - \frac{u_m}{w}\epsilon_s tan\beta(u5)^*\right)\end{aligned} \tag{5.4}$$

where $\delta_u = \bar{u}/u_m$ is the dimensionless steady flow, $\chi_1 = \langle|\tilde{u}|^2\tilde{u}\rangle/u_m^3$ is the first odd moment. $\chi_2 = \langle|\tilde{u}|^3\tilde{u}\rangle/u_m^4$ is the second odd moment, $(u3)^* = \langle|u|^3\rangle/u_m^3$ is the third central even moment, and $(u5)^* = \langle|u|^5\rangle/u_m^5$ is the fifth central even moment. $\bar{u}$ is the mean velocity component, u_m is the peak bed orbital velocity, and $\tilde{u}$ is the time-varying velocity. ρ_s and ρ_w are the sediment and water density respectively, c_f is the drag coefficient for the bed, and ϵ_b and ϵ_s are bed load and suspended load efficiencies. The sediment is advected by asymmetric orbital velocities, mean flows, or the downslope component of gravity (Nairn & Southgate, 1993). These three components were analysed further in the following section.

5.5.2 Cross-shore sediment transport components of COSMOS

The COSMOS code was analysed to determine how the factors on the cross shore sediment transport components affect the onshore sediment transport.

There are three main inputs that can be adjusted. They are:

- BAS (factor for the wave asymmetry component of sediment transport),
- BUN (factor for the mean flow component of sediment transport), and
- BSL (factor for the downslope gravity component of sediment transport).

The default value for each factor is 1, apart from BSL which can be more than 1 if the grain sizes are bigger than 1mm in diameter (Nairn, 1991). The operation manual specifies that these factors should not be used for calibration purposes, so these model runs are solely to test the sensitivity of the factors. The initial profile used was a profile with slope approximately 1 in 11, with a coarse sediment of d_{50}=1.5mm, run with a wave of T=1.47s, H=0.086m for 6 hours.

Wave asymmetry factor

As BAS is increased (while keeping BUN and BSL constant), the magnitude of the sediment transport overall is decreased. This factor does not appear to be particularly sensitive compared to BUN and BSL, as changes of a factor of 4 did not have a significant impact on the final profile.

Mean flow factor

BUN was changed while BAS and BSL were kept constant. The offshore sediment transport increased as BUN was increased. When BUN was decreased gradually to zero, the overall magnitude of the sediment transport decreased, showing that this is the major contributor to the overall sediment transport magnitude. The sediment transport is always in the offshore direction.

Downslope gravity factor

BSL was increased by a factor of 2, which showed no significant impact to the profile. The effect of this component is relatively small compared to the other components (Nairn & Southgate, 1993).

When BAS is 1 and BUN and BSL are relatively small, accretion occurs. This suggests that the wave asymmetry component is the major contributor to accretive sediment transport. This is supported by re-analysis of data collected by Schepers (1978) with regards to velocity skewness and acceleration skewness (Shimamoto et al., 2013).

Turning off two out of three parameters shows how each component of the cross-shore sediment transport behaves. Figure 5-21 (a) shows the profile when all the factors are equal to 1. The upper profile becomes eroded and the sediment is transported offshore. Figure 5-21 (b) shows the effects of the asymmetry of the orbital velocity on the sediment transport. The asymmetry alone causes onshore sediment transport in this model. Figure 5-21 (c) shows the sediment transport from the mean flows. This case has the largest volume of sediment transported, which is largely eroded from the upper profile. Figure 5-21 (d) shows the effect of downslope gravity component on the original profile. It causes erosion at the upper end of the profile and deposits sediment further offshore.

The COSMOS model considers wave asymmetry but not skewness, which is equivalent to incorporating velocity skewness, but not acceleration skewness as defined in Eq. (2.14) and (2.15). The efficiency coefficients on both the suspended and bedload sediment transport serve the purpose of compensating for the lack of these components in the model. It is for this reason that the model is unlikely to be able to predict the sediment transport rate correctly where accretive sediment transport is concerned.

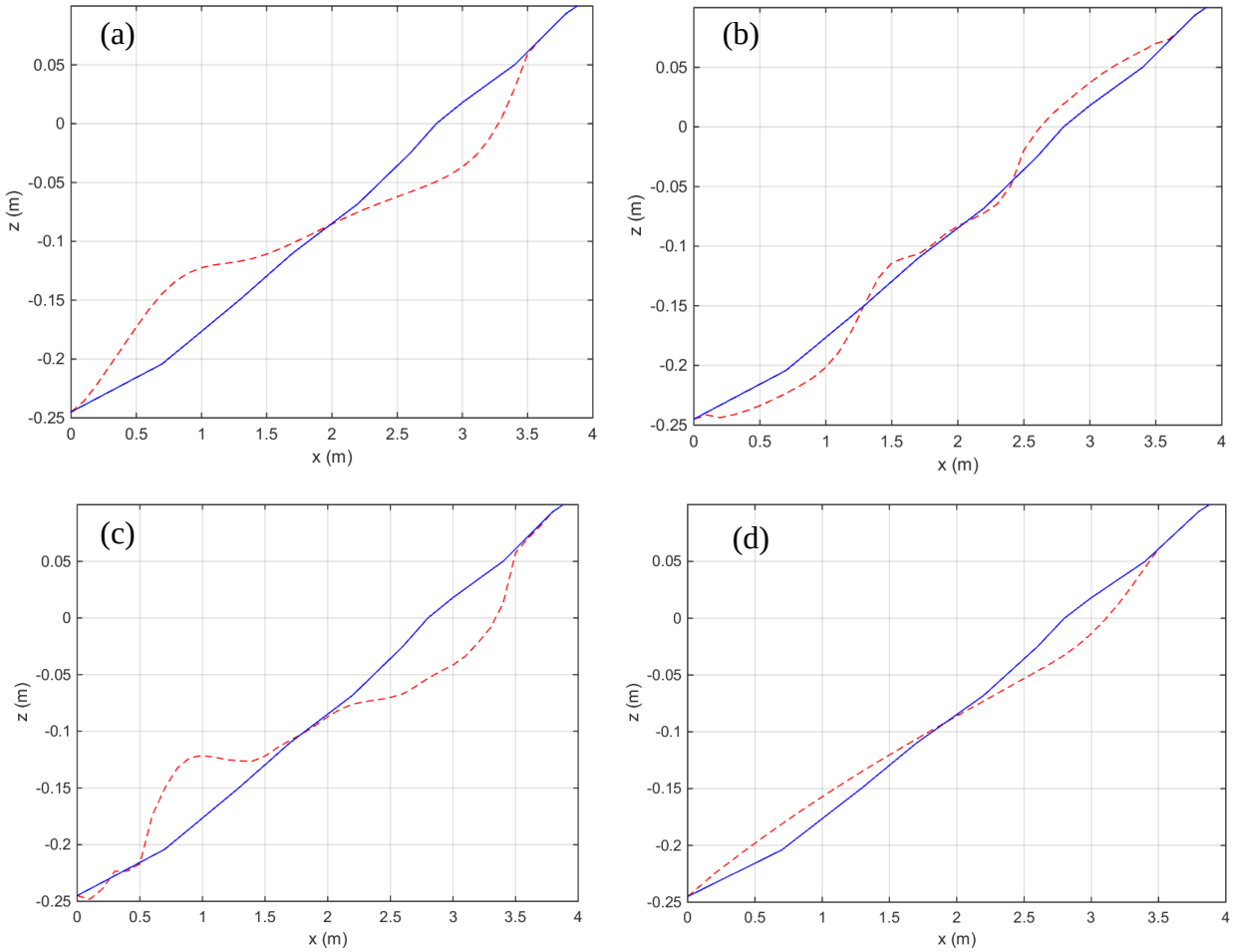

Figure 5-21. Profiles under conditions a) BAS=BUN=BSL=1; b) BAS=1, BUN=BSL=0; c BUN=1, BSL=BAS=0; d) BSL=1, BUN=BAS=0; Initial profile (solid) and predicted profile (dotted).

5.5.3 Model results for each test series

The COSMOS model was applied to the experimental conditions outlined in Section 5.2. For the *IH*-experiments, the initial profile used was the plane beach profile, and for the *DH*-experiments, the initial profile used was the final *IH010* profile.

As expected, the model shows consistently eroding profiles as wave height is increased. In Figure 5-22, the results for *IH006* are shown with the measured profile. The measured profile has a berm that is not reproduced by the model. The model also shows more erosion in the upper profile and deposition of sand offshore over a longer distance of the beach.

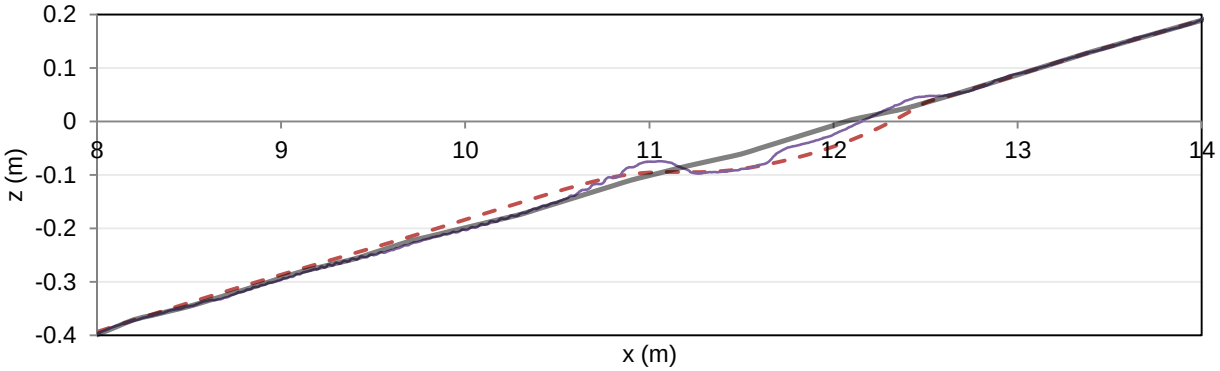

Figure 5-22. Measured *IH006* final profile (solid, thin), model initial profile (solid, thick), and modelled *IH006* profile (dashed)

The model was able to predict onshore sediment transport when the initial profile was set as the final *IH010* profile and either *DH002* or *DH001* cases were run. This was investigated further to determine if this was a legitimate prediction of onshore sediment transport or merely a result of the smoothing mechanism in the model. To do this, the step distance, Δx was changed to a finer resolution of 0.04m instead of 0.1m over the active portion of the profile. The resulting profile is shown in Figure 5-23; the onshore sediment transport does not occur in the model with the finer Δx, concluding that the model is not able to predict the beach recovery which occurs with decreasing wave height. While the overall Q_e value does not change significantly, the shape of the profile differs greatly depending on the step distance resolution.

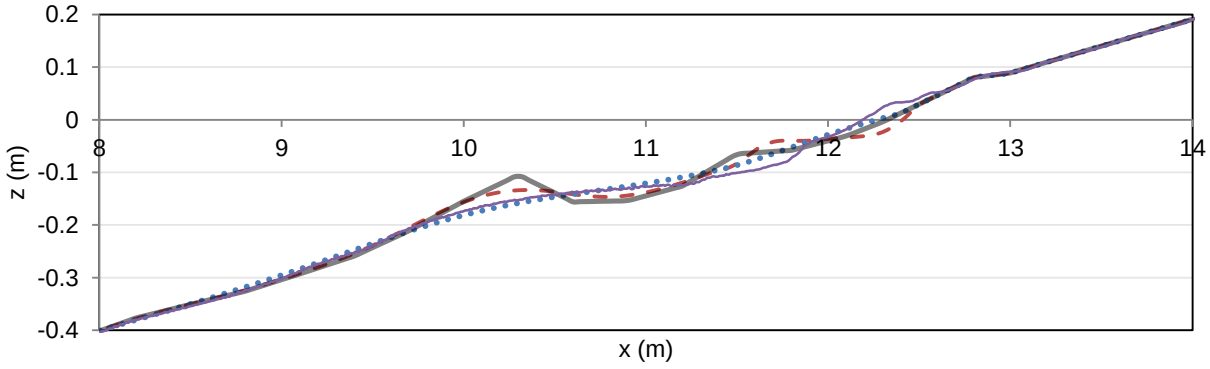

Figure 5-23. Measured *DH002* final profile (solid, thin), model initial profile (solid, thick), model with Δx =0.1m (dashed), model with Δx =0.04m (dotted).

The Q_e values calculated from experimental measurements and modelled results are shown in Figure 5-24. The measurement is significantly smaller than that of the model prediction. The model does not show any positive sediment transport and shows negative Q_e for all the wave heights tested.

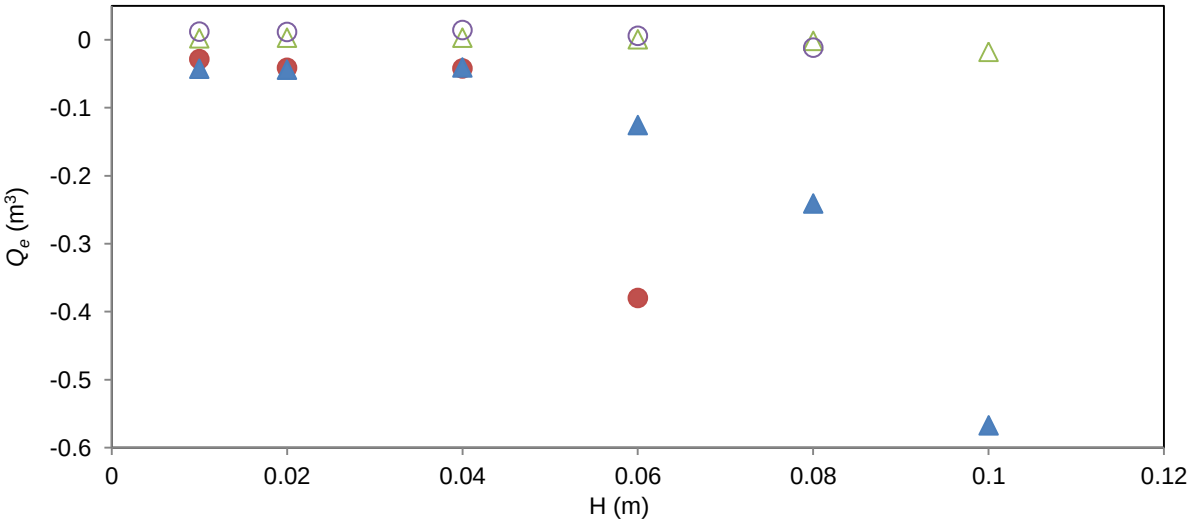

Figure 5-24. Q_e vs H for random wave experiments, *IH*- case points relative to initial profile, *DH*-case points relative to most eroded profile. (modelled *IH*-cases (filled triangles), and measured *IH*-cases (empty triangles), modelled *DH*- cases (filled circles), measured *DH*-cases (empty circles)).

Nairn and Southgate (1993) also found that onshore transport in small-scale experimental facilities was not well predicted by the model, mainly due to the model not accounting for the complex sediment transport over bed forms. For prototype scale experiments however, the model performance improved as detailed processes such as vortex ejection from ripples were not generally observed and hence a time-averaged sediment transport model was sufficient to represent the actual sediment transport rate (Nairn & Southgate, 1993) .

5.6 Scaling and comparison with LWT data

The results from this experiment, along with the monochromatic wave experiments were compared to the profiles from Kraus and Larson (1988) from monochromatic wave experiments carried out in the Large Wave Tank (LWT).

Q_e values from the larger sediment size (d_{50}=0.4mm) cases were compared to the results from this experiment, using only profiles which appeared close to, or at equilibrium; the criteria for equilibrium are outlined in Section 5.3.4. Using scaling laws from Van Rijn et al. (2011), Q_e can be scaled using $n_H n_L^2$, where n_H is the wave height scale and n_L is the length scale. All scale parameters are calculated using $n = \frac{p_p}{p_m}$, where p_p and p_m is the parameter value in the prototype and the model respectively. As the experiments had a range of wave heights and wave periods, the average values

between the experiments were used in the scaling. Additionally, as the slopes are different between the datasets, distorted scaling was applied.

In Figure 5-25, the Gourlay number and the scaled Q_e is plotted; the Gourlay parameter range is very different between the Kraus and Larson (1988) measurements and the UQ wave flume profiles. Of course, different beaches have varying Gourlay parameters, see Figure 7.2.2 in Nielsen (2009). Only the increasing wave height series were used for this comparison. The equilibrium Gourlay number, where the two beaches change from accretion to erosion is also different. Note that the last point of the monochromatic experiment is left out, as the value of $n_H n_L^2 Q_e$ is approximately -1600, for ease of comparison between the three cases.

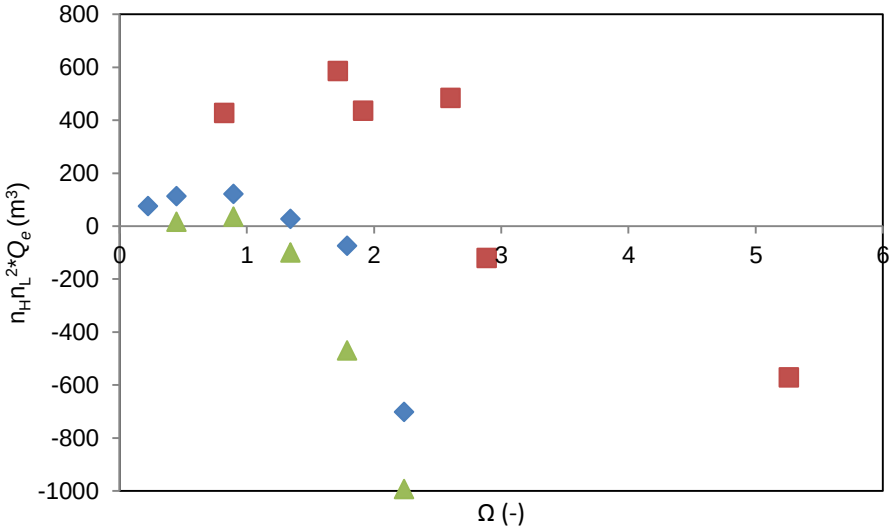

Figure 5-25. Gourlay number vs scaled Q_e with Kraus and Larson (1988) (squares), UQ random wave experiments (diamonds), UQ monochromatic experiments (triangles)

Other parameters were tested instead of the Gourlay parameter, still including H and T. Hattori and Kawamata (1980) incorporated the beach slope into the Gourlay parameter. Including the beach slope only slightly improves the scaling of the x-axis; this is shown in Figure 5-26.

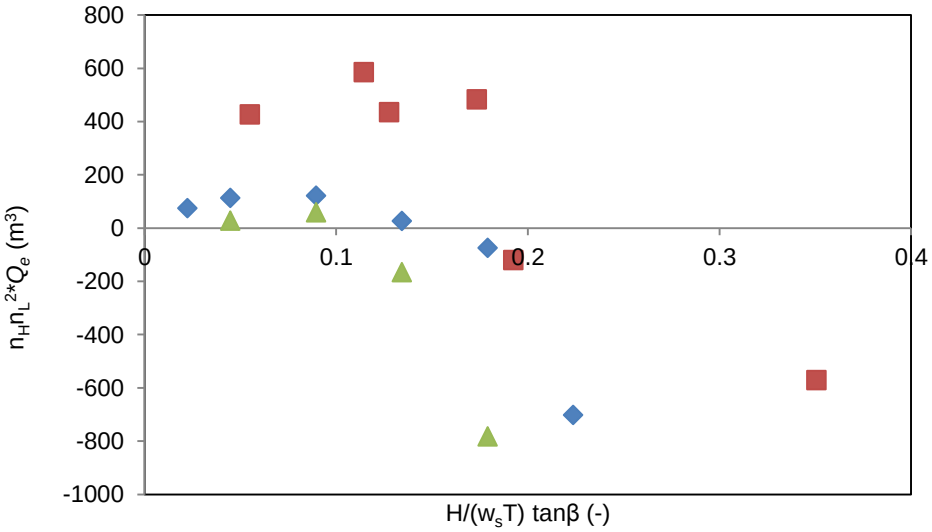

Figure 5-26. Gourlay number with slope vs scaled Q_e with Kraus and Larson (1988) (squares), UQ random wave experiments (diamonds), UQ monochromatic experiments (triangles)

Wave steepness, discussed previously in Section 2.3.1.1, is a function of both H and T; this is plotted with the scaled Q_e in Figure 5-27. The LWT tank data values of H/L become much smaller due to the larger T values in these experiments.

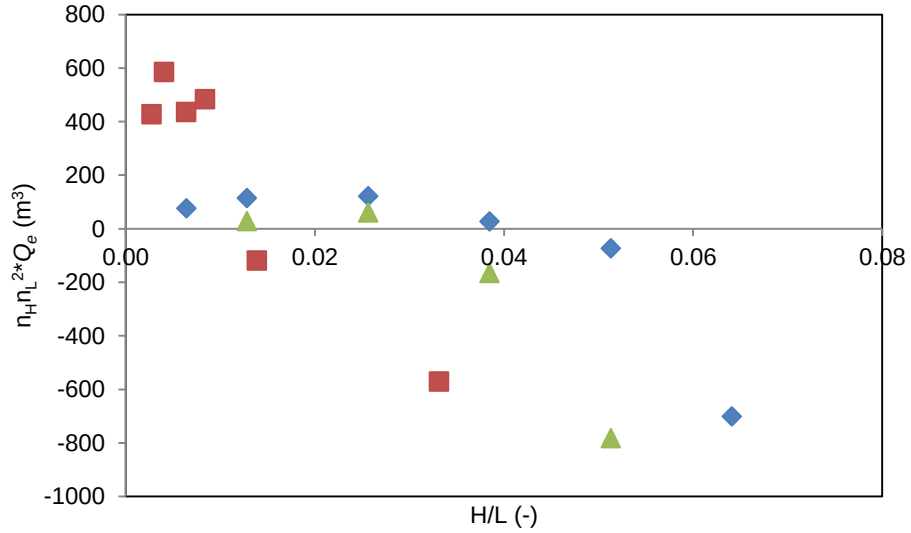

Figure 5-27. H/L vs scaled Q_e with Kraus and Larson (1988) (squares), UQ random wave experiments (diamonds), UQ monochromatic experiments (triangles)

Although the Gourlay number is a non-dimensional parameter, it appears to require an additional scaling factor in order to compare experiments conducted in different scales. Applying the surf zone slope as Hattori and Kawamata (1980) suggested improves the scale between the LWT data and the random wave experimental data. H/L is not as suitable for comparison between the experiments.

5.7 Limitations and conclusions

The present experiments are novel in the sense that there is currently a lack of datasets which have measured accretive and erosional profiles to equilibrium. Many laboratory experiments do not have long enough run times, and therefore the profiles do not have the time to reach equilibrium.

There are several limitations in this experiment, one of which is the laboratory scale. Many profile experiments are run in the prototype scale at facilities such as GWK, LWT, and CIEM, which can run similar wave conditions to the field and therefore have similar magnitudes of sediment transport. Although there are various scaling laws available, the effects of some parameters are still unknown, such as sediment density (Van Rijn et al., 2011). Therefore the sediment transport in a small scale laboratory may exhibit processes differently to those seen in the field. Another shortcoming is evaporation of the water from the flume, as these cases were run during the Queensland summer. Although best efforts were made to constantly fill the tank with water to maintain h=0.6m, there will be minor discrepancies in h within test cases, especially for the longer case runs. Additionally, the wave reflection may also be a potential issue. Although the wave absorption was active in the wave flume, the reflection coefficient was calculated as 0.17 (Atkinson, 2015, pers. comm., 22 Dec), so there is potential for some re-reflection from the wave maker. The alongshore averaging of the profiles measured by seven lasers may also affect the results somewhat; despite having some channel separators as to prevent the profile from developing asymmetrically, all seven profiles are not identical.

Starting at a plane beach of 1/10 is arbitrary, and hence would be contrary to a natural beach. The limitations in running a random wave series generated by the Pierson-Moskowitz spectrum are also evident – although H_{rms} and thus the average wave energy would be equal, the wave energy spectrum would differ to a natural beach. Perhaps it is the balance of the combination of the waves that are critical to beach recovery and therefore a laboratory experiment which can only run Pierson-Moskowitz waves are insufficient to reflect this behaviour.

Additionally, the variation of wave period could also contribute to the recovery of the beach in a manner different from changing H. It would be valuable to see if changing T is different to changing H, with the same Gourlay number. The effect of the arrested bars may be alleviated if the T was changed instead. However, monochromatic experiments with larger T values have produced very transverse variable profiles in the UQ hydraulics laboratory and therefore may be more difficult to undertake.

There were some key points from these experimental measurements and they include the following:

- The eroded profile does not start to recover when exposed to waves with smaller *H* when decreasing the wave height from 0.1m to 0.08m, due to the complex movement of the bar system;

- With the *DH* series, the outer bar is not moved onshore; instead it is destroyed and an inner bar is moved offshore, this results in a prolonged evolution of the profile and hence takes much longer to reach equilibrium;

- The *DH* and *IH* series have very different equilibrium profiles even with the same *H*, highlighting the importance of the antecedent condition.
- Random and monochromatic waves produce starkly different profiles, especially for the *DH* series, due to multiple arrested bars in the latter case.
- The erosive test cases have a much shorter time scale compared to the accretive cases, even for the same incident wave energy.
- Numerical modelling of the test cases showed that the COSMOS model cannot predict onshore transport under similar conditions to the laboratory experiments.

These experiments provide a new insight into profile evolution under random waves, and contribute to the increasing database which can be used in beach profile modelling.

6 Equilibrium type beach state models

While there are advancements in the understanding of detailed beach processes, the 2-D and 3-D process-based models which aim to predict the sediment transport on beaches are still time-consuming and considered cumbersome to apply. For this reason, various heuristic beach profile models have been developed (e.g. Davidson et al., 2013; Splinter et al., 2014; Yates et al., 2009), which in contrast are much simpler. These models by nature are data-driven and hence location-specific. Such models predict the development of a particular scalar beach state parameter, such as shoreline position or transported sediment volume. The shoreline position is often the key parameter in equilibrium models, as it is relatively easy to extract with remote video sensing technology. One such heuristic equilibrium shoreline model from Yates et al. (2009) is reviewed, various datasets are analysed with respect to Gourlay number, and finally an alternative form of the model is presented in this chapter.

6.1 Yates et al. (2009)'s model run to equilibrium

As reviewed in Section 2.3, Yates et al. (2009) developed a shoreline prediction model driven by wave energy over the seasonal (as opposed to individual storm) time scale, assuming a linear relationship between the shoreline position and wave energy. As mentioned previously, the shoreline position in this model is defined as the cross-shore location of the MSL contour. This model was tested using similar conditions to the random wave experiments conducted in the UQ wave flume (described in Section 5), where one wave height was maintained until equilibrium. The equilibrium profile is defined as the beach profile which ceases to change after a prolonged period of constant forcing, but in this model, one wave height is applied until shoreline position is equal to equilibrium shoreline position (S_{eq}) for a fixed energy E, using equations (2) to (5) from Yates et al. (2009), which are shown in Section 2 as Eq. (2.26) to (2.29).

The model with coefficients for Torrey Pines section T3, as specified in Yates et al. (2009), was run with synthetic wave heights. Wave height was increased from 1m to 1.5, 2 and 3m, and then decreased back to 1m in the reverse sequence. Figure 6-1 shows the resulting time series of wave energy and the predicted shoreline position. Once equilibrium is reached and wave height is decreased, the shoreline starts recovering immediately (e.g. at t=1.2 year mark). The timescale of the accretion process is longer compared to that of the erosion process, especially as wave energy decreases. The difference in time scale between the accretive and erosive case with equal wave

energy is due to the difference in the rate coefficient $C^{\pm}$ and the difference in initial shoreline position.

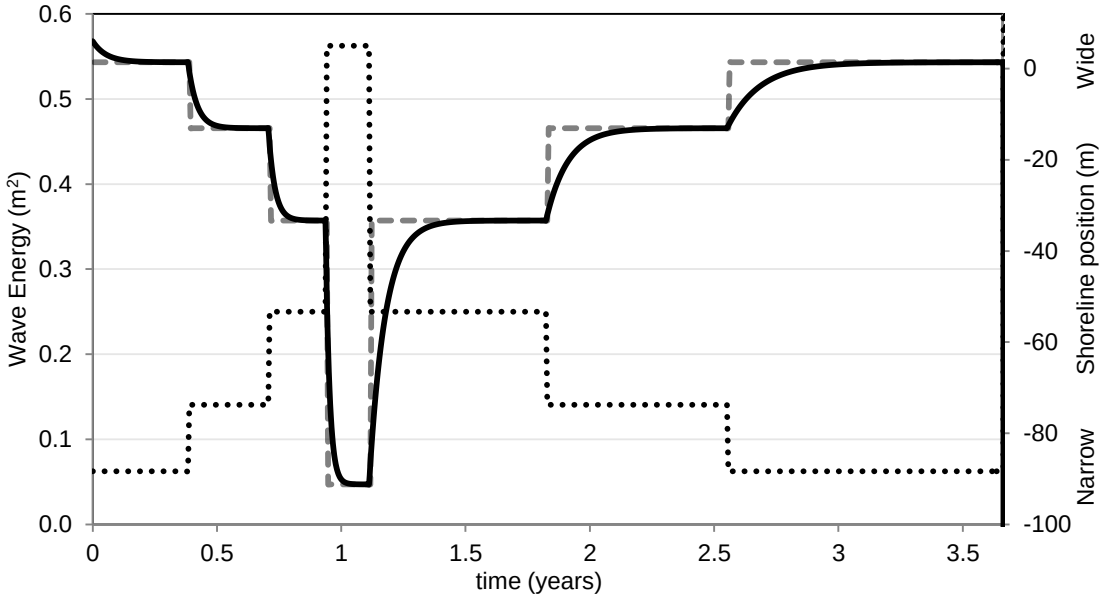

Figure 6-1. Time series of input wave energy *E* (dotted), predicted shoreline position *S* (solid) and S_{eq} line (dashed) from Yates et al. (2009) model using Torrey Pines section T3 coefficients.

Contrastingly, there are several instances in Yates et al. (2009) where the observations show the real shoreline position continues to recede when wave energy is decreasing. This could stem from the shoreline position interacting with other beach state variables, not just wave energy. This causes discrepancies between the modelled and observed shoreline position, as highlighted in the squares in Figure 6-2. Similar behaviour was observed in the laboratory experiments, when H_{rms} was decreased from 0.1m to 0.08m; the shoreline kept eroding instead of recovering (Section 5.4.1).

Another feature of the model which contrasts with observations from Yates et al. (2009) is that the peak shoreline position reaches a plateau in the model and therefore underestimates much of the peak shoreline position values. This is highlighted by the box in Figure 6-3. This is due to the equilibrium shoreline position being a linear function of wave energy, which is a shortcoming that is acknowledged by the authors. However, an asymptotic relationship instead of the linear function did not significantly improve the original model's predictive capability (Yates et al., 2009).

The model from Yates et al. (2009) predicts that if *E* starts to decrease before E_{eq} is reached, the shoreline position will keep eroding to the new S_{eq} provided that the new S_{eq}>*S*, otherwise it would accrete to the new S_{eq}. If *E* decreases after E_{eq} is reached, *S* will accrete to the new S_{eq}. This model

therefore cannot reproduce a beach profile which keeps eroding after a decrease in wave height after reaching equilibrium, as observed in the *DH008* case (see Section 5.3.3).

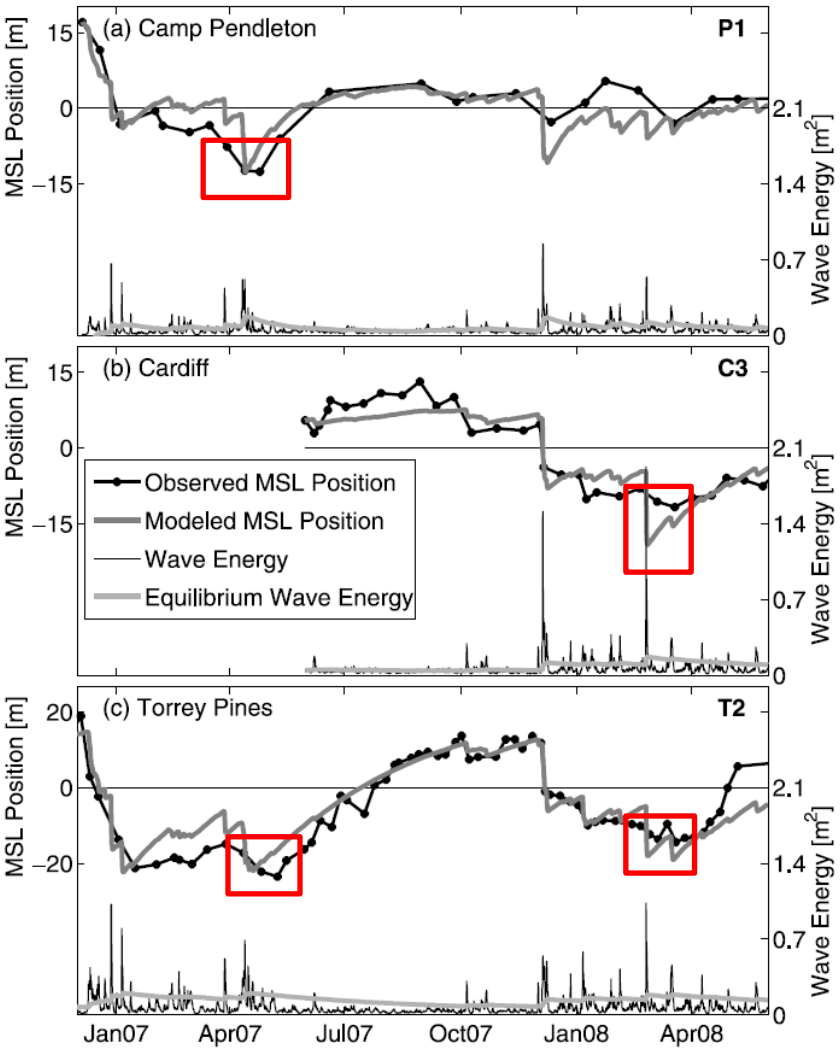

Figure 6-2. Figure 6 from Yates et al. (2009) showing shoreline position and wave energy over time, with points of interest highlighted with red squares.

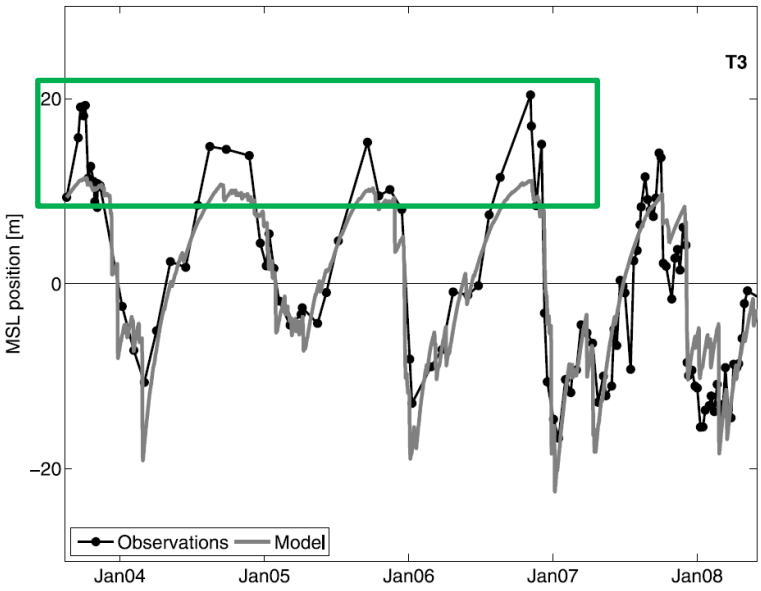

Figure 6-3. Figure 4 from Yates et al. (2009) showing shoreline position over time, with points of interest highlighted with green square.

6.2 Model based on Gourlay number

As discussed previously in Section 2.3.1, various parameters have been used previously to compare beach profiles. Seelig (1983) analysed data from Saville (1957) and arrived at a model which related breaker height H_b to sediment transport volume changes above the SWL. The data from these experiments are collated in Kraus and Larson (1988). Baldock et al. (2011) suggested a model using Gourlay number, Ω relative to cross-shore bulk transport at equilibrium, Q_e. The use of Ω incorporates wave period, which is thought to be a significant factor in differentiating between erosive and accretive sediment transport.

Baldock et al. (2011) suggested the equilibrium state relationship between Ω and Q_e takes the form of

$$Q_e = A(\Omega_{eq} - \Omega)\Omega^n \tag{6.1}$$

Where A is a constant, n is a power and Ω_{eq} the equilibrium Gourlay number, where no net cross-shore sediment transport occurs.

Three datasets were analysed with respect to Gourlay number and cross-shore bulk transport to determine if the Baldock et al. (2011) model is suitable for particular datasets. The datasets are from the random wave experiments previously discussed in Section 5, the data from prototype-scale laboratory experiments from Kraus and Larson (1988), and field data from Narrabeen, Australia.

6.2.1 Random wave experimental data analysis

The beach profiles from random wave experiments for both the *IH*- and *DH*-cases were analysed to calculate the cross-shore bulk transport as outlined in Section 5.3.1. These values were plotted with respect to their corresponding Gourlay numbers in Figure 6-4. Q_e is calculated relative to the initial plane profile for the *IH*-cases and relative to the last profile in *IH010* for the *DH*-series. The *IH*-series was previously presented in Section 5.6 alongside other experimental data.

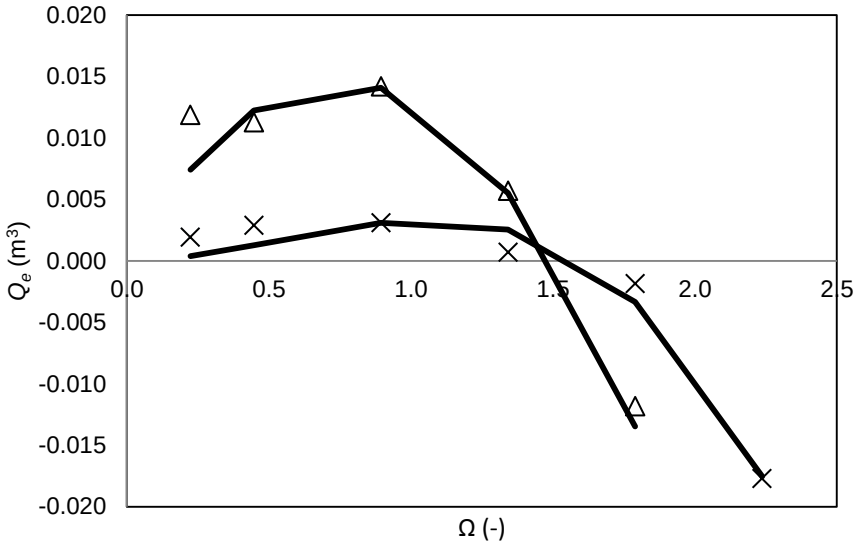

Figure 6-4. Q_e vs Gourlay number for *IH*-series (crosses) and *DH*-series (triangles), calculated with respect to initial plane profile and *IH010* final profile respectively. The fitted values for the *IH*-series is A=0.0055 m^3 and n=2, for the *DH*-series, A=0.026 m^3 and n=1.

It is clear that a relationship which resembles that of the model described in Baldock et al. (2011) exists between Gourlay number and Q_e for this dataset. The equilibrium Gourlay number Ω_{eq} appears to be similar for the *IH*- and *DH*- experiments. Maximum Q_e also occurs roughly at the same Gourlay number for both datasets. The power n and constant A is quite different, with the *DH*-series having a steeper gradient than the *IH*-series curve. It can be argued that as the starting point is a rather arbitrary plane beach, an alternative equilibrium profile is more suitable as the initial profile. However, as the model takes into account the antecedent profile, and the curve is relative to the initial profile, the initial beach profile was not considered particularly significant (it would merely vertically shift the curves shown in Figure 5-14 and Figure 5-15, for example). However, for comparison, Q_e was calculated relative to the previous profile for all cases (i.e. *IH004* relative to *IH002*, etc.) and plotted in Figure 6-5. All profiles compared are therefore equilibrium profiles. There is an outlier at Ω=1.34 for the *DH*-series which is case *DH006*, but otherwise there is a similar relationship between Gourlay number and Q_e to Figure 6-4.

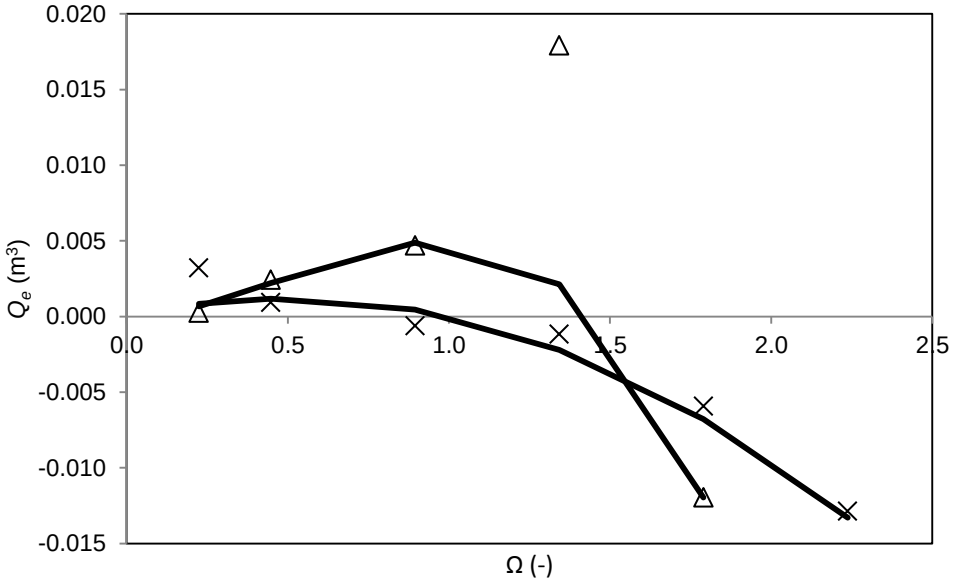

Figure 6-5. Q_e vs Gourlay number *IH*-series (crosses) and *DH*-series (triangles), calculated with respect to previous profile. The fitted values for the *IH*-series is A=0.005 m^3 and n=1, for the *DH*-series, A=0.011 m^3 and n=2.

6.2.2 Kraus and Larson (1988) experimental data analysis

Kraus and Larson (1988) collated experimental data from the 1950s and 60s conducted by the Beach Erosion Board (later Coastal Engineering Research Center) in their Large Wave Tank (LWT) facility in Dalecarlia, Washington, D.C. Tests were run with various combinations of wave height (0.55 to 1.83m) and wave period (3.75 to 16s) with two different sediment sizes, d_{50}=0.22mm and 0.4mm.

The data from Kraus and Larson (1988) were used to calculate Q_e and plotted against Ω. The coarser sediment case of d_{50}=0.4mm was used to plot Ω vs Q_e in Figure 6-6. From observation of the beach profile measurements over time, the point at Ω=6.87 does not appear close to equilibrium (i.e. the outer bar is still moving offshore), and therefore was not considered when fitting the best-fit curve to the data. A curve with parameter values A=100 m^3, n=1 is fitted to the remaining points; there is an outlier at Ω=2.9, but overall the data tend to follow the expected relationship between Ω and Q_e.

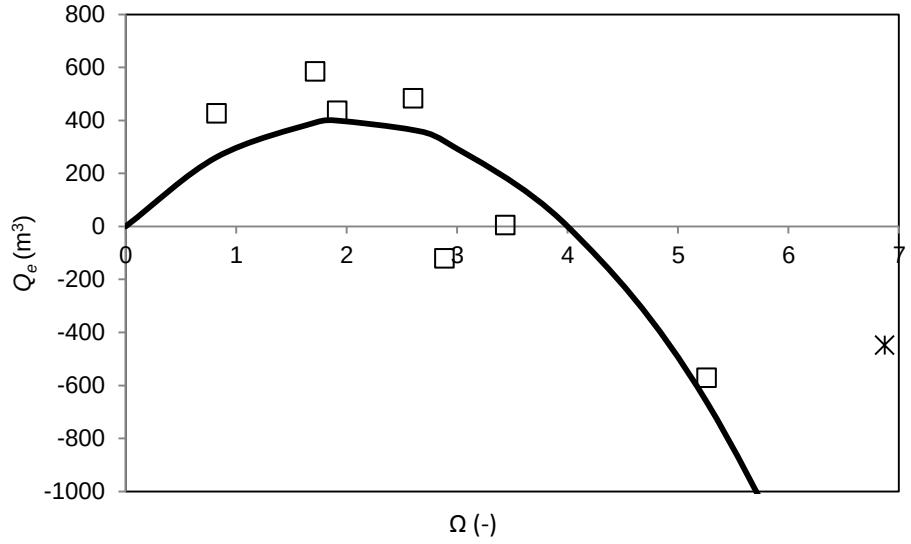

Figure 6-6. Q_e vs Ω for d_{50}=0.4mm from Kraus and Larson (1988). Line shows fitted function $A(\Omega_{eq} - \Omega)\Omega^n$ with A=100 m^3 and n=1. The data point not near equilibrium is shown by (*) marker.

Q_e vs Ω for the finer sediment (for d_{50}=0.22mm) from Kraus and Larson (1988) was plotted in Figure 6-7. As the settling velocity is much smaller the Gourlay numbers become much larger. The profiles at the larger Gourlay number values (Ω=4.5, Ω=9.3, Ω=13) have not yet reached equilibrium, hence have much lower Q_e values than if equilibrium had been achieved. Due to the sediment size, the beach profile tends to erode and hence there are only two accretive cases. Due to the lack of points for this sediment size, a best fit curve was not fitted to this dataset.

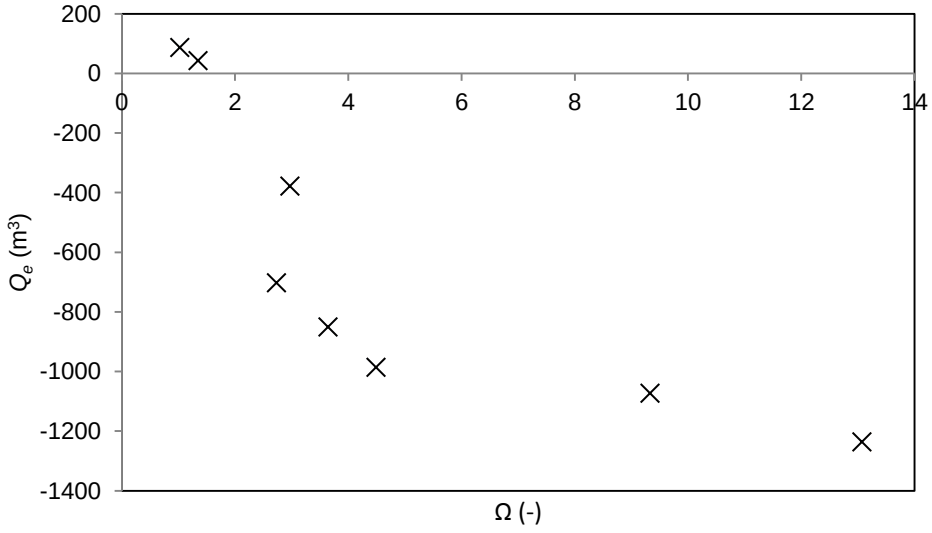

Figure 6-7. Q_e vs Ω for d_{50}=0.22mm from Kraus and Larson (1988).

6.2.3 Narrabeen beach analysis

The Narrabeen beach profiles used for analysis were measured approximately on a monthly basis, under the guidance of Professor Andrew Short. The Emery method (Emery, 1961) was used for surveying by the beach profile from 1976 to 2006. There has been extensive analysis conducted on this dataset (e.g. Callaghan et al., 2008; Davidson et al., 2013; Harley et al., 2011), as one of the biggest and continuous profile datasets in Australia. There have been additional measurement devices at Narrabeen including Argus coastal imaging stations and LiDAR in the last decade; these new survey methods are outlined in Harley et al. (2015).

Two profiles from Narrabeen are plotted in Figure 6-8. The bed elevation from the data ranges from -5m to 10m, and the profile length (x) ranges from 70m to 230m. The cross-shore bulk transport is calculated by limiting the profile length to 140m, as the majority of profiles do not extend beyond this length. The mean wave height and wave period from the Sydney wave gauge were used to calculate mean Gourlay number in between survey dates, while the peak wave height and peak wave period were used to calculate peak Gourlay number.

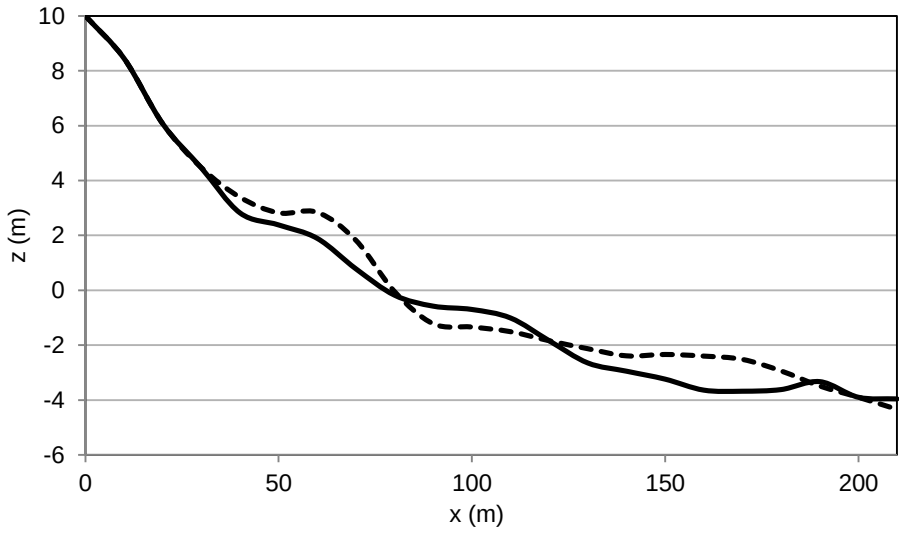

Figure 6-8. Example of Narrabeen Profile from 7th July 1978 (solid) and 28th July 1978

The peak Gourlay number vs Q is plotted in Figure 6-9. The plot shows considerable scatter and there is no discernible relationship between the two parameters. This is to be expected, as the beach profiles are not necessarily near equilibrium, as the other datasets were in previous sections. Additionally, Gourlay number with respect to shoreline position and change in shoreline position averaged over the number of days between profile measurements is plotted in Figure 6-10. The profiles were chosen so that the time difference between profiles was between 3 and 6 weeks. The

colours of the points indicate whether the profile is accreting or eroding. The plot suggests that wider beaches tend to erode and narrower beaches tend to accrete. It appears that $\frac{dS}{dt}$ is not correlated with change in Gourlay number in Figure 6-10, suggesting that this parameter is not particularly sensitive for this dataset. This is in agreement with Jara et al. (2015)'s suggestion that $\frac{dS}{dt}$ should not be a function of H (in their case, $E^{1/2}$). There appears to be a vertical equilibrium line through a shoreline position of approximately 100m, where the beach will accrete if narrower, and erode if wider. This also suggests that the beach does not tend to move around the width of 100m.

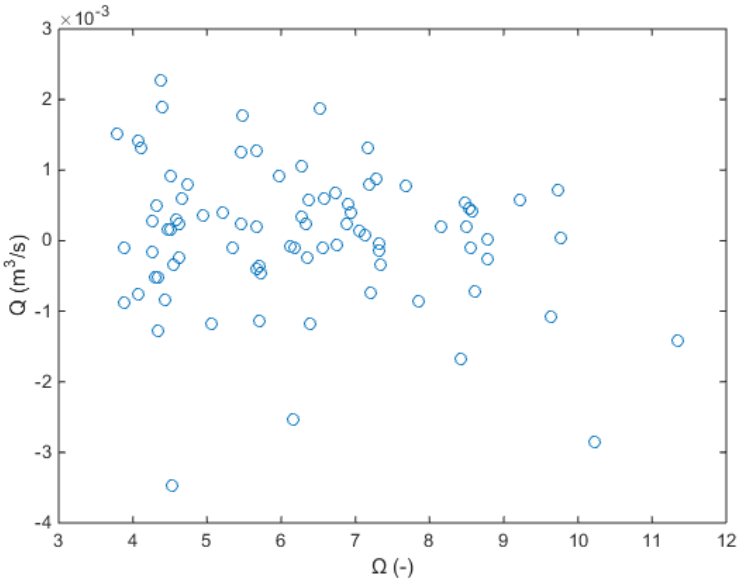

Figure 6-9. *Q* vs Gourlay number for Narrabeen beach

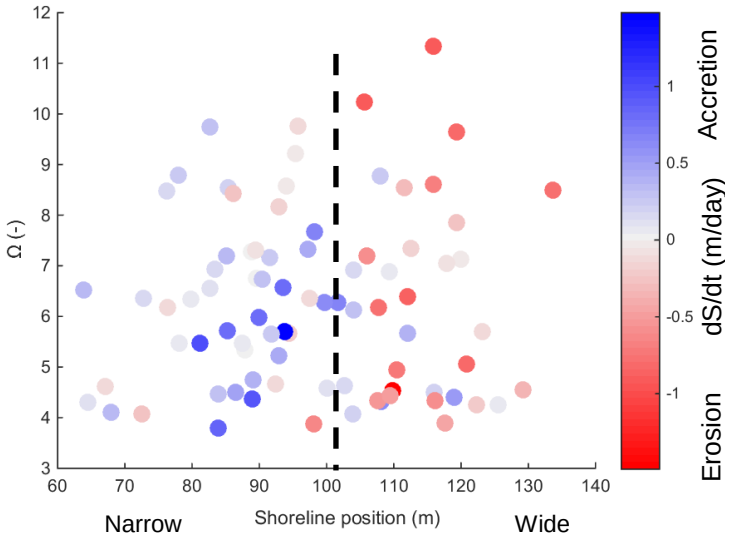

Figure 6-10. Shoreline position vs Gourlay number (Ω) for Narrabeen beach, with point colours representing shoreline position change rate. Potential equilibrium line is shown dashed.

A figure similar to that of Figure 3 in Yates et al. (2009) (see Figure 2-4) was made from suitable Narrabeen data, which is shown in Figure 6-11. The relationship between E and S, as well as $\frac{dS}{dt}$ is not as clear compared to the Torrey Pines dataset, chiefly due to the lack of data points. A potential equilibrium wave energy line is shown in the same figure, which follows a similar trend to that shown in the Torrey Pines data. The wave energy appears to have a more significant impact over $\frac{dS}{dt}$ compared to the Gourlay number. This is different to the observations made by Yates et al. (2009) for Torrey Pines, where Gourlay number was found to be equally effective as wave energy in being a model driver.

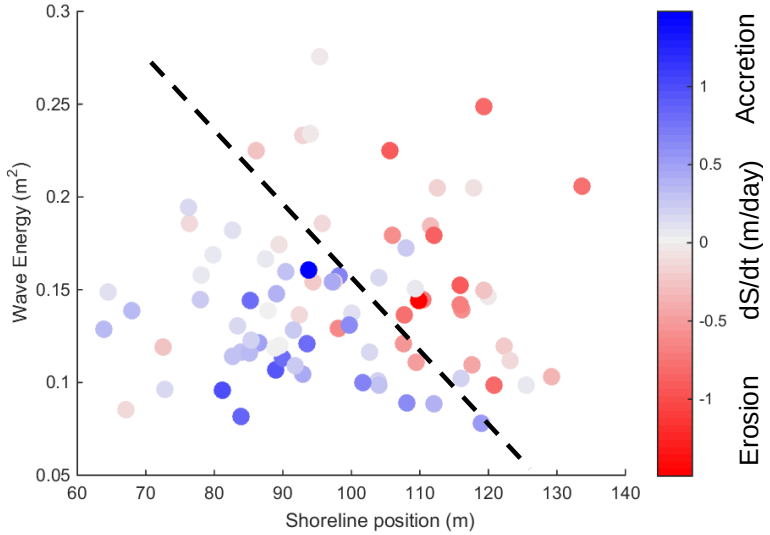

Figure 6-11. Shoreline position vs wave energy (as defined by Yates et al. (2009)), with point colours representing shoreline position change rate. Potential equilibrium energy line is shown dashed.

The Torrey Pines beach data exhibit a clear seasonal cycle, while Narrabeen does not (see Figure 6-12). Although averaging E between survey dates has the effect of smoothing out storms, it was deemed an acceptable method for the purposes of calculating the equilibrium wave energy line (Yates et al., 2009). Figure 6-12 shows that the peak H_{sig} values are drastically smoothed out by averaging between monthly profiles at Narrabeen; averaging between profiles when there is no seasonal signal perhaps also contributed to the weak correlation between wave energy and shoreline position.

Recently, Phillips et al. (2015) analysed daily beach widths (defined as the distance from the shoreline location to a fixed reference point) of Narrabeen from the last decade which show that there are distinct erosion and recovery periods (Figure 6-13), which suggest that using profiles measured in monthly timescales leads to aliasing. It is therefore more difficult to draw firm

conclusions from the analyses of the monthly survey data. Splinter et al. (2014) had much more success with their model for Narrabeen, which utilised alongshore-averaged weekly shoreline data captured by Argus. They also found that the Narrabeen shoreline is driven at a storm timescale rather than seasonal, therefore the more frequent shoreline data measurements would have correlated better with the model driver (in their case, wave energy flux and disequilibrium of the Gourlay number), compared to monthly measurements.

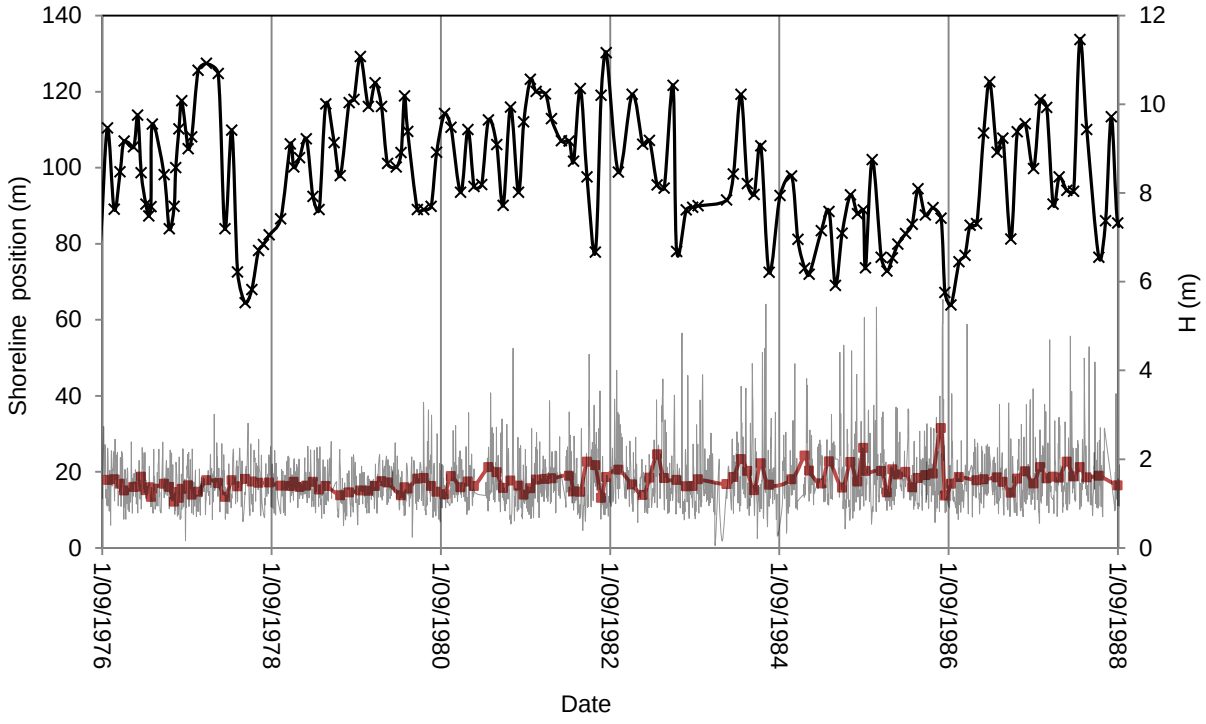

Figure 6-12. Shoreline position for survey dates (x), mean H_{sig} between survey dates using daily H_{sig} (■), daily available H_{sig} data (-).

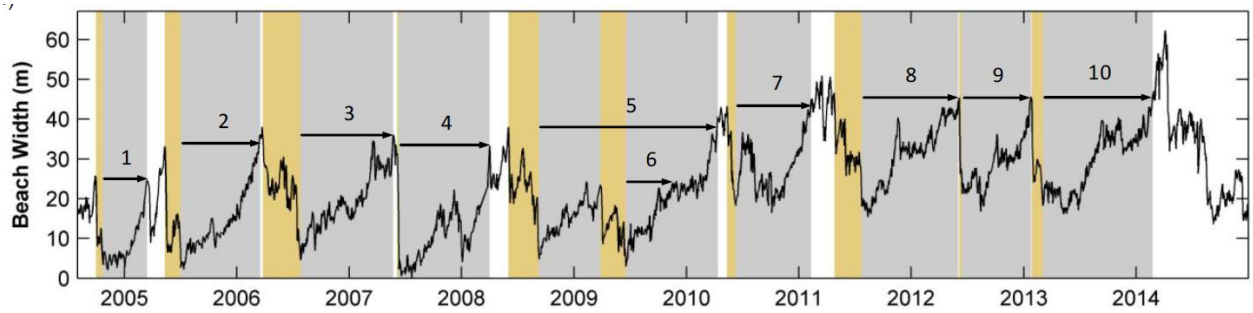

Figure 6-13. Daily beach width from Narrabeen beach from Phillips et al. (2015)

Narrabeen does not appear to be a suitable beach for an equilibrium shoreline model such as Yates et al. (2009) due to the lack of clear relationship between E, S, and $\frac{dS}{dt}$, when monthly profile

measurements are used. Despite this, three sections on Narrabeen beach have been modelled successfully using weekly shoreline data, driven by deep water wave power and a weighted Gourlay parameter (Davidson et al., 2013). This could be attributed to the shorter increment between shoreline measurements. However, their model skill was significantly decreased when wave power was replaced by Gourlay number, suggesting that a Gourlay number type model shown in Eq. (6.1) is not suitable for this beach.

6.3 Equilibrium type total sediment transport model development

The model based on Gourlay number was developed using the data from the UQ random wave experiments and the model from Yates et al. (2009) was rearranged to a form similar to the model proposed by Baldock et al. (2011).

6.3.1 Modelling Q_e relative to previous equilibrium

The data obtained from the random wave experiments were used to fit a model for dQ_e, the value of Q_e relative to the final profile from the previous case. dQ_e is plotted in Figure 6-14 with respect to time.

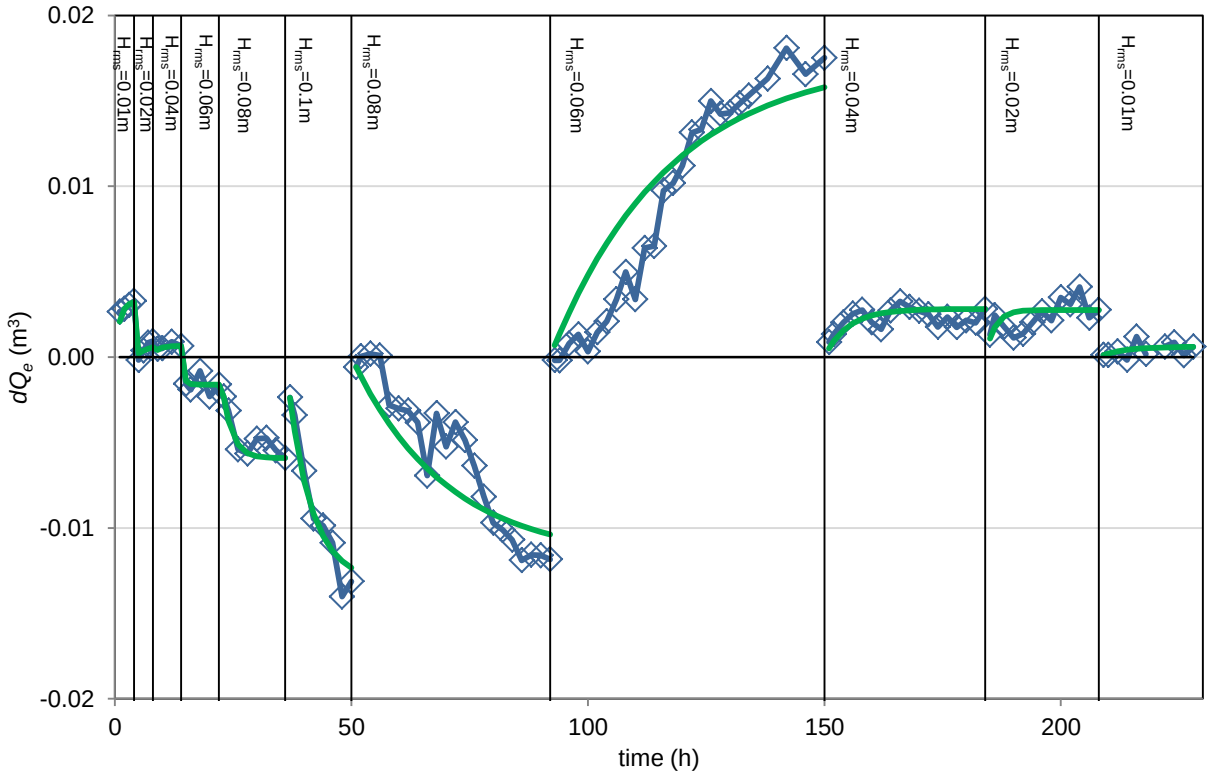

Figure 6-14. Time series of dQ_e (diamonds) and modelled dQ_e (solid line)

The modelled dQ_e is based on the equation

$$dQ_e = Q_e(1 - e^{-t/T_M}) \tag{6.2}$$

Where Q_e is the equilibrium Q value, t is the time since the previous equilibrium profile, and T_M is the morphological time scale. Q_e is obtained from Figure 6-5. T_M is treated as a calibration parameter to fit the model to the data, the values range from 0.5 to 25 hours depending on the wave height. The exponential relationship suits the *IH-* series of experimental data, but the *DH008* and *DH006* cases do not fit the curves, due to the dynamic profile movement during these two cases. The beach profile requires a much longer time period to adjust to the change in wave condition; additionally, the speed at which the profile evolved was exceedingly inconsistent through these cases. Note that the direction of the profile movement is correct for the *DH008* case as Q_e is specified (i.e. the final point is pre-determined by the model form given in Eq. (6.2)).

Other parameters for case *DH008* were investigated to determine if other profile features behaved in a similar manner. The cross-shore location and the crest elevation of the inner bar are plotted in Figure 6-15. The gradient of both curves increase dramatically at approximately t=20 hours, as the inner bar starts quickly moving offshore. At approximately t=30 hours, the gradient of both curves start to plateau. Additionally, the shoreline position is plotted alongside the cross-shore location of the inner bar crest in Figure 6-16. The shoreline position gradually moves onshore until approximately t=24 hours and starts to move offshore after this point.

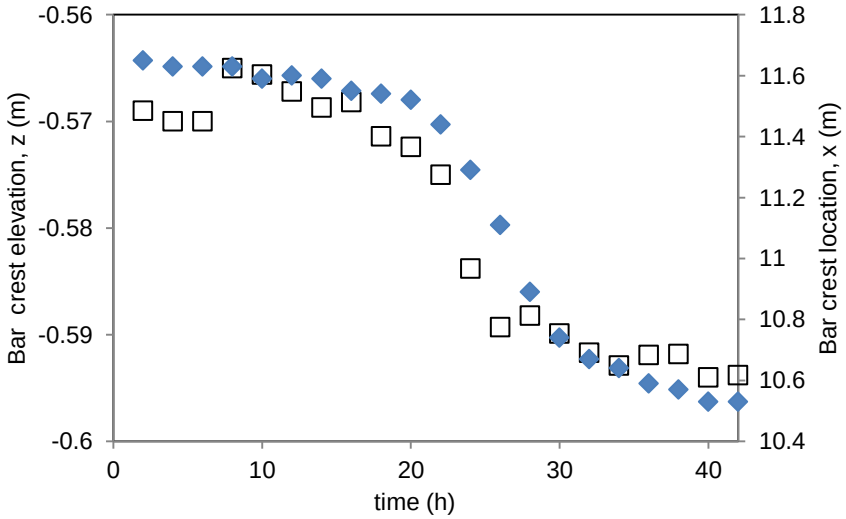

Figure 6-15. Time-series of inner bar crest elevation (z) (squares) and cross-shore location (x) (diamonds) of case *DH008*.

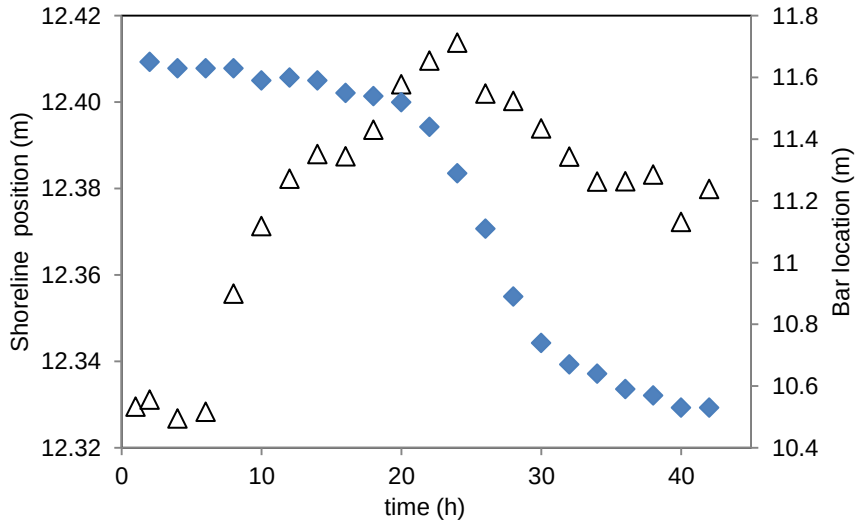

Figure 6-16. Time-series of shoreline position (triangles) and inner bar cross-shore location (diamonds) for case *DH008*.

The trend of both the bar crest elevation and cross-shore location is very similar for the UQ flume experiments; this is not a common occurrence, as shown by a similar plot for case 400 from Kraus and Larson (1988) in Figure 6-17. The bar crest elevation quickly reaches its final level while the bar continues to move offshore. This difference in bar crest elevation and location movement was typical for the barred profiles for the finer sediment with d_{50}=0.22mm.

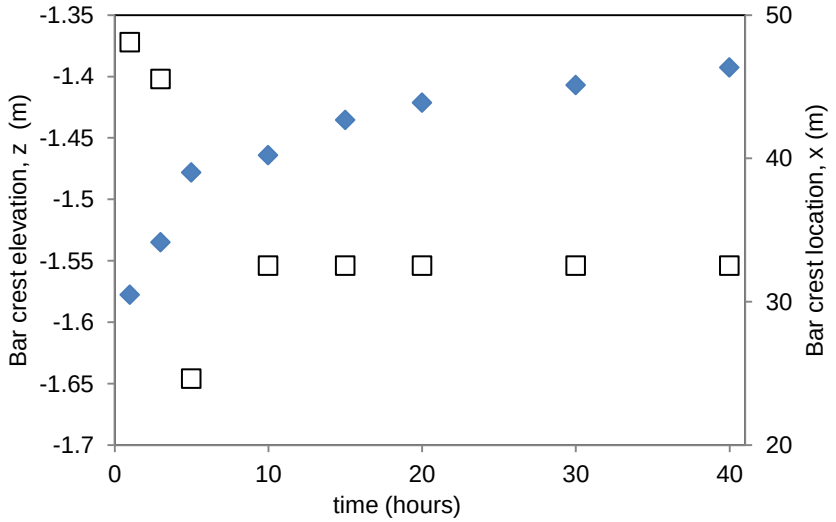

Figure 6-17. Time-series of bar crest elevation (z) (squares) and cross-shore location (x) (diamonds) of case 400 from Kraus and Larson (1988) [H=1.62m, T=5.6s, d_{50}=0.22mm].

Considering that natural systems do not necessarily reach equilibrium, equilibrium models based on field data are only required to fit the available data, most often the initial part of the dQ_e curve. As observed in the random wave experiments in the laboratory, the use of only one, or even two time

scales for one wave height case is perhaps unrealistic, especially for the *DH*- cases which have very dynamic profile changes. This finding has significant implications for equilibrium type models as mentioned in Figure 1-2 (d), where the morphological time scale features prominently and often not clearly defined.

Although the dQ_e model is suitable for the erosive cases, and can model the direction correctly for all cases, this is completely dependent on an accurate Ω - Q_e curve such as the one from Figure 6-5, as well as the initial profile (i.e. antecedent conditions). To accurately predict this relationship based on just wave and sediment characteristics will require additional experiments with a variety of scale, wave and profile characteristics with the aim of developing a firmer foundation for this model relationship.

6.3.2 Rearrangement of model from Yates et al. (2009)

The results from the model by Yates et al. (2009) were rearranged by plotting the data with respect to wave height and rate of change of shoreline position. Hourly wave data from San Clemente Basin (Station 46086) from 2004 to 2008 were applied to the model from Yates et al. (2009) with the calibrated coefficients for Torrey Pines section T3.

The predicted $\frac{dS}{dt}$ was plotted against wave height and the previous shoreline position is represented in the colour of the points in Figure 6-18. A wider beach experiences more erosion (more negative $\frac{dS}{dt}$) and a narrower beach is more likely to accrete. When fitted to curves in the form of $A(H_e - H)H^n$, where Ω is replaced with H from Eq.(6.1), these sets of curves mostly have a similar value of A and n, and are differentiated only by H_e, the H value when $\frac{dS}{dt}$=0. The behaviour of $\frac{dS}{dt}$ is very similar to that proposed for Q_e, perhaps suggesting that various beach states can be used in beach profile modelling in a similar manner.

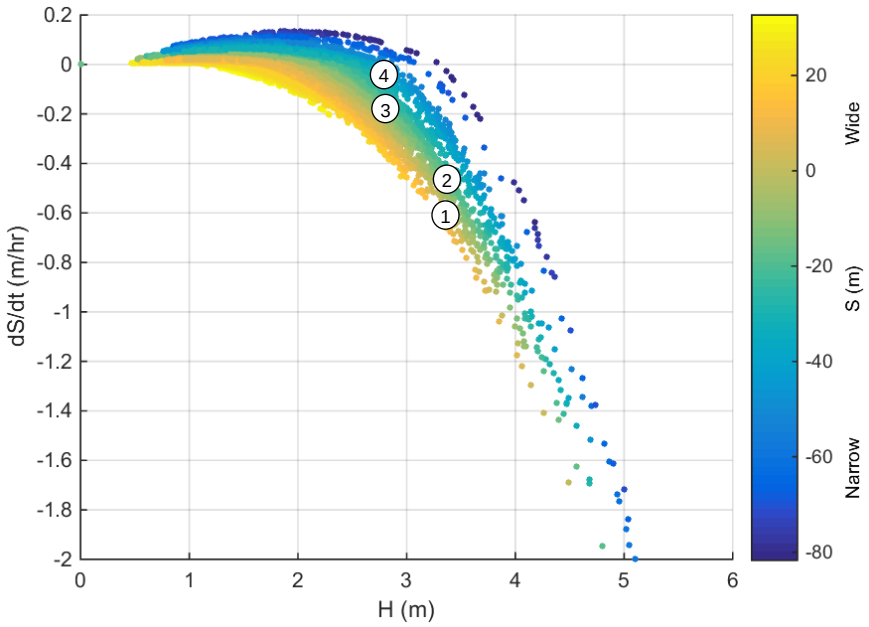

Figure 6-18. Torrey Pines model from Yates et al. (2009), replotted as a function of *H* and *dS/dt*. Colours of points represent the shoreline position with the mean removed for the previous time step.

Point 1 in Figure 6-18 represents the rate of change of shoreline position for a relatively wide beach. If the wave height is maintained, the beach becomes narrower (point 2). If the wave height is decreased, the point moves to a lower *H*, with the same initial shoreline position, hence on a same coloured point (point 3). If the same wave height is then applied for a longer period, the beach becomes narrower and $\frac{dS}{dt}$ is also decreased (point 4). The range of H_e is analogous to Ω_{eq} in the Ω - Q_e model.

Additionally, the Yates et al. (2009) model was run for synthetic wave height data consisting of *H*=1, 1.5, 2, and 3m in order to test the model under equilibrium conditions (i.e. the same conditions as Figure 6-1). The resulting $\frac{dS}{dt}$ with respect to wave height is shown in Figure 6-19. Starting from a wave height of 1m, the model was run long enough for the model to reach S_{eq}, i.e. until $\frac{dS}{dt} = 0$. Then the model was run for the increasing sequence of wave height until *H*=3m, and then for decreasing wave height; each case until S_{eq} was reached. This mimics the exponential sequence in Figure 6-1. The sequence of $\frac{dS}{dt}$ is shown by the black arrows in Figure 6-19. When wave height was increased, $\frac{dS}{dt}$ reached its maximum rate for that particular wave height. As the constant wave forcing continued, the shoreline approached S_{eq}. Also note that the S_{eq} value for each wave height is the same whether it succeeds a smaller or larger wave height, this differs from the lab data.

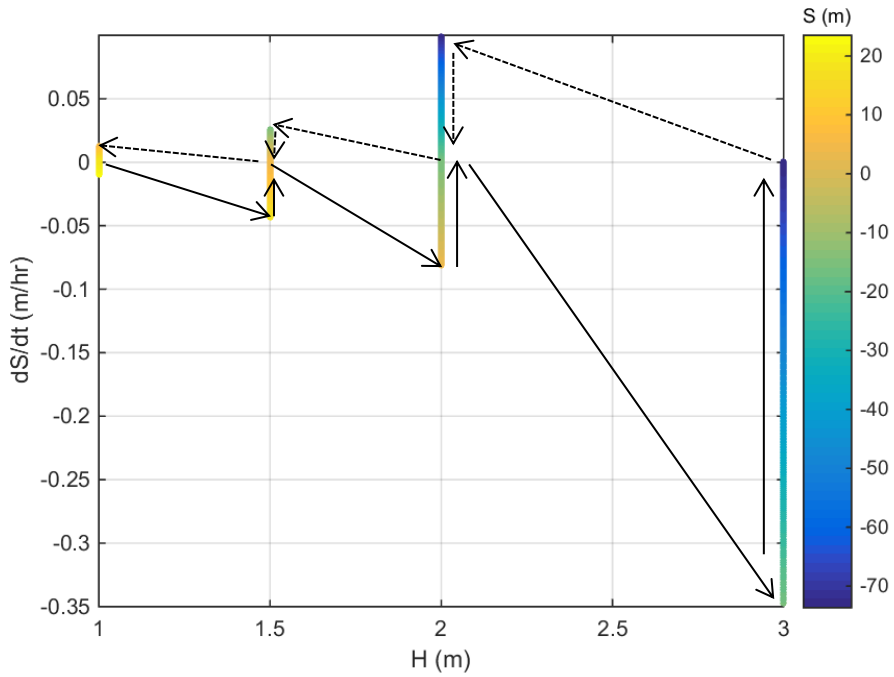

Figure 6-19. Wave height and $\frac{dS}{dt}$ from Yates et al.'s (2009) model on synthetic data run to equilibrium; black arrows show progression of $\frac{dS}{dt}$, and the colours represent the shoreline position from the previous time step.

The behaviour of $\frac{dS}{dt}$ to equilibrium with respect to wave height is unlike that of the Ω vs Q_e plots as $\frac{dS}{dt}$ must always be at zero when at equilibrium by definition. It is more comparable to dQ_e, see Figure 6-14. The magnitude of $\frac{dS}{dt}$ increases as wave height increases, with the magnitude slightly different depending on whether the beach at the previous time step was wide or narrow, reflecting the difference in rate coefficients for erosion and accretion.

Using the Torrey Pines T3 model coefficients, the maximum $\frac{dS}{dt}$ value at the first time step after equilibrium was plotted at various E values for two initial equilibrium shoreline positions in Figure 6-20. The larger curve started with an equilibrium shoreline position for H=2.2m. Any wave height smaller than 2.2m caused a positive $\frac{dS}{dt}$ and hence accretion, wave heights larger caused erosion. As the wave energy approaches zero, $\frac{dS}{dt}$ also approaches zero. The smaller curve shows the curve starting with an equilibrium shoreline position for H=1m.

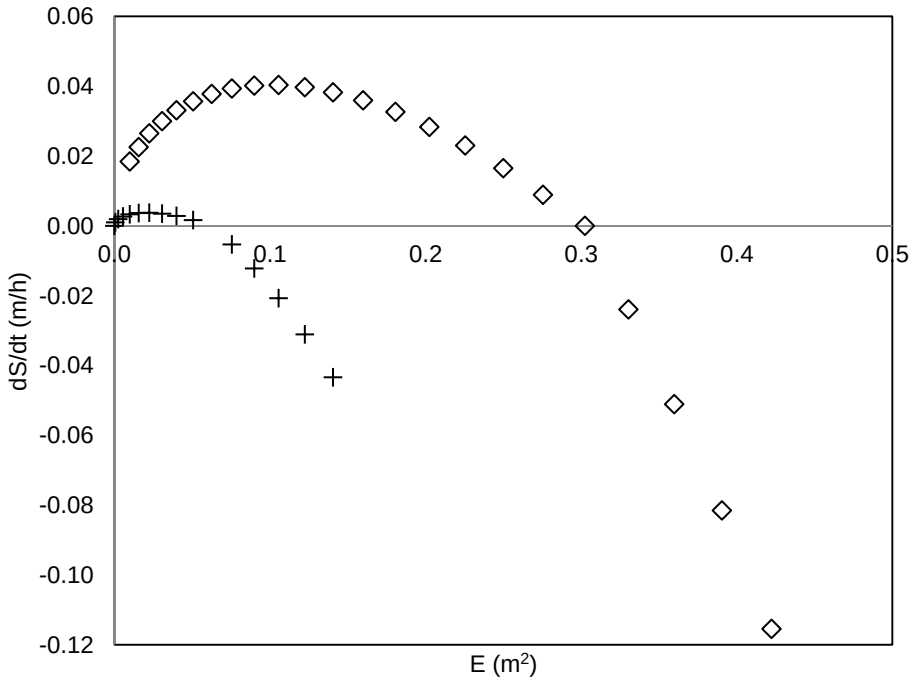

Figure 6-20. Maximum $\frac{dS}{dt}$ value (at first time step after equilibrium) at various E values, for initial shoreline positions at equilibrium under *H*=2.2m (diamonds) and *H*=1m (crosses) for Yates et al. (2009) model using Torrey Pines T3 model coefficients.

A similar plot was created for the UQ random wave experiments, shown in Figure 6-21. These points each represent points like those shown in Figure 6-20. $\frac{dS}{dt}$ behaves as expected, and is negative for all of the *IH*-series and positive for *DH*-series except for *H*=0.08m and *H*=0.06m, when the profiles are still eroding. Note that the sign convention for shoreline position is opposite to that of the Torrey Pines beach profile (i.e. the laboratory profile is considered to be eroding when the shoreline position increases, vice versa) and hence the sign convention was altered for clear comparison to Figure 6-20.

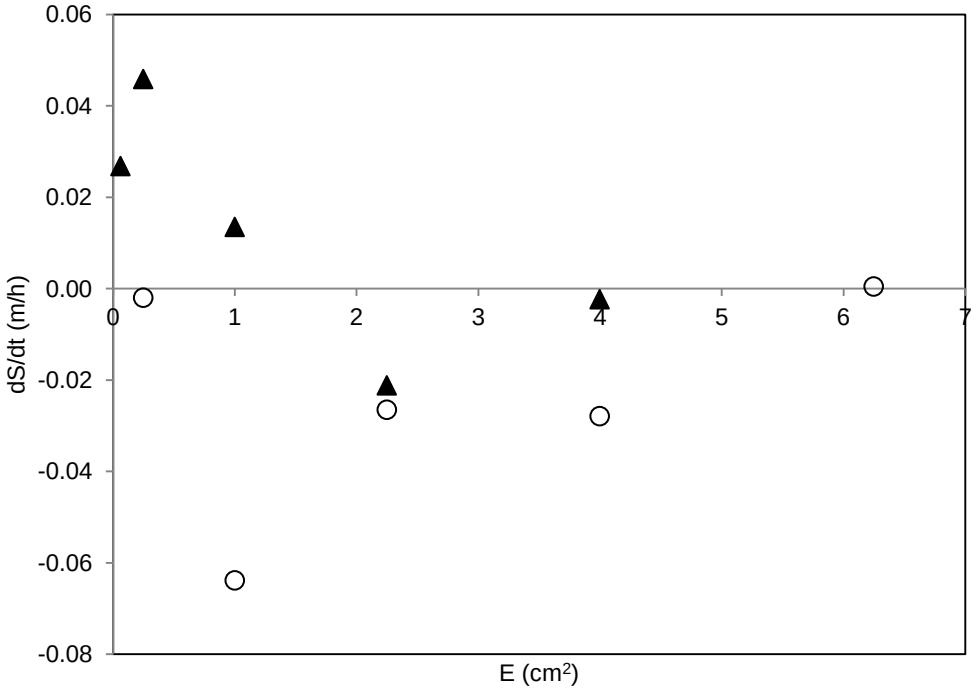

Figure 6-21. $\frac{dS}{dt}$ value at various *E* values for first hour after change in wave conditions from UQ random wave experiments for *IH*-series (circles) and *DH*-series (triangles)

The laboratory results show that the magnitude of $\frac{dS}{dt}$ does not increase as *E* (or *H*) is increased, contrasting from the model from Yates et al. (2009). Additionally, the data obtained from the random wave experiment from the UQ flume were plotted with respect to *E* and shoreline position, with the point colours represented by $\frac{dS}{dt}$ in Figure 6-22. This also shows that the rate of change of the shoreline does not show a trend related to *E* or *H*.

Note that the sign convention for shoreline position is opposite to that of Yates et al. (2009) Figure 3 (Figure 2-4). Therefore the relationship between *S* and *E* appears to be similar to that found in Yates et al. (2009). The E_{eq} line is shown on the figure as a dashed line.

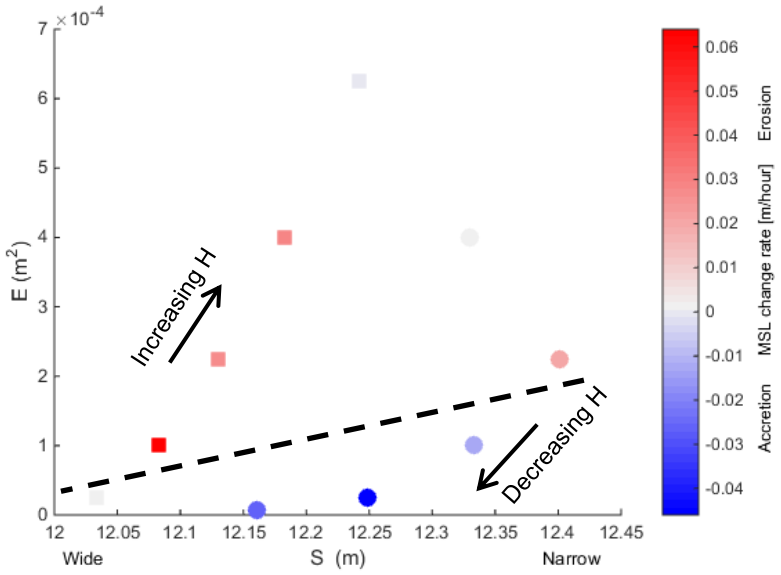

Figure 6-22. Shoreline position vs *E* plot, colours indicate $\frac{dS}{dt}$ in the first hour post-equilibrium for the previous *H*. Squares denote *IH*- series, circles are for *DH*- series. The dashed line is the approximate equilibrium wave energy line.

Figure 6-22 for the UQ flume data, together with Figure 2-4 for data from Yates et al. (2009), suggests that $\frac{dS}{dt}$ should not be a function of some power of *E*, as the model by Jara et al. (2015) claimed (outlined in Section 2.3.1.3). If $\frac{dS}{dt}$ was a function of some power of *E*, the points should be darkening in colour as *E* increases. But this does not appear to be true, hence the weighting factor (some function of *E*) employed in many previous shoreline models may not be entirely appropriate. This is also supported by the Figure 6-10 for Narrabeen, where there was no relationship between $\frac{dS}{dt}$ and Ω, which is a function of *H*.

6.4 Conclusions and future work

An alternative model for transport across a beach profile to equilibrium was proposed based on the model proposed by Baldock et al. (2011). Three datasets were tested to see whether the model has potential for development. As the laboratory tests from the UQ wave flume and Kraus and Larson (1988) were undertaken with constant wave height, the profiles chosen were largely close to equilibrium and hence more suited for the proposed model. The Narrabeen beach profile data on the other hand were found to be unsuitable for the model, due to the monthly observation periods being too coarse and the profiles unlikely to have been near equilibrium.

The model was developed further and the change in Q_e over time was fitted to a traditional exponential type model. This analysis suggested the dynamic morphological development which occurs when wave height is decreased cannot be reflected by a simple exponential relationship, due to the variation in speed at which the morphological features develop. The use of one morphological time scale for one wave height case was therefore found to be inappropriate, which has implications for equilibrium type beach state models. The instability of profiles subjected to a sudden change in wave characteristics could be considered irrelevant with regards to profile development over longer time scales of weeks and months. However over a shorter time scale, the profile adjusting to the abrupt change in wave conditions through increased profile development is a significant feature that beach profile modelling has seemed to have overlooked. Whether the beach profile would have reacted differently if the change in wave height was more gradual is a query which needs to be addressed in future experiments.

The equilibrium shoreline model from Yates et al. (2009) was analysed further using their model coefficients for Torrey Pines T3 and compared to the Ω - Q_e model; it was found that the rate of change of shoreline $\frac{dS}{dt}$ behaves similarly to the cross-shore bulk transport Q with respect to wave height, suggesting that these beach states react similarly to changing wave height. It was also suggested that $\frac{dS}{dt}$ does not appear to be a function of E for both the UQ experimental data and the data from Yates et al. (2009).

Future works related to this model include investigations into the effect of wave period in the model. Although wave height and wave period have equal weighting in the Gourlay number, it is not clear if they have the same effect on the Ω - Q_e model. It is clear from the various experimental datasets that there exists some relationship between Gourlay number, cross-shore bulk sediment transport and initial profile. It has been identified that some beaches can continue to erode with decreased wave height after reaching equilibrium; this warrants further revisions to existing equilibrium models to incorporate this morphological behaviour. As discussed in Section 5.3.3, storm bars on real beaches can become arrested (e.g. Aagaard, 1991) after sudden changes in wave height; the typical $\frac{dH}{dt}$ at the end of storms is perhaps too fast for the storm profiles. This is a feature that is not reflected in the Ω - Q_e model or the model from Yates et al. (2009); therefore additional experiments with more gradual changes in wave height should be undertaken to understand how quickly the Gourlay number can be changed without causing a shock to the evolutionary behaviour of the beach profile (i.e. to prevent stranding of bars, and very dynamic shoreline changes).

7 Conclusions and loose ends

7.1 Conclusions

This thesis analysed a net sediment transport model based on existing laboratory data, as well as an equilibrium type total sediment transport model, based on profile data collected from experiments conducted in the UQ hydraulics laboratory and previous laboratory and field experiments. A new method to convert surface elevation data to velocity was also investigated through the local approximation method. These analyses were conducted to contribute to the research area of accretive sediment transport, which until recently has been largely overlooked compared to erosive sediment transport. The following section outlines the main conclusions from each chapter.

The literature relevant to net sediment transport models, various onshore sediment transport components, and beach state modelling was reviewed. The key findings include:

- The Meyer-Peter and Müller (1948), typically used for bed load sediment transport, can be used for sediment transport over ripples, to use as a proxy for ripple migration;
- The half-cycle model (Dibajnia & Watanabe, 1996) and the grab and dump model (Nielsen, 1988) are both semi-unsteady net sediment transport models; the former has been updated regularly to accommodate recent findings in sediment transport research (e.g. Van der A et al., 2013; Watanabe & Sato, 2004);
- The grab and dump model which showed promising results for suspended sediment transport over ripples was deemed a simple model for developing further to suit a broader range of conditions;
- Acceleration skewness and boundary streaming were found to be essential contributors to onshore sediment transport. Shear stress rather than velocity was found to reflect acceleration skewness better than velocity (Nielsen, 1992);
- Wave energy and Gourlay numbers act as common predictors for beach state models; however the constant term in disequilibrium based beach state models (e.g. the $E^{1/2}$ term in Eq. (2.26)) has been criticised as being arbitrary and having no physical basis for its inclusion (Jara et al., 2015);
- Sediment size is considered a significant factor which contributes to beach morphological behaviour; it is incorporated in models through the sediment fall velocity through the Gourlay number and adjustments in calibration coefficients (Yates et al., 2011);
- The timescale of the model inputs was also found to affect model predictive capacity; if the wave averaging period was too long, individual storms would be overlooked and hence inversely affect model performance (Davidson et al., 2011). Antecedent conditions were

also emphasized in recent shoreline prediction models (Davidson et al., 2013; Splinter et al., 2014), where different types of beaches require different periods of antecedence, reflected in model parameters; and

- Shoreline position is often predicted in beach state models, however an alternative parameter, the cross-shore bulk sediment transport (Baldock et al., 2011; Jacobsen & Fredsøe, 2014) was suggested as a parameter which could reflect the morphological change on an active beach profile.

The grab and dump (GD) model (Nielsen, 1988) was updated to reflect the effects of acceleration skewness for a coarse sediment by using a shear stress equation, Eq.(2.19), based on both velocity and acceleration (Nielsen, 1992). While the original model based on velocity was unable to predict the net sediment transport for the coarse sediment along the flume, the updated model based on shear stress, was able to predict the sediment transport pattern very well. The main findings were:

- The inclusion of a critical Shields parameter, similar to that of Meyer-Peter and Müller (1948) improved the model performance;
- Applying boundary layer streaming did not improve the model performance for the data; this is thought to be due to the lesser impact of boundary streaming on a rippled bed (Bijker et al., 1974);
- The updated GD model was compared to another semi-unsteady net sediment transport model (Van der A et al., 2010b) using data from Schepers (1978); the two models performed similarly once the model by Van der A et al. (2010b) was calibrated to the data;
- The updated GD model was also applied to sheet-flow data from Van der A et al. (2010a), where the optimal phase shift angle φ_τ was fitted to each case, which was then found to scale with Reynolds number and roughness; and
- The GD model was applied to experiments with superimposed currents and further amendments to the model are suggested.

The updated GD model is a relatively simple model formula which can account for the acceleration skewness through the shear stress formula (Eq.(2.19)). As the magnitude of the sediment flux is based on an empirical relationship established in Nielsen (1986b), this equation will most likely require revision.

The updated GD model is suitable for data where acceleration skewness is dominant over velocity skewness. It is also suitable for cases over a rippled bed where the sediment transport is dominated by ripple migration rather than suspended sediment. For suspended sediment transport over ripples, use of the original GD model is more appropriate. Preliminary analyses have shown that the model may be suitable for use under sheet flow conditions, with the phase shift angle φ_τ used as a calibration parameter. With further amendments to the model structure, it will be suitable for use in a broader range of conditions.

The local approximation method from Nielsen (1989) was developed to convert surface elevation to velocity. This was undertaken as many sediment transport models require velocity time series as input; where there are no adequate velocity measurements collected, this method could be used to convert available data to sediment transport model inputs. The main conclusions include:

- Application to monochromatic waves from the SASME experiments shows that this method can estimate velocity as well as the spectral method;
- Increasing nonlinearities in shallower water can be predicted better using the additional multiplier $\frac{h}{(\eta+h)}$; this can be applied to both the spectral method and the local approximation method;
- The COULWAVE numerical model can predict the velocities well for the monochromatic wave for the SASME data until the wave has broken;
- The local approximation was also applied to random and bichromatic waves from the SASME dataset; the method did not perform well compared to the traditional spectral method. The multiplier which had worked for increasing non linearity for monochromatic waves did not consistently improve velocity predictions;
- When low frequency filters were applied to determine whether the poor performance was due to presence of long waves, the spectral method predictions were improved considerably but the local approximation method prediction did not improve for random waves. This stems from the local approximation method focusing on recreating the shape of the signal rather than the spectrum of the signal;
- Both the spectral method and the local approximation method performed better for the bichromatic wave data than the random wave data;
- The SUSCO data were poorly predicted by both the spectral method and local approximation methods. As there were only two locations where surface elevation and

velocity were measured together, the data used may have been unsuitable for comparison (e.g. too close to break point); and

- The local approximation method was able to predict the velocity well for data from Flick (1978) for spilling breakers. However, this was with limitations applied, such as specifying a maximum frequency and spacing for calculating the frequency.
- The local approximation method is best suited for monochromatic and bichromatic waves in its current state; it offers a good alternative to the spectral method, when combined with the multiplier, especially just prior to breaking where there are more non-linearities in the wave signal.

The beach profile experiments conducted in the UQ hydraulic flume resulted in new measurements of equilibrium beach profiles with random waves of H_{rms} values between 0.01 and 0.1m. These experiments were undertaken due to the lack of experimental data for equilibrium beach profiles under random waves. The aim was to collect profile measurements of relatively high frequency to observe the morphological behaviour of the beach profile under both erosive and accretive conditions, subsequently to be used towards equilibrium-type sediment transport models. Some interesting features of the experiment results include:

- The Q_e trend (Figure 5-14) did not reverse after wave height was decreased from 0.1m to 0.08m; this is in contrast with the model from Yates et al. (2009) where the beach starts to recover after the wave energy is decreased after reaching equilibrium. This is because the equilibrium shoreline position in the model is based on a simple linear relationship between shoreline position and wave energy. Similar behaviour of the shoreline is apparent in the Torrey Pines data used by Yates et al. (2009) but it is not commented on and their model does not reproduce it;
- The bar system became very dynamic when wave height was decreased. The outer bar was flattened and the inner bar moved offshore to create a new outer bar and this behaviour was repeated with further decrease in wave height. Similar behaviour of the outer bar being flattened is observed in Cáceres and Sanchez-Arcilla (2015) and the inner bar moving offshore to become the outer bar is observed in the field at Duck, North Carolina (e.g. Birkemeier, 1984; Lippmann et al., 1993);
- The numerical model COSMOS was unable to predict onshore sediment transport when similar wave conditions to the experiments were applied; and

- The equilibrium profiles were different for different antecedent conditions, under the same wave conditions, as they depend on antecedent conditions (e.g. arrested bars).

A model for total sediment transport across a beach profile at equilibrium was proposed. The model was based on the relationship between Gourlay number and cross-shore bulk transport (Baldock et al., 2011). The model was applied to data from the UQ experiments and profile data from the LWT (Kraus & Larson, 1988); both datasets showed a similar relationship as proposed by Baldock et al. (2011). The model was developed further and the change in Q_e over time was fitted to a traditional exponential type model. The main conclusions from this model include:

- The Narrabeen beach profile data, measured roughly in monthly intervals, were found to be unsuitable for the model, due to the measurement intervals as well as the total sediment transport being insensitive to changes in Gourlay number;
- The morphological behaviour of the experimental measurements could not be fitted to a simple exponential relationship, due to the variation in speed at which the morphological features developed. The way in which the beach profile reacts to an abrupt change in wave conditions is a significant feature that beach profile modelling has seemed to have overlooked;
- When the equilibrium shoreline model from Yates et al. (2009) was analysed further in order to compare to the form of the $Q_e - \Omega$ model, it was found that the rate of change of shoreline $\frac{dS}{dt}$ behaves similarly to the cross-shore bulk transport, suggesting that these beach states can be modelled in similar ways, with some function of *H* as a model driver; and
- It was found that $\frac{dS}{dt}$ does not appear to be a function of *E* for both the UQ experiments and the data from Torrey Pines in Yates et al. (2009) and perhaps the use of $E^{1/2}$ in equilibrium shoreline models is not appropriate, as suggested by Jara et al. (2015).

This equilibrium type total sediment transport model based on Gourlay number and cross-shore bulk transport can be applied to determine if a beach will accrete or erode. With beach profiles at or approaching equilibrium, the model behaves similarly to the original model by Baldock et al. (2011), however it is not applicable to field data measured at long time intervals.

7.2 Loose Ends

Further works for the updated GD model include how to determine the split between suspended and bedload sediment, as in many instances in the field, there is a mixture of sediment transport mechanisms (see Figure 1-1). It is recommended that experiments which have a well-defined split of the two components be used to develop a method to separate the suspended and bedload sediment. The updated GD model in its current state cannot predict sediment transport accurately when there is no acceleration skewness; further development of the model is recommended to rectify this shortcoming, as the model should accommodate a large range of wave conditions similarly to the model by Van der A et al. (2010b). The model with respect to superimposed current is also in the preliminary stages, and further work should be conducted with respect to understanding the value of the current multiplier, α_v, that is required. The empirical relationship of the sediment reference concentration and Shields number (Nielsen, 1986b) should be revised with more data points, as the magnitude of the sediment flux is based on this relationship. With these amendments, the model can be used for a wider range of conditions.

The local approximation method is an alternative method to convert surface elevation to velocity; it often performs similarly to the traditional spectral method, despite being a very different type of method. The local approximation method performs well with additional limitations and multipliers, but there are no guidelines for their application; the method should be tested on a larger dataset in order to develop these guidelines. Finally, the phase difference between surface elevation and velocity on sloping bottoms is not accounted for by both the local approximation and spectral methods; this should be addressed in future research.

The equilibrium beach profile experiments can be extended by varying the wave period, as well as wave height. The equilibrium beach profiles for the same Gourlay number, but with different wave height and wave period, could be compared. The evolution of the bar system when wave period is varied would be also interesting to compare with these experiments. In the current experiments, it was found that some beaches can keep eroding even when wave height is decreased after reaching the previous equilibrium; there should be further experiments conducted to determine under what conditions the beach profile has this reaction.

Future works regarding the equilibrium type total sediment transport model include revisions to existing equilibrium models which reflect the finding that beaches do not necessarily recover when wave height is decreased. In order to understand the changes in Gourlay number with cross-shore bulk transport, similar beach profile experiments to those outlined in Section 5, but with more gradual changes in wave height should be undertaken. Understanding how the beach responds to

changes in Gourlay number in smaller increments may lead to identifying the circumstances under which events such as stranding of bars and cyclic shoreline changes occur.

8 References

Aagaard, T 1991, 'Multiple-Bar Morphodynamics and Its Relation to Low-Frequency Edge Waves', *Journal of Coastal Research*, vol. 7, no. 3, pp. 801-13.

Aagaard, T, Hughes, M, Baldock, T, Greenwood, B, Kroon, A & Power, H 2012, 'Sediment transport processes and morphodynamics on a reflective beach under storm and non-storm conditions', *Marine geology*, vol. 326–328, pp. 154-65.

Anderson, AG 1942, 'Distribution of suspended sediment in a natural stream', *Transactions, American Geophysical Union*, vol. 23, no. 2, pp. 678-83.

Atkinson, A & Baldock, TE 2016, 'A high-resolution sub-aerial and sub-aqueous laser based laboratory beach profile measurement system', *Coastal Engineering*, vol. 107, pp. 28-33.

Atkinson, A, Shimamoto, T, Wu, S, Birren, F & Baldock, TE 2015, 'Beach profile evolution under cyclic wave climates', in *Coasts & Ports Conference 2015*, Auckland, New Zealand.

Austin, M, Masselink, G, O'Hare, T & Russell, P 2009, 'Onshore sediment transport on a sandy beach under varied wave conditions: Flow velocity skewness, wave asymmetry or bed ventilation?', *Marine geology*, vol. 259, no. 1–4, pp. 86-101.

Bagnold, R 1963, 'Beach and nearshore processes-Part 1, Mechanics of marine sedimentation', in MN Hill (ed.), *The sea - ideas and observations on progress in the study of the sea*, Interscience Wiley, New York, pp. 507–28.

Bagnold, RA 1954, *Experiments on a Gravity-Free Dispersion of Large Solid Spheres in a Newtonian Fluid under Shear*, vol. 225.

Bagnold, RA 1966, 'An approach to the sediment transport problem from general physics', *The physics of sediment transport by wind and water*, pp. 231-91.

Bailard, JA 1981, 'An energetics total load sediment transport model for a plane sloping beach', *Journal of Geophysical Research*, vol. 86, no. C11, pp. 10,938-10,54.

Baldock, T & Huntley, D 2002, 'Long–wave forcing by the breaking of random gravity waves on a beach', *Proceedings of the Royal Society of London. Series A: Mathematical, Physical and Engineering Sciences*, vol. 458, no. 2025, pp. 2177-201.

Baldock, TE, Alsina, JA, Cáceres, I, Vicinanza, D, Contestabile, P, Power, H & Sanchez-Arcilla, A 2011, 'Large-scale experiments on beach profile evolution and surf and swash zone sediment transport induced by long waves, wave groups and random waves', *Coastal Engineering*, vol. 58, no. 2, pp. 214-27.

Baldock, TE, Huntley, DA, Bird, PAD, O'Hare, T & Bullock, GN 2000, 'Breakpoint generated surf beat induced by bichromatic wave groups', *Coastal Engineering*, vol. 39, no. 2–4, pp. 213-42.

Banno, M & Kuriyama, Y 2014, 'Prediction of future shoreline change with sea-level rise and wave climate change at Hasaki, Japan', in *Proceedings of 34th International Conference on Coastal Engineering*, Seoul, Korea.

Battjes, JA & Janssen, JPFM 1978, 'Energy loss and set-up due to breaking of random waves', in *Proceedings of 16th Coastal Engineering Conference*, Hamburg, Germany, pp. 569-87.

Bijker, E, Kalkwijk, JPT & Pieters, T 1974, 'Mass transport in gravity waves on a sloping bottom', in *Proceedings of 14th International Conference on Coastal Engineering*, Copenhagen, Denmark, pp. 447-65.

Bijker, E, Van Hijum, E & Vellinga, P 1976, 'Sand transport by waves', in *Proceedings of 15th International Conference on Coastal Engineering*, Honolulu, Hawaii, pp. 1149-67.

Birkemeier, WA 1984, 'Time scales of nearshore profile changes', in *Proceedings of 19th International Conference on Coastal Engineering*, Houston, Texas, pp. 1507-21.

Birkemeier, WA & Mason, C 1984, 'The Crab: A Unique Nearshore Surveying Vehicle', *Journal of Surveying Engineering*, vol. 110, no. 1, pp. 1-7.

Boak, EH & Turner, IL 2005, 'Shoreline Definition and Detection: A Review', *Journal of Coastal Research*, pp. 688-703.

Cáceres, I & Sanchez-Arcilla, A 2015, 'Erosive and accretive mobile bed experiments in large scale tests', in P Wang, JD Rosati & J Cheng (eds), *Proceedings of the Coastal Sediments 2015*, San Diego, USA.

Calantoni, J & Puleo, JA 2006, 'Role of pressure gradients in sheet flow of coarse sediments under sawtooth waves', *Journal of Geophysical Research*, vol. 111, no. C1, p. C01010.

Callaghan, DP, Nielsen, P, Short, A & Ranasinghe, R 2008, 'Statistical simulation of wave climate and extreme beach erosion', *Coastal Engineering*, vol. 55, no. 5, pp. 375-90.

Clark, S & Nielsen, P 1996, 'Sheet flow modelled as pure convection', in *Proceedings of 25th International Conference on Coastal Engineering*, Orlando, Florida, pp. 3784-90.

Davidson, MA, Lewis, RP & Turner, IL 2010, 'Forecasting seasonal to multi-year shoreline change', *Coastal Engineering*, vol. 57, no. 6, pp. 620-9.

Davidson, MA, Splinter, KD & Turner, IL 2013, 'A simple equilibrium model for predicting shoreline change', *Coastal Engineering*, vol. 73, pp. 191-202.

Davidson, MA & Turner, IL 2009, 'A behavioral template beach profile model for predicting seasonal to interannual shoreline evolution', *Journal of Geophysical Research*, vol. 114, no. F1, p. F01020.

Davidson, MA, Turner, IL & Guza, RT 2011, 'The effect of temporal wave averaging on the performance of an empirical shoreline evolution model', *Coastal Engineering*, vol. 58, no. 8, pp. 802-5.

Davies, AG & Villaret, C 1999, 'Eulerian drift induced by progressive waves above rippled and very rough beds', *Journal of Geophysical Research*, vol. 104, no. C1, pp. 1465-88.

de Vroeg, JH, Smit, ESP & Bakker, WT 1988, 'Coastal genesis', in *Proceedings of 21st Conference on Coastal Engineering*, Torremolinos, Spain, pp. 2825-39.

Dean, RG & Dalrymple, R 2002, *Coastal processes with engineering applications*, Cambridge University Press, Cambridge, New York.

Dibajnia, M, Shimizu, T & Watanabe, A 1994, 'Profile change of a sheet flow dominated beach', in *Proceedings of 24th International Conference on Coastal Engineering*, Kobe, Japan, vol. 2, pp. 1946-60.

Dibajnia, M & Watanabe, A 1992, 'Sheet flow under nonlinear waves and currents', in *Proceedings of 23rd International Conference on Coastal Engineering*, Venice, Italy, vol. 2, pp. 2015-28.

Dibajnia, M & Watanabe, A 1996, 'A transport rate formula for mixed-size sands', in *Proceedings of 25th International Conference on Coastal Engineering*, Orlando, Florida, vol. 3, pp. 3791-804.

Dohmen-Janssen, CM 1999, 'Grain size influence on sediment transport in oscillatory sheet flow: phase lags and mobile-bed effects', PhD thesis, Delft University of technology.

Drake, TG & Calantoni, J 2001, 'Discrete particle model for sheet flow sediment transport in the nearshore', *Journal of Geophysical Research*, vol. 106, no. C9, pp. 19859-68.

Dubarbier, B, Castelle, B, Marieu, V & Ruessink, G 2015, 'Process-based modeling of cross-shore sandbar behavior', *Coastal Engineering*, vol. 95, pp. 35-50.

Emery, KO 1961, 'A simple method of measuring beach profiles', *Limnology and Oceanography*, vol. 6, no. 1, pp. 90-3.

Fenton, J 1985, 'A Fifth‐Order Stokes Theory for Steady Waves', *Journal of waterway, port, coastal, and ocean engineering*, vol. 111, no. 2, pp. 216-34.

Fernandez Luque, R & Van Beek, R 1976, 'Erosion And Transport Of Bed-Load Sediment', *Journal of hydraulic research*, vol. 14, no. 2, pp. 127-44.

Flick, RE 1978, 'Study of shoaling waves in the laboratory', PhD thesis, University of California, San Diego.

Flick, RE, Guza, RT & Inman, DL 1981, 'Elevation and velocity measurements of laboratory shoaling waves', *Journal of Geophysical Research: Oceans*, vol. 86, no. C5, pp. 4149-60.

Fredsøe, J & Deigaard, R 1992, *Mechanics of coastal sediment transport*, vol. 3., World Scientific, Singapore.

Gallagher, EL, Elgar, S & Guza, RT 1998, 'Observations of sand bar evolution on a natural beach', *Journal of Geophysical Research: Oceans*, vol. 103, no. C2, pp. 3203-15.

Gourlay, MR 1968, *Beach and Dune Erosion Tests*, M935/M936, Delft Hydraulic Laboratory.

Guza, RT & Thornton, EB 1980, 'Local and shoaled comparisons of sea surface elevations, pressures, and velocities', *Journal of Geophysical Research: Oceans*, vol. 85, no. C3, pp. 1524-30.

Hallermeier, RJ 1981, 'Terminal settling velocity of commonly occurring sand grains', *Sedimentology*, vol. 28, no. 6, pp. 859-65.

Hanes, DM & Huntley, DA 1986, 'Continuous measurements of suspended sand concentration in a wave dominated nearshore environment', *Continental Shelf Research*, vol. 6, no. 4, pp. 585-96.

Harley, MD, Turner, IL, Short, AD, Bracs, MA, Phillips, MS, Simmons, JA & Splinter, KD 2015, 'Four decades of coastal monitoring at Narrabeen-Collaroy Beach: The past, present and future of this unique dataset', in *Coasts and Ports 2015 Conference* Auckland, New Zealand.

Harley, MD, Turner, IL, Short, AD & Ranasinghe, R 2011, 'A reevaluation of coastal embayment rotation: The dominance of cross-shore versus alongshore sediment transport processes, Collaroy-Narrabeen Beach, southeast Australia', *Journal of Geophysical Research*, vol. 116, no. 4.

Hattori, M & Kawamata, R 1980, 'Onshore-offshore transport and beach profile change', in *Proceedings of 17th International Conference on Coastal Engineering*, Sydney, Australia, vol. 2, pp. 1175-93.

Hegge, B, Eliot, I & Hsu, J 1996, 'Sheltered Sandy Beaches of Southwestern Australia', *Journal of Coastal Research*, vol. 12, no. 3, pp. 748-60.

Henderson, SM, Allen, JS & Newberger, P 2004, 'Nearshore sandbar migration predicted by an eddy-diffusive boundary layer model', *Journal of Geophysical Research*, vol. 109, no. C6, p. C06024.

Hoefel, F & Elgar, S 2003, 'Wave-induced sediment transport and sandbar migration', *Science (New York, N.Y.)*, vol. 299, no. 5614, pp. 1885-7.

Holman, RA & Stanley, J 2007, 'The history and technical capabilities of Argus', *Coastal Engineering*, vol. 54, no. 6–7, pp. 477-91.

Hughes, SA & Fowler, JE 1990, 'Validation of movable-bed modeling guidance', in *Proceedings of 22nd International Conference on Coastal Engineering* Delft, The Netherlands, pp. 2457-70.

Hurther, D & Thorne, PD 2011, 'Suspension and near-bed load sediment transport processes above a migrating, sand-rippled bed under shoaling waves', *Journal of Geophysical Research*, vol. 116, no. C7, p. C07001.

Inman, DL & Bowen, AJ 1962, 'Flume experiments on sand transport by waves and currents', in *Proceedings of 8th International Conference on Coastal Engineering*, Mexico City, Mexico, vol. 1, pp. 137-50.

Jacobsen, NG & Fredsøe, J 2014, 'Formation and development of a breaker bar under regular waves. Part 2: Sediment transport and morphology', *Coastal Engineering*, vol. 88, pp. 55-68.

Jara, MS, González, M & Medina, R 2015, 'Shoreline evolution model from a dynamic equilibrium beach profile', *Coastal Engineering*, vol. 99, pp. 1-14.

Johnson, JW 1949, 'Scale effects in hydraulic models involving wave motion', *Eos, Transactions American Geophysical Union*, vol. 30, no. 4, pp. 517-25.

Kemp, PH & Simons, RR 1983, 'The interaction of waves and a turbulent current: waves propagating against the current', *Journal of Fluid Mechanics*, vol. 130, pp. 73-89.

King, DB, Jr 1991, 'Studies in oscillatory flow bedload sediment transport', Ph D thesis, University of California, San Diego (Scripps).

Kobayashi, N & Jung, H 2012, 'Beach Erosion and Recovery', *Journal of waterway, port, coastal, and ocean engineering*, vol. 138, no. 6, pp. 473-83.

Kranenburg, WM, Ribberink, JS, Schretlen, JJ & Uittenbogaard, RE 2013, 'Sand transport beneath waves: The role of progressive wave streaming and other free surface effects', *Journal of Geophysical Research: Earth Surface*, vol. 118, pp. 1-18.

Kraus, NC & Larson, M 1988, *Beach Profile Change Measured in the Tank for Large Waves 1956-1957 and 1962*, US Army Corps of Engineers.

Kraus, NC, Larson, M & Kriebel, DL 1991, 'Evaluation of beach erosion and accretion predictors', in *Coastal Sediments (1991)*, Seattle, Washington, pp. 572-87.

Kuriyama, Y 2012, 'Process-based one-dimensional model for cyclic longshore bar evolution', *Coastal Engineering*, vol. 62, pp. 48-61.

Larson, M & Kraus, NC 1992, *Analysis of cross-shore movement of natural longshore bars and material placed to create longshore bars*, DTIC Document.

Larson, M, Kraus, NC & Byrnes, MR 1990, *SBEACH: Numerical Model for Simulating Storm-Induced Beach Change. Report 2. Numerical Formulation and Model Tests*, DTIC Document.

Larson, M, Kraus, NC & Wise, RA 1999, 'Equilibrium beach profiles under breaking and non-breaking waves', *Coastal Engineering*, vol. 36, no. 1, pp. 59-85.

Lippmann, TC, Holman, RA & Hathaway, KK 1993, 'Episodic, Nonstationary Behavior of a Double Bar System at Duck, North Carolina, U.S.A., 1986-1991', *Journal of Coastal Research*, pp. 49-75.

Longuet-Higgins, M 1957, 'The mechanics of the boundary layer near the bottom in a progressive wave', in *Proceedings of 6th International Conference on Coastal Engineering*, Gainsville, Florida, pp. 184-93.

Ludka, BC, Guza, RT, O'Reilly, WC & Yates, ML 2015, 'Field evidence of beach profile evolution toward equilibrium', *Journal of Geophysical Research: Oceans*, vol. 120, pp. 1-24.

Lynett, PJ & Liu, PLF 2008, *Modeling Wave Generation, Evolution, and Interaction with Depth-Integrated, Dispersive Wave Equations, COULWAVE Code Manual ,Cornell Univerisity Long and Intermediate Wave Modeling Package*, vol. 2, Cornell Univeristy, Ithaca, NY.

Meyer-Peter, E & Müller, R 1948, 'Formulas for bed-load transport', in *Proc International Association of Hydraulic Structures Research* Stockholm, Sweden.

Miller, JK & Dean, RG 2004, 'A simple new shoreline change model', *Coastal Engineering*, vol. 51, no. 7, pp. 531-56.

Nairn, RB 1990, 'Prediction of Cross-Shore Sediment Transport and Beach Profile Evolution', Ph.D. thesis, Imperial College.

Nairn, RB 1991, *Operation manual for the advanced nearshore profile model*.

Nairn, RB & Southgate, HN 1993, 'Deterministic profile modelling of nearshore processes. Part 2. Sediment transport and beach profile development', *Coastal Engineering*, vol. 19, no. 1–2, pp. 57-96.

Newe, J, Peters, K & Dette, HH 1999, 'Profile development under storm conditions as a function of the beach slope', in *Coastal Sediments* Long Island, New York, pp. 2582-96.

Nielsen, P 1983, 'Entrainment and distribution of different sand sizes under water waves', *JOURNAL OF SEDIMENTARY PETROLOGY*, vol. 53, no. 2, pp. 423-8.

Nielsen, P 1986a, 'Local approximations: A new way of dealing with irregular waves', in *Proceedings of 20th International Conference on Coastal Engineering*, Taipei, Taiwan, vol. 1.

Nielsen, P 1986b, 'Suspended sediment concentrations under waves', *Coastal Engineering*, vol. 10, no. 1, pp. 23-31.

Nielsen, P 1988, 'Three simple models of wave sediment transport', *Coastal Engineering*, vol. 12, no. 1, pp. 43-62.

Nielsen, P 1989, 'Analysis of natural waves by local approximations', *Journal of Waterway, Port, Coastal and Ocean Engineering*, vol. 115, p. 384.

Nielsen, P 1992, *Coastal bottom boundary layers and sediment transport*, vol. 4., World Scientific, Singapore.

Nielsen, P 2006, 'Sheet flow sediment transport under waves with acceleration skewness and boundary layer streaming', *Coastal Engineering*, vol. 53, no. 9, pp. 749-58.

Nielsen, P 2009, *Coastal and estuarine processes*, vol. 29, Advanced Series on Ocean Engineering, World Scientific, Singapore.

Nielsen, P & Callaghan, DP 2003, 'Shear stress and sediment transport calculations for sheet flow under waves', *Coastal Engineering*, vol. 47, no. 3, pp. 347-54.

Nielsen, P & Guard, PA 2010, 'Vertical scales and shear stresses in wave boundary layers over movable beds', in *Proceedings of 32nd International Conference on Coastal Engineering*, Shanghai, China.

O'Hare, TJ & Davies, AG 1993, 'Sand bar evolution beneath partially-standing waves: laboratory experiments and model simulations', *Continental Shelf Research*, vol. 13, no. 11, pp. 1149-81.

Pape, L, Plant, N & Ruessink, B 2010, 'On cross-shore migration and equilibrium states of nearshore sandbars', *Journal of Geophysical Research*, vol. 115, no. F3, p. F03008.

Phillips, MS, Turner, IL, Cox, RJ, Splinter, KD & Harley, MD 2015, 'Will the sand come back? Observations and characteristics of beach recovery', in *Coasts & Ports 2015 Conference*, Auckland, New Zealand.

Plant, NG, Holman, RA, Freilich, MH & Birkemeier, WA 1999, 'A simple model for interannual sandbar behavior', *Journal of Geophysical Research: Oceans*, vol. 104, no. C7, pp. 15755-76.

Quartel, S, Kroon, A & Ruessink, BG 2008, 'Seasonal accretion and erosion patterns of a microtidal sandy beach', *Marine geology*, vol. 250, no. 1–2, pp. 19-33.

Ribberink, JS 1998, 'Bed-load transport for steady flows and unsteady oscillatory flows', *Coastal Engineering*, vol. 34, no. 1–2, pp. 59-82.

Ribberink, JS & Al-Salem, A 1990, 'Bedforms, sediment concentrations and sediment transport in simulated wave conditions', in *Proceedings of 22nd International Conference on Coastal Engineering*, Delft, The Netherlands, pp. 2318-31.

Ribberink, JS, McLean, SR, Dohmen-Janssen, CM, Hanes, DM & Vincent, C 2000, 'Near-Bed Sand Transport Mechanisms under Waves—A Large-Scale Flume Experiment (Sistex99)', in *Proceedings of 27th International Conference on Coastal Engineering*, Sydney, Australia, pp. 3263-76.

Roelvink, DA & Reniers, AJHM 1995, *LIP11D Deltaflume Experiments: A dataset for profile model validation* Delft Hydraulics, The Netherlands.

Saville, T, Jr. 1957, 'Scale effects in two dimensional beach studies', in *Proceedings of 7th IAHR Congress*, Lisbon, Portugal, vol. 1.

Schepers, JD 1978, 'Zandtransport onder invloed van golven en een eenparige stroom bij varierende korreldiameter', Masters thesis, Delft University of Technology.

Schretlen, JJLM, Ribberink, JS, Kleinhans, M & O'Donoghue, T 2010, 'Boundary layer flow and sand transport under full scale surface waves', in *Proceedings of 32nd International Conference on Coastal Engineering*, Shanghai, China, pp. 1-14.

Seelig, WN 1983, 'Understanding Beach Erosion and Accretion', *Journal of Waterway, Port, Coastal and Ocean Engineering*, vol. 109, no. 4, pp. 490-4.

Shimamoto, T, Nielsen, P & Baldock, TE 2013, 'Updated "grab and dump" model for sediment transport under acceleration skewed waves', in *Coastal Dynamics*, Arcachon, France, pp. 1495-504.

Short, AD 1975, 'Multiple offshore bars and standing waves', *Journal of Geophysical Research*, vol. 80, no. 27, pp. 3838-40.

Short, AD & Aagaard, T 1993, 'Single and Multi-Bar Beach Change Models', *Journal of Coastal Research*, pp. 141-57.

Silva, PA, Abreu, T, A, DAvd, Sancho, F, Ruessink, B, Van der Werf, J & Ribberink, JS 2011, 'Sediment transport in nonlinear skewed oscillatory flows: Transkew experiments', *Journal of hydraulic research*, vol. 49, no. sup1, pp. 72-80.

Soulsby, R 1997, *Dynamics of marine sands*, Thomas Telford Ltd, London.

Southgate, HN & Nairn, RB 1993, 'Deterministic profile modelling of nearshore processes. Part 1. Waves and currents', *Coastal Engineering*, vol. 19, no. 1–2, pp. 27-56.

Splinter, KD, Turner, IL, Davidson, MA, Barnard, P, Castelle, B & Oltman-Shay, J 2014, 'A generalized equilibrium model for predicting daily to interannual shoreline response', *Journal of Geophysical Research: Earth Surface*, vol. 119, no. 1-23.

Stive, M 1986, 'A model for cross-shore sediment transport', in *Proceedings of 20th International Conference on Coastal Engineering* Taipei, Taiwan, vol. 1.

Swart, DH 1974, *Offshore sediment transport and equilibrium beach profiles*, Delft Hydraulics Laboratory.

Thornton, EB, Galvin, JJ, Bub, FL & Richardson, DP 1976, 'Kinematics of breaking waves', in *Proceedings of 15th International Conference on Coastal Engineering*, Honolulu, Hawaii, vol. 1, pp. 461-176.

Tilmans, W 1979, 'Zandtransport in de golfrichting in relatief ondiep water', Delft University of Technology.

Traykovski, P, Hay, AE, Irish, JD & Lynch, JF 1999, 'Geometry, migration, and evolution of wave orbital ripples at LEO-15', *Journal of Geophysical Research*, vol. 104, no. C1, pp. 1505-24.

Uliczka, K & Dette, HH 1988, 'About the influence of erosion volume on cross-shore sediment movement at prototype scale', in *Proceedings of 21st Conference on Coastal Engineering*, Torremolinos, Spain.

Van der A, DA, O'Donoghue, T & Ribberink, JS 2010a, 'Measurements of sheet flow transport in acceleration-skewed oscillatory flow and comparison with practical formulations', *Coastal Engineering*, vol. 57, no. 3, pp. 331-42.

Van der A, DA, Ribberink, JS, van der Werf, JJ & O'Donoghue, T 2010b, 'New practical model for sand transport induced by non-breaking waves and currents', in *Proceedings of 32nd International Conference on Coastal Engineering*, Shanghai, China, vol. 1.

Van der A, DA, Ribberink, JS, van der Werf, JJ, O'Donoghue, T, Buijsrogge, RH & Kranenburg, WM 2013, 'Practical sand transport formula for non-breaking waves and currents', *Coastal Engineering*, vol. 76, pp. 26-42.

Van der Werf, JJ, Doucette, JS, O'Donoghue, T & Ribberink, JS 2007, 'Detailed measurements of velocities and suspended sand concentrations over full-scale ripples in regular oscillatory flow', *Journal of Geophysical Research*, vol. 112, no. F2.

Van der Werf, JJ, Magar, V, Malarkey, J, Guizien, K & O'Donoghue, T 2008, '2DV modelling of sediment transport processes over full-scale ripples in regular asymmetric oscillatory flow', *Continental Shelf Research*, vol. 28, no. 8, pp. 1040-56.

Van der Werf, JJ, Ribberink, JS, O'Donoghue, T & Doucette, JS 2006, 'Modelling and measurement of sand transport processes over full-scale ripples in oscillatory flow', *Coastal Engineering*, vol. 53, no. 8, pp. 657-73.

Van Rijn, LC, Nieuwjaar, MW, van der Kaay, T, Nap, E & van Kampen, A 1993, 'Transport of fine sands by currents and waves', *Journal of waterway, port, coastal, and ocean engineering*, vol. 119, no. 2, pp. 123-43.

Van Rijn, LC, Tonnon, PK, Sánchez-Arcilla, A, Cáceres, I & Grüne, J 2011, 'Scaling laws for beach and dune erosion processes', *Coastal Engineering*, vol. 58, no. 7, pp. 623-36.

Van Rijn, LC, Walstra, DJR, Grasmeijer, B, Sutherland, J, Pan, S & Sierra, JP 2003, 'The predictability of cross-shore bed evolution of sandy beaches at the time scale of storms and seasons using process-based Profile models', *Coastal Engineering*, vol. 47, no. 3, pp. 295-327.

Vellinga, P 1975, 'Zandtransport door golven en de invloed van stoorgolven', Masters thesis, TU Delft.

Watanabe, A & Sato, S 2004, 'A sheet-flow transport rate formula for asymmetric, forward-leaning waves and currents', in *Proceedings of 29th International Conference on Coastal Engineering*, Lisbon, Portugal, vol. 29, p. 1703.

Wright, LD & Short, AD 1984, 'Morphodynamic variability of surf zones and beaches: A synthesis', *Marine geology*, vol. 56, no. 1, pp. 93-118.

Wright, LD, Short, AD & Green, MO 1985, 'Short-term changes in the morphodynamic states of beaches and surf zones: An empirical predictive model', *Marine geology*, vol. 62, no. 3, pp. 339-64.

Yates, ML, Guza, RT & O'Reilly, WC 2009, 'Equilibrium shoreline response: Observations and modeling', *Journal of Geophysical Research*, vol. 114.

Yates, ML, Guza, RT, O'Reilly, WC, Hansen, JE & Barnard, PL 2011, 'Equilibrium shoreline response of a high wave energy beach', *Journal of Geophysical Research*, vol. 116.